High-performance metallo-dielectric photonic crystals: Design, fabrication, and testing of a practical emitter for portable thermophotovoltaic generators

by

Reyu Sakakibara

Submitted to the Department of Electrical Engineering and Computer Science
in partial fulfillment of the requirements for the degree of

Doctor of Philosophy in Electrical Engineering and Computer Science

at the

MASSACHUSETTS INSTITUTE OF TECHNOLOGY

September 2021

© Massachusetts Institute of Technology 2021. All rights reserved.

Author .....
Department of Electrical Engineering and Computer Science
August 27, 2021

Certified by .....
Ivan Čelanović
Principal Research Scientist, Institute for Soldier Nanotechnologies
Thesis Supervisor

Accepted by .....
Leslie Kolodziejski
Professor of Electrical Engineering and Computer Science
Chair, Department Committee on Graduate Students

High-performance metallo-dielectric photonic crystals: Design, fabrication, and testing of a practical emitter for portable thermophotovoltaic generators

by

Reyu Sakakibara

Submitted to the Department of Electrical Engineering and Computer Science
on August 27, 2021, in partial fulfillment of the
requirements for the degree of
Doctor of Philosophy in Electrical Engineering and Computer Science

Abstract

Hydrocarbon thermophotovoltaic (TPV) systems, a concept first proposed in the 1950s, are emerging as a viable power source for small, portable generators for a spectrum of applications such as UAVs and robotic platforms. In a TPV system, an emitter is heated to above 1000 K, producing thermal radiation that is then converted to electricity by a low-band-gap photovoltaic cell (in hydrocarbon TPV, the heat source is fuel combustion). Unfortunately, state of the art TPV systems still have low efficiencies (<10%).

One approach to increase both the efficiency and power density of the system is to use a selective emitter (one which preferentially emits in the wavelength range that can be converted by the photovoltaic cell). A promising class of broadband selective emitters is two-dimensional photonic crystals, which consist of a square array of cavities etched into a refractory metal substrate, and whose emission spectrum can be tuned by adjusting the geometry of the cavities. In particular, previous work has shown that photonic crystals made of tantalum and conformally coated with hafnium oxide can achieve in-band emissivities up to 0.6, allowing for prototype systems with 4.4% fuel-to-electricity efficiency. Even higher in-band emissivities of 0.8-0.9 are theoretically possible using a metallo-dielectric, or filled, photonic crystal: a tantalum photonic crystal both filled and capped with hafnium oxide.

This thesis presents a metallo-dielectric photonic crystal with close to full theoretical performance. Using a combination of numerical simulations and cross section images, I identified a number of major geometric imperfections in previous prototypes: a hollow air core within the cavity, a thick and uneven capping layer of hafnium oxide, and the recession of hafnium oxide from the top of cavity. I then developed and implemented a fabrication process to achieve a better-filled cavity and a thin capping layer of hafnium oxide, enabling in-band emissivities of 0.7-0.9. Full system simulations predict an up to 37.5% increase in system output power: 6.0 W for 100 W fuel input, compared to 4.4 W system output power for my group's previous prototype

system. This selective emitter paves the way towards efficient, practical, and portable mesoscale generators.

Thesis Supervisor: Ivan Čelanović
Title: Principal Research Scientist, Institute for Soldier Nanotechnologies

Acknowledgments

My PhD would not have been possible without all the support and encouragement I got from people at MIT and beyond.

I was very fortunate to have as my advisor Ivan Čelanović, who on top of being incredibly patient and understanding, supported me in taking on the more-ambitious projects of writing a review paper and working on the filled photonic crystal for this thesis. I also enjoyed my chats with him about non-technical books and movies.

I am indebted to my labmates Veronika Stelmakh and Walker Chan for their help, especially in the early days when I was just starting out. Veronika showed me her fabrication and characterization process, Walker walked me through system simulations and trained me on the furnace; both of them helped me get set up with simulations on S^4 and Jupyter notebook.

I would also like to thank my closest collaborators. Bob Geil of CHANL at UNC Chapel Hill, who did the DRIE on the tantalum substrates as well as most of the ALD, who provided the idea on how to fill the photonic crystal, and to whom I kept shipping the same battered old box filled with samples. I relied on the know-how of Stephan Krämer of Harvard CNS to prepare the cross sections and image them (as well as SEM elemental analysis) and we worked closely especially during COVID, via Zoom and TeamViewer. I worked with Tim Savas of LumArray early in my PhD: he did the exposures with a Mach-Zehnder interferometer, and provided valuable advice about designing the tri-layer stack.

I am also grateful to my thesis committee members, Leslie Kolodziejski and Farnaz Niroui, for their feedback and encouragement. Leslie, my academic advisor, I've known since I began my studies at MIT. Farnaz I've known since my early days as well, first as a PhD student and then as a professor.

I would also like to thank my friends and family. A special mention to: the Friday dinner crew, Parker Gould, Mitchell Hsing, Peter Krogen, Koustuban Ravi, Greg Stein, and Samantha Dale Strasser; Thomas Bourgeat, Xiaowei Cai, Vanessa Carlson, Sara Mouradian, Amy McCarthy (thanks for the snacks!), and Naomi Ginsberg. I

am also grateful to my family and the Pit-Claudel family, especially Clément for even more chocolate cakes and LaTeX tips.

Finally, some other shout-outs, in no particular order:

- Simulations help
  - Michael Ghebrebrhan, a former group member, with whom I had several valuable discussions about the theory of the photonic crystal, and simulations.
  - Adrian Yi Xiang Yeng, another former group member, who answered many of S^4 simulation-related questions.
  - Li Jing and Peter Lu, who answered my questions about the ab-initio server, where I ran most of my S^4 simulations.
- Fabrication assistance
  - Jim Daley of NSL for help with interference lithography - for training me on the Lloyd's Mirror.
  - Jun Yan of CHANL at UNC Chapel Hill, for training me on several tools during my visit to UNC in August 2019, and for suggesting the use of combined CHF_3 and CF_4 gas to change the etch selectivity of an RIE process step.
  - Ryan O'Keefe and Tim Turner, who trained me on and helped me troubleshoot the diesaw (when it turned out it was difficult to dice tantalum wafers).
  - Kurt Broderick, who answered my random fabrication questions.
- Planarization and etch back assistance
  - Mark Mondol who suggested using FOx e-beam resist for planarization and suggested writing to the Elionix and NSL users mailing list.
  - Mark Schattenburg for suggesting CMP, though I didn't take that route in the end.
  - Qingyang Du, who kindly offered to lend his group's FOx, which he had used successfully for planarization (though I didn't take up his offer).
  - Ian Christen, for the suggestion to use Filmtronics Silicates 15A, as an

alternate to FOx, lending some of his old Silicates 15A, and sending some recipes.

  - Jim Daley for training me on the RTA at NSL for initial anneals of spin-on glass, and for evaporating HfO_2 films on my samples.
  - Ella Wassweiler, for sputtering HfO_2 on my samples.
  - Scott Wheelock especially, as well as Ben and Seth Burtner of Filmtronics, for extensive troubleshooting help with Silicates 15A spin-on glass.

- Hafnium oxide sol-gel help

  - Zhanjie Wang and Hiroyuki Kokawa, whose paper on sol-gel-based hafnium oxide fabrication we consulted
  - Daisuke Kotegawa and Masami Kawahara of Kojundo Chemical Laboratories, for sol-gel troubleshooting

- Characterization assistance

  - Amar Kumbhar of CHANL at UNC Chapel Hill, for several SEM and focused ion beam imaging sessions during my visit to UNC in August 2019.
  - Josh Kubiak and Lennon Luo for training me on the TGA at ISN.
  - Mayuran Saravanapavanantham, for pointing me to the Perkin Elmer Lambda 1050 UV-vis spectrophotometer at CMSE / MRL.
  - Gary Riggott, for training me on the Cary 5000 UV-vis spectrophotometer.
  - Anna Osherov, for training me on the Cary 5000 UV-vis spectrophotometer, and also for advice on how to perform elemental analysis on my samples.
  - Steve Kooi, for training on the Cary 7000 UV-vis spectrophotometer and for lending me diffuse reflectance standards.
  - Tim McClure, for training on the Lambda 1050 UV-vis spectrophotometer (both the integrating sphere and VN absolute reflectance mode), for training on the absolute reflectance VW accessory on the Cary 5000, and for getting Agilent tech support to recalibrate the detectors on the Cary

5000.
  - Yi Huang, for lending the plastic cover for the UV-vis spectrophotometer.
  - Austin Akey of Harvard CNS, for focused ion beam imaging assistance.

- Technical communication assistance from the EECS Communication Lab, especially Diana Chien, Alison Takemura, Deanna Montgomery, Alex Hanson, Nili Persits, Greg Stein, and Samantha Dale Strasser.
- Administrative assistance
  - Josh Freedman and Maureen Caulfield for help with anything financial
  - Marlisha McDaniels for help with the fax machine, the printer, and for letting me into the ISN building several times
  - Amy Tatem-Bannister for lending me a TGA pan and for help looking over chemical SOPs.
  - Donna Johnson for reminding me to label the chemical waste tag properly.
  - Janet Fischer, Alicia Duarte, and others in the EECS grad office for miscellaneous program-related things.

Contents

List of Figures

List of Tables

Chapter 1

Introduction

In the thermophotovoltaic (TPV) energy conversion scheme, a heat source heats to high temperature an emitter that emits thermal radiation that is subsequently converted to electricity by a photovoltaic cell. In other words, a TPV system converts heat to electricity using light as an intermediary. A TPV system consists of at least three components: a heat source, an emitter, and a photovoltaic cell. While TPV conversion seems unnecessarily convoluted, it has some advantages, for example the physical separation of the hot side (with the heat source) from the cold side where electricity is generated. However, it is difficult to develop high-performance TPV systems in part due to the need to coordinate multiple subsystems. In addition, there are several design parameters for TPV, such as (but not limited to) the choice of heat source (typically fuel combustion, solar energy, or radioisotope decay), hot side temperature, photovoltaic cell band-gap, choice of emitter, and the distance between the emitter and cells.

While the concept of TPV is decades old, proposed independently by H.H. Kolm in 1956 [4] and Pierre Aigrain in 1960 [5], TPV development has historically been slow. The 1960s saw early development in TPV in the US, due to the US Army's interest in TPV as a potential portable microgenerator powered by fossil fuels, but in the 1970s the US Army passed over TPV in favor of thermoelectric technology, which was more advanced at the time. In the 1970s, 1980s, and 2000s, there was renewed interest, in Europe in particular, in TPV with solar energy as the heat source. However, one

of the major limitations for early TPV development was the lack of high-quality, low-band-gap photovoltaic cells (GaSb, InGaAs, and InGaAsSb) that are required to operate at the hot side at relatively "more moderate" high temperatures of 1000-1500 K. Following the development of low-band-gap photovoltaic cells in the 1990s to mid-2000s, much of the research on TPV in the 2000s-2010s focused on development of components for spectral control, including selective emitters, front side filters, and back surface reflectors. A detailed timeline of TPV development can be found in Appendix A of Veronika Stelmakh's PhD thesis [6].

The focus of this thesis is specifically on a selective emitter developed for TPV systems that use hydrocarbon fuel combustion as heat source.

1.1 Motivation

TPV systems that use hydrocarbon fuel combustion are emerging as a viable power source for portable generators for off-the-grid applications in the 1-100 W range, such as sensors, robotic platforms, and other portable computational and communication equipment. With the current state of the art, there are two choices for portable power at the mesoscale (characteristic length scales of millimeters): to take several lithium-ion batteries ($\sim$100 mW) or take a bulky, conventional diesel generator ($\sim$1 kW). However, lithium-ion batteries are approaching their theoretical limit in terms of energy density ($\sim$200 Whr/kg) [7]; on the other hand, the size of conventional generators cannot be reduced due to scaling laws that govern internal combustion engines [8]. Meanwhile, conventional hydrocarbon fuels have higher energy densities of $\sim$12 kWhr/kg [8], so that even a relatively inefficient generator can provide more power than batteries.

Several alternatives to batteries have been researched for both military and commercial applications, but they have different advantages and downsides [6, 8]:

- Mechanical engines, such as microturbines [9] or Wankel engines [10, 11], have moving parts and are subject to wear and frictional and thermal losses. These losses are especially pronounced at the millimeter scale, where the surface area

to volume ratio is high.

- Electrochemical approaches, such as solid oxide or direct methanol fuel cells [12, 13], have high efficiencies but use catalysts that are sensitive to poisoning by impure fuels. A discussion of the Horizon MiniPak, a commercially available hydrogen fuel cell, can be found in Walker Chan's thesis [8].
- Thermal approaches, such as thermoelectrics [14, 15] and TPV, have quiet and static conversion processes (no moving parts) but have low efficiencies and require high temperatures. Thermoelectrics in particular use materials that must simultaneously support a high temperature gradient and allow for the flow of carriers (electrons).

Some advantages specific to TPV are as follows [6, 8]:

- Physically separated hot and cold sides: the hot side with the heat source and emitter are physically separated from the cold side where electricity is generated. In addition, there are no fundamental temperature gradients across materials that would lead to thermal stresses during startup and operation.

- Quiet and static conversion process: fundamentally, TPV does not require no moving parts, meaning no noise, wear, or vibration. That said, a microgenerator would likely need auxiliary components such as cooling and combustion air fans and a fuel pump.

- High power density: for a standard TPV system (not near-field TPV), thermal emission (from the emitter) is fundamentally limited only by Planck's blackbody law, with a T^4 dependence on temperature.

- Continuous combustion, for fuel-combustion-based TPV: unlike discontinuous combustion in a piston engine, continuous combustion enables efficient fuel utilization.

- Conventional fuel usage, for fuel-combustion-based TPV: conventional fuels (gasoline, diesel, JP-8) and biofuels can be used.

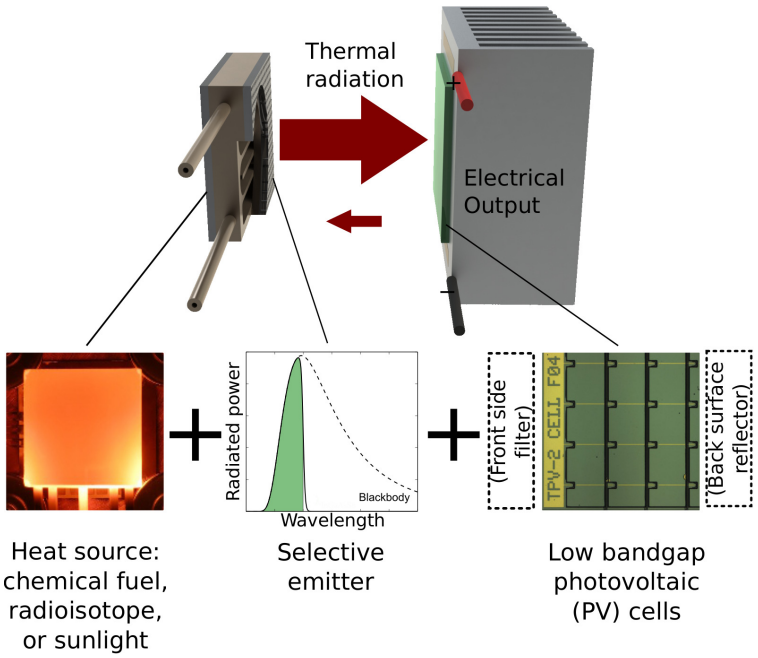

Figure 1-1: TPV system schematic. In a TPV system, a heat source heats an emitter to high temperature, and the thermal radiation from the emitter is converted to electricity by the photovoltaic cell. A TPV system consists of a hot side (on the left, consisting of a heat source in contact with an emitter) physically separated from the cold side (on the right, consisting of a low-band-gap photovoltaic cell, often cooled). In some cases the cold side has a front side filter or back surface reflector, as spectral control elements that reflect back out-of-band radiation to the hot side.

1.2 TPV components and some notes on system design, in brief

A TPV system has at least three components: a heat source, an emitter, and a low-band-gap photovoltaic cell, as shown in Figure 1-1.

1.2.1 Heat source

There are a few major kinds of heat sources for TPV:

- Fuel combustion. As discussed, TPV systems that use fuel combustion are being explored as portable power sources [16, 3].

- Radioisotope decay. Radioisotope TPV systems are powered by decay heat

released by plutonium-238, and can be useful as space power generators or in other cases where there is no external energy input [17, 18]. A broader discussion of power sources for space applications can be found at [19].

- Waste heat, for example from steel mills [20].

- Solar energy. Examples of prototype solar TPV systems can be found at [21, 22, 23, 24, 25, 26, 27]. Solar TPV systems typically have a concentrator that collects sunlight, which is then absorbed by a selective absorber as heat, and then an emitter that is in thermal contact with the absorber emits thermal radiation. The selective absorber has high absorptivity in the short wavelength regions in the the ultraviolet to visible range, whereas the emitter primarily emits lower-energy, near-infrared radiation [28, 29].

The key figures of merit to evaluate a TPV system may be specific to the application, for example radioisotope TPV systems are typically developed for deep space missions, which requires low weight, while cost and efficiency are likely a greater concern for stationary (non-portable) applications [30]. In our group's case, we are concerned with both system efficiency and overall system output power (or power per area).

1.2.2 Emitter

An emitter is any material that is heated to high temperature and emits thermal radiation. There is no one way to make an emitter; there are several types of emitters, and any given emitter can involve a different set of materials and different geometric configuration. To first order, one could consider the emitter as a blackbody radiator.

A more detailed discussion of emitters will follow in Sections 1.3 and 1.4 of this chapter.

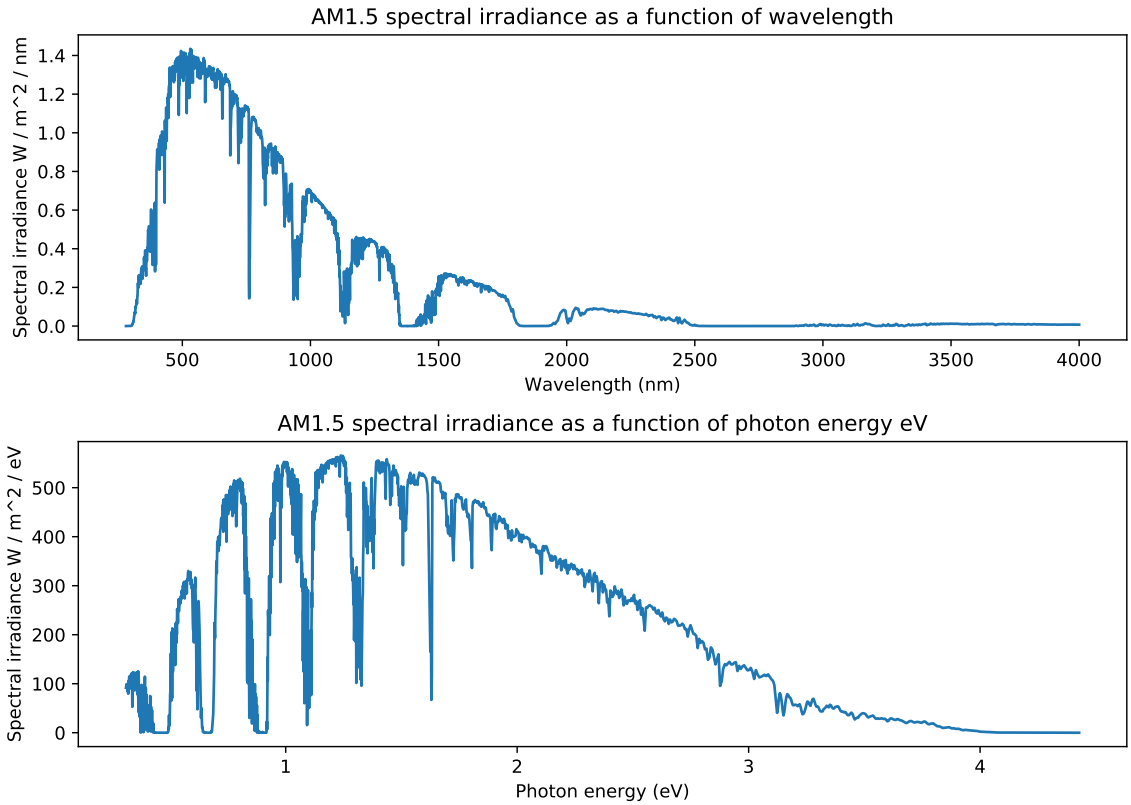

Figure 1-2: In the field of solar photovoltaics, where sunlight is directly converted to electricity, using cells such as silicon with band-gaps of 1.1 eV = 1.1 µm makes sense because of most of the solar spectrum is in the ultraviolet to visible range. TPV systems, however, typically rely on photovoltaic cells with lower band-gaps of 0.54-0.68 eV.

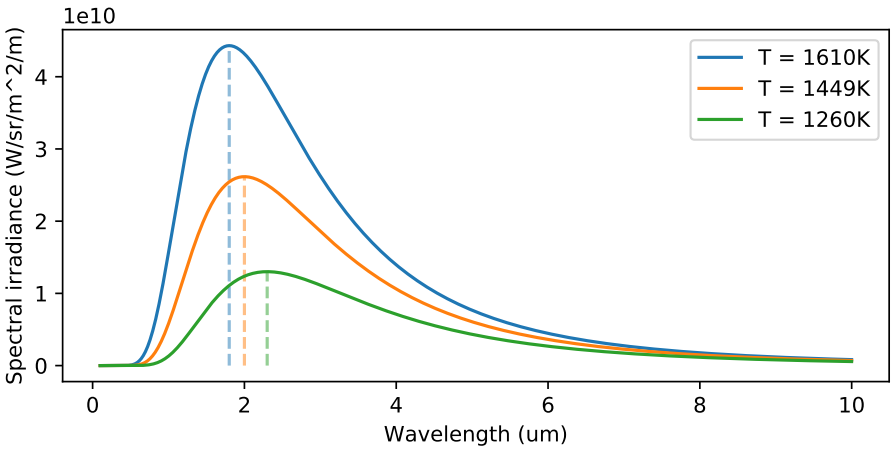

Figure 1-3: For TPV, the peak thermal radiation is typically in the near to mid-infrared (because of the emitter temperature), which requires low band-gap photovoltaic cells to convert the radiation. This plot shows blackbody radiation curves at three different temperatures where the peak emission corresponds to typical TPV photovoltaic cell band-gaps of 1.8, 2.0, and 2.3 µm. In addition, a higher emitter temperature leads to more radiated power per area (which scales as T^4) but also the requirement that the emitter be stable at this temperature.

1.2.3 Low band-gap photovoltaic cells

In TPV systems, the photovoltaic cell (also known as a TPV cell) converts thermal radiation to electricity. While some initial TPV experiments incorporated silicon or germanium photovoltaic cells with band-gap close to 1.1 eV (= 1.1 µm) [4], many TPV systems today are designed to use low band-gap photovoltaic cells such as GaSb (0.68 eV = 1.8 µm [31]), InGaAs (0.62 eV = 2.0 µm [32]), and InGaAsSb (0.54 eV = 2.3 µm [33]).

A typical photovoltaic cell in a TPV system works conceptually in the same way as a solar photovoltaic cell, but is designed to convert longer wavelengths of light. A silicon photovoltaic cell, with a band-gap of 1.1 eV = 1.1 µm, works well for the solar spectrum AM1.5 (Figure 1-2) that consists primarily of ultraviolet and visible light. On the other hand, the peak emission for a typical TPV emitter is in the near-infrared, as emitter temperatures are often in the 1000-1500 K range, at much lower temperatures compared to the sun's surface temperature of about 5772 K. As according to Wien's displacement law, the peak emission is at 1.8 µm for a blackbody

emitter 1337 °C = 1610 K, at 2.0 µm for 1176 °C = 1449 K, and at 2.3 µm for 987.0 °C = 1260.0 K, as shown in Figure 1-3.

The efficiency of the photovoltaic cell decreases as cell temperature decreases [34], so the photovoltaic cell is typically cooled either by passive cooling (our group's TPV system has the cells mounted on a heat sink [3]) or active cooling (water cooling is common [20, 24, 35]). According to [30], PV cells may require active cooling for applications with high power densities.

While operating the hot side at a higher temperature would enable the use of a higher band-gap photovoltaic cell and also lead to more radiated power per area from the emitter (as shown in Figure 1-3), it would also require the emitter to be stable at this higher temperature.

A more detailed discussion on the outstanding challenges in photovoltaic cells for TPV can be found at this review [30].

1.2.4 Configuration of the optical cavity

In a TPV system, the hot side and cold side are physically separated, forming an optical cavity, but must be arranged so that the radiation losses within the cavity are minimized.

The system schematic in Figure 1-1 shows a planar optical cavity, with a rectangular emitter parallel to an also-rectangular photovoltaic cell. In our group the distance between the cell and emitter is set to <1 mm so that the view factor (proportion of radiation from emitter that strikes photovoltaic cell surface) is above 0.9 [8].

An alternative configuration is one where the emitters and cells are arranged cylindrically [28, 16] or hexagonally [24].

One note: our group focuses on standard TPV systems, rather than near-field TPV systems, where there is a sub-wavelength gap between the emitter and the photovoltaic cell.

1.3 Overview of spectral (and angular) control

Without spectral control, a TPV system with a blackbody or greybody emitter suffers from high losses: the part of the thermal radiation cannot be converted to electricity by the photovoltaic cell is lost as heat.

The goal of spectral control to prevent such losses, and there are two general approaches: one, by reflecting these low-energy photons back to the emitter using filters or reflectors on the cold side, or two, by using a selective emitter that suppresses the emission of these photons. These approaches are not exclusive: it is possible to have a TPV system with a selective emitter and front side filter or a back surface reflector, or all three.

For several applications, angular control is also important: for example, angular selective absorption can enable more efficient solar absorbers, while in many cases for TPV it is beneficial to have spectral control over a wide range of angles [28, 36].

1.3.1 Cold side filters and reflectors

There are two approaches to cold side filters or reflectors: (1) allow all photons to reach the PV cell and then reflect back the below-band-gap or out-of-band photons and (2) filter out and reflect back out-of-band photons before they reach the PV cell. The first approach makes use of back surface reflectors (BSR) that are placed behind the photovoltaic cell, while the second approach uses front side filters placed in front of the photovoltaic cell, as shown in Figure 1-1. There are three main types of front side filters: interference filters, tandem filters, and frequency selective (FSS) filters. A more detailed discussion of cold side filters and reflectors can be found in the Appendix.

There has been recent demonstrations of efficient InGaAs photovoltaic cells with back surface reflectors, including one with a gold reflector [35] in 2019, and another with a layer of air or "air-bridge" [37] in 2020.

This approach enables the use of a greybody (non-selective) emitter, but it also usually requires that the optical cavity (formed by the emitter and the cell, with

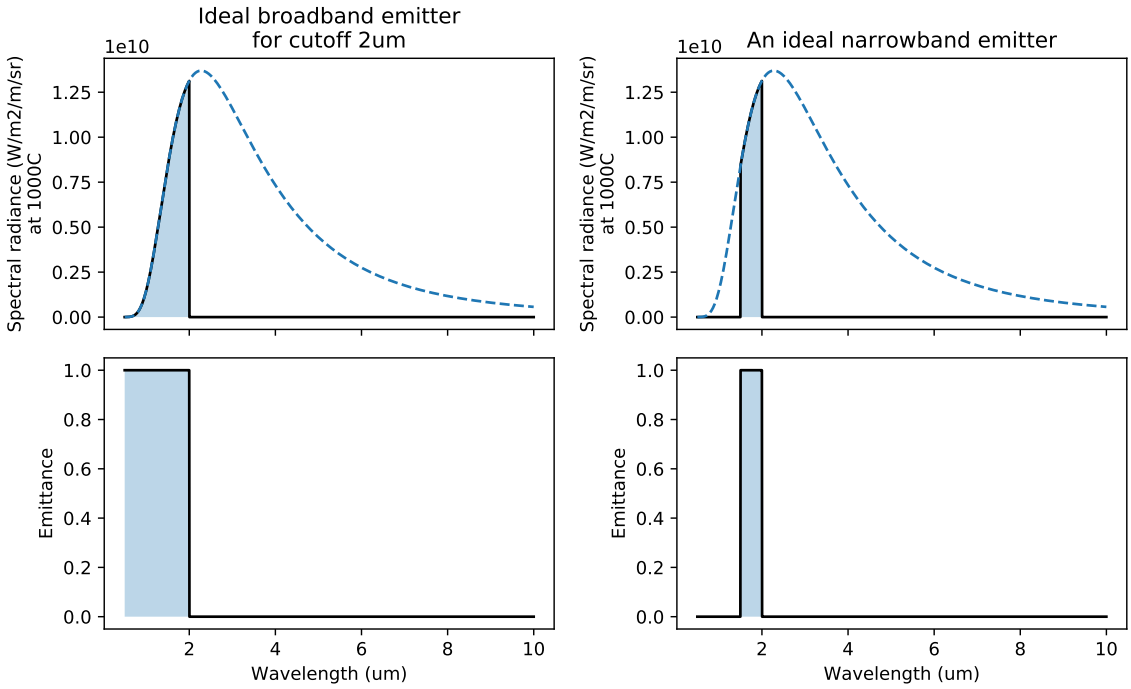

Figure 1-4: A selective emitter preferentially emits in-band photons and suppresses the out-of-band photons. A selective emitter may be designed to be broadband, as on the left, or narrow-band, as on the right. The top row shows radiated power per area per steradian, with the blue dotted line showing a blackbody at 1000 °C. The bottom row shows emittance, a measure of how close an emitter is to a blackbody. The blue shaded regions correspond to the region of emission.

perhaps a front side filter in between) have low loss [6]. Even if a front side filter or back surface reflector has high reflectance for out-of-band photons, due to view factor losses not all of these photons would be recycled back to the emitter.

1.3.2 Selective emitters

A selective emitter is an emitter that preferentially emits in-band (above band-gap photons) while suppressing the emission of out-of-band photons. As shown in Figure 1-4, a selective emitter may be designed to be broadband or narrow-band [38]. A broadband emitter leads to higher radiated power per area, but a narrow-band emitter can enable higher conversion efficiency at the photovoltaic cell. A useful metric is emittance, which is a measure of how close an emitter is to a blackbody (but it is independent of temperature).

In the 2000s-2010s there were many advances in selective emitters research, including naturally selective emitters, and engineered emitters including bulk emitters consisting of metals or metals without an anti-reflection coating, metamaterials, aperiodic multilayer stacks, and photonic crystals (PhCs) with one, two, and three dimensions [39].

In a review [39] my group and I proposed five key metrics for evaluating the performance and practicality of TPV emitters, which include 1) optical performance, 2) ability to scale to large areas, 3) long-term high-temperature stability, 4) ease of integration within the TPV system, and 5) cost. We expanded on three metrics previously proposed in our group [40, 6].

In our evaluation of the practicality of emitters in literature, we did not find a type of emitter that yet fulfills all criteria for practicality [39]:

- Metals with or without an antireflection coating are easy to fabricate in large areas. The emission can be enhanced in a narrow band across the band-gap. [41, 42, 43, 24, 44, 45, 23, 46]

- Naturally selective emitters (based typically on the oxides of rare earth metals such as erbium or ytterbium) are easy to fabricate in large areas and exhibit high-temperature stability. However, because they leverage natural transitions of the material, the emission wavelengths are not tunable. [47, 48, 21, 49, 50, 51]

- One-dimensional aperiodic multilayer stacks, which consist of alternating metal and dielectric layers of varying thicknesses have good optimal performance but the long-term high-temperature stability is unclear, as these stacks have many interfaces [26, 27]

- Photonic crystals, periodic structures with wavelength-scale features, that have forbidden and allowed energy bands

  - 1D photonic crystals, or dielectric mirrors, which consist of alternating layers of high index of refraction and low-index materials, are easy to

fabricate in large areas, but are not typically made from high temperature materials. [52, 25, 53]

  - 2D photonic crystals typically consist of a 2D array of features - cylindrical [29, 3, 17] or rectangular [54, 55] cavities etched into substrate, or protrusions on a substrate [56, 57, 58, 59]. Photonic crystals with cylindrical cavities etched into tantalum in particular promising optical performance as broadband selective emitters and some high-temperature stability, but studies of longer-term high-temperature stability and thermal cycling are required.

- Metamaterials (with sub-wavelength features typically) are emerging as emitters with high optical performance, although studies of high-temperature stability are currently limited. [60, 61, 62, 63, 64, 65, 66, 67]

1.4 Intermediate metrics for evaluating emitters

Because it is difficult to evaluate all five metrics ([39] and discussed above) independently of actually integrating and testing the resulting TPV system, I have used three intermediate metrics to evaluate my PhC emitters:

1. Optical performance, with four different sub-metrics
2. High-temperature stability
3. Estimated system impact

1.4.1 Optical performance

A high-performance emitter would enable both high TPV system efficiency and high output electrical power.

While ideally I would characterize the emitter's thermal emission at multiple temperatures, over a wide range of angles, and over a wide ranges of wavelengths from 300 nm to 10-20 µm, this was not feasible.

Instead, I measured the room-temperature reflectance measurements for a near-normal angle (∼8°), and for 0.3-3.3 µm (I also did ∼45° for about 0.3-2.6 µm). From reflectance I calculated the emittance, as reflectance = 1 - absorptance, where absorptance is equal to emittance according to Kirchoff's law.

Using the measured room temperature reflectance, I calculated the following four sub-metrics:

- In-band radiated power per area: Since only in-band power can be converted to output electrical power, the absolute in-band radiated power should be high. This is the most important sub-metric. A note on symbols: in my review paper [39] I used $M_{\text{rad, in-band}}$ to refer to this in-band radiated power per area, to distinguish it from radiated power; however, for most of this thesis I'll refer to this as P_{in}.

$$\pi \int_0^{\lambda_c} \varepsilon(\lambda, T) e_b(\lambda, T) d\lambda \tag{1.1}$$

- Out-of-band radiated power per area: This should be reduced as much as possible, because this is lost as heat and reduces the overall TPV system efficiency. (in my review paper [39] I used $M_{\text{rad, out-band}}$ to refer to this in-band radiated power per area, to distinguish it from radiated power; however, for most of this thesis I'll refer to this as P_{out}.)

$$\pi \int_{\lambda_c}^{\infty} \varepsilon(\lambda, T) e_b(\lambda, T) d\lambda \tag{1.2}$$

  Since the UV-vis spectrophotometers I have used don't extend past 3.3 µm, I have typically used simulations to estimate the long-wavelength emittance up to 10-20 µm to do the integration.

- Spectral selectivity: This measures relative in-band power to out-of-band power. For a high overall TPV system efficiency, the spectral selectivity should be high.

$$\frac{\int_0^{\lambda_c} \varepsilon(\lambda,T)e_b(\lambda,T)d\lambda}{\int_0^{\infty} \varepsilon(\lambda,T)e_b(\lambda,T)d\lambda} \tag{1.3}$$

- Deviation from a step-function emittance: The sum of square error is normalized to the number of sampled points. This measures how close the PhC emittance is to that of an more-"ideal" step-function emittance. However, in this case the emittance is not weighted with the blackbody, so it is not directly related to power. Generally, the lower the deviation the better. However, it is possible that two PhCs share the same deviation value, where one PhC deviates mostly in-band (low in-band emittance) while another PhC deviates mostly out-of-band (high out-of-band emittance): in this case, this second PhC would provide higher in-band power.

  where λ is wavelength, λ_c is the cutoff wavelength, which often corresponds to the photovoltaic (PV) cell band-gap, T is temperature (we calculate for 1000 °C), $\varepsilon(\lambda,T)$ is the emittance (we use room temperature data however), e_b is Planck's blackbody law:

$$e_b(\lambda,T) = \frac{2hc^2}{\lambda^5}\frac{1}{e^{hc/\lambda k_B T}-1} \tag{1.4}$$

We seek to simultaneously increase the in-band radiated power per area and spectral selectivity and decrease the out-of-band radiated power per area and deviation from step function.

1.4.2 High-temperature stability

A good emitter should be able to sustain its optical performance at high temperatures for extended periods of time, either continuously or over multiple thermal cycles.

However, at high temperatures the kinetic energy of atoms increases and atoms diffuse more easily, leading to a number of potential thermodynamic effects [6, 39]:

- Sharp edges and features can become more rounded. [68, 54, 69, 70, 71, 72, 73, 74]

- A phase change may occur (e.g. the emitter might melt) [75], accompanied also by changes in morphology and optical properties [54]. This can happen also for crystalline phases [76]. However, it is important to keep in mind that the melting point of a material at nanometer scale is lower than for bulk [75].

- The sizes of grains can grow in polycrystalline materials [68, 54, 69, 70, 72, 74, 77, 78, 79]. However, this can actually stabilize the material, so some substrates such as polycrystalline tantalum are annealed prior to use [77]. It is also possible to use large-grain or single crystal substrates[54, 80, 81, 78, 82].

- Chemical degradation may occur, such as the formation of tungsten oxides[68, 69, 72, 74] and tantalum carbide [82, 78]. This can necessitate that the emitter operate in inert atmosphere or vacuum [69, 72, 74], which requires special packaging and complicates the TPV system integration. Chemical degradation of 2D and 3D tungsten and 2D tantalum photonic crystals can be mitigated by capping the surface with a 20 - 40 nm protective coating of hafnium dioxide (HfO_2) [71, 73, 6, 78, 79, 81]. One comparison of HfO_2 and Al_2O_3 in 3D photonic crystals [71] has found HfO_2 to be more thermally robust than Al_2O_3, but Al_2O_3 is less expensive and has been used to protect a metasurface emitter [64].

- Thermal expansion could lead to the cracking of a material [71, 71, 79, 83]. Also emitters with interfaces between different materials are at risk of delamination due to varying thermal expansion coefficients.

There are a few strategies to design an emitter with the high-temperature stability: selecting materials that are known to have good high temperature properties, alloying to promote a solute drag effect [69, 72, 74], and modifying the geometry of a structure to change diffusion rates[74, 84].

So far there do not appear to be any published long-term (>1000 hours) studies. The longest reported studies I have seen are 300 hours each for an erbium-doped yttrium aluminum garnet (Er-YAG) crystal used in an solar TPV system[47] and our group's 2D photonic crystal made of tantalum-tungsten alloy and capped with

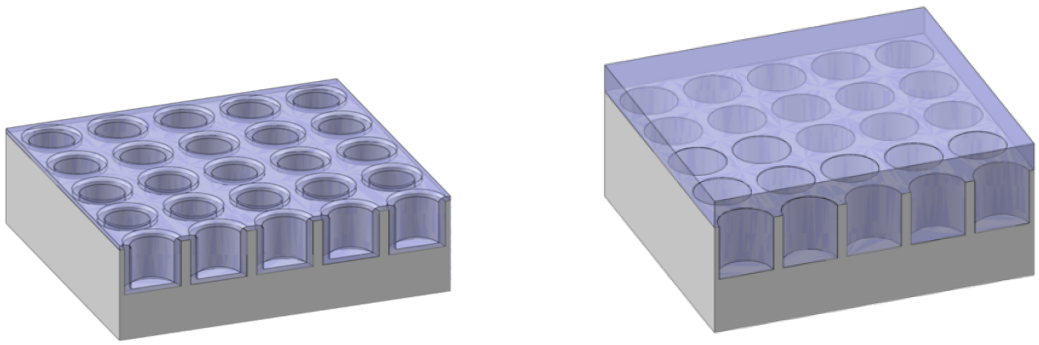

(a) "Coated" or "conformal" photonic crystal. Cylindrical cavities are etched into tantalum, tungsten, or tantalum-tungsten alloy, and the surface is coated with 20-40 nm of hafnium oxide.

(b) "Filled" or "metallodielectric" photonic crystal. Cylindrical cavities are etched into tantalum, tungsten, or tantalum-tungsten alloy, then the cavities are filled with and the top surface capped with hafnium oxide.

Figure 1-5: Schematics of our group's photonic crystals (PhCs)

20-40 nm HfO_2[6] used in an radioisotope TPV prototype [17]. The former cracked and darkened after 300 hours in the sun, although the authors attribute it potentially to a water leak. The 2D photonic crystal showed little to no degradation in optical performance after annealing for 300 hours at 1000 °C (1273 K) [6] and also 1 hour at 1200 °C (1473 K) [81], but this was under vacuum.

1.4.3 Estimated system impact

From the measured emittance I estimate the output power and efficiency of a TPV system, using a model such that described in Chapter 2 of my labmate Walker Chan's PhD thesis [8]. This model describes a propane-based TPV system, with the same system parameters as the three systems described in [3] except for the emittance. Model information and the system parameters are also included in Appendix D.

1.5 Our group's two-dimensional photonic crystal broadband selective emitter

For our group's hydrocarbon thermophotovoltaic system, we seek to develop a broadband selective emitter to control the following properties of thermal radiation: wave-

length/frequency and direction, but not polarization.

Our approach is to use a two-dimensional photonic crystal (PhC), which consists of a square array of cylindrical cavities that are etched into a refractory metal substrate, works by enhancing the emission of photons with energy above the photovoltaic cell band-gap, and whose emission can be tuned by changing the cavity geometry.

In particular, our group's previous generation PhC, the "coated" or "conformal" PhC whose substrate is tantalum or tantalum-tungsten alloy (Ta3%W) and whose surface is coated with 20-40 nm of hafnium oxide (schematic in Figure 1-5a), has been used in a prototype system demonstration with 4.4 W output power for fuel input of 100 W [3], and is promising for satisfying the metrics of practicality for TPV emitters:

1. Optical performance: this PhC, with in-band emittance ε_{in} of 0.58 and out-of-band emittance ε_{out} of 0.18, has realized 67% of the ideal selective emitter limit of a combustion-driven TPV system [6].
2. Ability to scale to large areas: this PhC has been fabricated on 2-inch wafers, using standard semiconductor process [6].
3. High-temperature stability: Minimal degradation of the PhC after annealing under vacuum 5×10^{-6} Torr at 1000 °C at one hundred hours [3] and three hundred hours [6].
4. Ease of integration within the TPV system: this PhC was integrated with the heat source by brazing with the microcombustor [85, 3]

Even higher optical performance is possible, with in-band emissivities of 0.8-0.9, with a tantalum photonic crystal both filled and capped with hafnium oxide - a metallodielectric, or "filled" photonic crystal (schematic in Figure 1-5b) [86, 87].

The metallodielectric or filled photonic crystal has high in-band emittance over a wider range of angles, compared to the conformal PhC, as shown in Figure 1-6. The filled PhC can have high performance even when the parameters are slightly non-ideal; in Figure 1-6, where the filled PhC has a cavity depth less than half that of the depth for an optimized filled PhC.

On the four optical metrics front: as expected, a filled PhC leads to higher in-

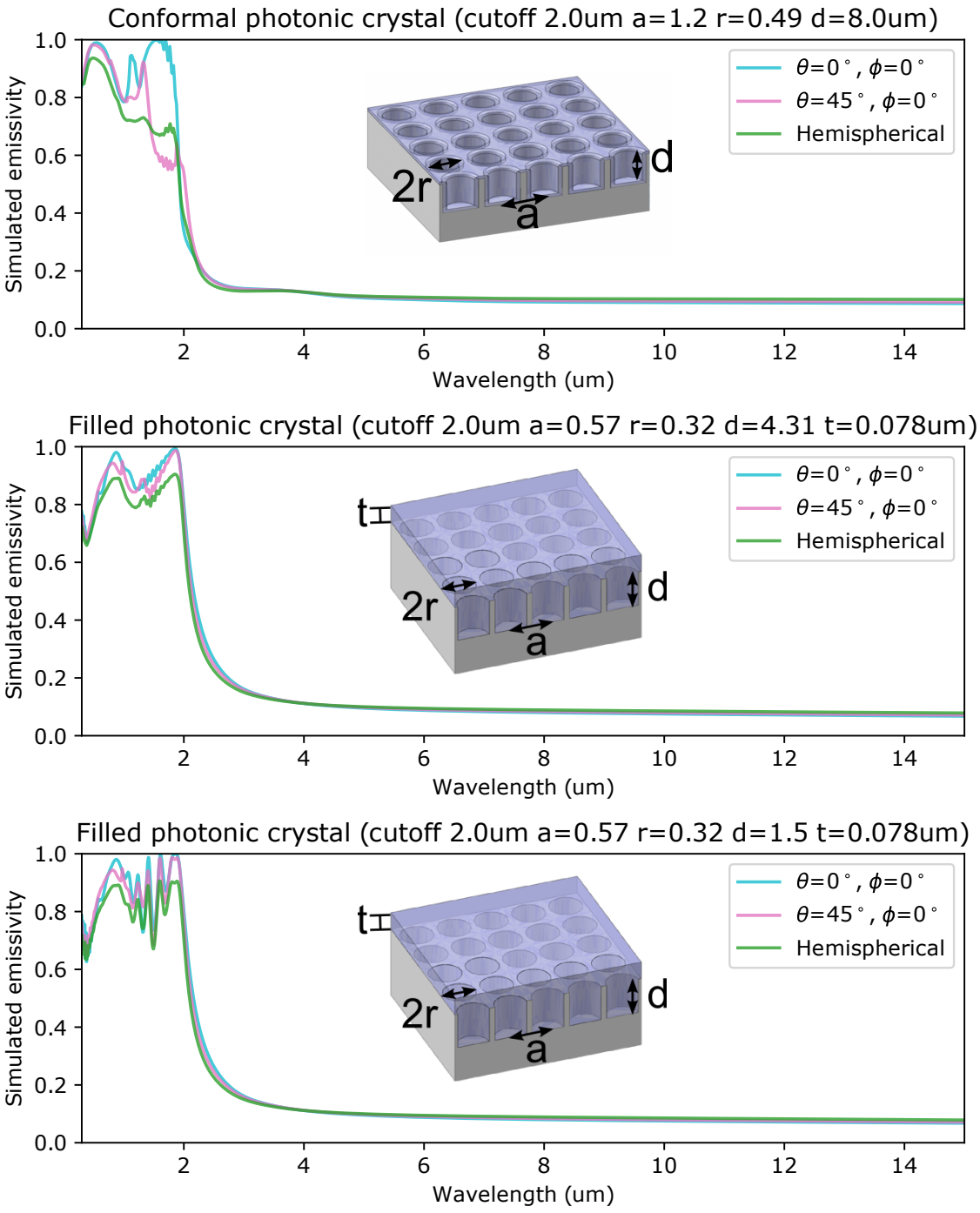

Figure 1-6: The in-band hemispherical emittance (green) is low for a conformal PhC, but high for a filled PhC, even if the depth is not ideal. Middle row shows a perfect filled PhC with cavity depth of 4.31 µm (see Appendix A), while the bottom row shows a non-ideal PhC with 1.5 µm.

PhC type	Cutoff wavelength (µm)	Period a (µm)	Radius r (µm)	Depth d (µm)	Capping layer thickness t
Conformal PhC (hemispherical, simulated) [83]	2.0	1.1	0.49	8.0	-
Conformal PhC (hemispherical, Energy Environ. Sci.) [3]	2.0	1.2	0.52	5.4	-
Perfect filled PhC (simulated $\theta = 0, \phi = 0$) [87]	2.0	0.57	0.23	4.31	0.078
Perfect filled PhC (simulated, hemispherical) [87]	2.0	0.57	0.23	4.31	0.078
Shallower than filled PhC (simulated, hemispherical) [87]	2.0	0.57	0.23	1.5	0.078

Table 1.1: Parameters for PhCs shown in Figure 1-7

PhC type	In-band radiated power per area for cutoff 2 µm, 1000 °C ($\mathrm{W\,m^{-2}}$)	Out-of-band radiated power per area for cutoff 2 µm, 1000 °C ($\mathrm{W\,m^{-2}}$)	Spectral selectivity for cutoff 2 µm	Deviation from step function with $\varepsilon_{in} = 1$, $\varepsilon_{out} = 0$
Conformal PhC (hemispherical, Energy Environ. Sci.)	14166.093	27622.25	0.33878	0.18339
Conformal PhC (hemispherical, simulated)	16729.474	16991.957	0.49587	0.12844
Perfect filled PhC, (simulated, θ=0°, ϕ=0°)	23734.703	21950.499	0.51915	0.10292
Perfect filled PhC, (simulated, hemispherical)	21611.118	20136.574	0.5173	0.11401
Shallower than perfect filled PhC, (d=1.5um, simulated, hemispherical)	21134.664	20131.784	0.51179	0.11524

Table 1.2: Numerical values of metrics for PhCs shown in Figure 1-7

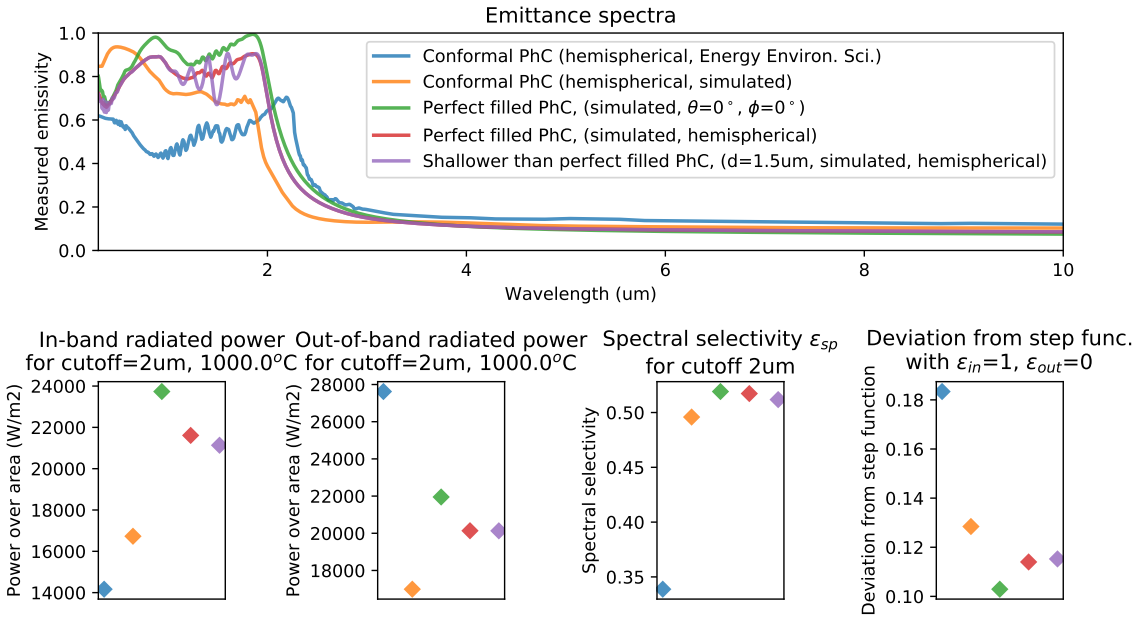

Figure 1-7: Parameters are listed in Table 1.1, numerical values in Table 1.2.

band radiated power per area, higher spectral selectivity, and lower deviation from a step function (Figure 1-7). However, the out-of-band radiated power per area can be higher for filled PhC than for a conformal PhC.

However, its performance relies on key geometric features that are difficult to realize simultaneously. In particular, there are the cavity radius of the filled PhC is about half that of the coated PhC, and with a smaller radius, the cavities have a higher sensitivity to slight variations in dimensions, as well as higher aspect ratios (even with the cavity depth is set to be smaller), which makes them harder to etch and fill.

The focus of this thesis is on photonic crystals designed for a cutoff of 2 µm, which corresponds to the band-gap for InGaAs photovoltaic cells, with target cavity depth of about 1.5 µm (the performance does not suffer very much when the cavities are made shallower.)

1.6 Thesis contributions

This thesis reports on the fabrication of a metallodielectric or filled photonic crystal with close to full theoretical performance. Contributions include the following:

- Identified major geometric imperfections that adversely affect the photonic crystal optical properties: a hollow air core within the cavity, a thick and uneven capping layer of hafnium oxide, and the recession of hafnium oxide from the top of cavity. When I began this project, there were two fabricated filled photonic crystals with unexplained emittances, which I then explained using a combination of numerical simulations and photonic crystal cavity cross section images.
- Developed fabrication steps to overcome the major geometric imperfections, in particular a planarization and etch back process to control the thickness of the hafnium oxide capping layer without causing the removal of hafnium oxide from within the cavity. I implemented these fabrication steps to achieve a better-filled cavity and a thin capping layer of hafnium oxide.
- Tested the stability of filled PhCs under vacuum (1×10^{-7} mbar - 1×10^{-5} mbar) at 1000 °C for up to a continuous 48 hours (cumulative annealing time of the sample was 94 hours and 30 minutes).

The resulting filled photonic crystal has an in-band emittance of 0.7-0.9 and an out-of-band emittance of about 0.2. According to full system simulations, the system output power for the same system as my group's previous prototype system would be as high as 6.0 W for a fuel input power of 100 W, corresponding to a 37.5% increase in power output and approaching the estimated 6.5 W output for a "perfect" metallodielectric PhC.

1.7 Thesis organization

This thesis is organized as follows:

- Chapter 2 discusses the theory, development history, and fabrication process of our group's photonic crystals.

- Chapter 3 discusses the work to identify the major geometric imperfections that adversely impact the emittance of the first two filled PhCs that were fabricated by my predecessor.
- Chapter 4 discusses the characterization of filled PhCs that I made that addressed one of the geometric imperfections addressed in the previous chapter.
- Chapter 5 discusses the planarization and etch back strategy implemented to address another geometric imperfection, and the characterization of the final filled PhC.
- Chapter 6 discusses the simulation of the photonic crystals at high temperature, the potential ways the optical properties might degrade at high temperatures, and anneals of the photonic crystal at 1000 °C under vacuum.
- Chapter 7 evaluates the filled photonic crystal whose fabrication is discussed in this thesis, using the metrics of practicality proposed in this chapter.

The Appendices include the following:

- Tables of photonic crystal parameters for different designs
- Calculation of the hemispherical emittance
- Discussion on the calibration of room temperature reflectance measurements
- Discussion of the model for system performance and parameters
- Tests of spin-on glass on silicon, for planarization and etch back
- Investigation of alternate planarization methods
- Tables of some materials properties
- Tests of hafnium oxide sol-gel to planarize and fill the cavities

Chapter 2

Photonic crystal design, development history, and fabrication

Our group's approach to a broadband selective emitter is to enhance the emittance of a low-emissivity metallic substrate using a microstructure: in our case, by etching into this substrate a two-dimensional, square, periodic array of cylindrical air cavities.

The emission spectrum can be tuned by changing the geometry; in particular, the radius of the cavities r sets the cutoff wavelength, where the transition from high emittance to low emittance occurs. The cutoff wavelength of the photonic crystal (PhC) is typically set to the photovoltaic cell band-gap.

The other geometric features such as cavity depth d and periodicity a are optimized to maximize the amplitude of the emittance in the in-band region (where wavelengths are shorter than the cutoff wavelength).

The cavity features are the same order of magnitude as the light wavelengths of interest: on the order of microns; Appendix A includes parameters of several PhC designs for cutoffs of 1.7-1.8, 2.0, and 2.3 µm.

This chapter discusses the theory for the photonic crystal briefly, as well as the development history in our group, and fabrication process.

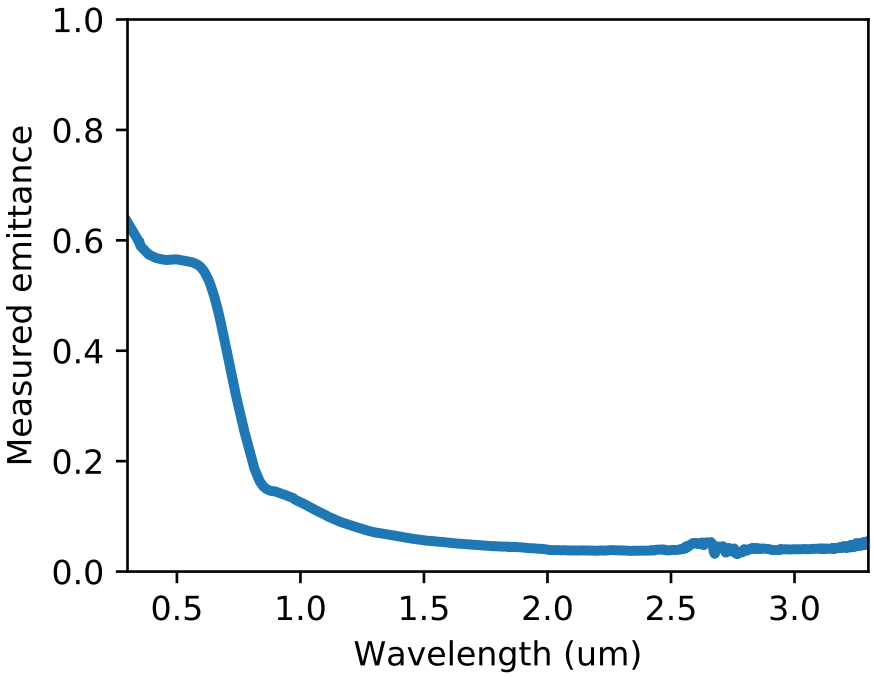

Figure 2-1: Measured emittance spectrum of a flat tantalum wafer.

2.1 Theory and design

2.1.1 Metallic photonic crystal

The basic structure of the photonic crystal is a two-dimensional, square, periodic array of cylindrical air cavities etched into a metallic substrate (we have used tantalum or tantalum-tungsten alloy most recently), as shown in Figure 2-2a. The measured emittance spectrum of a flat tantalum wafer is shown in Figure 2-1.

To first order, one can consider the behavior of a single cylindrical air cavity (Figure 2-2b). The enhancement in emission comes from the increased interaction time of radiation with the metallic substrate, which occurs when light couples into resonant cavity electromagnetic modes. Increased interaction time leads to increased absorption and thus increased emission, as according to Kirchoff's law of thermal radiation, where absorption equals emission for a body in thermal equilibrium. The intuition is that light can interact with the cavity only if the optical wavelength is smaller than the cutoff wavelength, which is related to the physical size of the

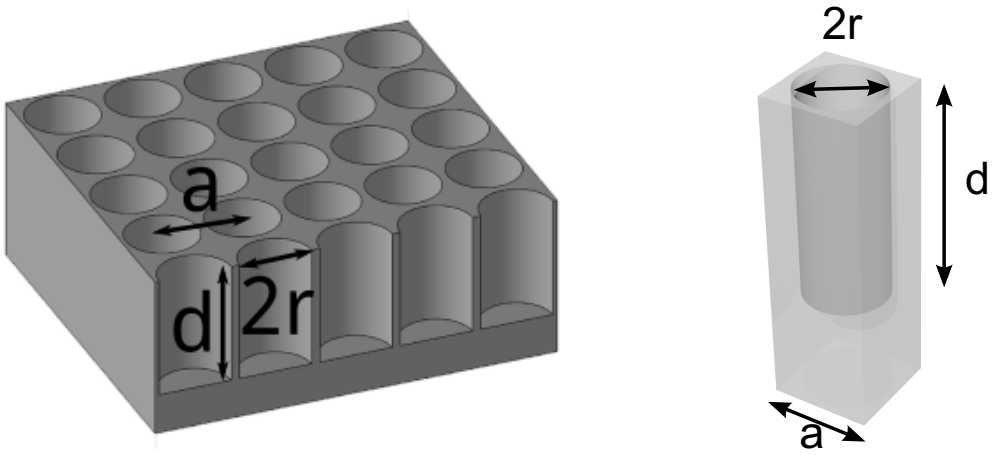

(a) Bare photonic crystal, where geometry is characterized by a cavity period, r cavity radius, and d cavity depth.

(b) To first order, one can consider the behavior of a single cylindrical air cavity.

Figure 2-2

cavity. For wavelengths longer than the cutoff wavelength, light cannot interact with the cavities, so the emittance is low. The emittance in this long-wavelength region is given by effective medium theory, where the high ratio of air to metal surface area reduces the index contrast, leading to lower reflectance thus higher emittance [88, 89, 36].

The cutoff wavelength is approximately given by the fundamental cavity resonances for an isolated, finite depth cavity [88, 89, 6]:

$$\omega_{n,\mathrm{TE}} = \sqrt{\left(\frac{lr}{4d}\right)^2 + \left(\frac{\xi'_{mn}}{2\pi}\right)^2} \tag{2.1}$$

for TE modes, and

$$\omega_{n,\mathrm{TM}} = \sqrt{\left(\frac{lr}{4d}\right)^2 + \left(\frac{\xi_{mn}}{2\pi}\right)^2} \tag{2.2}$$

for TM modes, where ξ_{mn} is the nth root of the mth order Bessel function, ξ'_{mn} is the nth root of the mth order Bessel function derivative, d is the cavity depth, r is the cavity radius, and l integer number.

The cutoff wavelength is mainly affected by cavity radius r.

There is an optimal choice of d for a given r, which is governed by a Q-matching

condition, from coupled-mode theory [90, 36, 6]. Although intuitively one might imagine that deeper cavities (higher d) would lead to more increased interaction time and thus higher emittance, this is not the case. There are two major types of loss for cavity resonances: radiation through the top and absorption on the sidewalls and bottom, which are characterized as quality factors Q_{rad} and Q_{abs} respectively. Incident radiation is completely absorbed when $Q_{\text{rad}} = Q_{\text{abs}}$. (In the case of undercoupling, $Q_{\text{rad}} > Q_{\text{abs}}$, not enough cavity radiation enters the cavity, while in the case of overcoupling, $Q_{\text{rad}} < Q_{\text{abs}}$, radiation escapes before it is completely absorbed.) Q_{rad} scales as $(d/r)^3$.

The period a strongly affects the emittance through diffraction losses, which for polar angle $\theta = 0^\circ$ manifest at $\lambda \leq a$ [36]. At $\lambda \leq a$, the Q-matching condition is broken, because cavity resonances can couple to diffracted plane waves (the far-field of neighboring holes can destructively interfere - diffraction), thus leading to decreased Q_{rad}.

Thus cavity period a should be made as small as possible, though realistically one must have $a - 2r >$100 nm; in other words the sidewalls should be 100 nm thick at a minimum to prevent sidewall breakdown, and to be robust to fabrication imperfections and high temperature effects such as diffusion.

2.1.2 Metallodielectric filled photonic crystal

One of the main limitations of the bare and conformal PhCs is that its off-normal emittance is lower compared to the normal (0°) emittance, leading to a reduced hemispherical emittance (as shown in the introductory chapter). This is because the onset of diffraction occurs for angles greater than $\theta = \arcsin(\lambda/a - 1)$ where a is the period. In the case of metallic PhCs, the peak emittance starts to decrease around ±30°. The onset of first order diffraction occurs at $\theta = \arcsin(\lambda/a \mp 1)$; a larger the ratio of λ/a increases the value of θ at which the onset of diffraction occurs [86]. At normal incidence $\theta = 0^\circ$ diffraction losses manifest at $\lambda \leq a$ [36].

One way to compensate for this is to make a PhC with two characteristic radii [91]: the cavity with a smaller radius has a cutoff at a shorter wavelength and can be

designed so that the peak is in the range where the onset of diffraction for the larger cavity occurs.

Another method is to make a filled PhC. A 2D metallo-dielectric "filled" PhC is conceptually similar to a metallic PhC, but with a few major differences: 1) the PhC radii are smaller 2) the PhC cavities are filled with a dielectric (instead of being air cavities) and 3) on the top surface of the PhC is a thin layer of dielectric. The metallo-dielectric PhC is similarly characterized by the parameters cavity period a, radius r, and d, and also has an additional parameter t, which describes the thickness of the dielectric layer above the metal.

Originally, the filled PhC came about as part of an effort to mitigate the structural degradation of the metallic PhCs at high temperatures [74]; filling the cavities (silicon microcavities in the paper) was intended to prevent the surface diffusion, evaporation, and condensation. The authors in Ref [74] chose hafnium dioxide (HfO_2) for three reasons: its thermal expansion coefficient was compatible with that of tungsten, it was IR transparent, and it could be manufactured in thin films by sol-gel deposition. In their work, they filled PhCs made of silicon; the emittance of these silicon PhCs showed little degradation after annealing for 100 hours at 673 K.

A filled PhC cavity has increased in-band emittance at off-normal angles because it enables a smaller period but for the same optical wavelength. Filling the PhC cavity changes its index of refraction n and thus the optical wavelength (λ/n), which allows for the cavity dimensions and the period to be smaller [86]. In other words, for an air cavity $r \sim \lambda/2$, but for a filled cavity the radius is smaller with $r \sim \lambda/2n$. A smaller cavity radius allows for a shorter period a; a shorter period increases the angle for which the onset of diffraction occurs and reduces diffraction losses for in-band emittance at off-normal angles.

In addition to filled PhC cavities, a metallo-dielectric PhC has a thin capping layer of dielectric on the top, which acts as an anti-reflection coating that enhances the emittance for in-band wavelengths [87]. This leads to the additional parameter t.

The out-of-band emittance for a metallo-dielectric PhC is somewhat higher than that of a bare metallic or conformal PhC because of the dielectric. The dielectric

reflectance is lower, which leads to a lower emittance.

2.1.3 Simulations

For simulations I have used S^4 (Stanford Stratified Structure Solver) [92], an electromagnetics solver for layered periodic structures that uses rigorous coupled wave analysis (RCWA) methods.

Tantalum dispersion parameters are based on a Lorentz-Drude model fit to the measured reflectance of flat tantalum wafers, while the index of refraction of HfO_2 is set to 2.

The four major parameters of a typical filled PhC are the period a, radius r, depth d, and thickness of HfO_2 capping layer t. I introduced geometric imperfections into the models by modifying the layered structure, and adding additional geometric variables.

For the fits to the measured emittance spectra, I typically used as initial guesses the measurements from cross section images. I included the constraint $a > 2r - 0.1\,\mu m$; typical bounds were $0.1 < a < 1$, $0.1 < r < 1$, $0.1 < d < 10$, $0.02 < t < 1$. After each iteration was calculated the sum of the square error $\sum(\text{measured}(\lambda) - \text{simulated}(\lambda))^2$.

2.2 Development history of our group's photonic crystal

Over time, both the design and substrate of our group's photonic crystals has changed. Recent work on metallic PhCs with deep cylindrical cavities has focused on both enabling their large-area fabrication and improving their high-temperature stability by two means: a) change of substrate from tungsten to polycrystalline tantalum and then tantalum-tungsten alloy and b) a conformal coating of hafnium dioxide HfO_2 using atomic layer deposition (ALD).

1. Initially, the PhC fabrication was developed on single crystalline tungsten (W) [93, 94, 88, 80]. These PhCs showed thermal stability over 10 hours post ther-

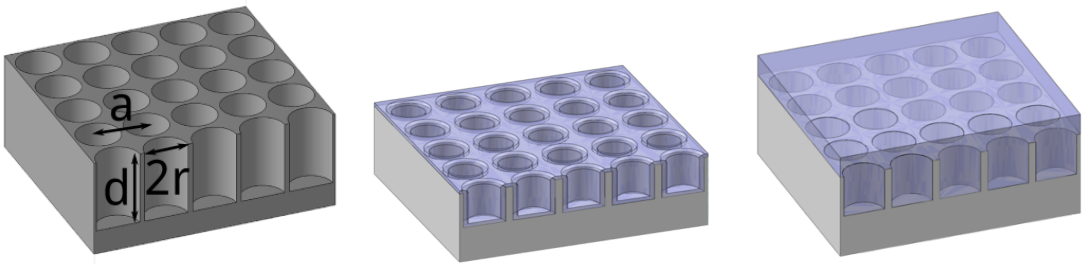

(a) Bare photonic crystal

(b) Conformal or coated photonic crystal, covered with 20-40 nm

(c) Metallodielectric or filled photonic crystal, both filled and capped with HfO_2

Figure 2-3: Three kinds of photonic crystals developed in our group (not to scale).

mal cycling, where each cycle involved heating up to 1200 K over an hour [80]. However single crystalline tungsten is costly and is typically available in small sizes of ∼1-1.5 cm diameter wafers; in addition tungsten is brittle and and difficult to machine and weld, which would make system integration difficult [77]. (Schematic shown in Figure 2-3a)

2. Then, the PhC substrate was changed to 2 inch diameter wafers of polycrystalline tantalum, which is both easier to weld and machine and can be annealed to produce larger grains and thus increase the high-temperature stability [77, 29]. However, because tantalum is soft, tantalum wafers must be thicker (and therefore more expensive) than tungsten wafers to achieve the same mechanical stability. The PhCs made in polycrystalline tantalum had cavities with depths of ∼8.5 µm and aspect ratio of ∼8. Both the optical performance and structure were stable up to 1 week at 910 °C; however, annealing the tantalum PhC at high temperatures led to atomic diffusion and the formation of tantalum carbide [6].
3. To improve the high-temperature stability of the tantalum PhC, the PhC surface was coated with 20-40 nm of hafnium dioxide. This enabled sustained optical performance during both anneals of 900 °C for 144 hours (6 days) and at 1000 °C for 1 hour [78]. (Conformal PhC schematic shown in Figure 2-3b)
4. More recently, a conformal PhC was made in tantalum-tungsten alloy (3% tung-

sten), which combines the better thermomechanical properties of tungsten with tantalum's ability to be more easily machined and welded [6, 81]. This tantalum-tungsten PhC has shown one of the longest high-temperature stability known: it showed little to no degradation in optical performance after annealing for 300 hours at 1000 °C (1273 K)[6] and also 1 hour at 1200 °C[81].

5. The filled PhC (schematic in Figure 2-3) was first fabricated in 2016 by Veronika [1]

The 2D metallic PhCs made of polycrystalline and tantalum-tungsten alloy have been used in prototype system demonstrations [29, 3, 17, 18] and are promising as practical emitters. Their practical attributes are summarized in Table G.3. As shown

Emitter	Cutoff (µm)	ε_{in}	ε_{out}	θ	$T_{emitter}$ (K)	Area	High temp. stability	Vacuum?	Direct fabrication with heat source?	Measured system efficiency (%)
HfO_2-coated, 2D PhC made in polycrystalline Ta [29]	2.3	0.52	0.29	all	1270	-	900 °C for 144 hours (6 days) and at 1000 °C for 1 hour [78]	Yes, <0.3 Pa	Yes	3.74
HfO_2-coated, 2D PhC made in polycrystalline Ta [3]	2.0	0.58	0.18	all	1327	21 mm x 21 mm	>100 hours at 900 °C[3]	Yes	No	4.3
HfO_2-coated, 2D PhC made in Ta3%W alloy [17, 18]	2.25	0.75	0.26	∼0°	1233	1 cm x 1 cm	300 hours at 1000 °C, 1 hour at 1200 °C[81, 6]	Yes, 1×10^{-5} Torr	No	0.1-0.3

Table 2.1: Some practical attributes of the most promising 2D metallic PhC emitters, which have been used in prototype system demonstrations. ε_{in} is in-band emittance, ε_{out} is out-of-band emittance, $T_{emitter}$ is the emitter's temperature in this system demonstration.

in Table G.3, 2D metallic PhCs have a fairly large area on the order of cm^2, and have shown high temperature stability on the order of hundreds of hours. Although 2D metallic PhCs require vacuum operation, they have been successfully integrated within a system. Finally, they are decent selective emitters - at least at normal

incidence; the omnidirectional in-band emittance is moderate and could be improved.

2.2.1 Materials selection

The above materials (tantalum, tungsten, Ta-W alloy, hafnium oxide) have been used for the following reasons:

- Substrate
  - Tungsten is a refractory metal with high melting point, very low vapor pressure, good thermo-mechanical properties at high temperatures, as well as low emissivity in long wavelength regions [89, 36]. However, tungsten is brittle so is hard to machine, must be single crystalline, and forms a volatile oxide [95].
  - Tantalum is also a refractory metal with high melting point and low emissivity in long wavelength regions, but compared to tungsten is more ductile and can be machined more easily. Polycrystalline tantalum was used as substrate. The formation of the tantalum carbide is prevented by coating the surface with hafnium oxide and by heating the emitter under vacuum [6].
  - Tantalum-tungsten alloy combines the better thermo-mechanical properties of tungsten with the more compliant material properties of Ta, allowing for easier machining and welding [81]

- Hafnium oxide (HfO_2) is chosen as the dielectric material for cavity filling for several reasons: it has a high index of refraction of 1.9-2, is transparent in the visible and infrared regions, can be deposited using atomic layer deposition, and is stable at high temperatures [87]. HfO2 has been used as a protective coating for several TPV emitters, including 3D PhCs [71, 73], 1D periodic stacks [27, 96], metamaterials [67, 95].

The filled PhCs originally began as a way to increase the high-temperature stability of photonic crystals, in a paper describing filling silicon microcavities with HfO_2

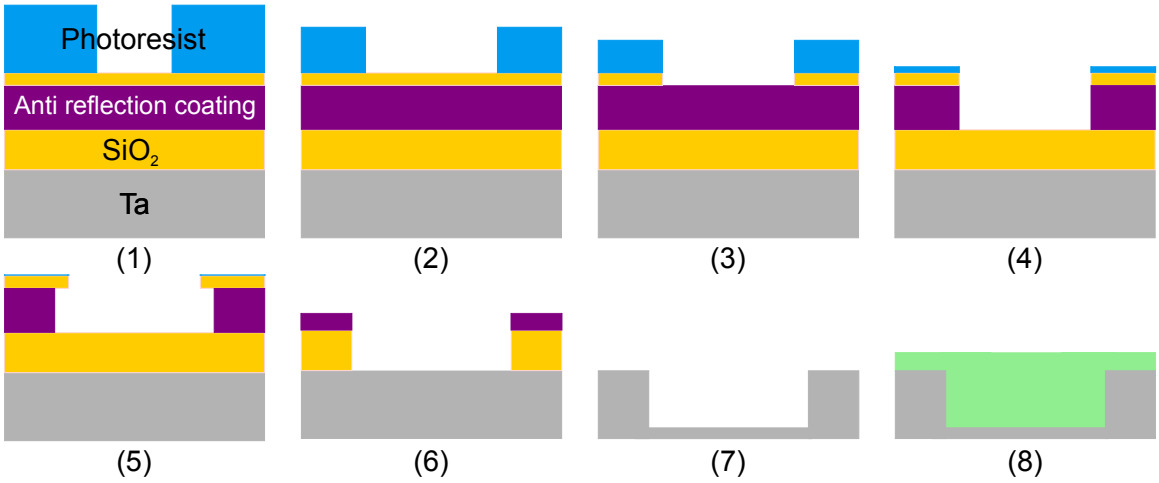

Figure 2-4: Fabrication process, details explained in main text.

[74].

2.3 Fabrication

The fabrication process, which is shown in Figure 2-4, is broadly as follows:

1. Interference lithography to generate the pattern into the top layer of the tri-layer resist (photoresist, SiO_2 adhesion layer, anti-reflection coating ARC)
2. Isotropic plasma ashing with O_2 to increase the size of the cavities
3. Pattern transfer through the SiO_2 adhesion layer, through reactive ion etching (RIE) with CF_4 gas
4. Pattern transfer through the ARC layer, using He and O_2 RIE
5. If necessary, plasma ash the ARC to increase the cavity sizes further
6. Pattern transfer through the SiO_2 hard mask
7. Generate cavities in tantalum substrate using deep reactive ion etching (DRIE) process, using mixture of SF_6 and C_4F_8 gases (Our collaborator Bob Geil of UNC Chapel Hill did this for us).
8. Filling the cavities with atomic layer deposition - Veronika originally used only standard mode atomic layer deposition.

While the fabrication process had mostly been developed by my predecessor

Veronika Stelmakh [6] (and the results of her first two PhCs discussed in Chapter 3), I made a few changes and contributions:

- I did the fabrication 4-inch tantalum wafers, which are larger than the 2-inch substrates Veronika used
- I replaced HMDS (hexamethyl-disilazane) as an adhesion promoter, to use instead diluted XHRiC-16 ARC, but this leads to an additional ∼10 nm that must be accounted for during the etch through the SiO_2 interlayer
- I modified the 6th step, the pattern transfer into SiO_2 hard mask, to use a 1:1 mixture of CHF_3 and CF_4 instead of solely CF_4, in order to increase the etch selectivity of the ARC layer over the SiO_2 hard mask
- I also modified the cavity filling step, to use a combination of standard mode and exposure mode ALD. The filled PhC resulting from this step is discussed in Chapter 4
- I added additional processing steps to control the HfO_2 capping layer on the top surface of the PhC. These efforts and the result are detailed in Chapter 5.

A few complications or difficulties were as follows (some of these out of my control):

- The tantalum wafer was not completely flat (though this did not pose too much of a problem for spincoating).
- The cavity radii were not uniform across the wafer (meaning the sidewalls were neither), which is likely related to the beam quality at long distances away from the center of the wafer.
- The thicknesses of each of the layers (the tri-layer resist stack and the SiO_2 hard mask) must be designed so that the reflectivity of the entire stack is <1.5% at the exposure wavelength of 325 nm, but it also must take into account the etch selectivities of the layers, and the cavity aspect ratios must not be too high (I tried to target <1).

- Lateral etching during the pattern transfer layers meant that the cavity sizes expanded during the processing.
- The RIE etch rate were not consistent between a silicon and tantalum substrate. This made it difficult to confirm that I had etched through layers on the tantalum sample: silicon was the dummy sample I could cleave to image the cross section. Tantalum I could not cleave. Generally, the etch rates on tantalum were found to be slower.
- Plasma ashing
  - Etch rate was higher at the center and lower at the edges (but not enough to compensate for the cavity size nonuniformity)
  - Long ash times would crosslink the resist, so I had to keep the resist time to $<2\,\mathrm{min}$
  - The etch rate was not linear with time

Moving forward, many of these problems can likely be circumvented by using a stepper, where the cavity sizes are defined in the mask, and where there are fewer layers through which to pattern transfer.

Chapter 3

Characterization and modeling of first two fabricated filled metallo-dielectric PhCs (previous iterations)

The first two filled metallo-dielectric PhCs were fabricated by my predecessor, Veronika Stelmakh [1, 6]. At the beginning of this project, I had two unexplained emittance spectra (from two samples) from Veronika, which I sought to understand using a combination of cross section imaging and simulations.

3.1 Samples history

Conceptually, the filled PhC is like the coated PhC, except that the cavities are filled and the cavity dimensions are smaller (due to the high index of refraction of HfO_2). So Veronika and our collaborator Bob Geil (of UNC Chapel Hill) made the cavities in tantalum, then filled the cavities with hafnium oxide using atomic layer deposition (ALD).

The measured spectrum and cross section are shown in Figure 3-1. The measured spectrum shows many in-band resonance peaks and what appears to be an out-of-band resonance peak around 3 µm. Meanwhile, the cross section image (that Veronika took) shows two major geometric imperfections: one, a thick and uneven capping layer, and

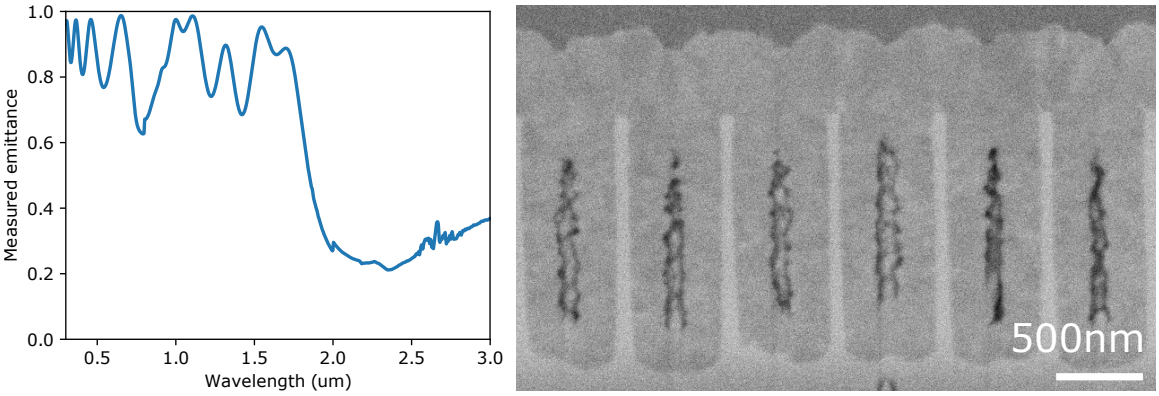

Figure 3-1: The first filled PhC (made by Veronika Stelmakh). The spectrum has many prominent resonance peaks, including one out-of-band around 3 µm. Cross section imaging shows a thick and uneven capping layer as well as a hollow air core.

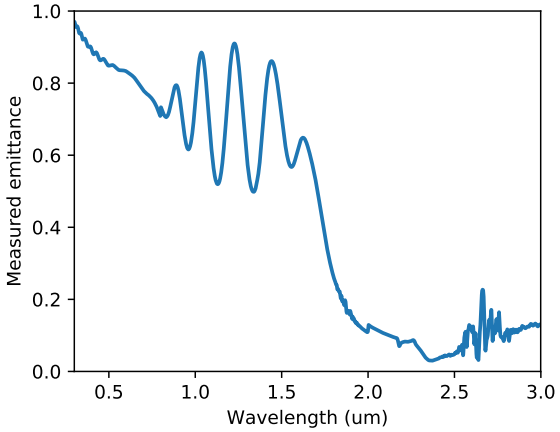

Figure 3-2: The second filled PhC (made by Veronika Stelmakh). After filling the cavities with exposure mode ALD, the sample was argon ion milled in order to reduce the thickness of the capping layer. The measured spectrum however was unexpected.

two, a hollow air core within the center of the cavity.

Based on these results, Veronika and Bob sought to correct the two imperfections using the following methods:

- Exposure mode ALD (as opposed to standard mode ALD). During each cycle, more time is allowed for the gaseous precursors to diffuse and adsorb onto the sample, so it is better suited for filling high aspect ratio cavities.
- After filling the cavities, argon ion mill the sample to reduce the thickness, then deposit an additional 20-40 nm of HfO_2 with ALD.

The measured spectrum of Veronika's second filled PhC is shown in Figure 3-2.

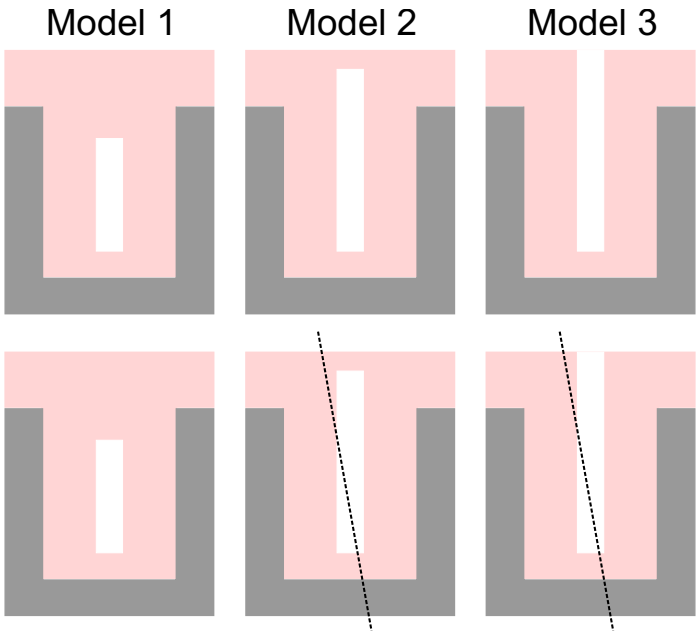

Figure 3-3: Initially I considered three potential models for the PhC cross section, with varying heights for the hollow air core (top row). The possibilities where that the hollow core might be contained within the cavity, might protrude out of the cavity, and might protrude all the way to the PhC surface. Bottom row: the black dotted lines indicates non-ideal cuts through the cavity that might make it appear in the cross section image as though the hollow air core is contained within the cavity.

I used a combination of cross section images and simulations to identify the major fabrication imperfections that impact the PhC optical properties.

3.2 Understanding the first filled PhC

The cross section image in Figure 3-1 shows a number of different imperfections: there is a large hollow air core in the center of the cavity, the HfO_2 capping layer is thick, and the HfO_2 capping layer is also uneven.

I incorporated two of these imperfections 1) the hollow air core and 2) the thick HfO_2 capping layer (I modeled it as a flat capping layer) into simulations. Initially, I considered three potential models with various heights for the hollow air core, as shown in the top row of Figure 3-3 to account for the possibility that in reality the hollow air core protrudes out from the cavity but is not visible because of the cavity cross section was not prepared properly (the cut was not parallel with the cavity

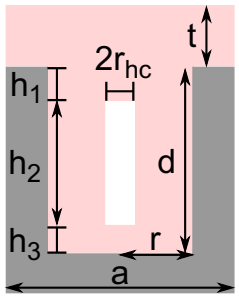

Figure 3-4: The model I ultimately used for the PhC cross section has two imperfections, 1) a hollow air core and 2) a flat, thick HfO_2 capping layer. It has four additional parameters: the radius of the hollow core r_{hc}, distance from top of the PhC cavity to top of hollow core h_1, height of hollow core h_2, and distance from bottom of hollow core to the bottom of the PhC cavity h_3.

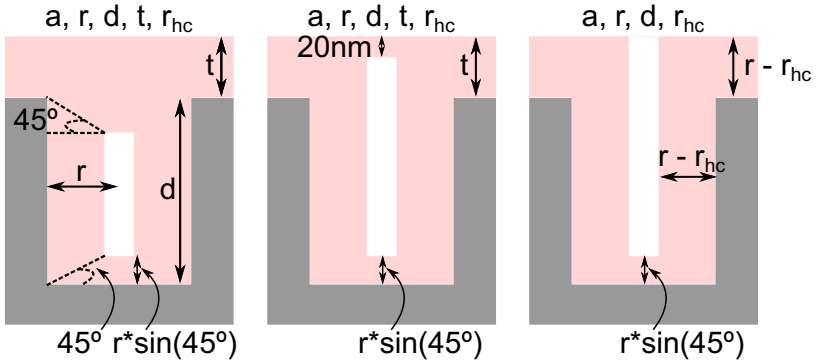

Figure 3-5: For each model, I made a few assumptions to decrease the number of independent variables to 4 or 5.

sidewalls).

These models included an additional four parameters: an additional four parameters: the radius of the hollow core r_{hc}, distance from top of the PhC cavity to top of hollow core h_1, height of hollow core h_2, and distance from bottom of hollow core to the bottom of the PhC cavity h_3, as shown in Figure 3-4.

Because this would lead to eight variables total, I made some assumptions to constrain the height and position of the hollow core to use four to five independent variables, as shown in Figure 3-5. Based on the cross section images I made the assumption that the bottom of the hollow core was situated r * sin(45°) away from the bottom of the PhC cavity.

The results of the initial fits, shown in Figure 3-6, indicated that the most likely model was the Model 1, model with the hollow core contained entirely within the

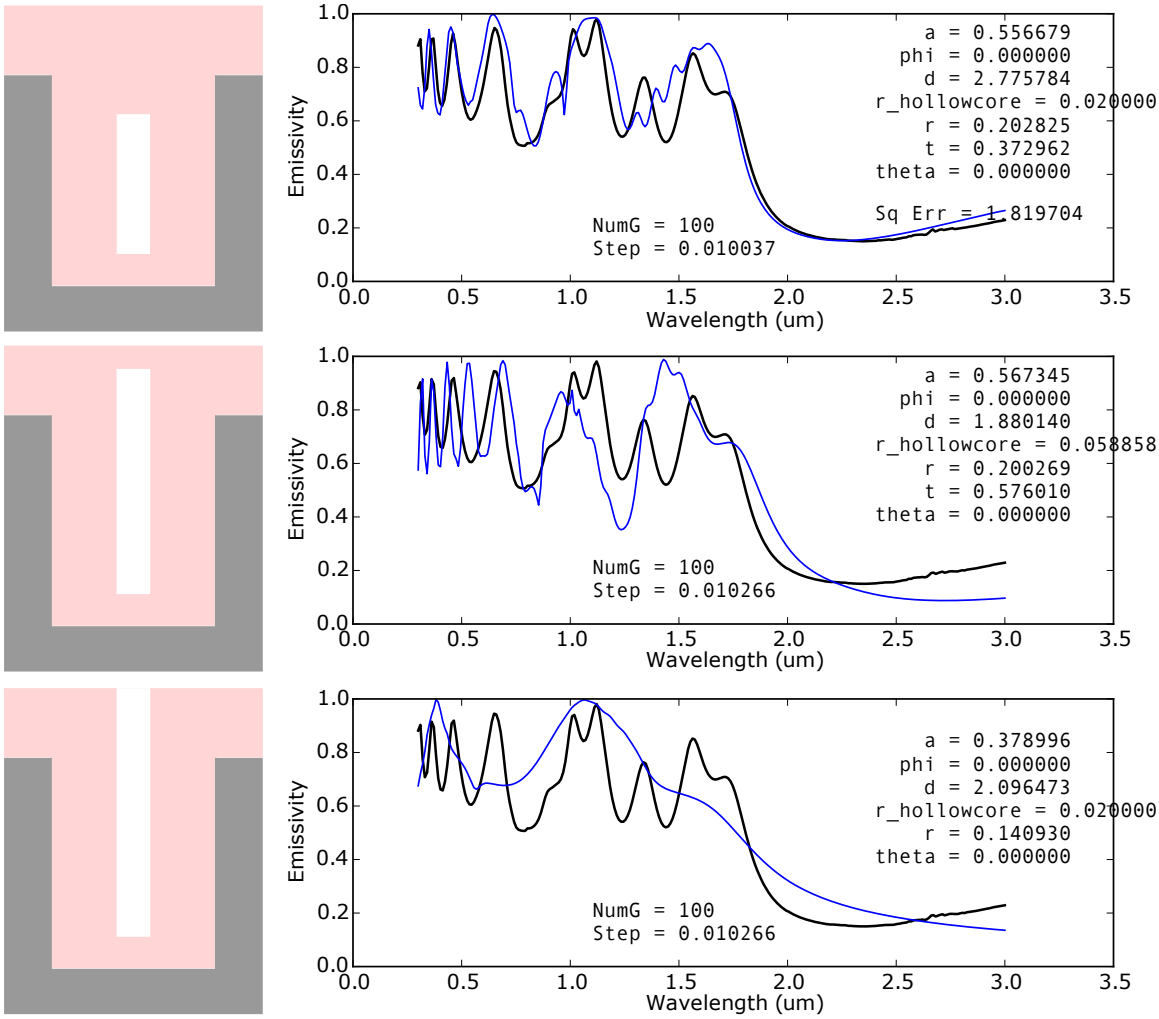

Figure 3-6: Results of initial fits showed that the radius was probably close to 0.2 µm (see fit results to model 1 and 2).

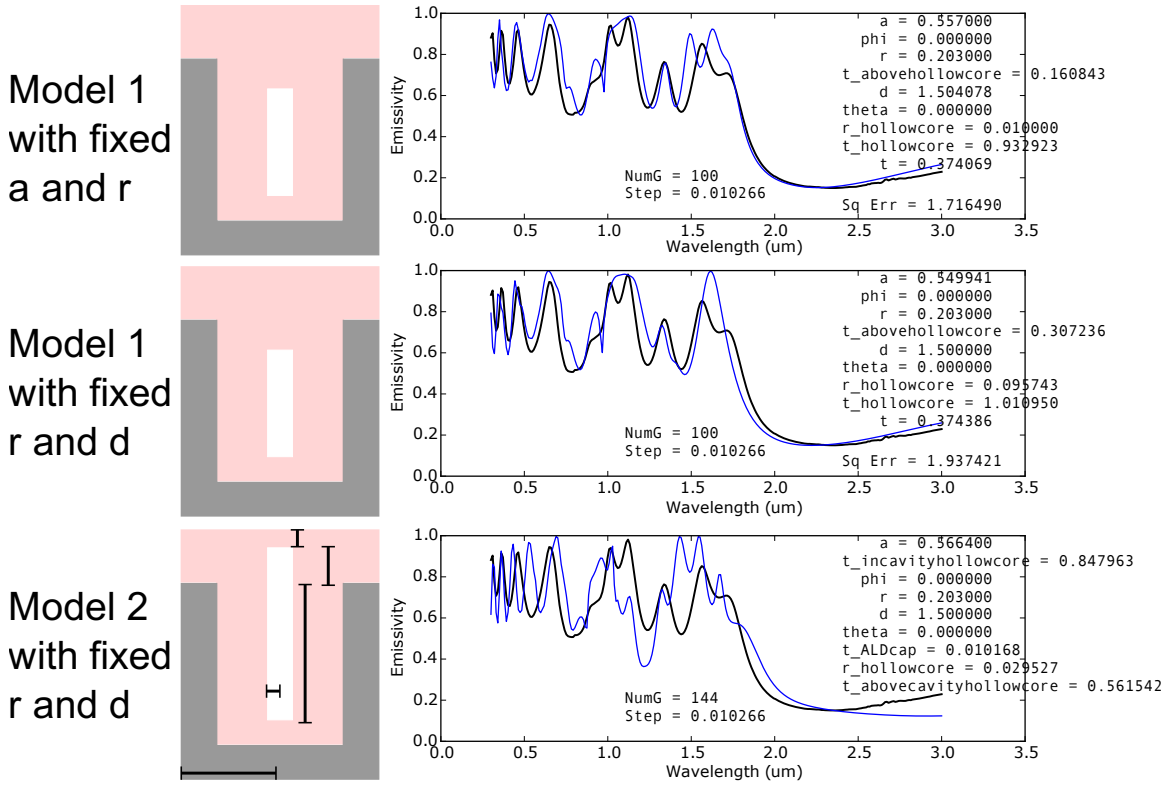

Figure 3-7: Fits round 2.

cavity. For initial guesses, I used measurements from the cross section images (I also used low resolution simulations to speed up the fits). The best fit was the model with the hollow core within the cavity: the cutoff around 1.8 µm matched the measured emittance, and many of the peaks between the simulated and measured spectra were consistent as well. The fit for model 2 (hollow core protrudes out of the cavity) was reasonable, with some of the peaks that seemed close.

There were a few other takeaways from the initial fits:

- Although the fit for model 1 looked good, the depth of 2.8 µm it gave was unreasonably high.
- Both the fit results from model 1 and model 2 gave radius r as $\sim$0.2 µm.
- The fit to the first model showed a good fit to the cutoff around 1.8 µm, which likely meant that the fit to the radius r of 0.203 µm was accurate.

Based on these initial fits I fine-tuned models 1 and 2, to try the following, the

results of which are shown in Figure 3-7:

- Model 1: fixed $a = 0.557$ and $r = 0.203$, and varied the hollow core variables (r_{hc}, h_1, h_2, and h_3), depth d, and capping layer thickness t. The resulting fit: quite reasonable, with the cavity depth d 1.5 µm much closer to what we expected. However the hollow core radius at 0.01 µm was at the lowest limit of the bound I had set.

- Model 1: fixed $r = 0.203$ and $d = 1.5$, and varied the hollow core variables (r_{hc}, h_1, h_2, and h_3), periodicity a, and capping layer thickness t. The resulting fit: a looked reasonable, but this fit did not capture the two resonance peaks close to the cutoff, around 1.6 µm and 1.8 µm.

- Model 2: $r = 0.203$ and $d = 1.5$, and varied the periodicity a, the hollow core radius r_{hc}, the hollow core height within the cavity, and the hollow core height above the cavity, and the thickness of the capping layer at the very top. The resulting fit did not look very good.

- Two model 1 fits: one of the major differences between these fits was the period a, as well as the position of the hollow core within the cavity (in other words, how deep was the hollow core within the cavity).

For the third round of fits, I decided to keep the radius r and d fixed (0.203 and 1.5 µm), while varying the period a starting with $a = 0.5$ µm. This resulted in a fit with $a = 0.452$ µm as shown in Figure 3-8.

Finally, for the fourth round of fits, I fixed the radius $r = 0.203$ µm and $a = 0.452$ µm and varied the depth d. This resulted in a fit with $d = 1.7$ µm.

The final fit result is shown in Figure 3-10. The results of the fit are fairly consistent with the cross section images: the capping layer is thick, with $t = 0.38$ µm from the model, and there is a hollow core in the center of the cavity, even though according to the model the hollow core is deeper in the cavity and shorter than what is shown in the cross section image.

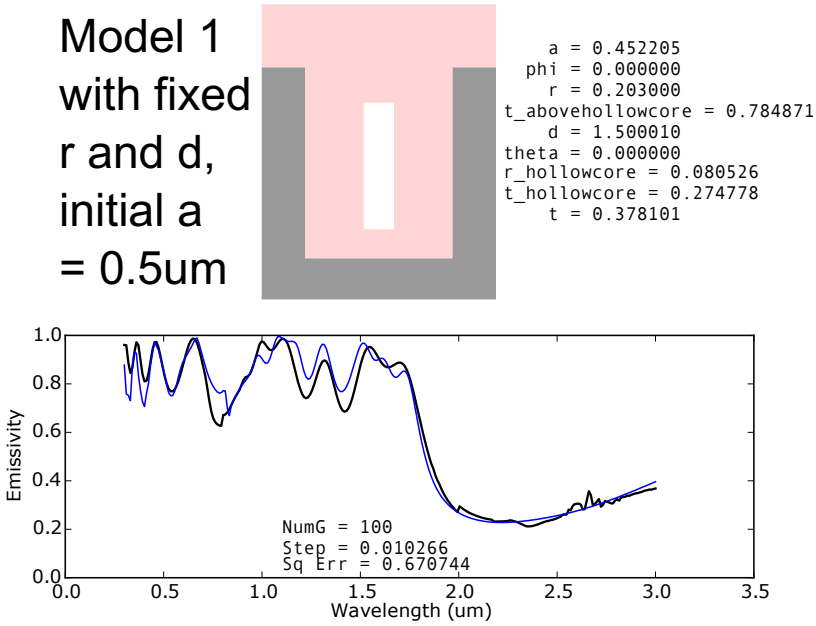

Figure 3-8: Fits round 3.

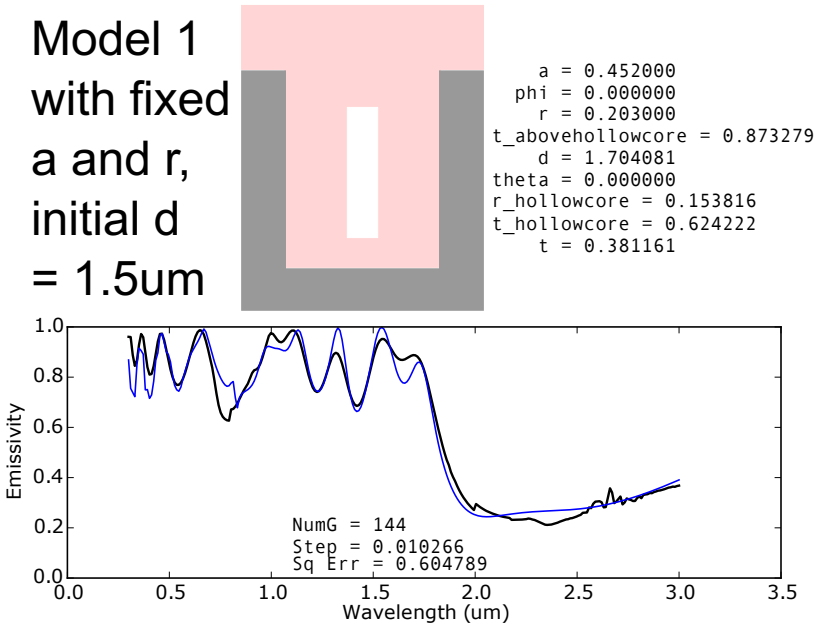

Figure 3-9: Fits round 4.

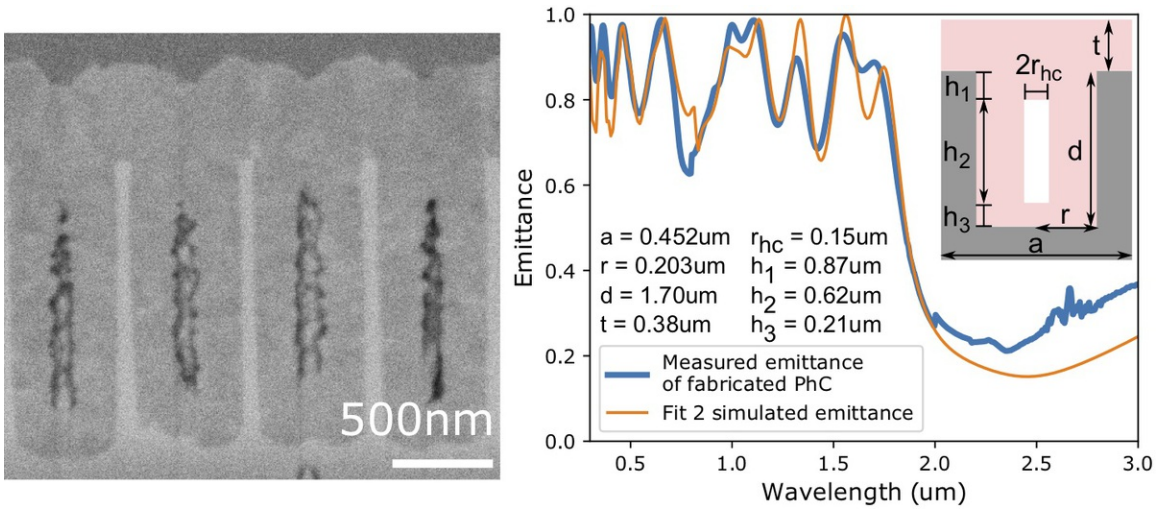

Figure 3-10: Final fit result.

3.3 Understanding the second filled PhC (filled and then milled)

First I tried the same three models I used to try to fit to the first filled PhC, where the best fit was given by the third model where the hollow core extends to the top surface, as shown in Figure 3-11. In this fit, the radius $r = 0.19\,\mu\text{m}$ is quite reasonable, although the period is large $a = 0.58\,\mu\text{m}$ and the cavity is quite shallow ($d = 0.98\,\mu\text{m}$). Also, the hollow core is rather thin (radius of 18 nm and there is very little HfO_2 above the cavity ($t = 16\,\text{nm}$).

The cross section image Figure 3-13 clearly shows a very different geometry: there is very little HfO_2 above the cavity, and in fact HfO_2 was removed from within the cavity, creating a kind of "bowl" shape. In addition, this cross section shows a very thin and almost negligible hollow core.

I modeled the bowl shape as a parabola, after first considering a few other ways (as a circle, an ellipse, a sinusoid). The model is shown in Figure 3-13, with the parabola discretized into six different layers, as the geometry must be described as a layered structure for S^4. The layer thickness and radii are shown in Table 3.1. I assumed a proportionality constant of 1, in other words $\alpha = 1$ for a parabolic equation of $y = \alpha x^2$.

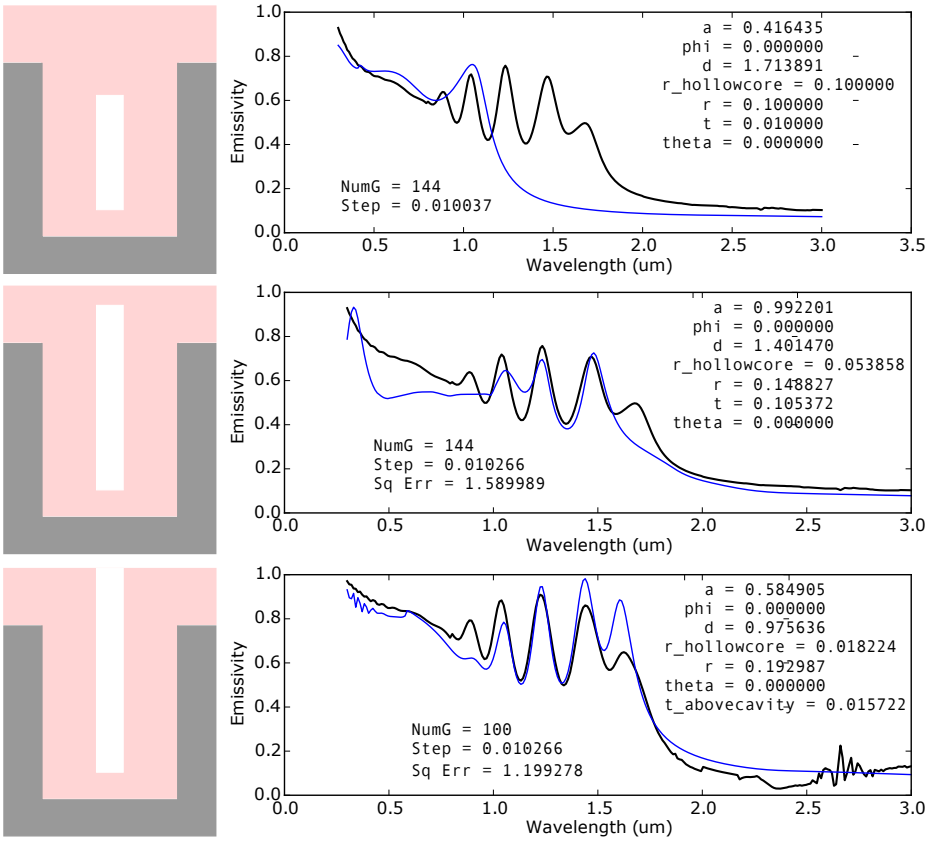

Figure 3-11: Out of the three models, the best fit to the second filled PhC (the one that is milled after filling) uses the third model. The radius $r = 0.19\,\mu\text{m}$ is quite reasonable, although the period is large $a = 0.58\,\mu\text{m}$ and the cavity is quite shallow ($d = 0.98\,\mu\text{m}$). In addition, according to this fit the hollow core is rather thin (radius of 18 nm and there is very little HfO_2 above the cavity ($t = 16\,\text{nm}$).

Layer	Radius (from center of cavity)	Thickness
1 (top layer)	0.8 * r	0.36 * t_{bowl}
2	0.6 * r	0.28 * t_{bowl}
3	0.4 * r	0.2 * t_{bowl}
4	0.2 * r	0.12 * t_{bowl}
5	0.1 * r	0.03 * t_{bowl}
6	0.05 * r	0.01 * t_{bowl}

Table 3.1: For the second filled PhC I used a model where HfO_2 is recessed from the cavity, as a bowl shape. I modeled this bowl shape as a parabola using six discrete layers.

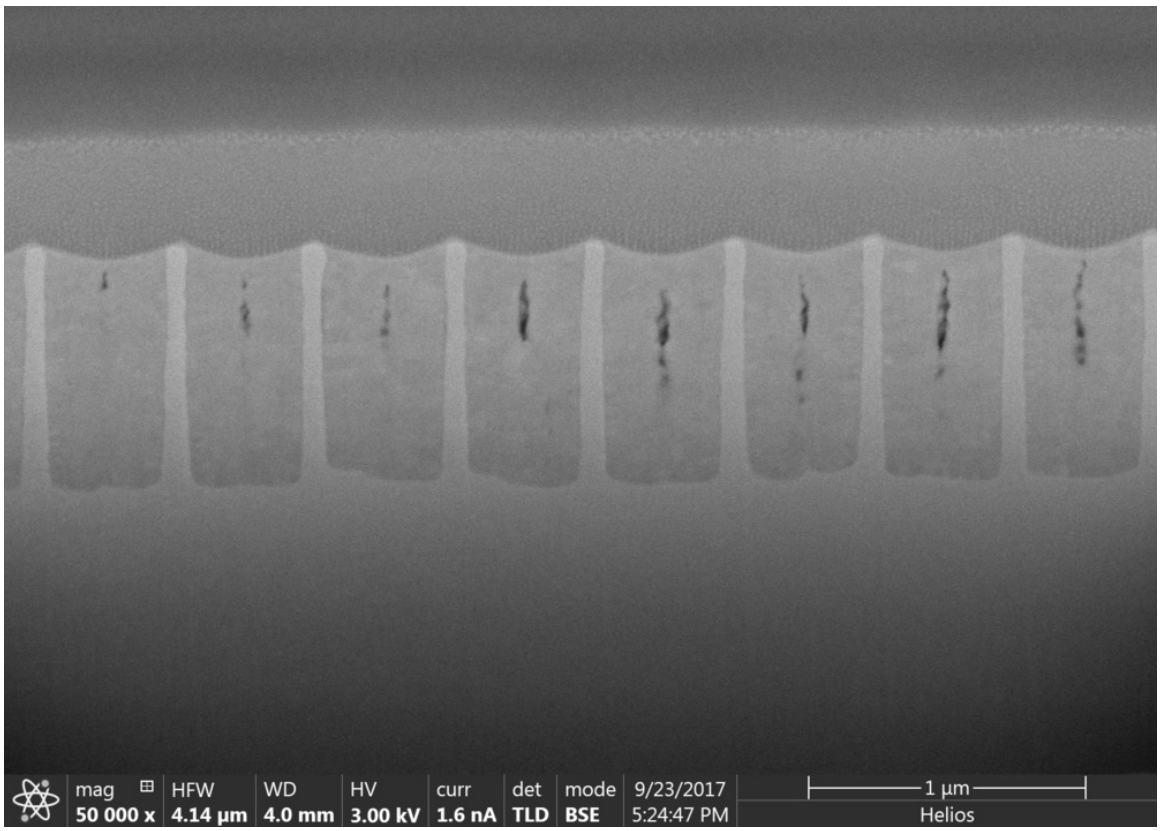

Figure 3-12: The cross section image of the second filled PhC sample shows HfO_2 recessed from the top of the cavity, forming a bowl-like shape.

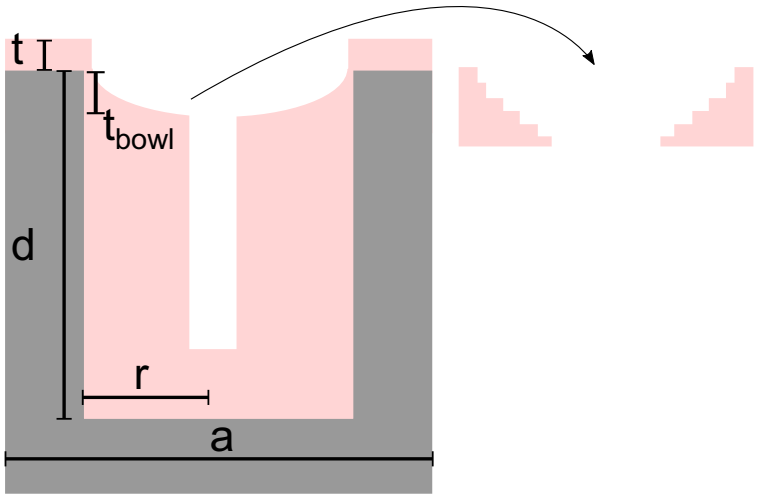

Figure 3-13

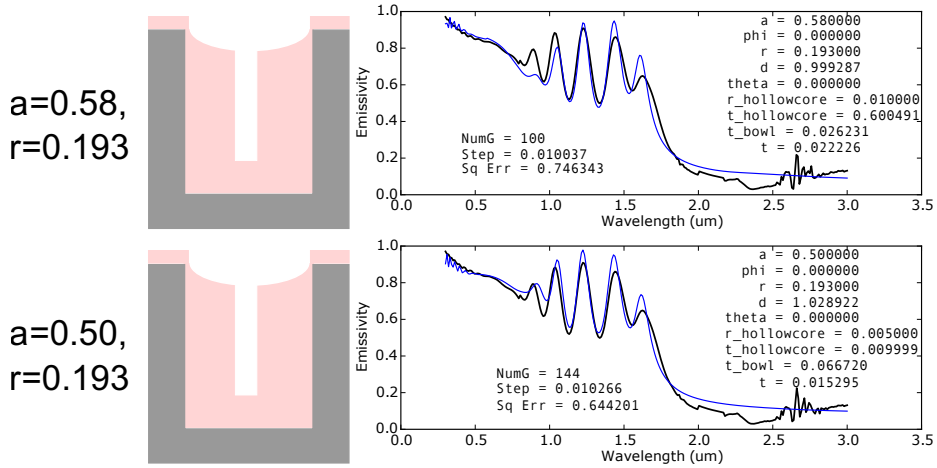

Figure 3-14: The model where the HfO_2 is recessed within the cavity describes the measured reflectance well, although the two fits return varying parameters.

I tried fits with this new model while keeping the period a and r fixed. In one case I tried $a = 0.5\,\mu m$ and in another $a = 0.58\,\mu m$; in both cases I set $r = 0.193\,\mu m$.

This new model with the recessed HfO_2 describes the measured spectrum quite well, as shown in Figure 3-14. The two fits show a consistent cavity depth of about $1\,\mu m$, and the thicknesses of the HfO_2 are similar, at 15 and 22 nm. They diverge on other parameters: the size of the hollow core and the depth of the bowl. The hollow core is narrow in both cases, which is consistent with the cross section image. The bowl depth is 26 nm in one case and 67 nm in the other. However, both fits seem to indicate that the removal of HfO_2 from within the cavity leads to this kind of emittance spectrum for the PhC.

A summary of these results is shown in Figure 3-15.

3.4 Crucial parameters of the filled PhC, and improvements

The major geometric imperfections in the two filled PhCs were a hollow air core and thick HfO_2 capping layer, for the first filled PhC, and the recession of HfO_2 within the cavity, for the second filled PhC.

In the case of the first filled PhC, I varied the parameters one at a time (while

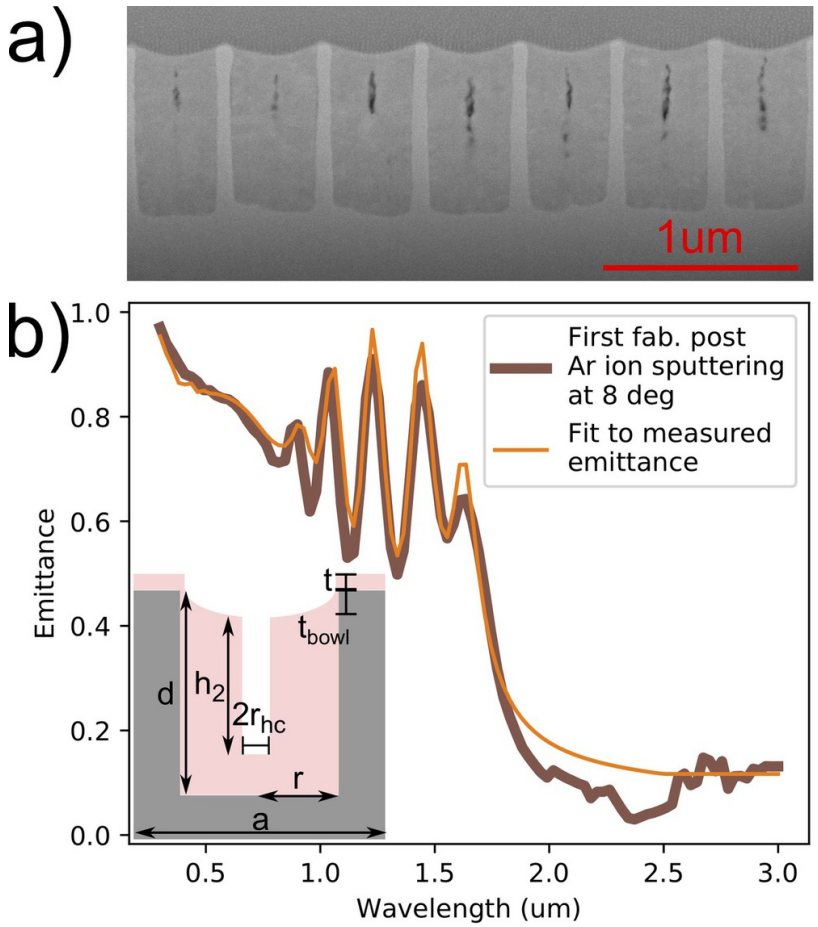

Figure 3-15: The focused ion beam image (a), of a metallo-dielectric PhC cross section after Ar ion sputtering, enabled the construction of a geometric model (b, inset) that corresponds well to the measured emittance (b). Geometric parameters are (in µm) $a = 0.5$, $r = 0.193$, $d = 1.03$, $t = 0.015$, $r_{hc} = 0.005$, $h_2 = 0.01$, and $t_{bowl} = 0.067$.

keeping everything equal) and calculated the impact on the four sub-metrics:

- Hollow air core: Eliminating the hollow air core improves all the metrics (Figure 3-16)
  - r_{hc}: reducing the hollow core radius improves all metrics (Figure 3-17)
  - h_1 or $t_{\text{abovehollowcore}}$: reducing this (bringing hollow core closer to the top of the cavity) tends to worsen the metrics, although the trend is not monotonic (Figure 3-18)
  - h_2 or $t_{\text{hollowcore}}$: reducing the height of the hollow air core improves the metrics (Figure 3-19)
- Period a: Increased period a improves three of the metrics: this simultaneously reduces both in-band and out-of-band radiated power per area, leading to higher spectral selectivity and lower deviation (Figure 3-20)
- Depth d: Changing d minimally changes the emittance (Figure 3-21)
- Radius r: Decreasing to the radius r from 0.2 µm to 0.19 µm (where 0.19 µm is the target radius for this cutoff) improves all metrics (Figure 3-22)
- Thickness of capping layer t: for in-band and out-of-band radiated powers and spectral selectivity, reducing t worsens the metrics until the thickness reaches below 0.12 µm or so (Figure 3-23)

The calculations showed it was possible to improve the metrics by tweaking a parameter, but in most cases changing a parameter not change the fundamental shape of the PhC emittance spectrum - except in the cases of small t, a prominent out-of-band resonance peak remains. In addition, our group's fabrication process made it difficult to precisely control the radius and period, and the results from the second filled PhC showed that reducing the capping layer thickness t was not straightforward.

However, the results from the second filled PhC indicated it was possible to more fully fill the cavities.

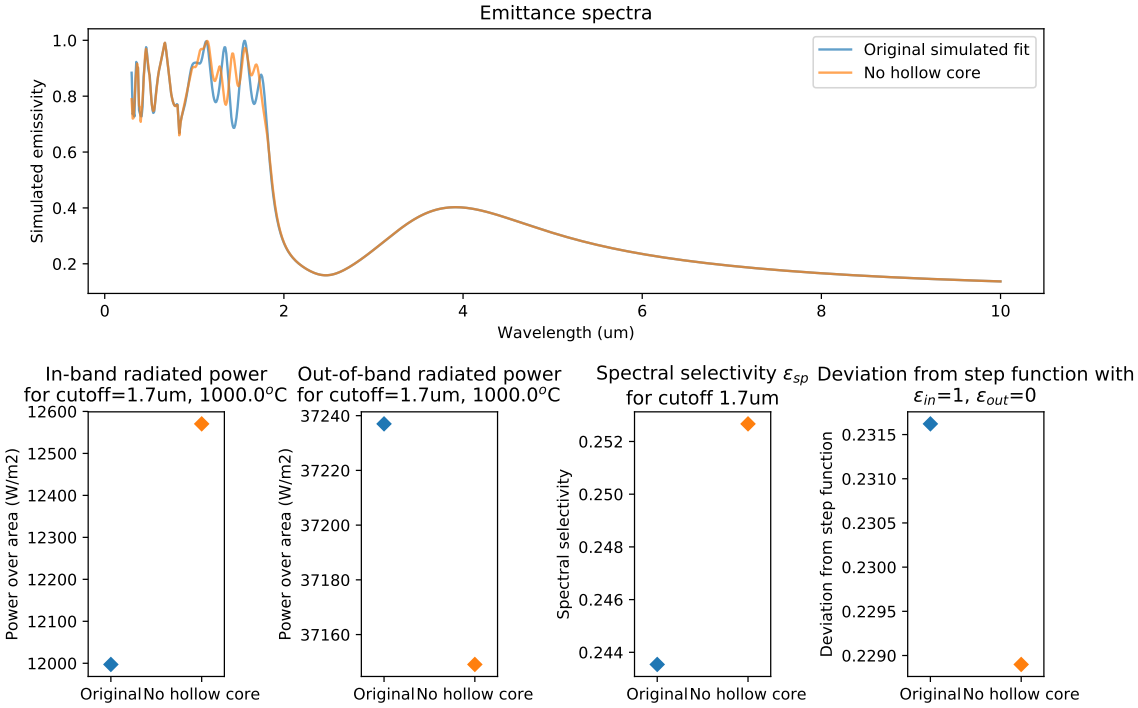

Figure 3-16: Eliminating the hollow core improves all metrics (all else equal).

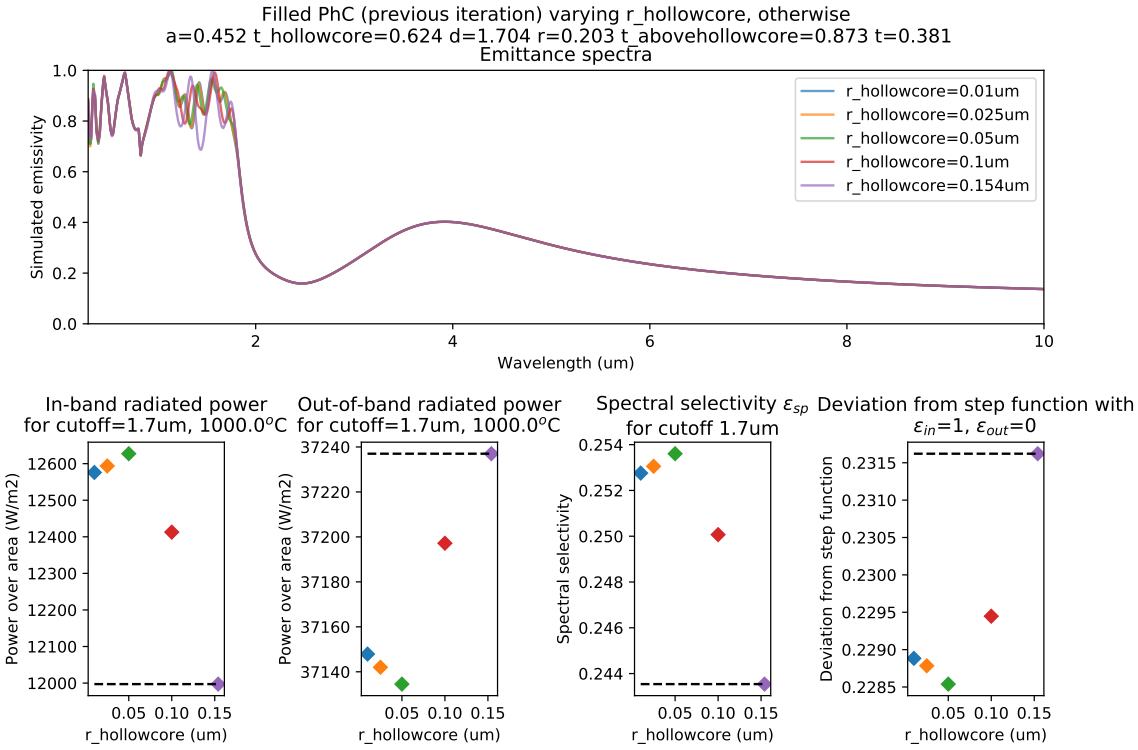

Figure 3-17: Reducing the hollow core radius improves all metrics (all else equal).

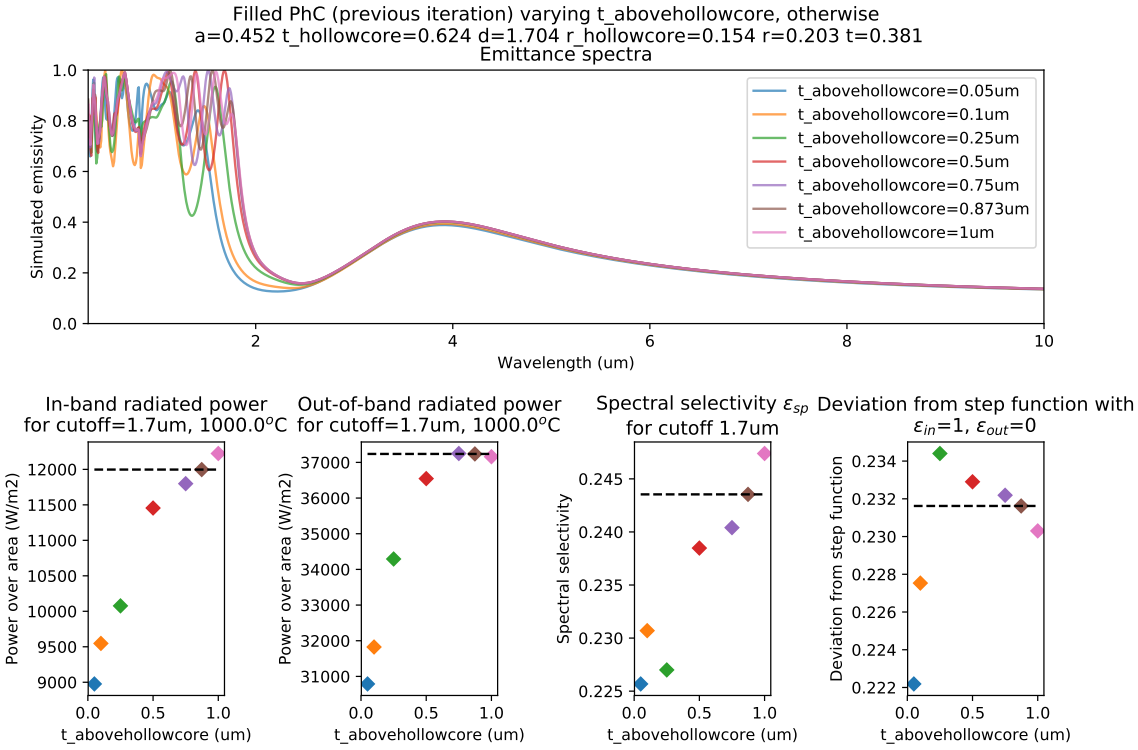

Figure 3-18: Reducing $t_{\text{abovehollowcore}}$ (bringing hollow core closer to the top of the cavity) tends to worsen the metrics, although the trend is not monotonic (all else equal).

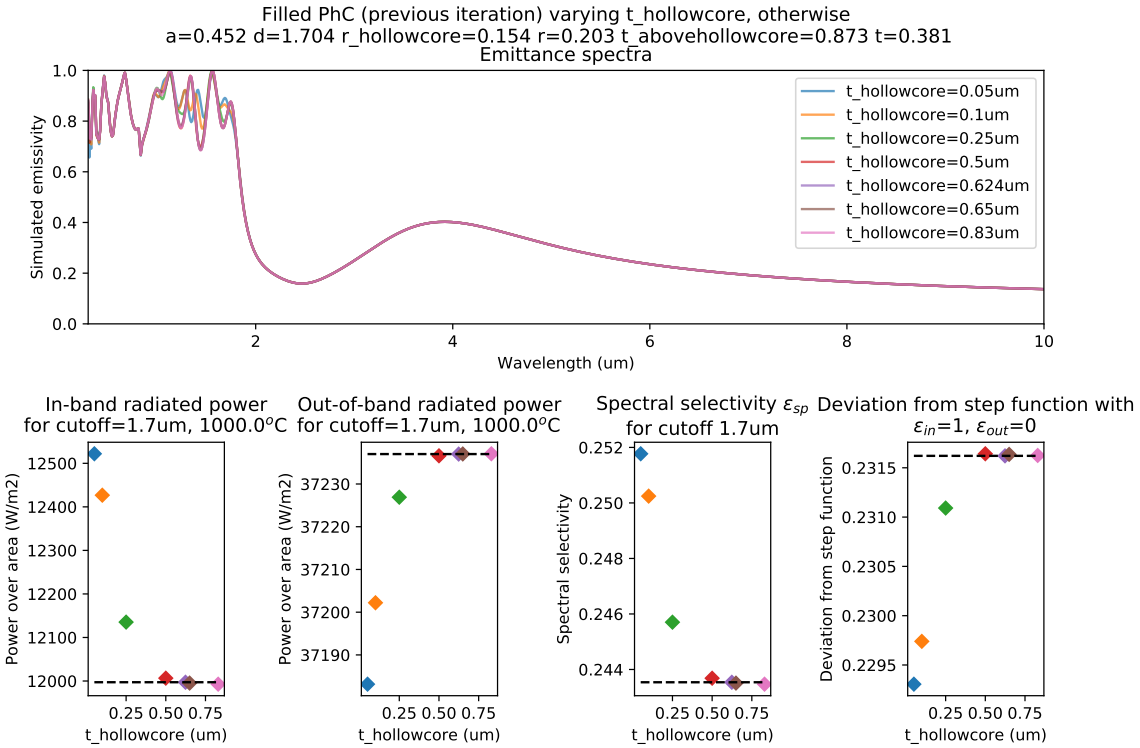

Figure 3-19: Reducing the height of the hollow air core improves the metrics (all else equal).

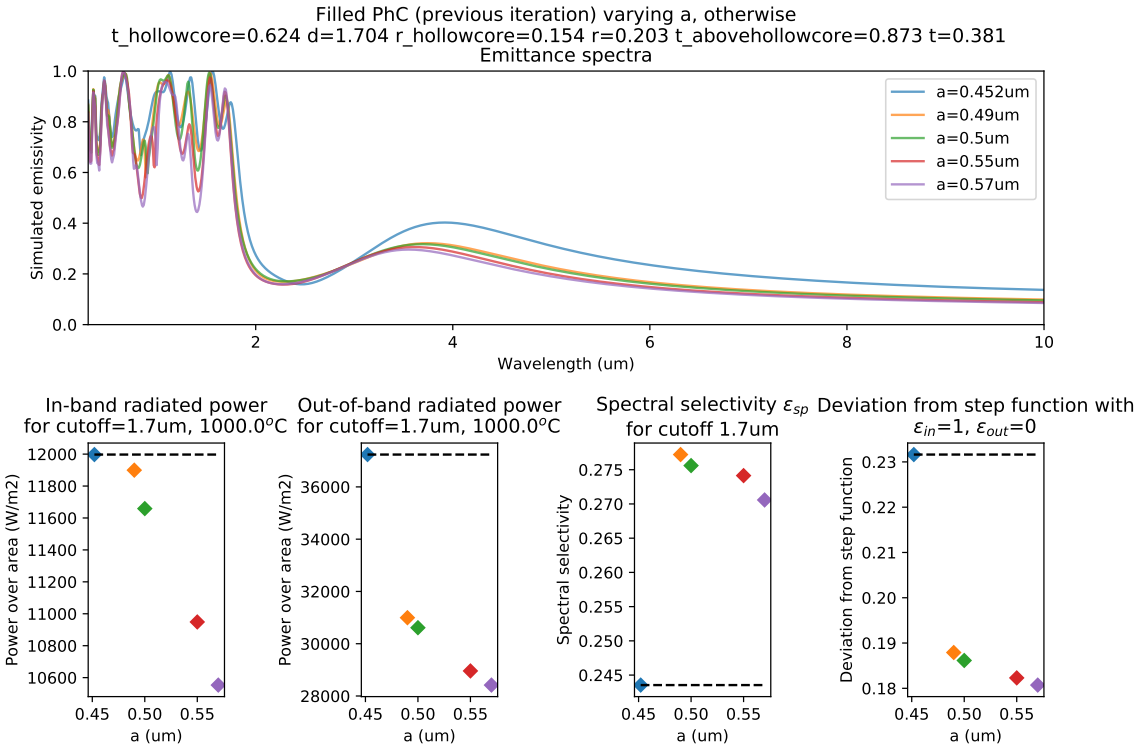

Figure 3-20: Increased period a improves three of the metrics (all else equal).

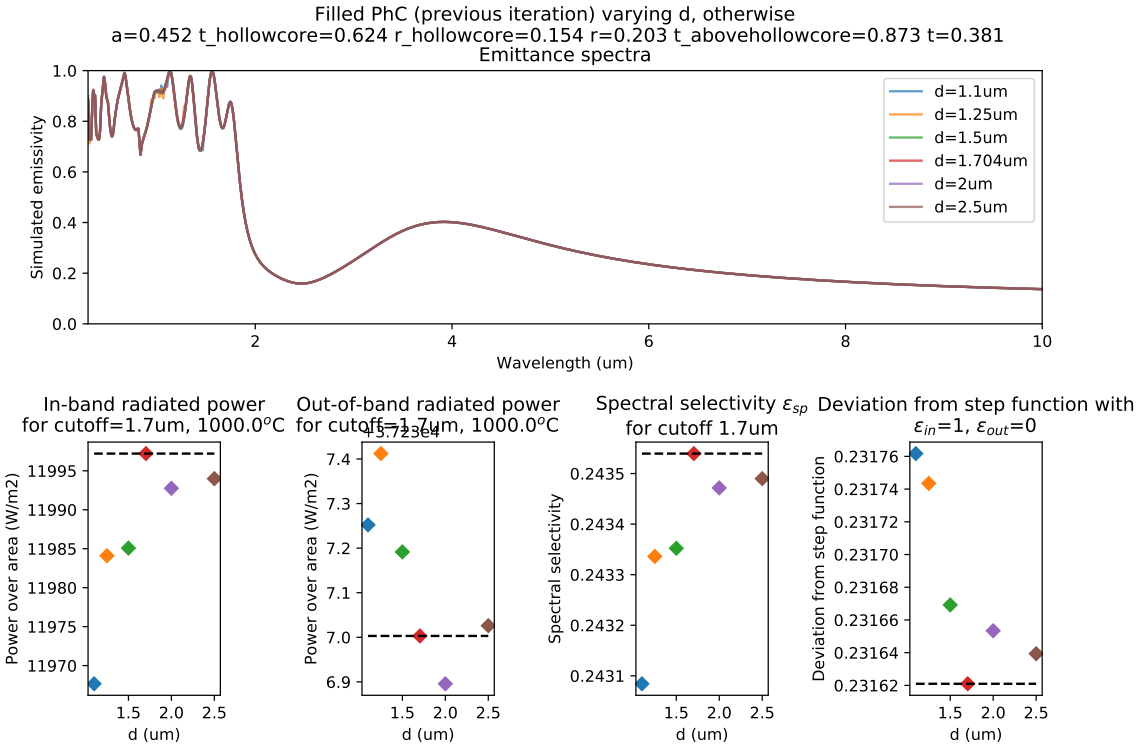

Figure 3-21: Changing d minimally changes the emittance (all else equal).

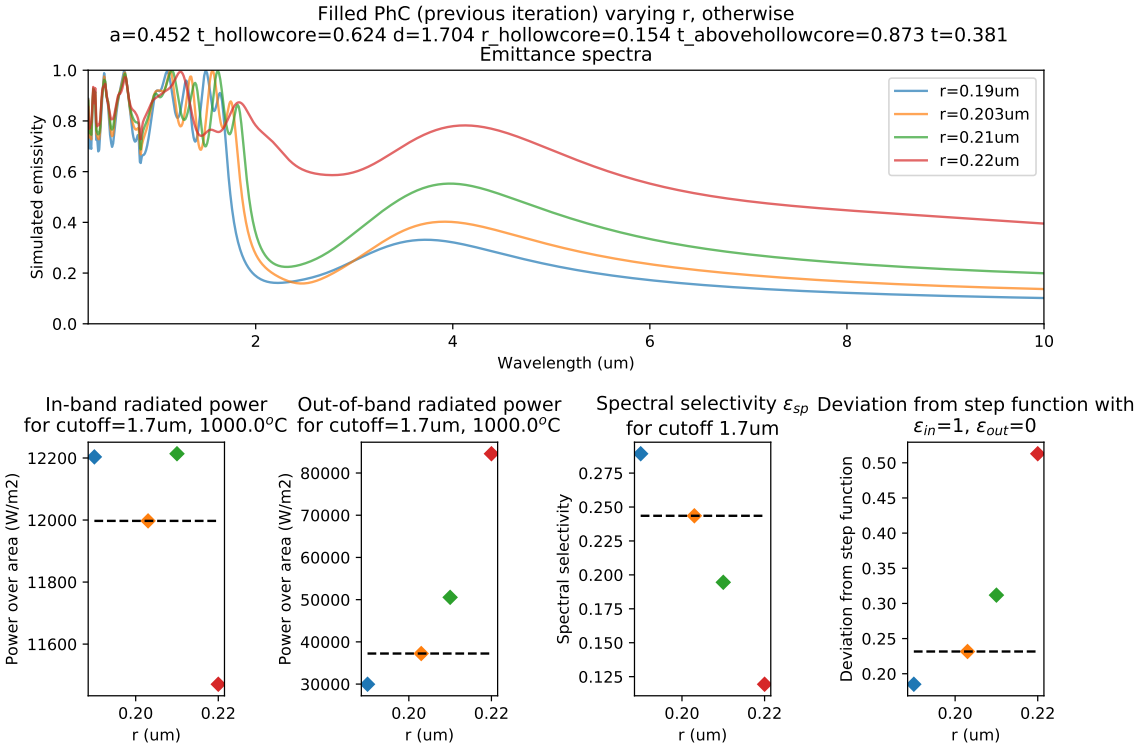

Figure 3-22: Decreasing to the radius r from 0.2 µm to the target radius (0.19 µm) improves all metrics (all else equal).

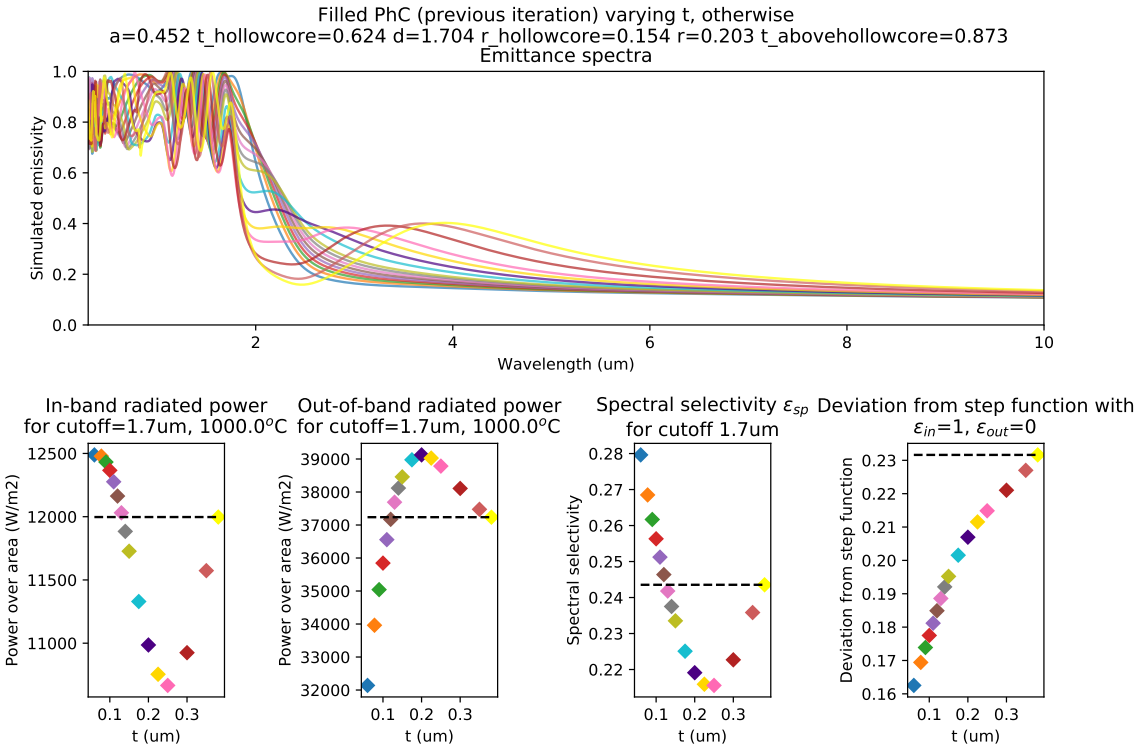

Figure 3-23: Decreasing t: three of the metrics worse at first, then improve as thickness reaches below 0.12 µm (all else equal).

In the next fabrication of the filled PhC (see next chapter), I sought to make filled PhCs with larger radius (0.23 µm as opposed to 0.2 µm), for 2.0 µm cutoff (InGaAs), and to fill them more fully using exposure mode ALD as discussed at the beginning of this chapter.

Chapter 4

Characterization and modeling of next-generation filled metallo-dielectric PhCs

Chapter 3 discusses the three major geometric imperfections that adversely impacted the two emittance of the first two fabricated filled PhCs.

A change was made to the fabrication process to address one of these imperfections, a hollow air core: a combination of standard mode and exposure mode atomic layer deposition (ALD) to more fully fill the PhC cavities. The cavity is first filled with standard mode ALD until the cavity aspect ratio reaches about 20, then the cavity is filled with exposure mode ALD.

This chapter discusses this new filled PhC, made as a result of this change to the fabrication to better fill the PhC cavities.

The characterization of these metallo-dielectric PhCs is in three parts:

- Room temperature reflectance measurements to measure optical properties (Section 4.3)
- Focused ion beam (FIB) cross sections to identify important geometric features (Section 4.2)
- Simulations to model and fit to the PhC emissivity (Section 4.5)

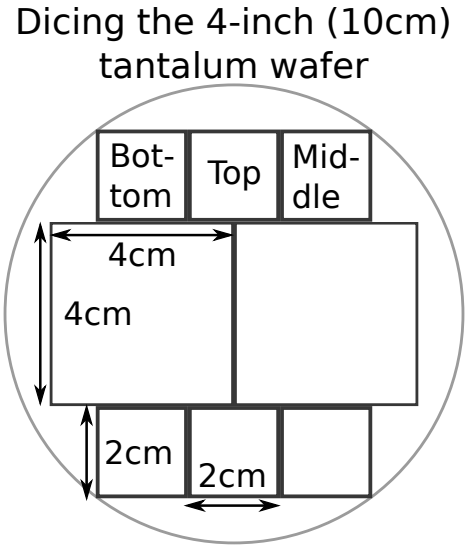

Figure 4-1: The three characterized pieces, 'top', 'middle', and 'bottom' come from the edge of the wafer, where some of the PhC structure may have collapsed, leading to degraded optical properties. This likely explains why the bottom piece emittance looks particularly odd.

Following characterization, I used simulations to fit to the emittance and understand the critical features that impact and the best ways to improve the PhC emissivity (Section 4.6)

4.1 Sample information

After dicing the wafer (this was before filling the cavities with HfO_20, I primarily worked with three 2 cm x 2 cm pieces that were taken from near the edge of the wafer, as shown in Figure 4-1. The pieces were (unimaginatively) named "top," "middle," and "bottom" pieces.

The pieces were not identical to one another and the underlying PhC structure was also not uniform across each piece. This is because, as noted in the the Fabrication section of Chapter 2, the cavity diameters increase radially from the center. In particular towards the wafer edge, the cavities begin to merge (there is partial degradation in the sidewall that would separate individual cavities).

The "top" piece had the best performance; "middle" piece had decent performance towards one corner of the piece (the corner closest to the wafer center); the "bottom"

piece had okay performance but only at the very corner, and was difficult to measure.

4.2 A few notes on focused ion beam(FIB) imaging

There were a few difficulties with FIB imaging, which in some cases led to imaging artifacts:

- The cross section cut was not always parallel to the cavity walls. This was especially true for the tantalum samples, which were not flat. This had the following effects: a) in the cross section images, the cavity walls would not appear straight (they would taper towards the top or the bottom) and b) the cavities appeared taller than they actually were.
- Curtaining effects: ion beam milling often leads to aperiodic stripes. Curtaining effects were especially in prominent in many of my images: they appeared as lines extending downward from the cavity walls. The “curtains" do not correspond to actual features in the sample, but may have been caused by the difference in milling rate between cavity filling material and tantalum.
- Before imaging the PhC cavities after DRIE (so they are empty, not yet filled with HfO_2), the cavities were filled with platinum, so that they would mill more evenly. However, at first glance it may appear that they were filled with HfO_2. However, in part due to the high aspect ratio of the cavities, they were difficult to fill. Air pores are visible within the cavity where the platinum did not fill completely. (The cavities were also topped with platinum, see next point)
- To prepare cross sections for FIB imaging I deposited two layers of platinum on top of the PhC to protect the top surface. The two layers appear distinctly in the images and are not part of the PhC. The first (bottom) layer is electron-beam deposited platinum, and the second (top) layer is ion-beam deposited platinum.
- Because of the variation across the wafer and across the pieces, the imaged area and measurements taken there are not necessarily representative of the whole wafer or piece.

Figure 4-2: Schematic of PhC cross sections at each of the three stages they are characterized

4.3 Room-temperature reflectance measurements and focused ion beam (FIB) images

I characterized the samples at three processing stages (Figure 4-2):

- After the cavities in tantalum have been generated, using deep reactive ion etching (DRIE), but before dicing into smaller pieces (Figure 4-3)
- After partially filling three (top, middle, bottom pieces) of the diced smaller pieces with HfO_2. I only imaged the bottom piece with FIB (Figure 4-4)
- After fully filling (top piece and middle piece) of the diced smaller pieces with HfO_2, and after 1 minute of argon ion sputtering for the middle piece only

After DRIE (Figure 4-3), the cavity walls looked reasonably straight and the emittances showed a sharp cutoff behavior, as expected. Around the center of the wafer, cavity depth was about 1.5 µm, radius ∼0.4 µm, and period 0.58-0.6 µm.

At this point, I diced the tantalum wafer and selected three pieces, labeled “top," “middle," and “bottom."

Based on the cavity radius information, I calculated the appropriate number of cycles each for standard mode and exposure mode ALD, as explained in the. Bob Geil did 1500 standard mode cycles of ALD to partially fill the cavities, up to about an aspect ratio of 20.

After partial filling (Figure 4-4), the emittances of the PhCs were different. The top and bottom piece emittances showed something like a cutoff next to an out-of-

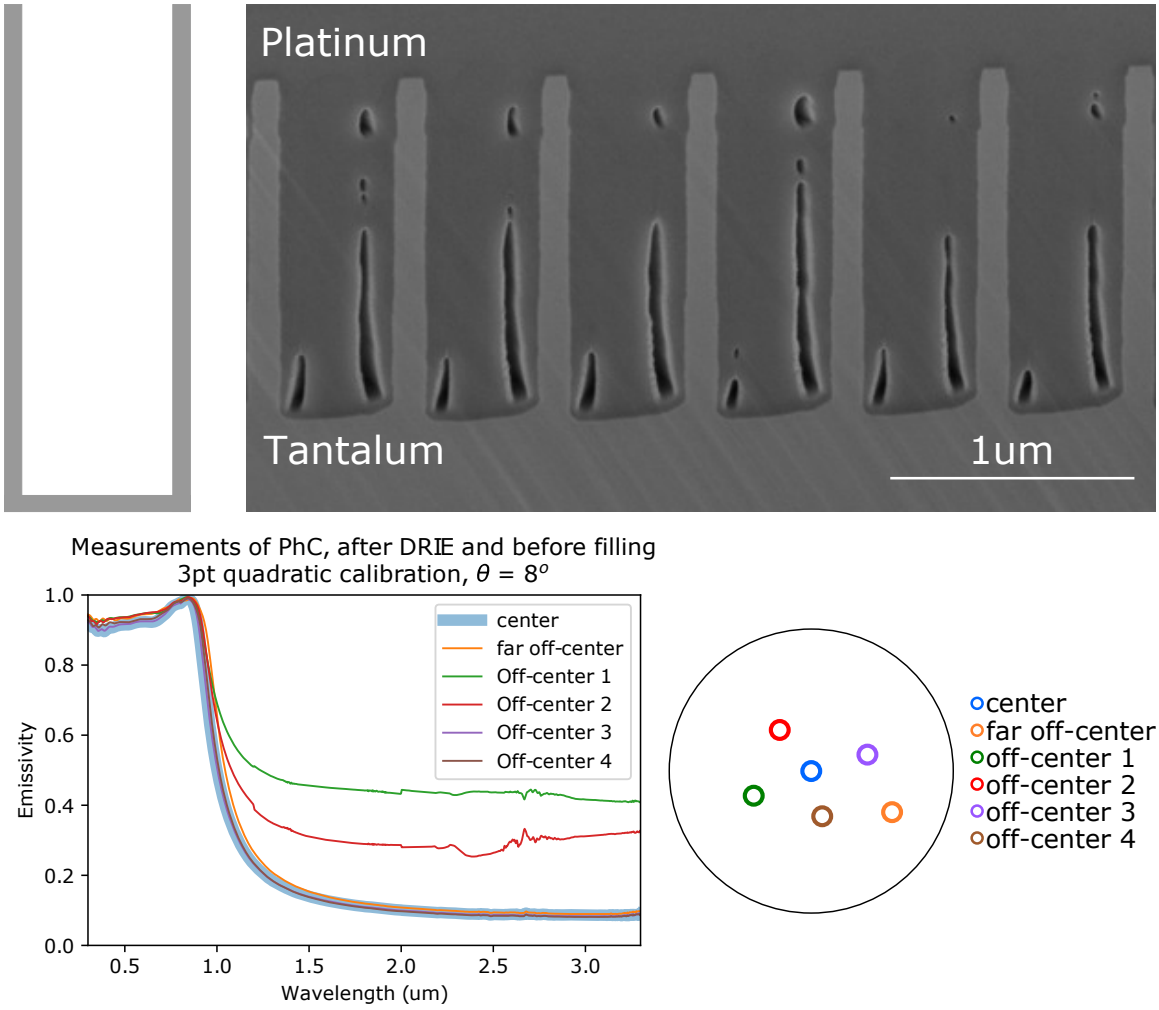

Figure 4-3: At this stage in processing (after DRIE and before filling with HfO_2), the sample consists of cavities etched into tantalum. The FIB image shows cavities filled with platinum (not HfO_2) for more-even milling, with diagonal curtaining image artifacts. The cavity depth is about 1.5 µm. The emissivity, measured at multiple points on the wafer, is as expected: a sharp cutoff for a much shorter wavelength than the target wavelength (∼2 µm). A potential reason why the out-of-band emittances are high for a few points is that the wafer is bowed.

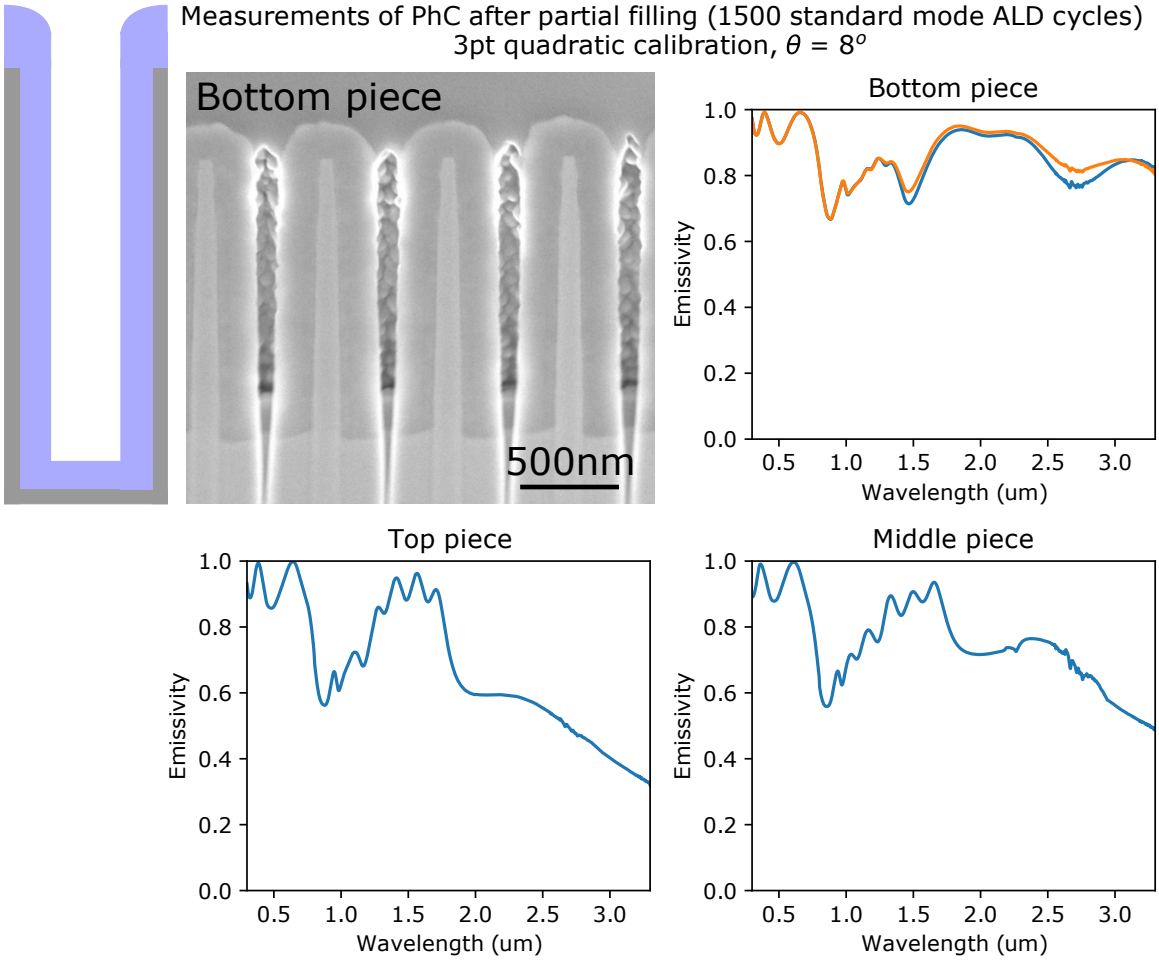

Figure 4-4: After partially filling the tantalum cavities with HfO_2, all three pieces (labeled 'top', 'middle', and 'bottom') have high emittance. While emittance of the top and middle pieces seem to suggest a cutoff between 1.5 and 2.0 µm - where there is an out-of-band resonance visible - the bottom pieces does not show a similar behavior. The FIB image of the bottom piece shows strong curtaining effects.

band resonance peak, but the bottom piece emittance did not.

I did not fully fill the bottom piece at this stage (it was only partially filled).

The top and middle pieces were then fully filled with 405 cycles of exposure mode ALD; the middle piece was then milled for 1 minute with argon ion. The characterization results are shown in Figure 4-5 and Figure 4-6.

For the emittances of both, the cutoff behavior is clearer, and there are distinct in-band resonance peaks as well as a wide out-of-band resonance peak. I was able to measure the pieces both in absolute and relative reflectance modes.

The cross section images of both pieces show cavities almost completely filled,

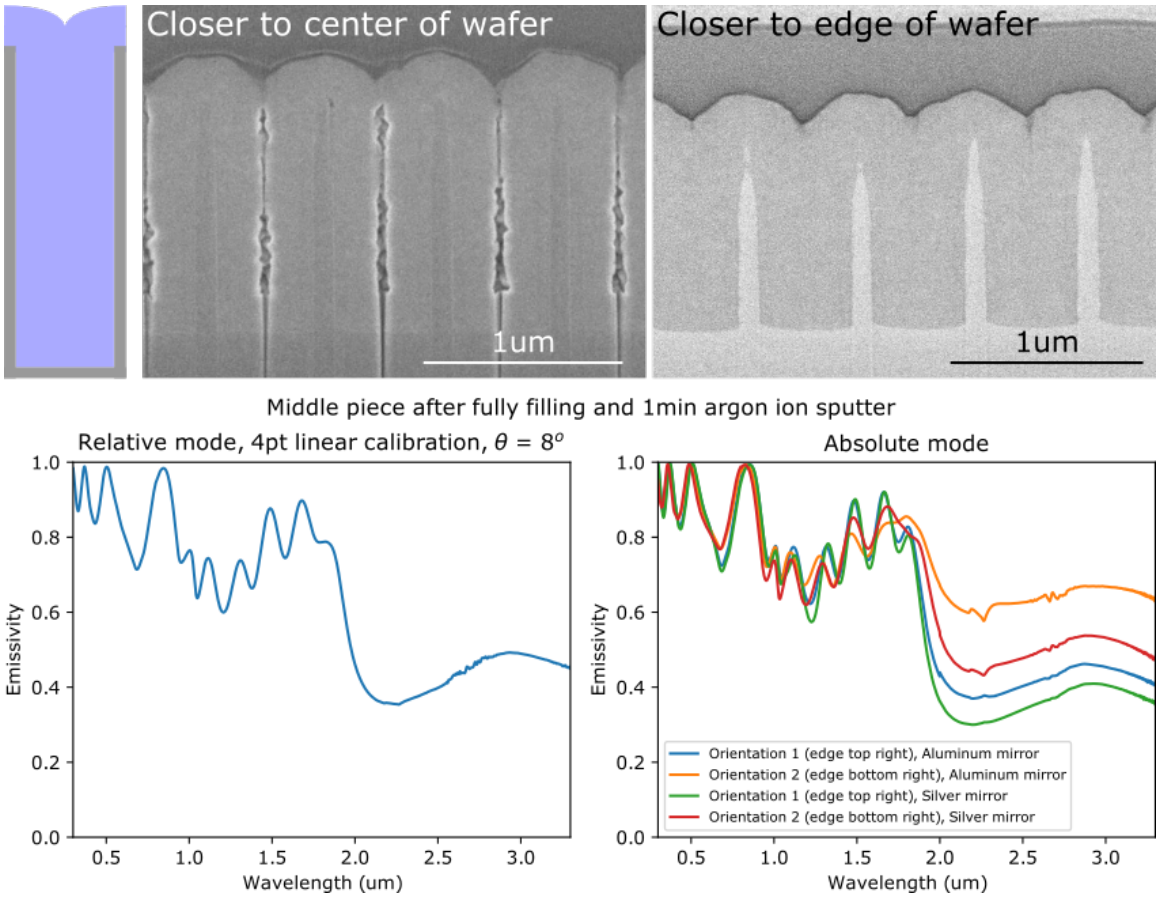

Figure 4-5: Middle piece after fully filling the middle piece with ALD: the HfO_2 capping layer looks scalloped instead of flat. Cavities near the wafer center show a thin hollow air core within; in some areas near the wafer edge, cavity sidewalls have begun to degrade, which would affect optical performance. The emittance shows a cutoff around 2 µm, and an out-of-band resonance peak around 2.7 µm.

with a very narrow and tall hollow air core, and scalloped (not flat) capping layers.

For the middle piece, I also imaged the cross sections of the cavities near the edge of the wafer, which showed some degradation of the tantalum cavity walls. This corresponded to non-PhC-like emittance in that area of the sample, which is not shown.

The middle and top pieces were qualitatively similar but had slightly different cavity geometries. Their differences in cavity depth and capping layer thickness were corroborated in cross section images and suggested by the emittance measurements (Figure 4-7). In particular the middle piece appeared to have shallower cavities and a thinner capping layer.

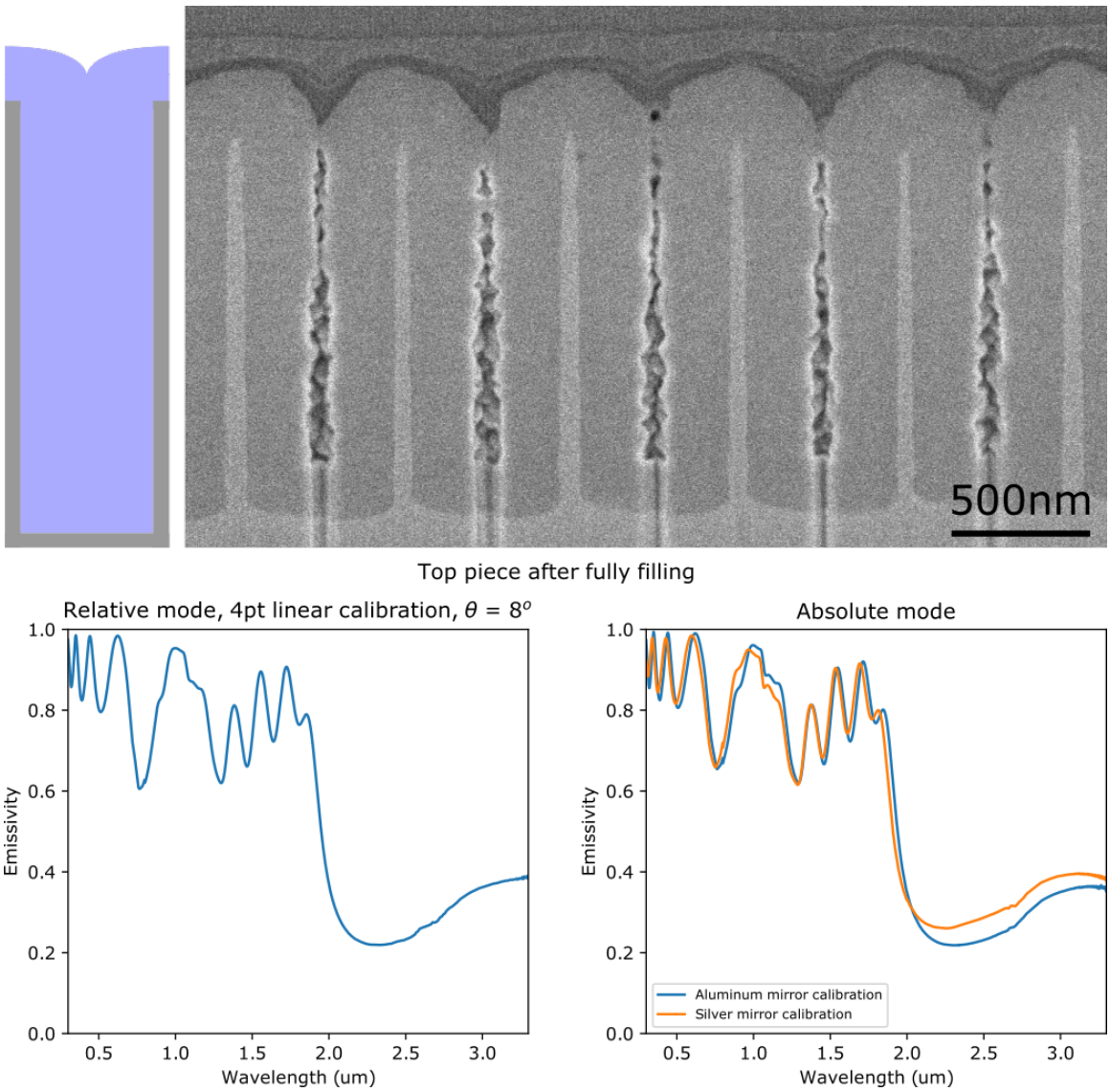

Figure 4-6: Middle piece after fully filling the middle piece with ALD: the HfO_2 capping layer looks scalloped instead of flat. Cavities show a thin hollow air core within The emittance shows a cutoff around 2 µm, and an out-of-band resonance peak around 3.3 µm. Compared to the middle piece, the cutoff behavior is more obvious.

The difference in capping layer thickness is likely because only the middle piece was etched after fully filling.

4.4 Comparison of results with previous iteration of filled PhC

I compared the results of the top and middle pieces with those of the previous iteration of the filled PhC (Figures 4-8 and 4-9). This previous iteration was made by my labmate Dr. Veronika Stelmakh and previously reported in [1], and I found a simulated fit to its emittance in [2].

Qualitatively, the emittances are not very different (Figure 4-8): in each of the emittance spectra there is a clear cutoff wavelength, in-band and out-of-band resonance peaks. The emittance spectrum of the previous iteration looks reasonably similar to that of the top piece: they share some in-band resonance peaks and the cutoff wavelength is approximately at the same position.

Two main geometries are identified by comparing the cross sections (Figures 4-9):

- The hollow core was much thinner than before.
- The layer of HfO_2 above the cavity was thinner than before and much more uneven, with the thinnest area of the HfO_2 near the center of the cavity. Previously, the HfO_2 layer was thick; it still had scalloping but was much less pronounced.

I also compared the four optical metrics for the previous iteration and the pieces, as shown in Figure 4-10. The metrics are calculated for the measured wavelength range 0.3-3 µm, a cutoff of 2 µm, emitter temperature of 1000 °C, and ideal step function with $\varepsilon_{in} = 1$ and $\varepsilon_{out} = 0$. Both the top and middle pieces have higher in-band radiated power compared to the previous iteration. However, the middle piece has relatively high out-of-band emittance, and as such is worse on out-of-band radiated power, spectral selectivity, and deviation from step function. The top piece performs better than the previous iteration on all metrics.

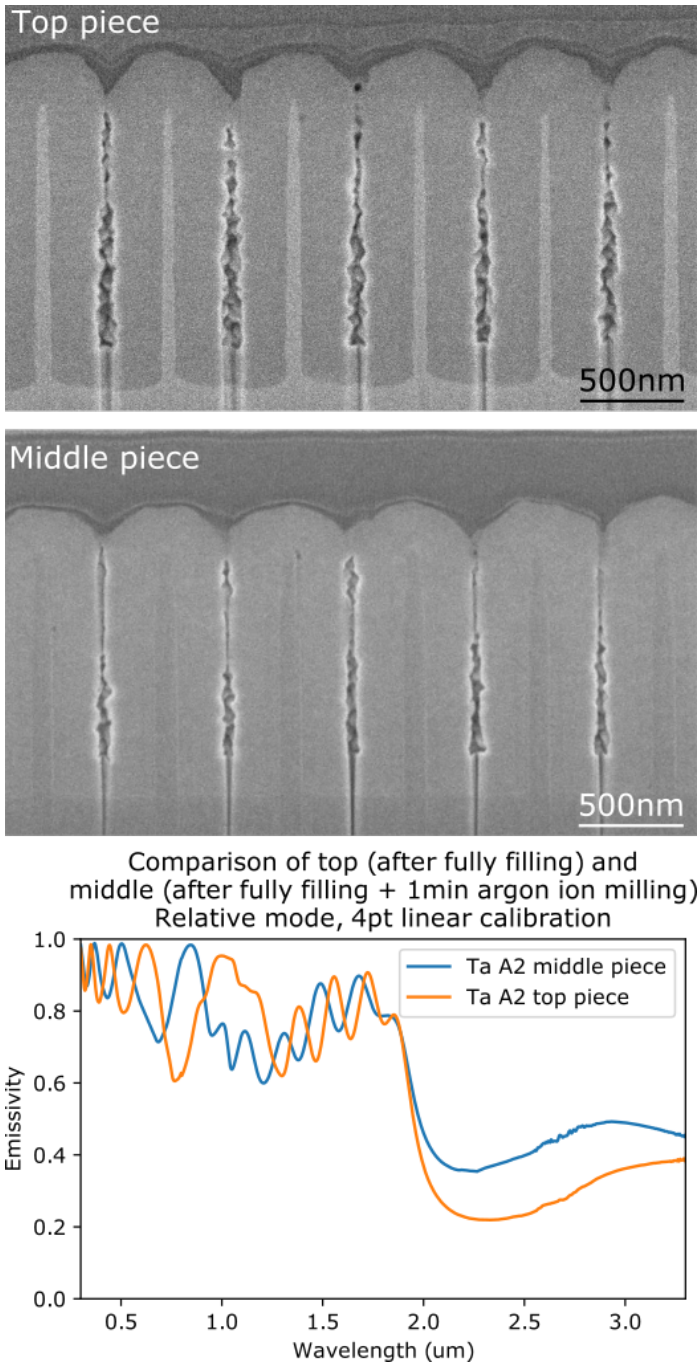

Figure 4-7: Comparison between top and middle pieces. In the middle piece, the cavities appear to be less deep, and the capping layer seems to be less thick, compared to those of the top piece. This seems consistent with the emittance measurements: the positions of the in-band resonance peaks are different (which can be caused by different cavity depths) and the out-of-band resonance peak for the top piece is at a longer wavelength

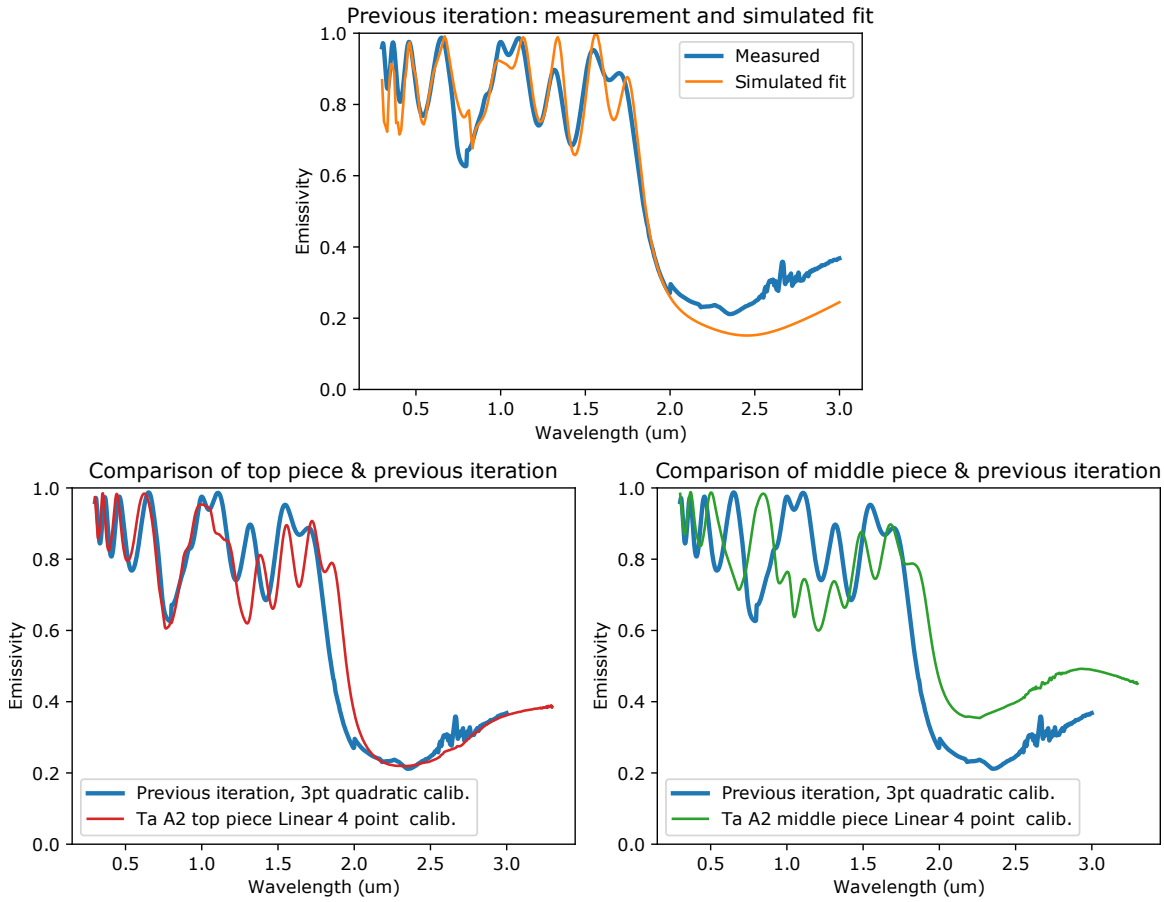

Figure 4-8: Comparison of the top and middle pieces with previous iteration of the filled PhC [1, 2]. The emittance of the latter is shown at the top, with its simulated fit. On the bottom left, the emittances of the top piece and previous iteration: many of the in-band and out-of-band resonance peaks are at the same position. On the bottom right, the emittances and the middle piece: qualitatively the behavior is similar (in-band resonance peaks, cutoff, out-of-band resonance peaks) but the positions of peaks and cutoff wavelength are different.

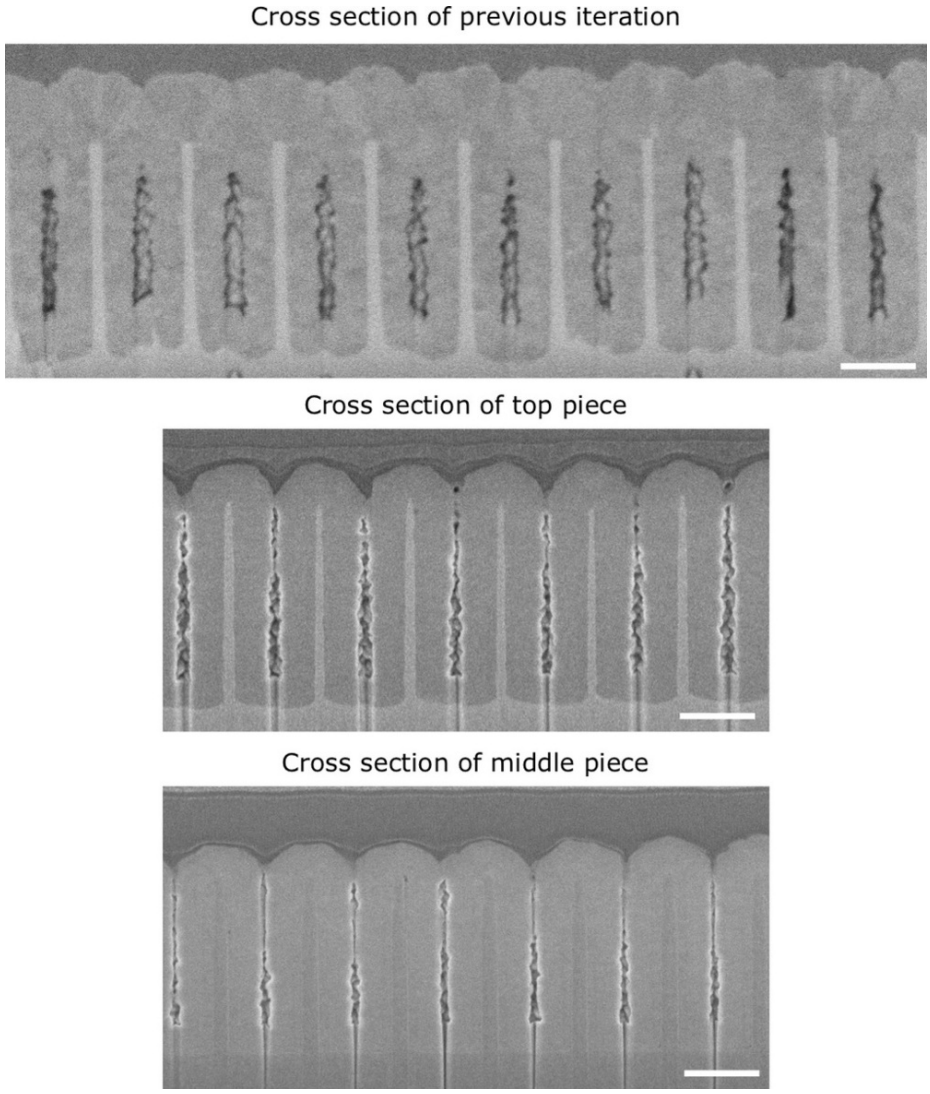

Figure 4-9: Comparison of the top and middle pieces with previous iteration of the filled PhC [1]. All three show tantalum cavities filled with hafnium oxide. Compared to the previous iteration, in the two pieces 1) the hollow core within the cavity seems thinner but taller and 2) the capping layer is overall thinner but has a much more pronounced roughness. Scale bar is 500 nm.

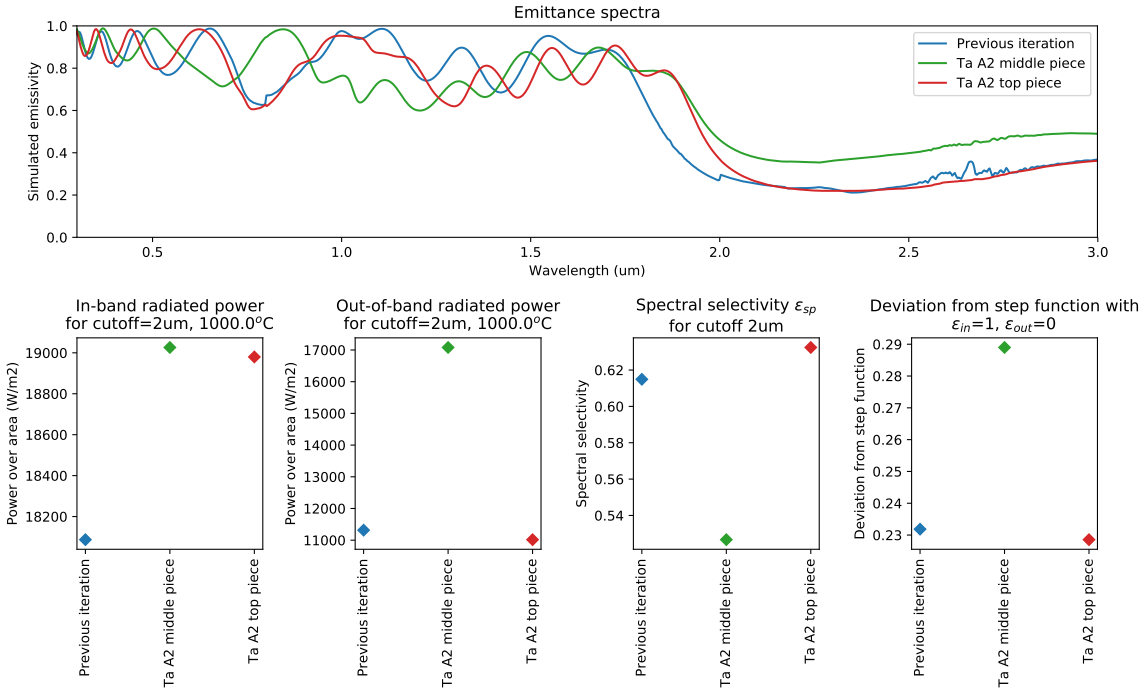

Figure 4-10: Comparison of the four optical metrics for the previous iteration and the top and middle pieces, calculated for the wavelength range shown (0.3-3 µm). Both the top and middle pieces have higher in-band radiated power compared to the previous iteration. However, the middle piece has relatively high out-of-band emittance, and as such is worse on out-of-band radiated power, spectral selectivity, and deviation from step function. The top piece performs better than the previous iteration on all metrics.

All four metrics should improve as the capping layer is thinned.

4.5 Simulations to fit to the measured PhC emissivity

Although I first expected that the capping layer surface roughness impacted the emittance, in fact the PhC emittance can be adequately described using a geometric model with a flat capping layer. Simulated fits to the top and middle pieces are shown in Figure 4-11. For the middle piece, the fit parameters are $a = 0.574\,295$ µm, $r = 0.235\,025$ µm, $d = 1.346\,833$ µm, $t = 0.273\,285$ µm; whereas for the top piece they are $a = 0.561\,190$ µm, $r = 0.229\,492$ µm, $d = 1.506\,053$ µm, $t = 0.350\,010$ µm.

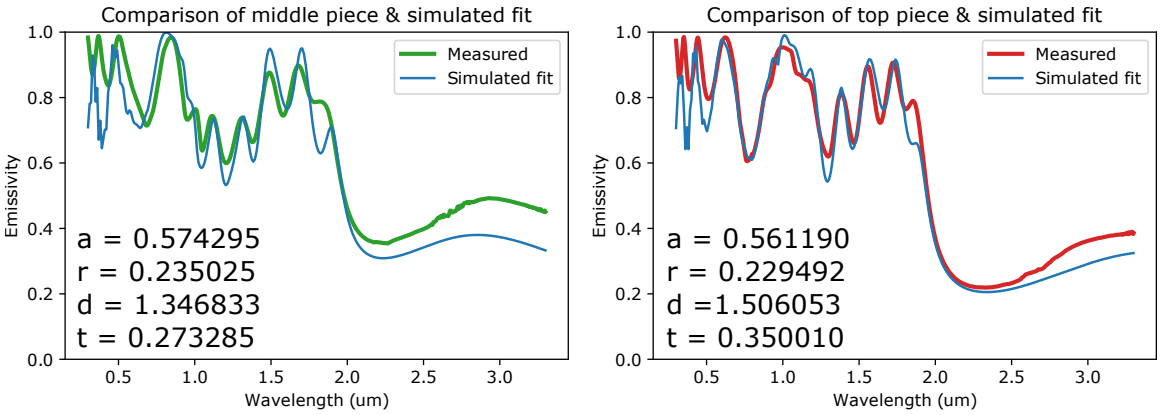

Figure 4-11: Simulated fits to the top and middle pieces, measurements are shown in µm. The period is about the same (a = 0.56-0.57 µm). It makes sense that the middle piece cavities have, relative to the top piece cavities, larger radius, thinner capping layer, and more shallow cavity, because the middle piece cavities correspond to a location closer to the wafer edge.

The thicknesses from the simulated fits, 270 nm for the middle piece and 350 nm for the top piece, are consistent with measurements from the FIB cross section. It makes sense that the middle piece cavities have, relative to the top piece cavities, larger radius, thinner capping layer, and more shallow cavity, because the middle piece cavities correspond to a location closer to the wafer edge.

Also, although a thin hollow core is visible in the FIB cross sections, according to the simulated fits they do not appear to greatly impact the PhC emittance.

I also simulated PhC models with rough capping layer, by approximating the capping layer as two halves of an ellipse, as shown in Figure 4-12. The capping layer is characterized by two thickness parameters t_1 (the thickest part) and t_2 (the thinnest part). When $t_1 = t_2$ the emittance matches that of the PhC model with flat capping layer.

The surface roughness does, however, affect the PhC emittance, as shown in Figure 4-13, which compares the measured spectrum and two simulated fits, one where the capping layer is flat and one where t_1 - t_2 = 0.2 µm. Both simulated emittance spectra look quite similar, with a few differences. In the case where the capping layer is rough, the out-of-band resonance peak is at a slightly lower wavelength; this makes sense because the capping layer is overall thinner. In addition, one of the in-

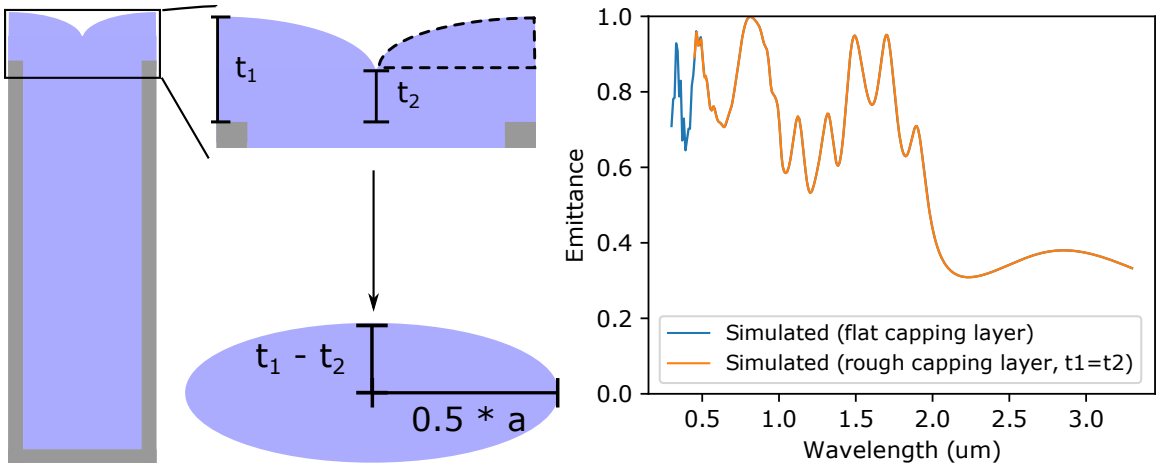

Figure 4-12: The PhC model with a rough capping layer has two parameters t_1 and t_2 describing the capping layer. The capping layer is modeled as an ellipse. When t_1 = t_2 the emittance matches that of the PhC model with flat capping layer.

band peaks (near 0.8 µm for the middle piece and 0.5 µm for the top piece) has also blue-shifted slightly.

4.6 Simulations to improve the PhC emissivity

I also used simulations to investigate the following:

- The optimal capping layer thickness, assuming that ideally the capping layer should be flat
- Whether the capping layer actually should be flat, for best performance
- If the capping layer should not be flat, what is the combination of t_1 and t_2 that gives the best optical performance

For the simulations I used the parameters for the middle piece: $a = 0.57$, $r = 0.235$, and $d = 1.35\,\mu m$.

The impact of the flat capping layer thickness (t, varied from 0.02 to 0.35 µm) on four optical metrics, is shown in Figure 4-14. None of the metrics show a monotonic increase or decrease, and the best t is different for each metric. Out-of-band radiated power and spectral selectivity are best (lowest and highest respectively) for a low t of 20 nm, while lowest deviation from step function occurs for $t = 30\,nm$. Highest in-band radiated power is for $t = 90\,nm$.

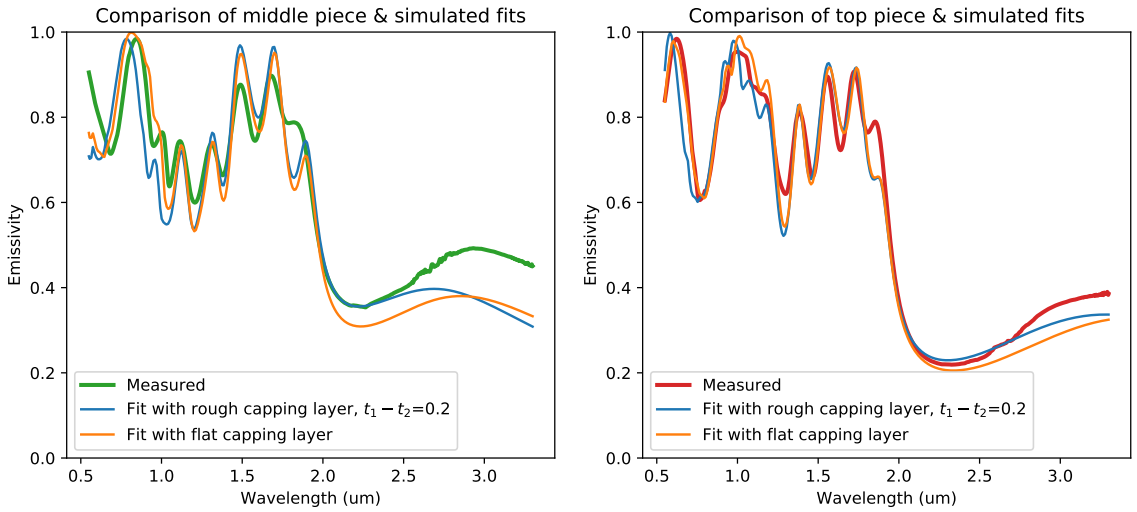

Figure 4-13: Comparison of measured spectra and two simulations, one with a flat capping layer and other with a rough capping layer ($t_1 - t_2 = 0.2\,\mu$m.. The simulated spectra look very similar, but for the rough capping layer spectrum the out-of-band resonance peak is at a slightly lower wavelength, because the capping layer is overall thinner.

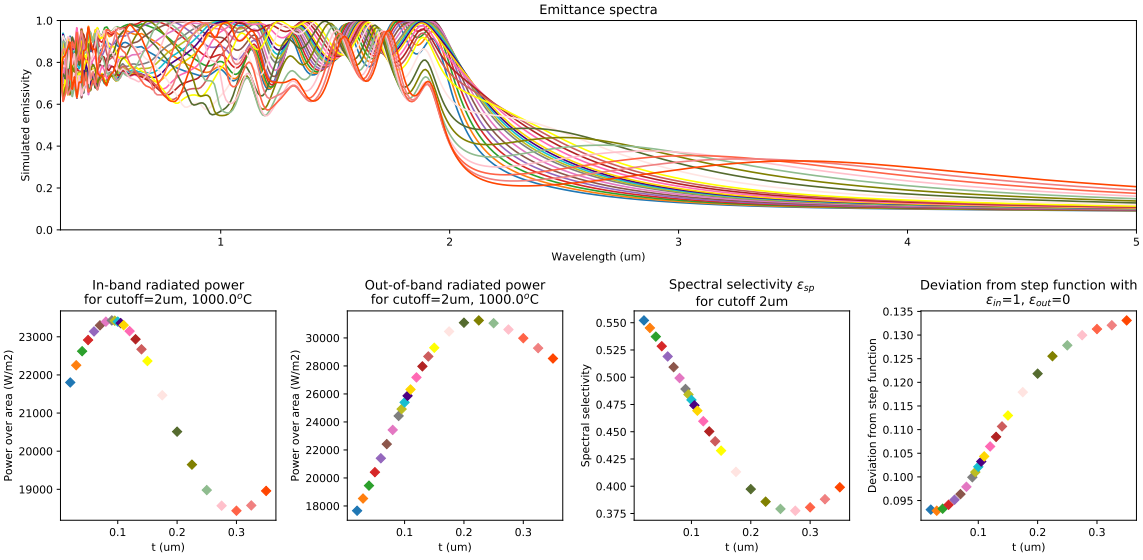

Figure 4-14: Impact of flat capping layer thickness (t, varied from 0.02 to 0.35 µm) on four optical metrics. Parameters a, r, d are the same as those for middle piece (a = 0.57, r = 0.235, d = 1.35 µm). None of the metrics show a monotonic increase or decrease; the best t is different for each metric. Highest in-band radiated power is for t = 90 nm.

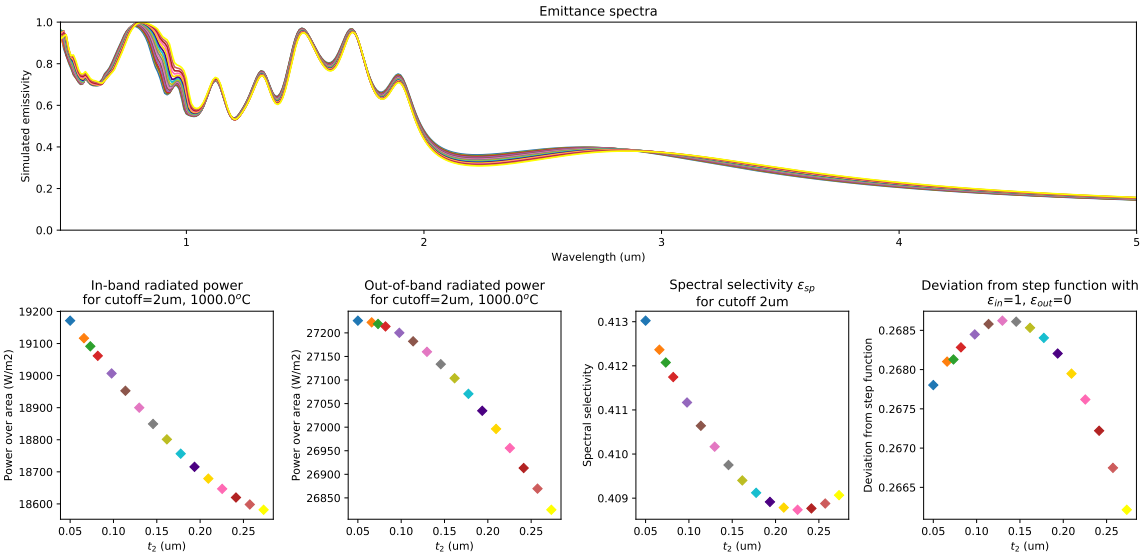

Figure 4-15: Impact of capping layer roughness (t_2) on the four optical metrics. Parameters a, r, d are the same as those for middle piece ($a = 0.57$, $r = 0.235$, $d = 1.35\,\mu m$); $t_1 = t = 0.273\,\mu m$. Increased capping layer roughness (lower t_2) appears to improve three of the metrics (in-band radiated power, spectral selectivity, and deviation from step function)

According to simulations, increased capping layer roughness (lower t_2) appears to improve three of the metrics (in-band radiated power, spectral selectivity, and deviation from step function), as shown in Figure 4-15. This may be because the in-band resonance peaks have a higher emittance when the surface roughness is flat. However, out-of-band radiated power also increases as capping layer roughness increases.

In fact, the aforementioned trends for t_2 hold for several values of t_1 (0.07-0.15 µm), as shown in Figure 4-16.

It is hard to tell whether these simulations results can be observed experimentally - whether experimentally a rough capping layer will lead to a higher performance. My model is not completely accurate: in particular, the absolute emittance values of the resonance peaks are not consistent between the measured spectra and the simulated fits.

It appears it is not absolutely crucial to get a perfectly flat capping layer - however, the thickness of the thickest part of the capping layer does matter, and HfO_2 should not be removed from within the cavity.

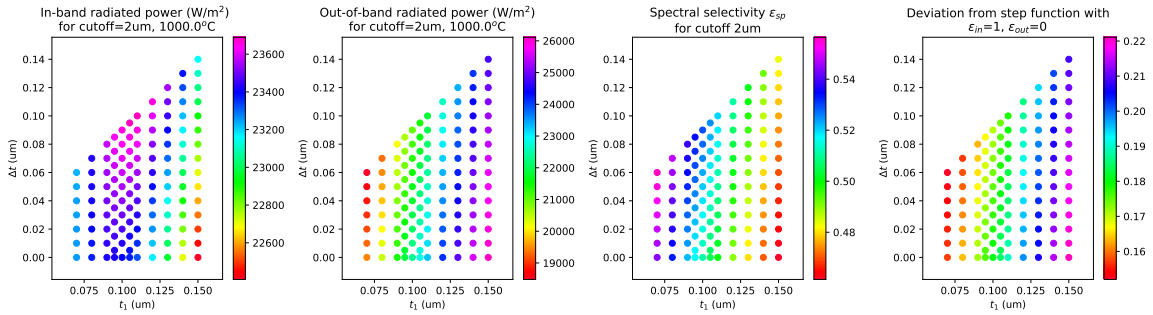

Figure 4-16: For at least some values of t_1, increased capping layer roughness (lower t_2) appears to improve three of the metrics (in-band radiated power, spectral selectivity, and deviation from step function).

4.7 System performance simulations

While the four optical metrics are useful, it can be hard to tell how a particular TPV system would perform, or how much better the performance would become, by changing the PhC emittance.

I did system performance simulations to estimate the power outputs for various PhC designs (measured and simulated), using parameters for three systems described in the group's system performance work [3]; also, details of the system model and parameters are described in Appendix D.

For each of the three systems, I varied the emittance while keeping everything else the same, and plotted the maximum power point (MPP) as a function of input fuel power.

To calculate emittance for a broad range (0.1-15 µm, I either interpolated (for measured emittances) or used simulated emittances. The interpolation for the measured emittances often resulted in high out-of-band emittance values, as shown in the figures, which are not necessarily indicative of actual behavior - but probably could be considered an upper bound on out-of-band emittance.

The filled PhCs included the following:

- Perfect PhC with 2 µm cutoff - the upper bound. Simulated in [87], with parameters $r = 0.23\,\mu\text{m}$, $d = 4.31\,\mu\text{m}$, $a = 0.57\,\mu\text{m}$, $t = 78\,\text{nm}$.
- Previous iteration ([1, 2]) of the filled PhC, two versions: measured and inter-

polated, simulated

- Middle piece, two versions: measured and interpolated, simulated
- A PhC with capping layer thickness $t = 90\,\text{nm}$, otherwise same parameters as the middle piece, simulated

One of the main findings from this calculation is that even moderately high out-of-band emittance can reduce overall system power - so much so that it cancels out a high in-band emittance. In all figures (fig:sysmod-inconel-vary-emitter, fig:sysmod-conformalPhC-vary-emitter, 4-19), the trend is that the higher the out-of-band emittance, the lower the system output power.

In fact, according to the calculations shown in Figure 4-18, the filled PhCs that have been fabricated so far (red, orange, green, purple, previous iteration and middle piece) show no significant improvement over the original conformal PhC emitter (black). The conformal PhC outperforms the two measured and interpolated filled PhCs that have high out-of-band emittances around 0.4-0.5. On the other hand, the simulated versions of these fabricated PhCs have comparable performance to the conformal PhC; even though the filled PhCs have higher in-band emittance, this is canceled out by the moderately high out-of-band emittance.

Therefore, there are two requirements to have high system output power: low out-of-band emittance and high in-band emittance. This can be enabled by having a filled PhC with thin capping layer thickness, as shown for the simulated PhC with $t = 90\,\text{nm}$ (purple, with parameters otherwise the same for the middle piece filled PhC).

In fact the system performance for the simulated filled PhC with t 90 nm approaches that of the “perfect" simulated PhC.

4.7.1 Varying capping layer thickness t

The main takeaway from the system modeling is that the higher the out-of-band emittance, the more this penalizes the system output power.

The question then becomes: what is the optimal capping layer thickness t between

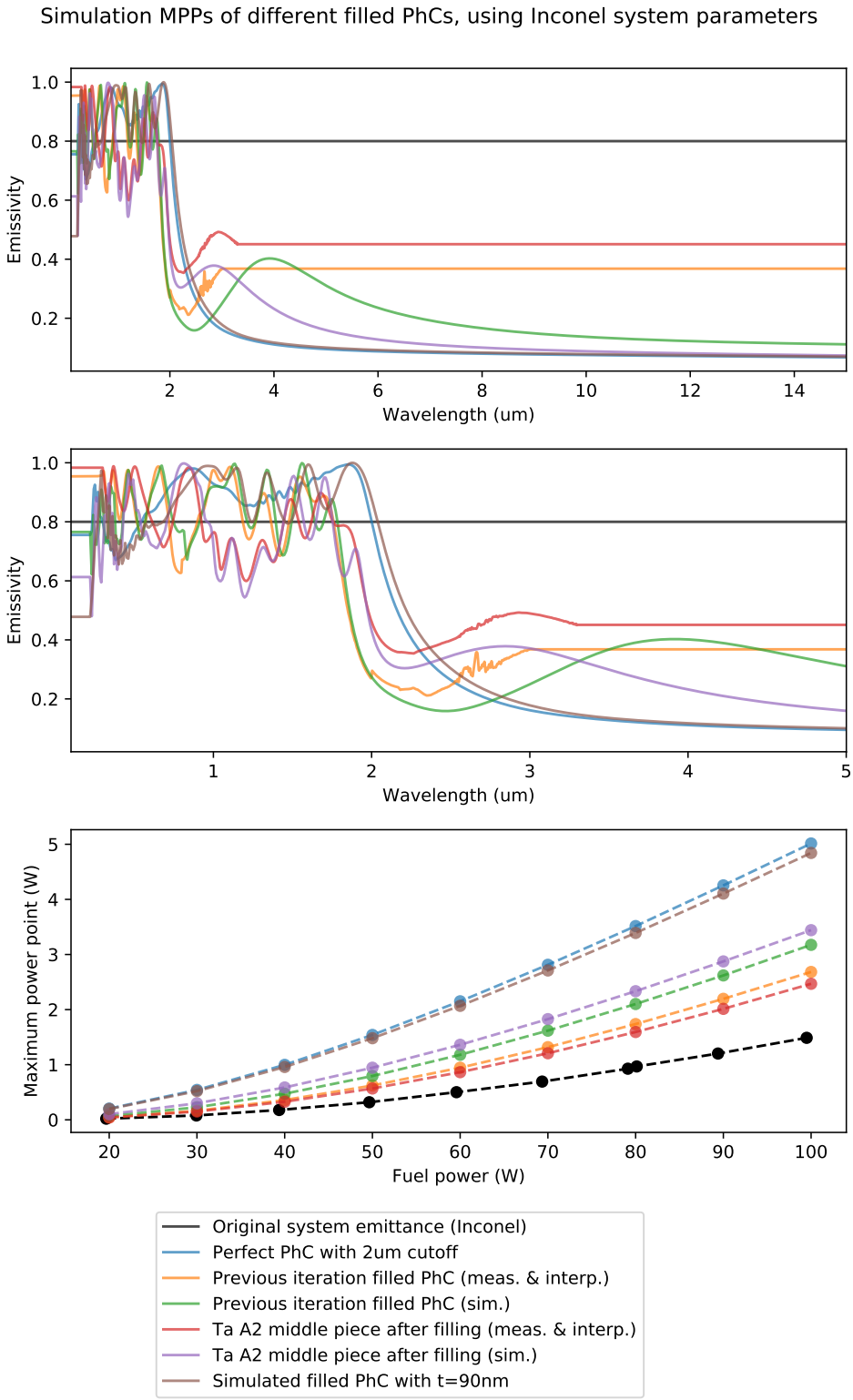

Figure 4-17: Modeling system output power (maximum power point) using different emitters for a system whose original emitter was a greybody (Inconel metal) with ε=0.8. (Parameters available in Appendix D and [3]). All filled PhCs give higher output power, compared to the original Inconel emitter.

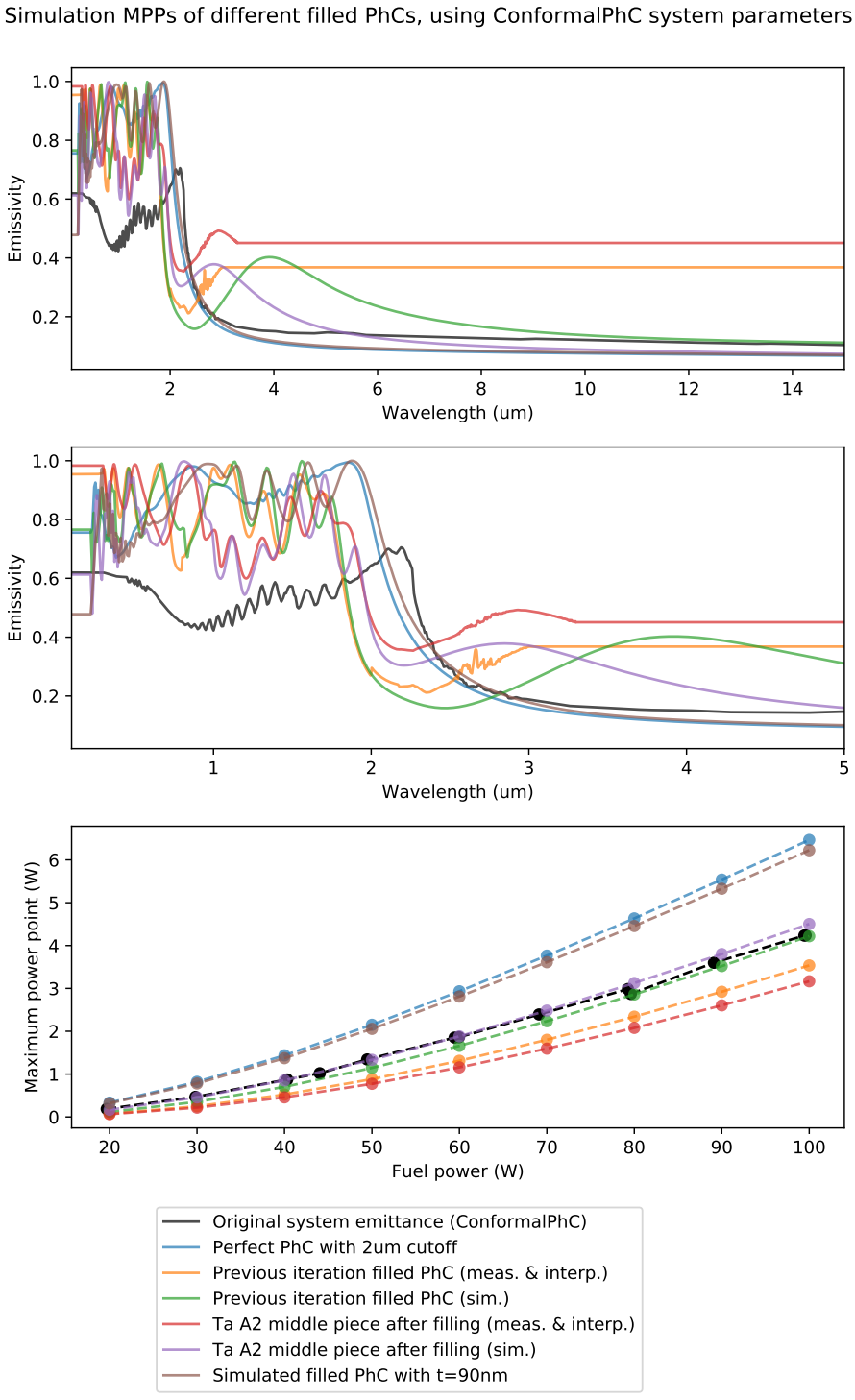

Figure 4-18: Modeling system output power (maximum power point) using different emitters for a system whose original emitter was a conformal PhC, shown in black. (Parameters available in Appendix D and [3]). Interestingly, the systems with the measured and interpolated PhCs (previous iteration and middle piece, orange and red) both lead to lower output power than the original system. This is likely because of the high out-of-band emittance. For the system with the simulated previous iteration (green), it seems the increase in in-band emittance almost cancels out the adverse impact of the higher out-of-band emittance.

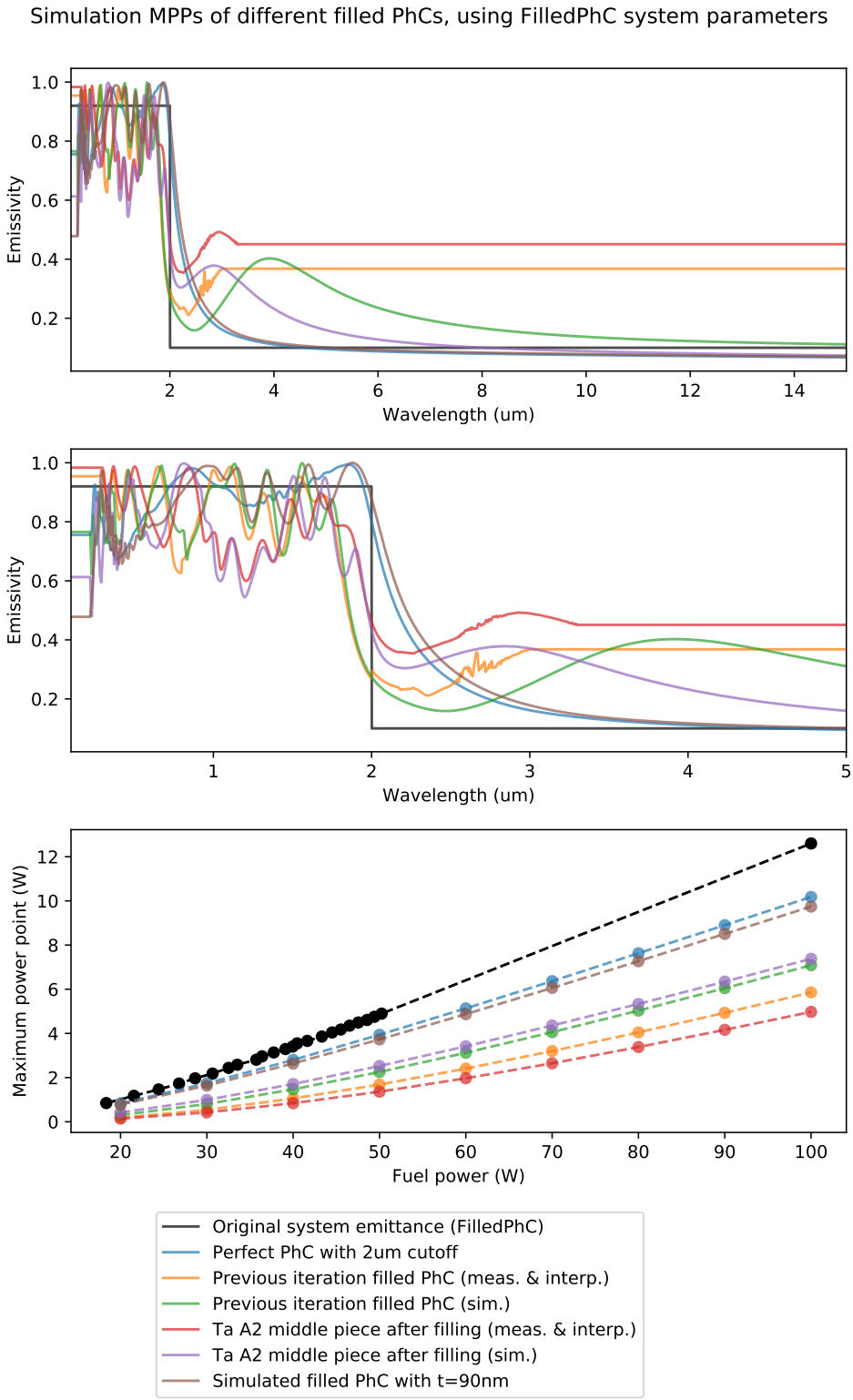

Figure 4-19: Modeling system output power (maximum power point) using different emitters for a system whose original emitter was a filled PhC with ε_{in} = 0.92 and ε_{out} = 0.16, shown in black. (Parameters available in Appendix D and [3]). None of the other filled PhCs seem to match up to the original PhC's simulated performance.

20-90 nm according to system performance simulations.

In previous simulations of the filled PhC with varying capping layer thickness t (the impact on the four optical metrics shown in Figure 4-14), I found that reducing the thickness t starting at 90 nm down to 20 nm simultaneously reduces both the in-band and out-of-band radiated powers. Because both decrease at the same time as the thickness decreases, it is hard to tell what is their relative impact on the system output power.

It appears that the maximum power points do not vary significantly when the capping layer thickness changes, as shown in Figure 4-20.

Examining the results more closely (see Figures 4-21, 4-22, 4-23), I found that the optimal capping thickness layer depends on both the input fuel power as well as the system conditions. The percent improvement that can be achieved by tuning the capping layer thickness varies from about 4% to 9% for input fuel power of 100 W. The main difference between the systems is the loss through the sides of the microcombustor (highest for the Inconel system and lowest for the filled PhC system).

4.8 Main takeaways

Through a combination of characterization (room-temperature reflectance and SEM cross sections) and simulations (including at the system level), I found that having a thin (but not necessarily flat) capping layer thickness is key to having high emitter and system performance. The target thickness lies between about 20 and 90 nm.

While system simulations predict higher system output power for thinner capping layers of $20-40$nm (for 100 W fuel input, for conformal and filled PhC system parameters), but it may not be prudent to target such thin capping layer thickness for the following reasons:

- I calculated using room temperature emittance, rather than for that for the operating temperature
- A thicker capping layer of HfO_2 may be able to better protect the tantalum

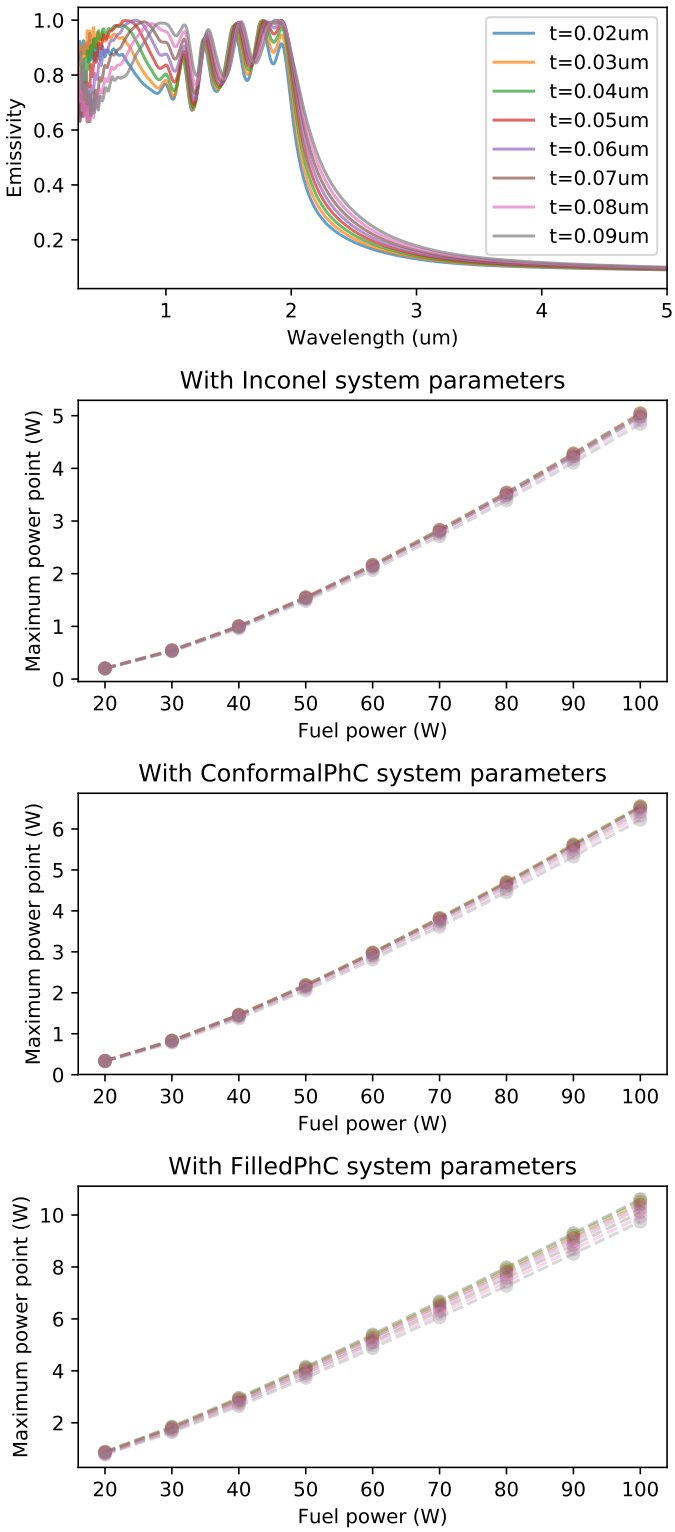

Figure 4-20: Varying the thickness of the capping layer t is varied between 20 and 90 nm does not seem to have a large impact on the system performance, for any of the three systems.

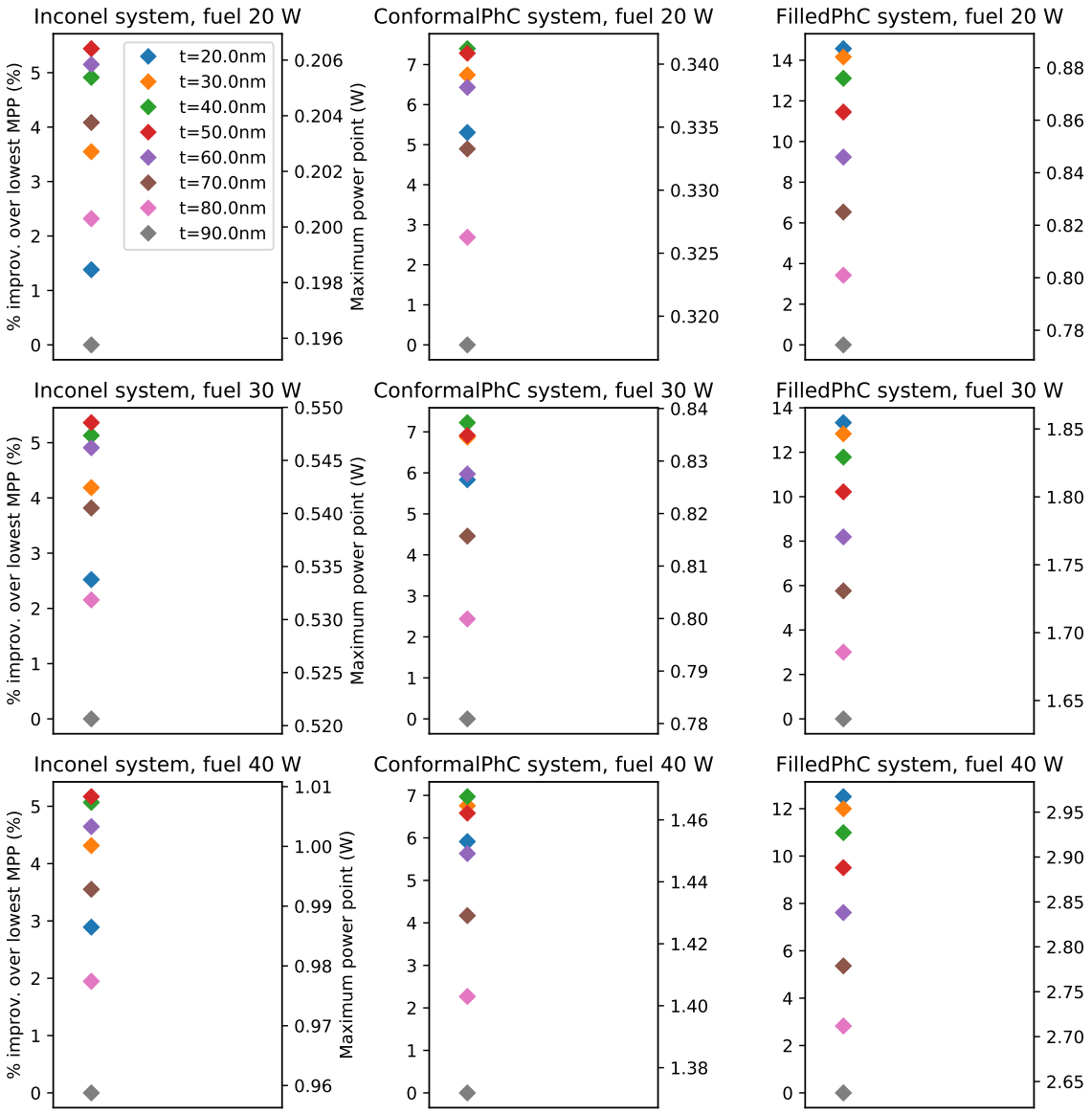

Figure 4-21: Which capping layer thickness t (between 20 and 90 nm) is optimal appears to depend on both the system conditions and the input fuel power. Pictured: input fuel powers 20, 30, 40 W.

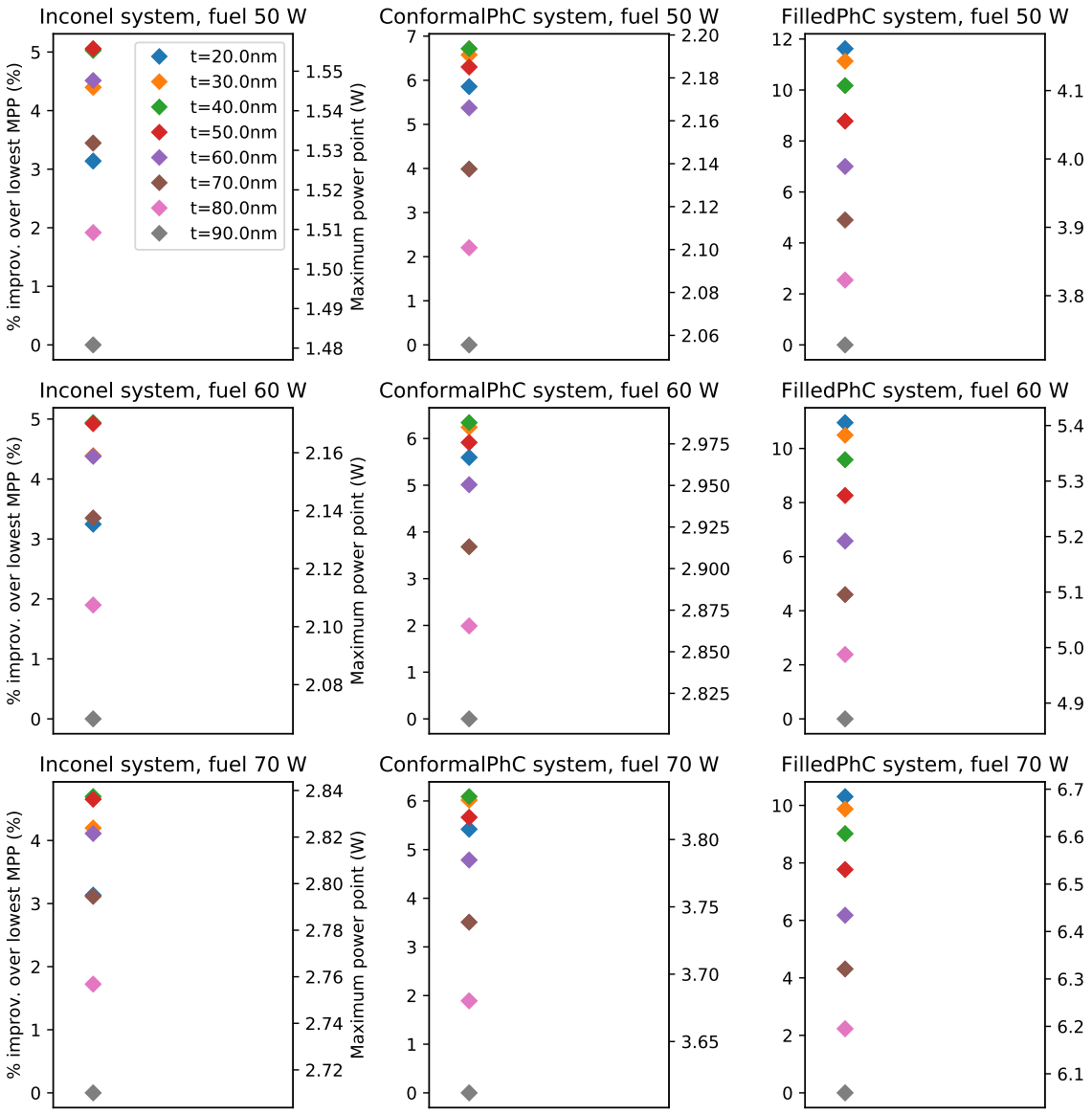

Figure 4-22: Which capping layer thickness t (between 20 and 90 nm) is optimal appears to depend on both the system conditions and the input fuel power. Pictured: input fuel powers 50, 60, 70 W.

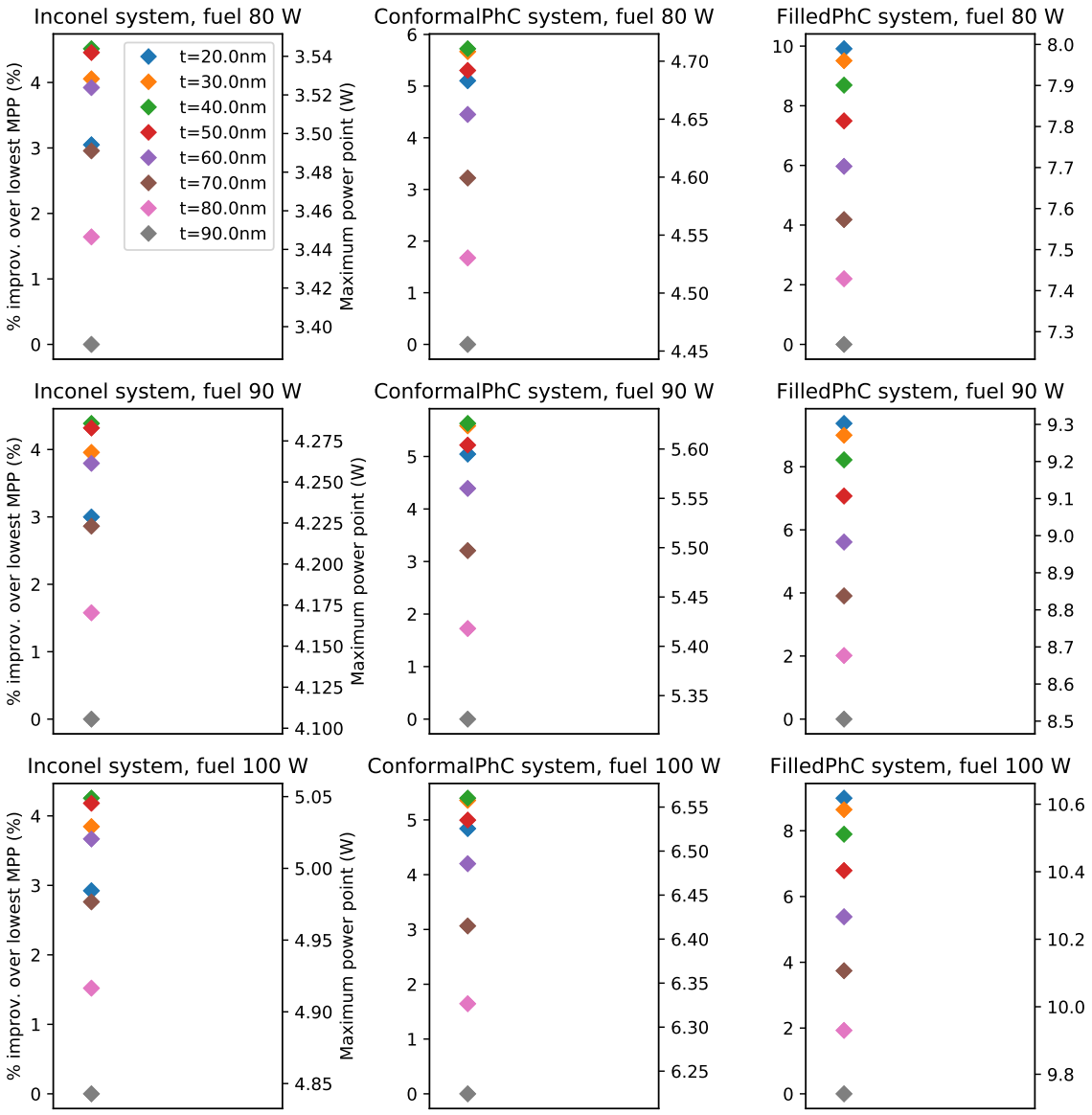

Figure 4-23: Which capping layer thickness t (between 20 and 90 nm) is optimal appears to depend on both the system conditions and the input fuel power. Pictured: input fuel powers 80, 90, 100 W.

- The capping layer is not flat
- It is crucial not to overetch the tantalum, and a thinner target thickness makes overetching easier

Chapter 5

Planarization of hafnium oxide capping layer

While filling the tantalum PhC cavity with hafnium oxide using exposure mode atomic layer deposition (ALD) fills the cavity well, it leaves the top surface of the photonic crystal (PhC) both too thick and uneven, with an average crest to trough z-height difference of 200 nm. Although the thickness is the more critical parameter compared to surface roughness, the problem is when attempts to reduce the thickness do not reduce the surface roughness, and remove HfO_2 filling from within the cavity.

I took the approach of 1) depositing a sacrificial layer, in particular spin-on glass (SOG), that planarizes (smoothes) the uneven surface, which is then 2) etched back, in particular using a physical etch using argon ions, to the desired thickness [97], as shown in Figure F-1.

The ideal characteristics of the sacrificial layer are that 1) it planarizes the uneven top HfO_2 and 2) its etch rate should be similar to that of HfO_2. Commonly used materials for the sacrificial layer include photoresist and spin-on glass, but I decided against photoresist because it etches much more quickly than oxides. I used spin-on glass (Filmetrics 15A, silicates-based spin-on glass) instead. Spin-on glass tests on silicon are described in Appendix E; through these tests, I found that spin-on glass adhesion issues are less likely to arise when spincoating under low humidity conditions.

As detailed in Appendix F, I also tried other methods of HfO_2 deposition to evaluate if it would be possible to planarize the uneven surface, including: sputtering, electron beam evaporation, and sol-gel-based chemical solution deposition.

The sample I used was the one referred to as middle piece in Chapter 4.

5.1 Processing steps overview

I first did two passes of planarization and etch back. After the second pass, I deposited HfO_2 owing to some confusion about how much HfO_2 remained on the PhC top surface (this later turned out to be a mistake).

After these two rounds of planarization and etch back, as well as HfO_2 deposition, the top surface of the PhC seemed sufficiently flat (right side of Figure 5-11a) so that further planarization did not appear necessary.

From that point on, the sample was etched and its reflectance measured in four (additional) successive steps until the desired reflectance behavior was achieved.

The progression is as shown in Table 5.1.

Step	Capping layer thickness t from simulated fits	Figures
0. Before planarization and etch back	273 nm	In a previous chapter
1. First pass of planarization and etch back (24 min)	131-142 nm	5-4, 5-5, 5-6
2. Second pass of planarization and etch back (16.5 min, HF etch (30 s), 105-110 nm HfO_2 deposition	236-243 nm	5-11, 5-12, 5-13
3. Argon ion milling, 8 min	173-183 nm	5-14
4. Argon ion milling, 7 min (cumulative 15 min after second planarization)	137-143 nm	5-15
5. Argon ion milling, 4 min (cumulative 19 min after second planarization)	106-112 nm	5-16
6. Argon ion milling, 4 min 30 s (cumulative 23 min 30 s after second planarization)	62-78 nm	5-17

Table 5.1: Processing on middle piece

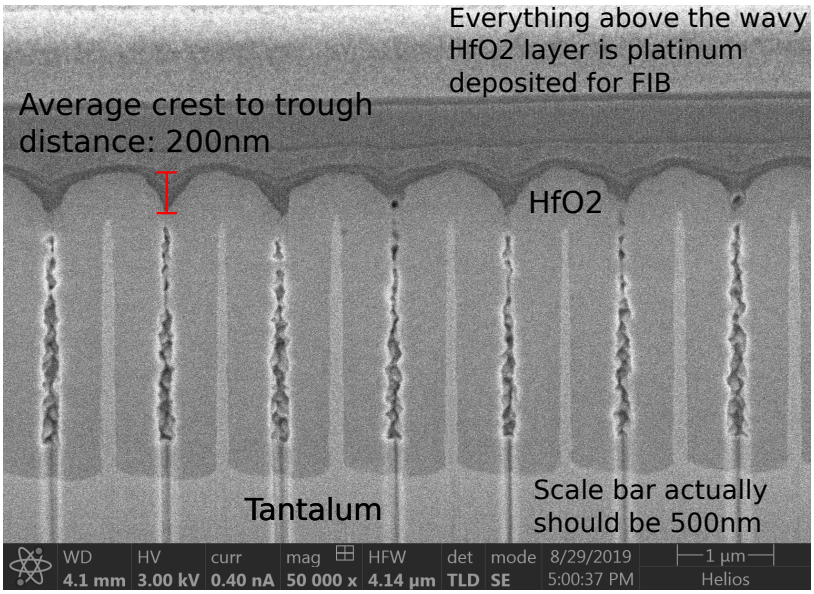

(a) The average crest to trough z-height difference in the HfO_2 top surface is 200nm. This SEM image has a tilt angle correction of 52° but it should be 38°.

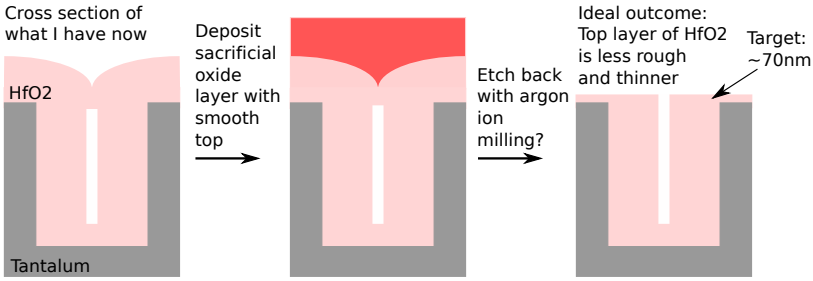

(b) The approach was deposit a sacrificial layer and etch back until the desired thickness is achieved. (Several iterations of spin-on glass deposition might have been necessary.)

Figure 5-1: Approach for smoothing out uneven HfO_2 top surface

5.2 Approach

The procedure for spin-on glass deposition is as shown in Table E.1.

Spincoating	Spin at 3000rpm for 60s (under humidity <39%) Prebake ∼80 °C for 60s Prebake 200 °C for 60s
Repeat for second coating	Spincoat and prebake again
Anneal under vacuum (1×10^{-6} Torr) at 475 °C	Ramp 25-475 °C at 3 °C/ min Hold at 475 °C for 1 hour Cool down to room temperature
Argon ion milling	Argon flow 200 sccm Source power 500 W Substrate power 150 W Pressure ∼1mTorr Valve position 100% Substrate temperature 20 °C Source position 120 mm

Table 5.2: Procedure for preparation and etching of spin-on glass films

I prepared films on blank silicon pieces as well as the tantalum PhC in order to 1) check for possible adhesion issue and 2) test the etch rate of spin-on glass on silicon.

Following deposition and anneal, I imaged the PhC cross sections to measure the thickness of the spin-on glass film.

Since the tantalum PhCs were to be annealed, I deposited HfO_2 on the back of the PhC (some tens of nanometers), in order to cover any exposed tantalum metal.

5.3 Planarization and etch back, first pass

I deposited the spin-on glass at 68°F and 38-39% humidity, and annealed as described in Table E.1 above, with starting pressure of 1.2×10^{-5} Torr (pressure at end of anneal was 8.6×10^{-7} Torr). The photographs of the silicon and tantalum pieces are shown in Figure 5-2. The spincoating on the silicon went well; tantalum pieces looked dirty but that was likely because of the sample itself, rather than any problems with the

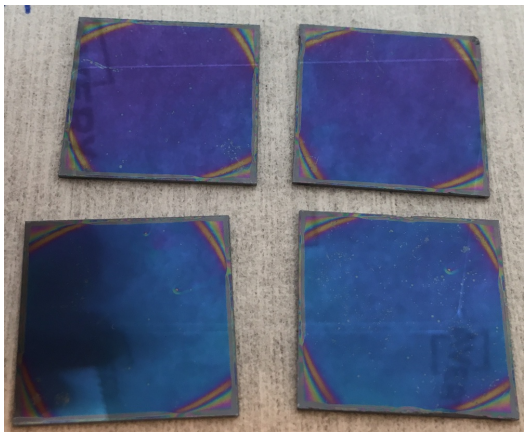

(a) After deposition, before anneal: Silicon pieces had few bubbles after depositing spin-on glass.

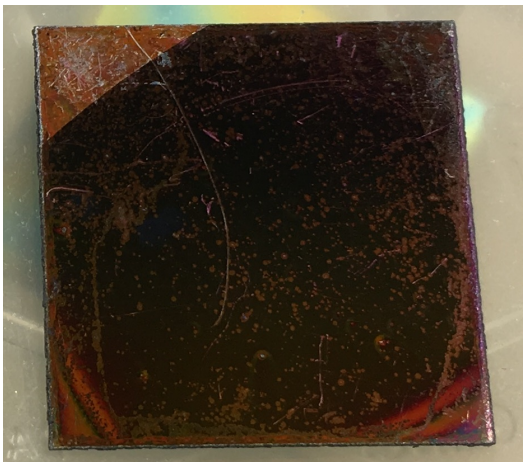

(b) After deposition, before anneal: Tantalum PhC sample was full of bubbles and had scratch marks, likely because it was not very clean and flat to begin with.

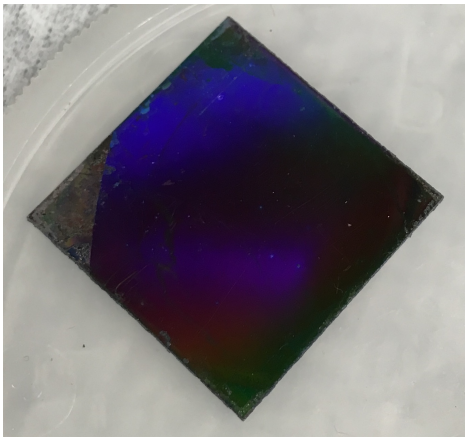

(c) Post anneal: Tantalum PhC piece appears iridescent.

Figure 5-2: First pass of planarization and etch back: Photographs of silicon pieces and tantalum PhC after deposition and after anneal. Tantalum PhC was quite dirty looking and full of bubbles, but this was possibly because the sample was not very clean and not flat.

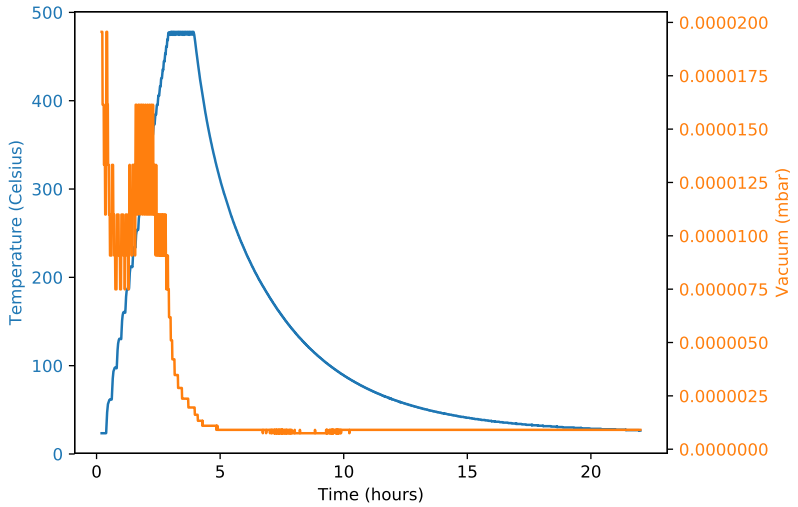

Figure 5-3: First pass of planarization and etch back: Anneal. During the ramp-up of temperature, the pressure also went up, which likely corresponds to the degassing of spin-on glass solvents.

spin-on glass spincoating conditions. Temperature and pressure during the anneal are shown in Figure 5-3.

The resulting cross section (top row, left side of Figure 5-4) shows that the spin-on glass planarized well. The test etch of spin-on glass (SOG) on silicon yielded an etch rate of 19.1 nm min^{-1}. The distance from the top of the spin-on glass (SOG top) to the trough of the HfO_2 capping layer was about 360 nm, which would take 18.8 min to etch through, assuming that HfO_2 and SiO_2 etched at the same rate. I had asked for the samples to be etched for 20 min, but in fact they were etched for longer at 24 min.

The cross section after etch back is shown in the top row, right side of Figure 5-4: after planarization and etch back, the HfO_2 capping layer is both thinner and less uneven.

The emittance was consistent with a reduction in the capping layer thickness (bottom row of Figure 5-4). Before, on the left, there was a prominent out-of-band resonance peak around 2.9 µm; after the planarization and etch back, the cutoff was superimposed with the out-of-band resonance peak around 2 µm.

Indeed, simulated fits to the measured spectra showed a decrease in t from 270 nm

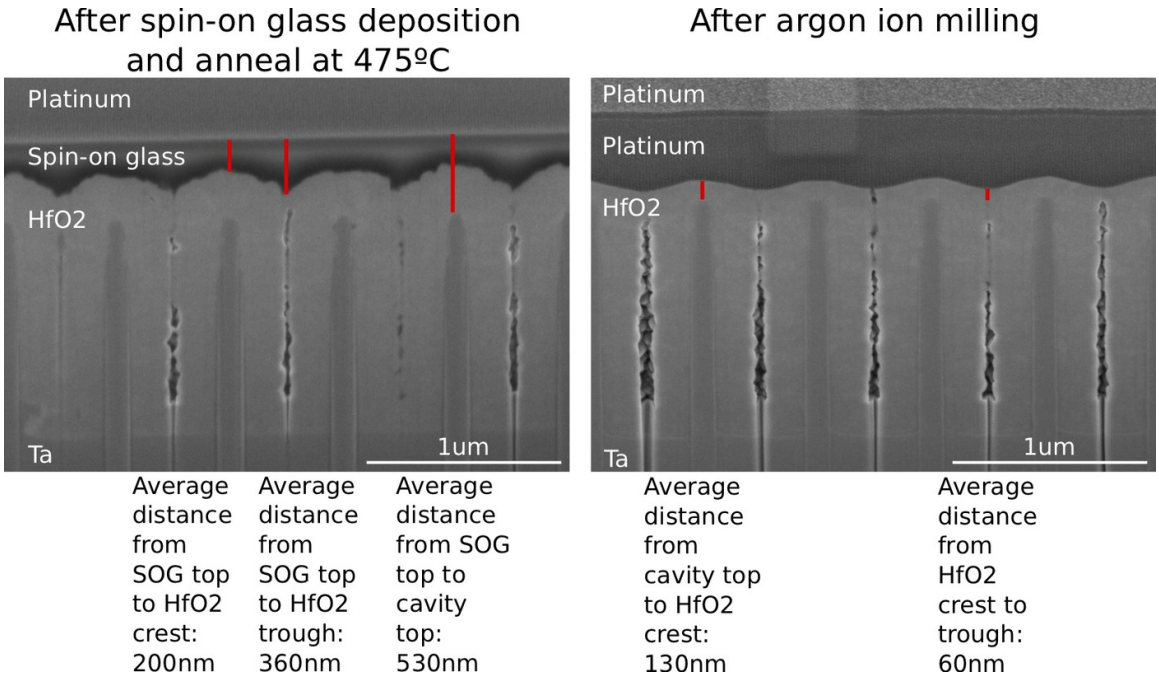

(a) After planarization and etch back, the HfO_2 capping layer is both thinner and less uneven. Left side, after spin-on glass deposition and anneal: the spin-on glass planarized well. The black halo is caused by charging is and just an image artifact. Right side is after argon ion milling for 24 min.

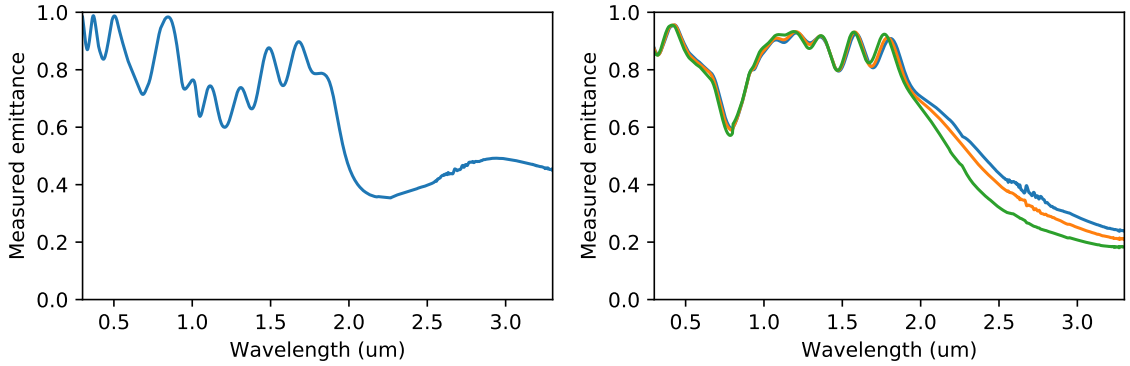

(b) After planarization and etch back, the out-of-band resonance peak blue-shifts. Left shows the emittance spectrum before, and the right shows after.

Figure 5-4: Results of first pass of planarization and etch back

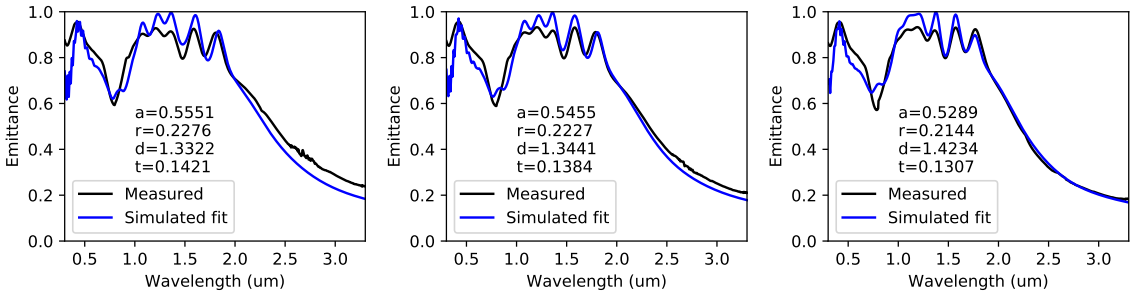

Figure 5-5: First pass of planarization and etch back: Simulated fits to the measured spectra show decrease in capping layer thickness to about 130-140 nm, which is consistent with the simulated fits.

to 130-140 nm (Figure 5-5)

A comparison of the four optical sub-metrics (Figure 5-6) showed improvement across all four after the planarization and etch back.

5.3.1 Variation about spin-on glass etch rate

After the silicon trials and the first pass etching spin-on glass, I noticed that the etch rates seemed to vary. It is likely that the varying humidity and temperature played a role, though initially I tracked neither humidity nor temperature.

In addition, the etch rates between films on flat silicon and films on PhCs seemed different: SOG on PhC seems to etch about 15-21% faster. I measured the etch rates of the films on the PhCs by comparing cross section images before and after.

In some cases it was difficult to accurately time the etch to etch through the spin-on glass, for fear of etching all the way to the cavity top surface.

Sample	SOG on flat Si etch rate ($nm\,min^{-1}$)	PhC SOG etch rate ($nm\,min^{-1}$)	PhC HfO_2 etch rate ($nm\,min^{-1}$)
Silicon PhC	26.2	30.17	18.73
First pass on tantalum PhC middle piece	19.1	23.15	13.01

Table 5.3: Variation in spin-on glass etch rates

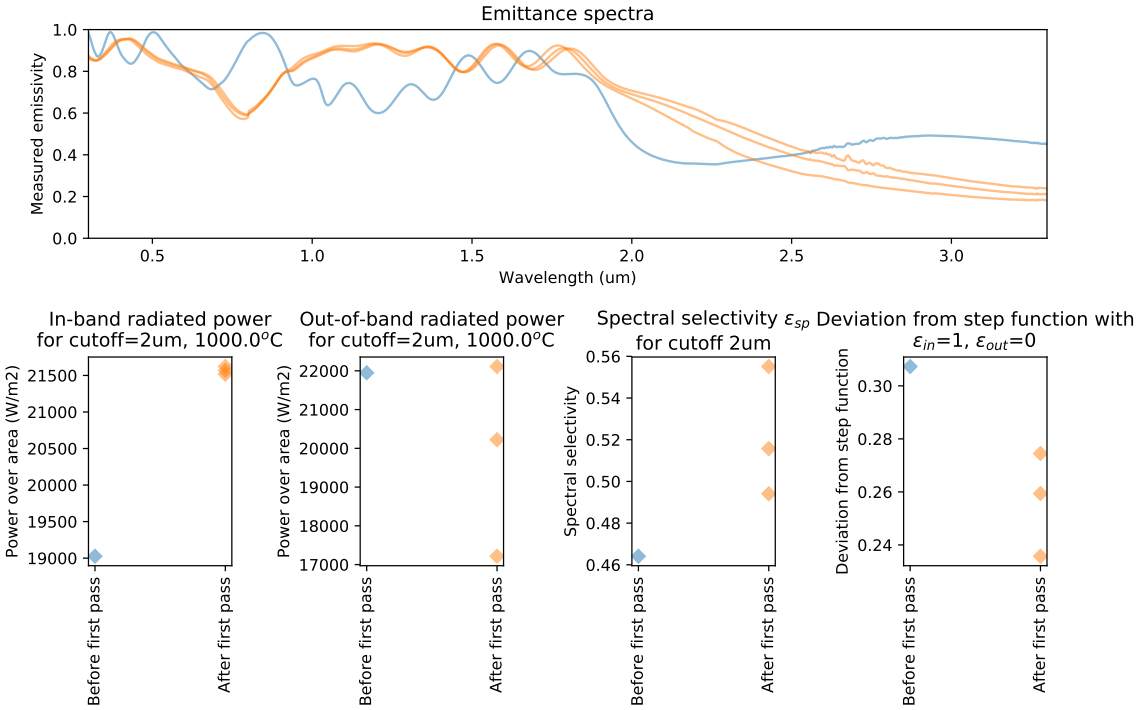

Figure 5-6: Optical metrics improved after the first pass of planarization and etch back (except in one case out-of-band radiated power per area increased, but only moderately).

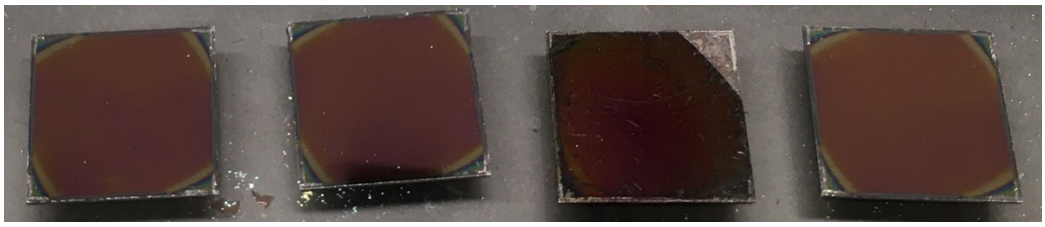

(a) Second pass of spin-on glass deposition, post anneal. The second from the right is the tantalum piece.

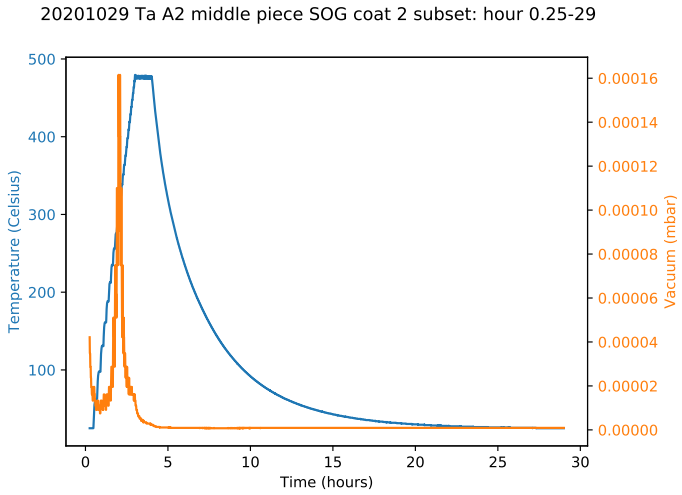

(b) During the anneal: as the temperature ramps up, the solvents degas and pressure also increases.

Figure 5-7: Second pass of planarization and etch back

5.4 Planarization and etch back, second pass

After the first pass, I decided to do a second pass to planarize further.

For the second pass, I spuncoat the spin-on glass at 66°F and 36% humidity. Perhaps because of the slightly lower humidity (36% as opposed to 28-29%), I did not observe any bubbles after spincoating (however, I forgot to take photographs). A photograph of the samples and anneal temperature and pressure are included in Figure 5-7.

The cross section after spin-on glass deposition is shown in Figure 5-8.

The etch rate of SOG on flat silicon was about $20\,\mathrm{nm\,min^{-1}}$. Based on the historical etch rates, I assumed that there would be a 21% increase in etch rate on the PhC sample, leading to an etch rate of $24\,\mathrm{nm\,min^{-1}}$, and estimated that the HfO_2

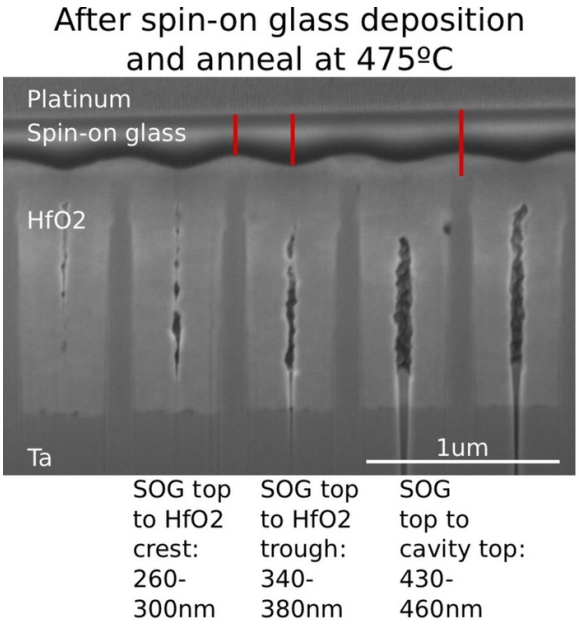

Figure 5-8

etch rate was 13.6-18.7 nm min^{-1}. From this I calculated an etch time of 16.5 min.

After this etch, I had my collaborator image the samples in the SEM, to see if the samples were etched sufficiently. This was intended to be quick, hence the top view. The images (Figure 5-9) showed patches of slightly darker contrast, likely indicating difference in height.

The sample was then wet etched in 5% HF for 30 s to remove any residual spin-on glass (which is SiO_2-like). HF also etches HfO_2: for 5% HF (1:10 dilution, with 50% HF solution), the etch rate was about 10 nm for HfO_2.

After the HF etch, when the sample was imaged again (top view only, Figure 5-10), it appeared as though the HF etch had been too long. The contrast in the images was marked. The hollow air core in the cavity center was visible, and in some areas it appeared that tantalum was exposed (the gray areas outside the cavities).

One possible reason for this apparent difference is that potentially two different areas on the sample were imaged. There is variation across the piece: the cavities are larger (larger radius) towards the wafer edge. Because at the wafer edge the cavities are larger, it takes more HfO_2 to fill them, and the capping layer is likely thinner.

Out of concern that there was barely any HfO_2 left on the top of the PhC, I had

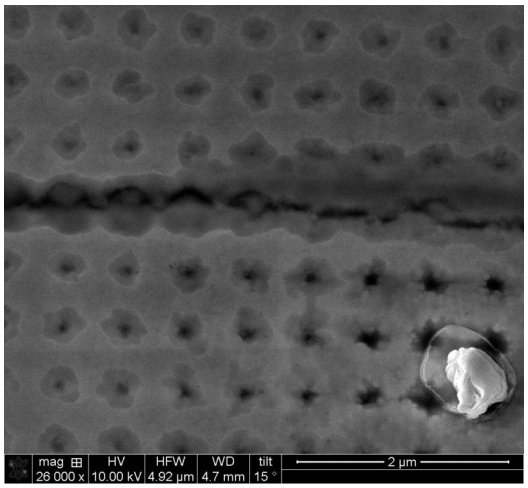

(a)

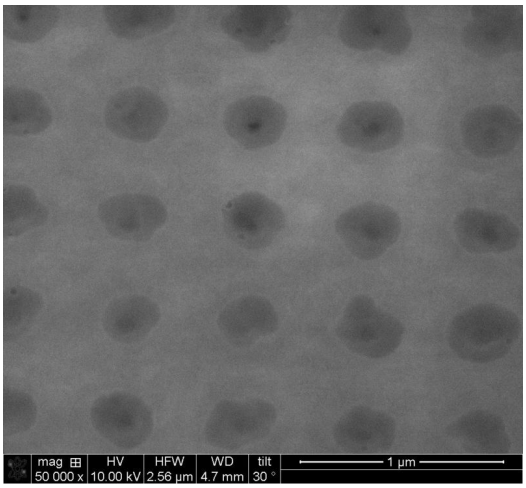

(b)

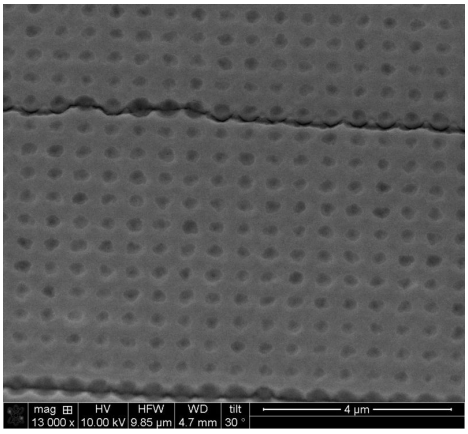

(c)

Figure 5-9: Second pass of planarization and etch back: after etching for 16.5 min, top view only. The patches with darker contrast likely indicate a difference in height.

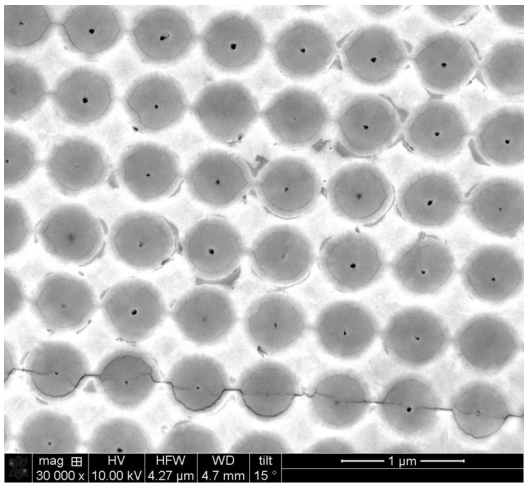

(a)

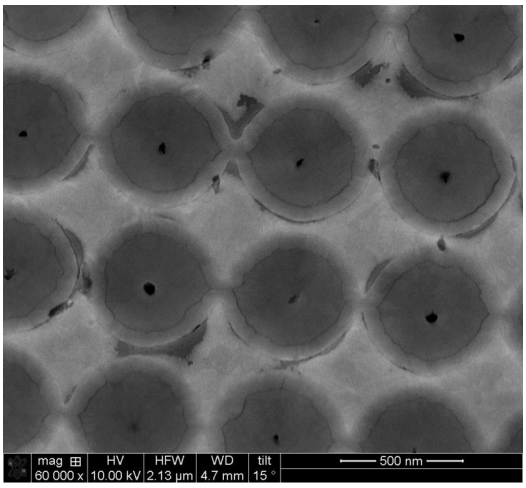

(b)

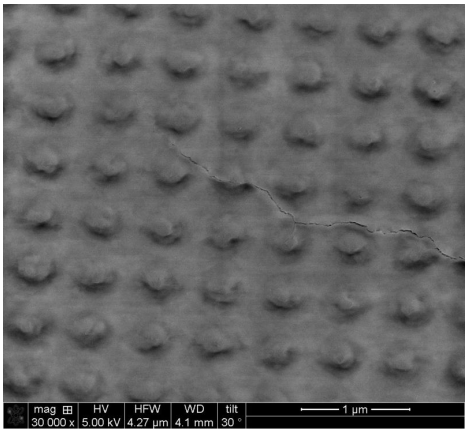

(c)

Figure 5-10: Second pass of planarization and etch back: after etching for 16.5 min and then 30 s of HF etch, top view. It looked as though the sample had been overetched, although this could simply be because a “bad area" on the sample had been imaged.

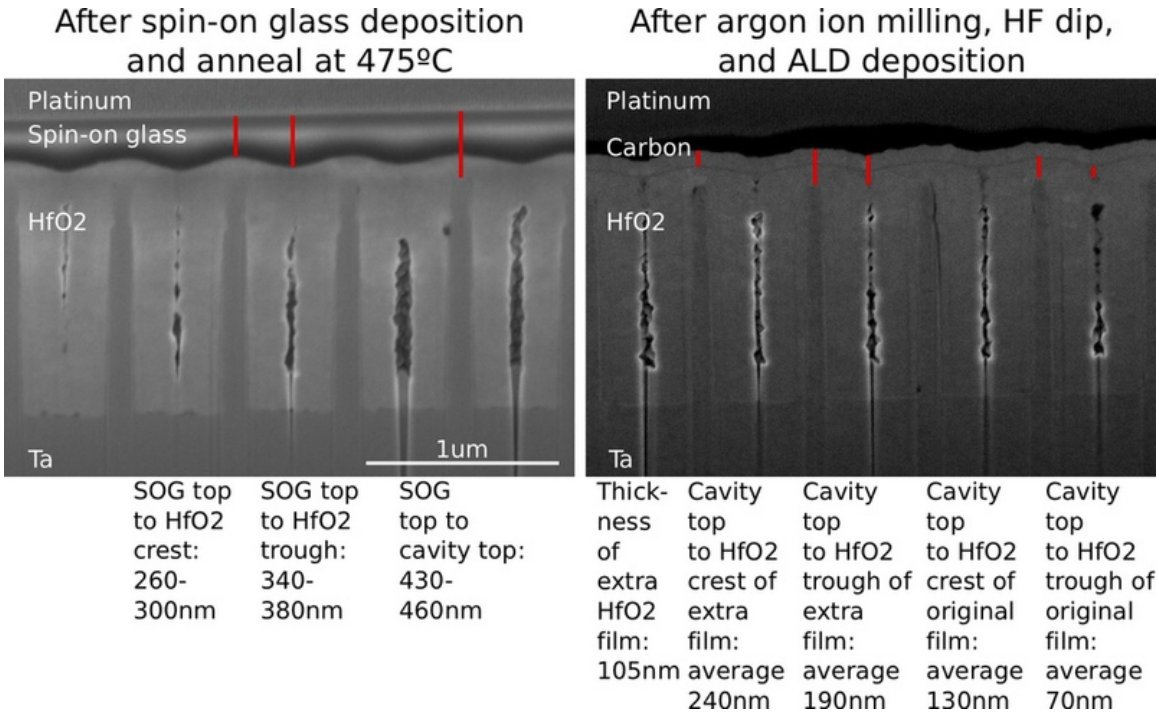

(a) The extra layer of HfO_2 is obvious in the cross section, and leads to a thicker layer of HfO_2 than before.

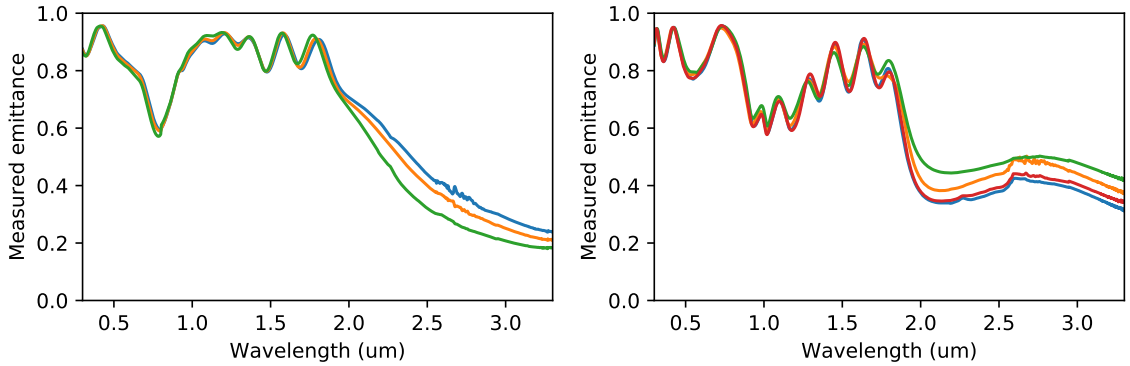

(b) The deposition of extra HfO_2 led to a thicker HfO_2 layer as indicated by the out-of-band resonance peak. Left side is before the second pass, right side after.

Figure 5-11: Results of second pass of planarization and etch back plus HF etch plus HfO_2 deposition. Depositing more HfO_2 was a mistake.

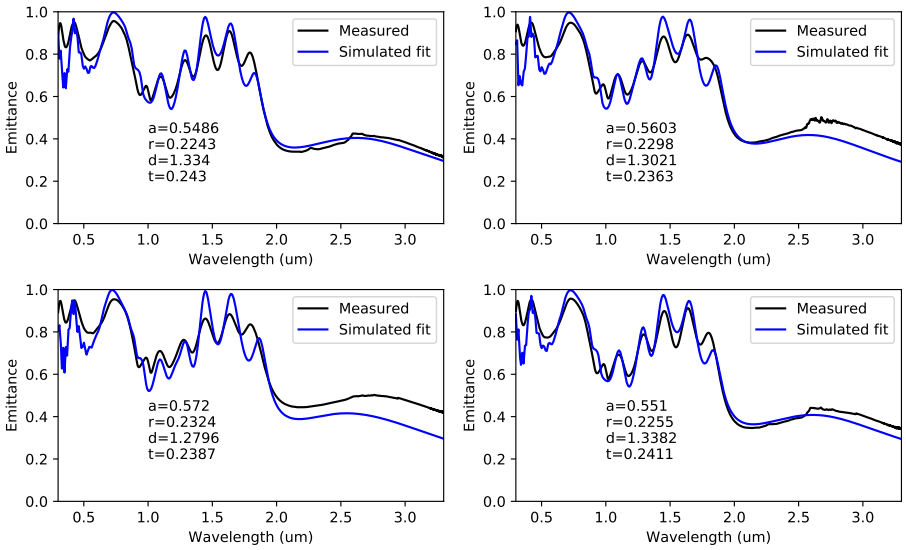

Figure 5-12: Results of the second pass of planarization and etch back, plus HF and 105 nm of ALD HfO_2: Depositing more HfO_2 was a mistake, leading to a thicker HfO_2 layer. Simulated fits indicate a capping layer thickness t of about 240 nm.

105-110 nm of HfO_2 deposited on the sample via ALD (1048 cycles).

This was a mistake, however, as evident from the cross section shown on the right side of Figure 5-11a. The extra layer of HfO_2 was clearly visible and measured at about 105 nm, leading to a total thickness of240 nm, thicker than after the first pass of planarization and etch back.

The increase in capping layer thickness was also evident in the emittance spectra, through the re-emergence of an out-of-band resonance peak (see right side Figure 5-11b). This is consistent with the results of the simulated fits, shown in Figure 5-12.

The deposition of extra HfO_2 reversed the improvement in the optical metrics after the first pass of planarization and etch back, as shown in Figure 5-11a.

5.5 Etch back, steps three through six

I calculated the optical metrics at each step; the results are shown in Figure 5-18, plotted as a function of thickness t (hence not in chronological order of processing). The general trend was that as thickness decreased, all metrics improved.

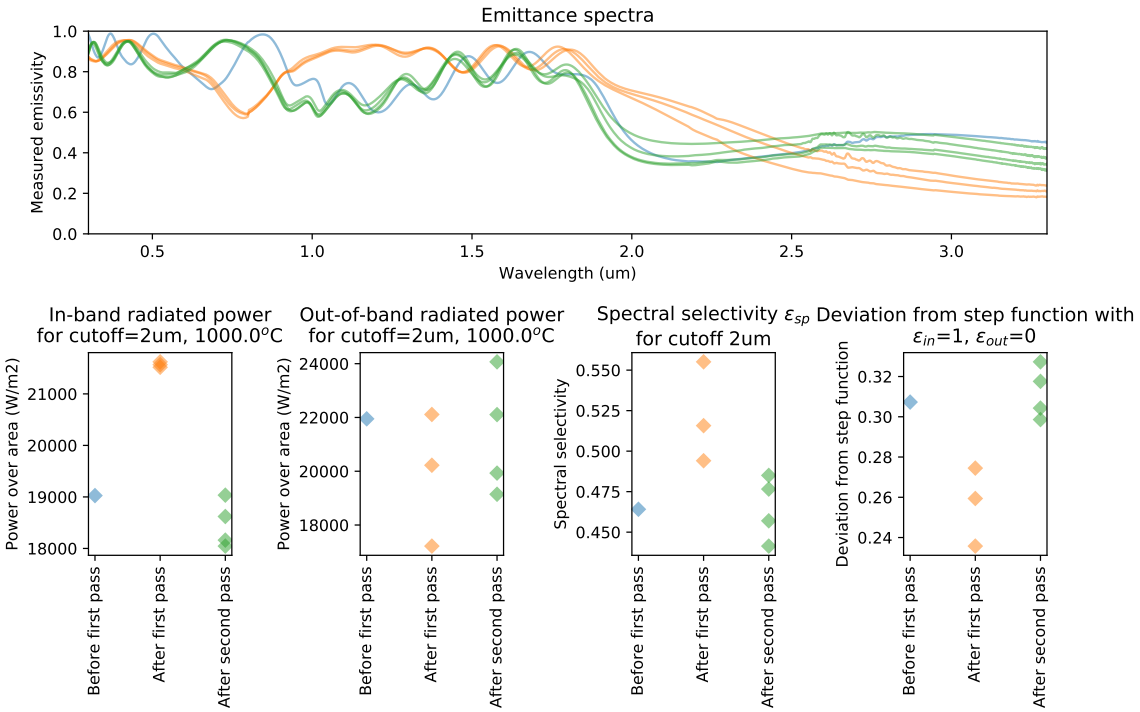

Figure 5-13: Results of the second pass of planarization and etch back, plus HF and 105 nm of ALD HfO_2: Depositing more HfO_2 was a mistake, leading to a thicker HfO_2 layer and metrics worse or about the same as before any planarization and etch back processing.

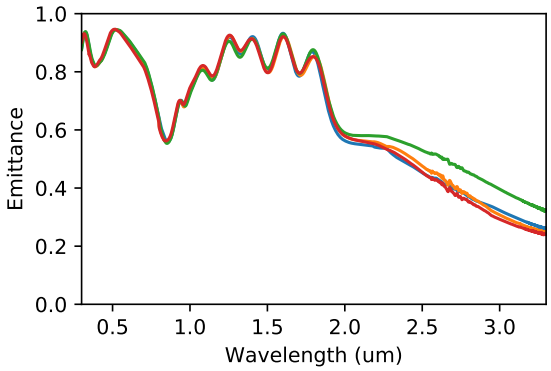

(a) Measured emittance spectra

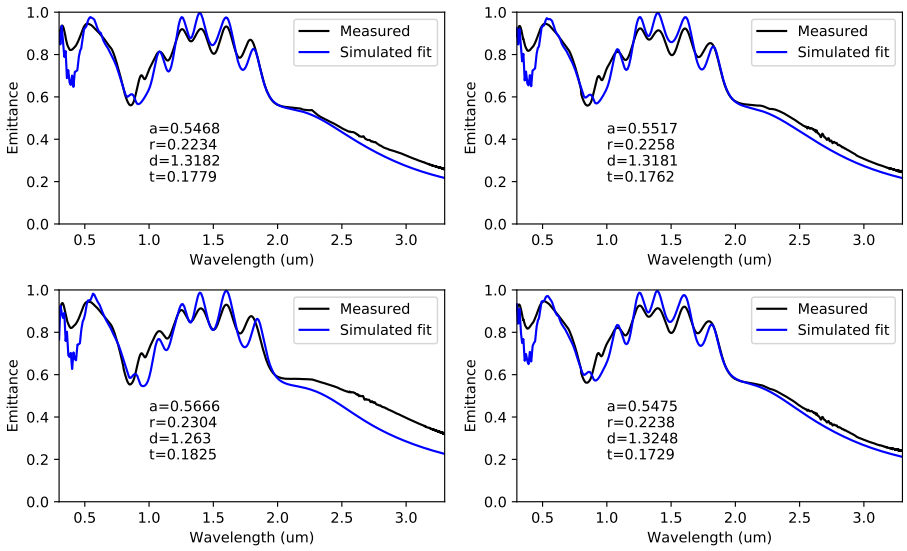

(b) Simulated fits

Figure 5-14: After third etching step, capping layer thickness was about 173-183 nm

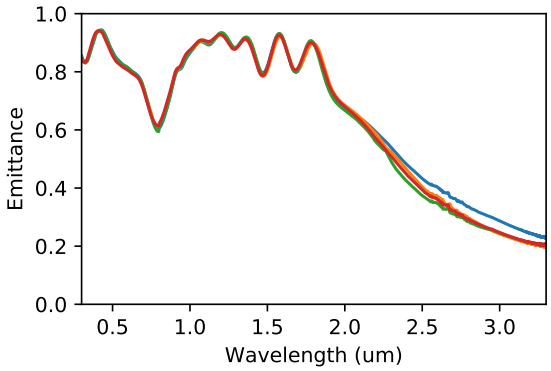

(a) Measured emittance spectra

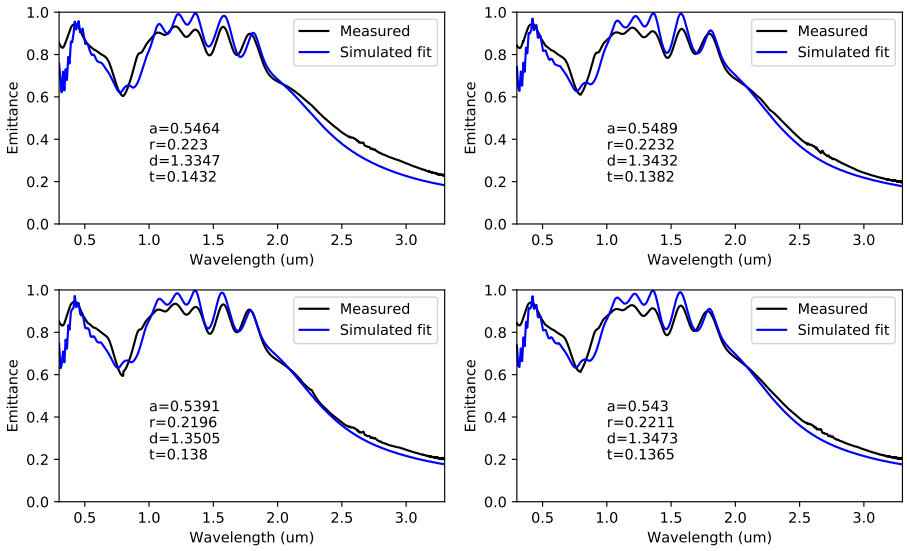

(b) Simulated fits

Figure 5-15: After fourth etching step, capping layer thickness was about 137-143 nm

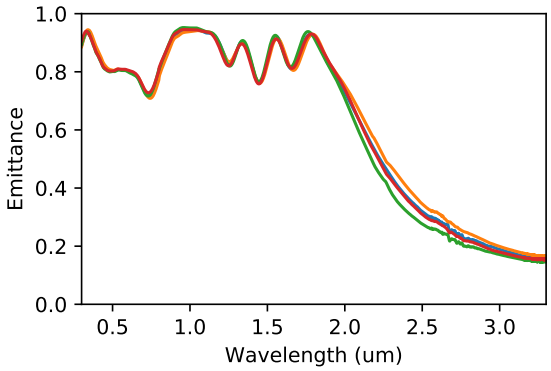

(a) Measured emittance spectra

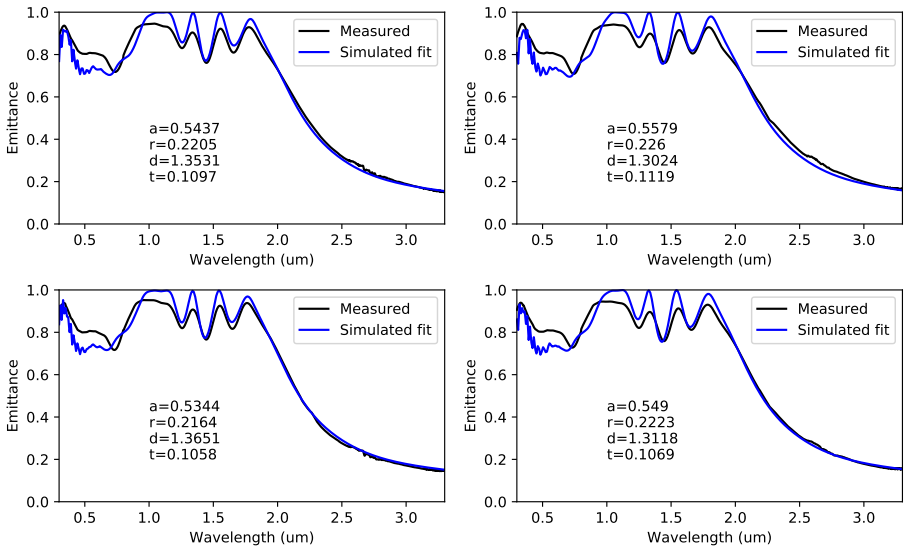

(b) Simulated fits

Figure 5-16: After fifth etching step, capping layer thickness was about 106-112 nm

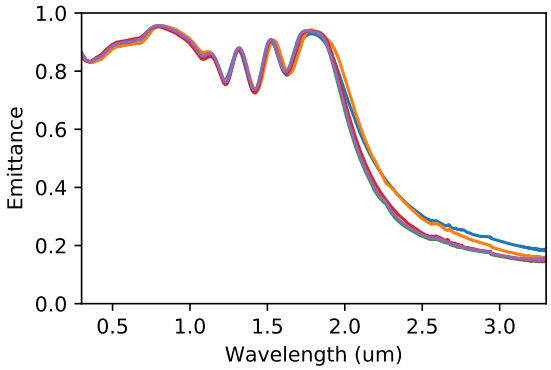

(a) Measured emittance spectra

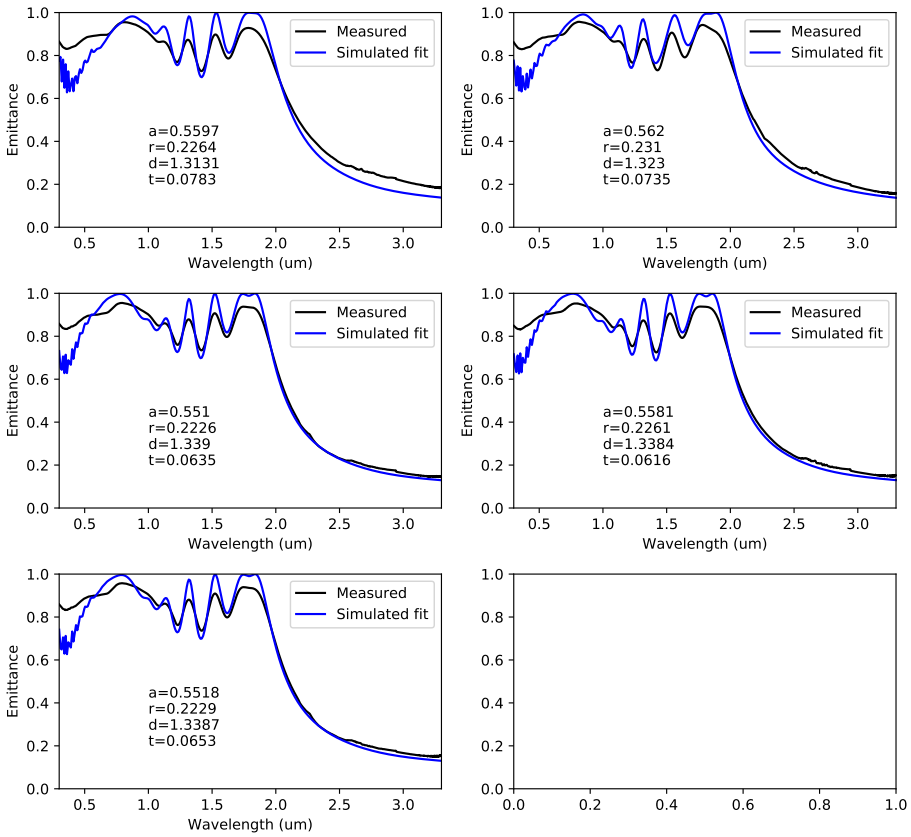

(b) Simulated fits

Figure 5-17: After sixth etching step, capping layer thickness was about 62-78 nm (average 69 nm). (This is the last processing step.)

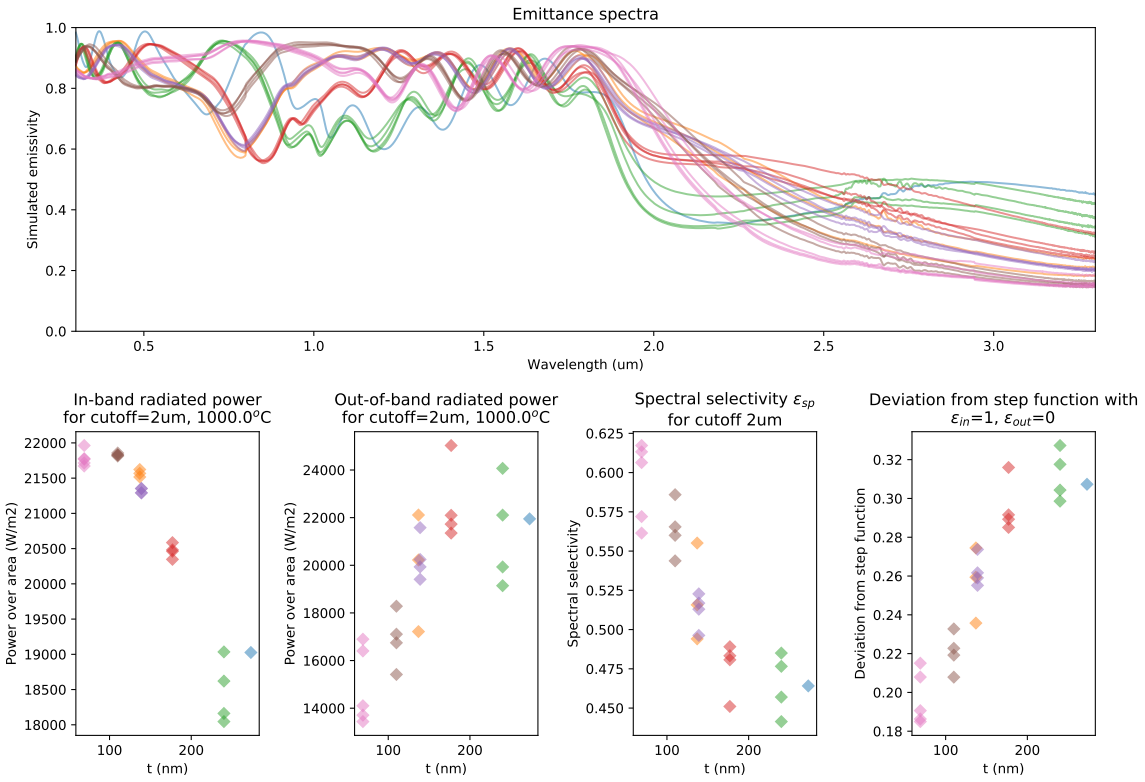

Figure 5-18: As capping layer thickness t decreased, the optical metrics improved. Note that each of the x-axes of the plots in the bottom row is thickness t - and therefore does not correspond to the chronological order in which the sample was processed.

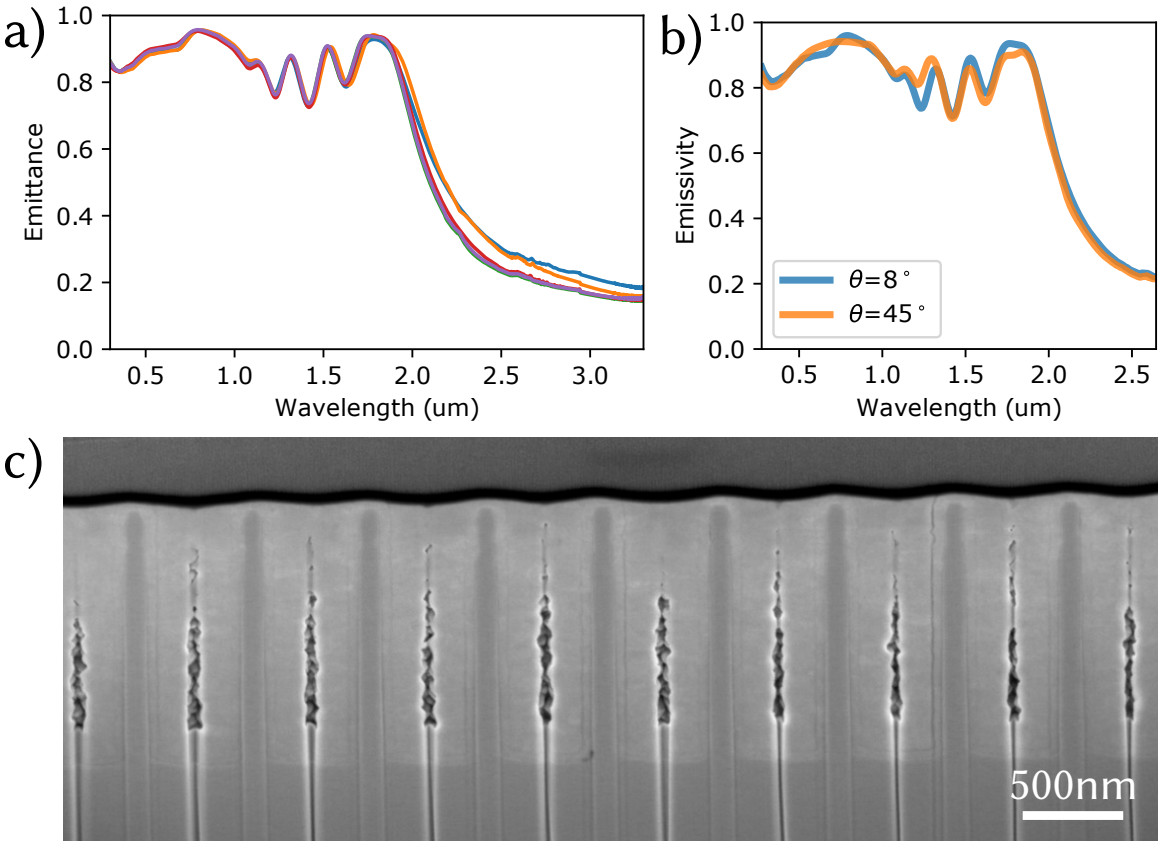

Figure 5-19: Characterization of final PhC.

5.6 Characterization of the final filled PhC

The final PhC emittance showed a sharp transition from high emittance to low emittance starting around 2 µm (the target cutoff), as shown in Figure 5-19a.

The capping layer thickness t according to the fits (62-78 nm, Figure 5-17b) is roughly consistent with the 50-55 nm measured in the cross section image of Figure 5-19c.

While the cross section image (Figure 5-19c) clearly shows that the capping layer is not perfectly flat, this did not adversely impact the emittance (as expected from the simulations).

This PhC also exhibited high in-band emittance of 0.7-0.9 and low out-of-band emittance of ∼0.2 both at 8° and 45° (Figure 5-19b). This is the primary advantage of the filed PhC: that it exhibits high in-band emittance over a wide range of angles, leading to an overall higher hemispherical emittance.

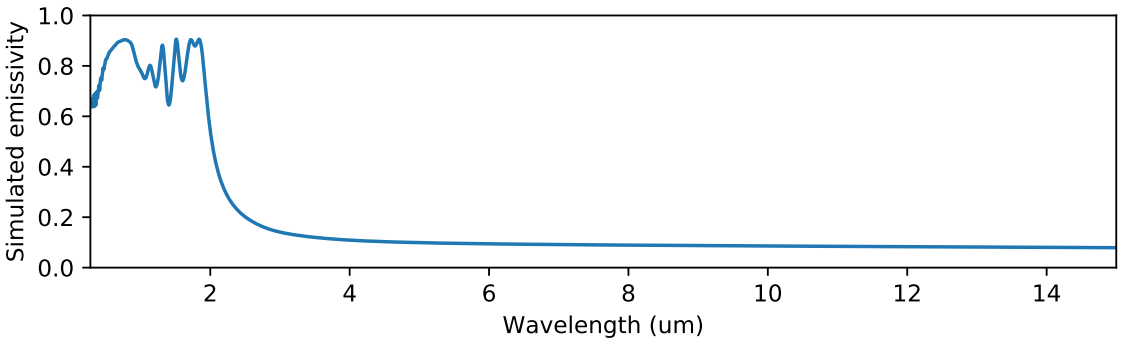

Figure 5-20: Simulated hemispherical emittance of filled PhC, with parameters: $a = 0.551$, $r = 0.222588$, $d = 1.34$, $t = 0.0635\,\mu\text{m}$.

One note is that, according to the fits (Figure 5-17), the absolute emittance of this PhC should be as high as 1, instead of 0.9 as from our measurements. This discrepancy might be because the tantalum substrate was more lossy than expected.

The simulated hemispherical emittance, shown in Figure 5-20, likely overestimates the PhC performance, as it is calculated from simulations that predict a higher in-band emittance. I calculated the hemispherical emittance based on one of the simulated fits for this PhC (parameters: $a = 0.551$, $r = 0.222588$, $d = 1.34$, $t = 0.0635\,\mu\text{m}$), using a combination of simulations at multiple (θ, ϕ) as described in Appendix B.

5.7 System performance simulations with final filled PhC

I did system performance simulations to estimate the power output for this PhC and compare it those of other emitters, as I had done in Chapter 4, using the system model and parameters described in Appendix D.

Essentially, the approach is to vary the emittance while keeping everything else the same.

The PhCs I simulated are the following:

- The original PhC for the system (as plotted in Appendix D), one of the following:

  - Inconel $\varepsilon_{in} = \varepsilon_{out} = 0.80$ (so it is not selective at all)
  - Conformal PhC
  - A step function "Filled PhC" emitter with $\varepsilon_{in} = 0.92$ and $\varepsilon_{out} = 0.16$
- Perfect PhC with 2 µm cutoff - the upper bound. Simulated in [87], with parameters $r = 0.23\,\mu m$, $d = 4.31\,\mu m$, $a = 0.57\,\mu m$, $t = 78\,nm$.
- Middle piece filled PhC as simulated for 8° in Chapter 4, with $t = 273\,nm$ (so after filling and before any planarization as described in this chapter)
- Simulated hemispherical emittance of the final form of the middle piece filled PhC, after planarization and etch back, with capping layer thickness 50-60 nm, with parameters $a = 0.551$, $r = 0.222588$, $d = 1.34$, $t = 0.0635\,\mu m$ (see Figure 5-20)

The results are shown in Figures 5-21, 5-22, 5-23.

Of particular interest are the systems whose original emitters were the conformal PhC and step function.

For the system whose original emitter was the conformal PhC: the system with the fabricated filled PhC with $t = 63.5\,nm$ yields a power output of 6.0 W, a 37.5% increase over the 4.4 W output reported in [3], and approaches the 6.5 W predicted for the perfect PhC.

This output power 6.0 W is likely a slight overestimate however, as the actual PhC is probably a bit lossier and would have lower in-band emissivity.

For the system whose original emitter was the step function: the original system has a power output of >12 W, which is at least twice the output power predicted for both the fabricated filled PhC and perfect filled PhC. Based on just these results, it is hard to tell which region of emittance, in-band or out-of-band, has a higher impact on the system output power.

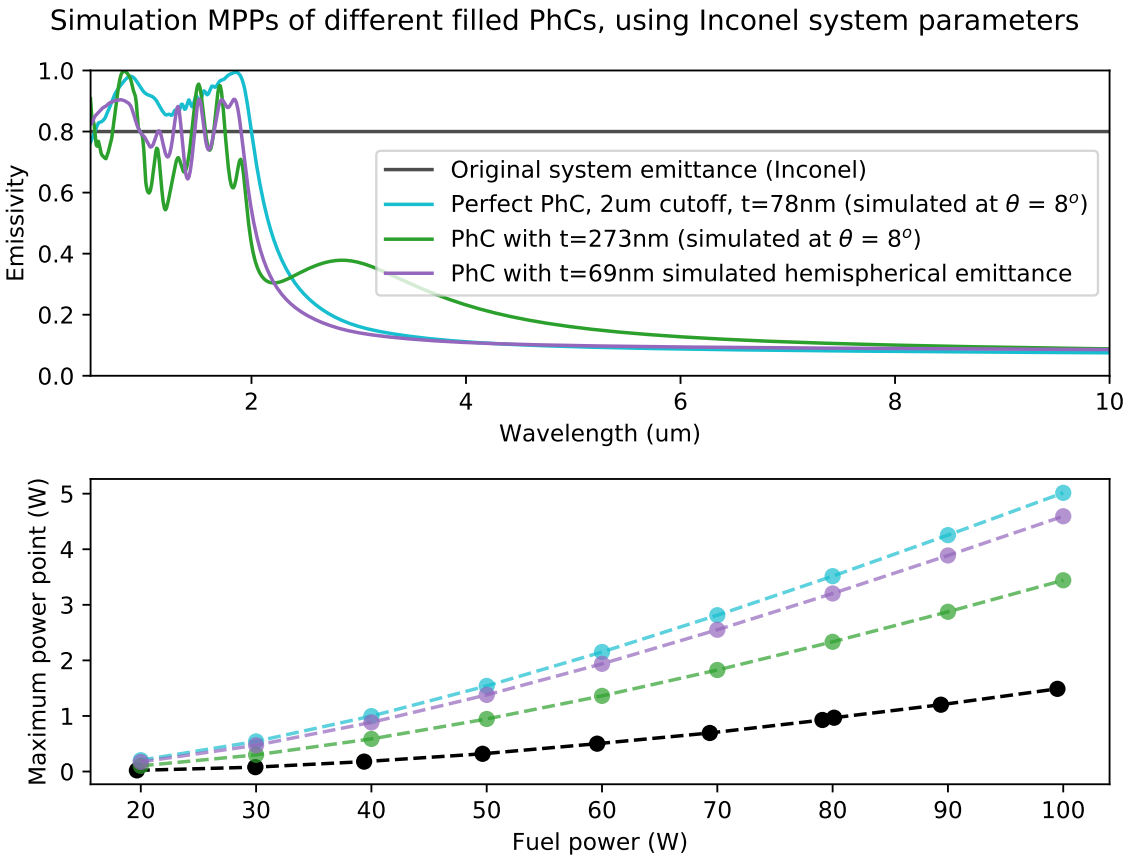

Figure 5-21: System performance simulation with a system whose original emitter was a greybody (Inconel metal) with ε=0.8. (Parameters available in Appendix D and [3]). All filled PhCs give higher output power, compared to the original Inconel emitter.

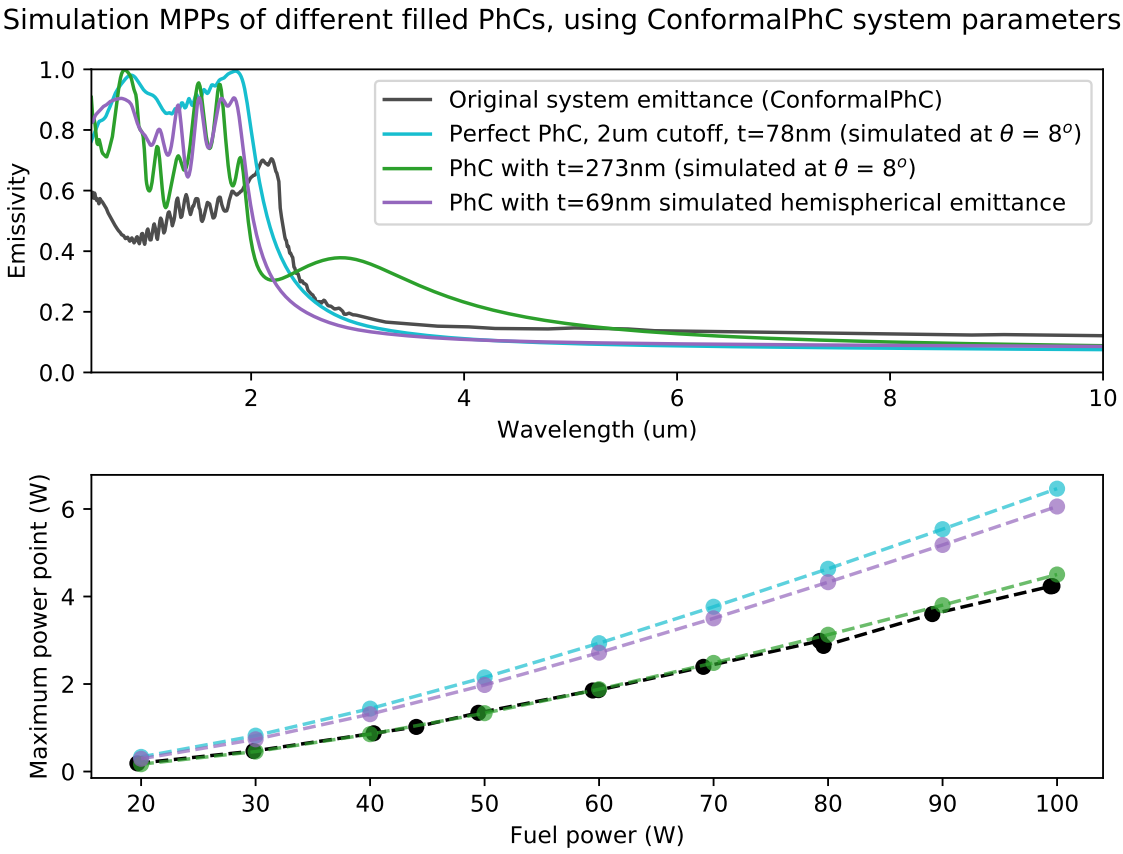

Figure 5-22: System performance simulation with a system whose original emitter was a conformal PhC, shown in black. (Parameters available in Appendix D and [3]). The final filled PhC

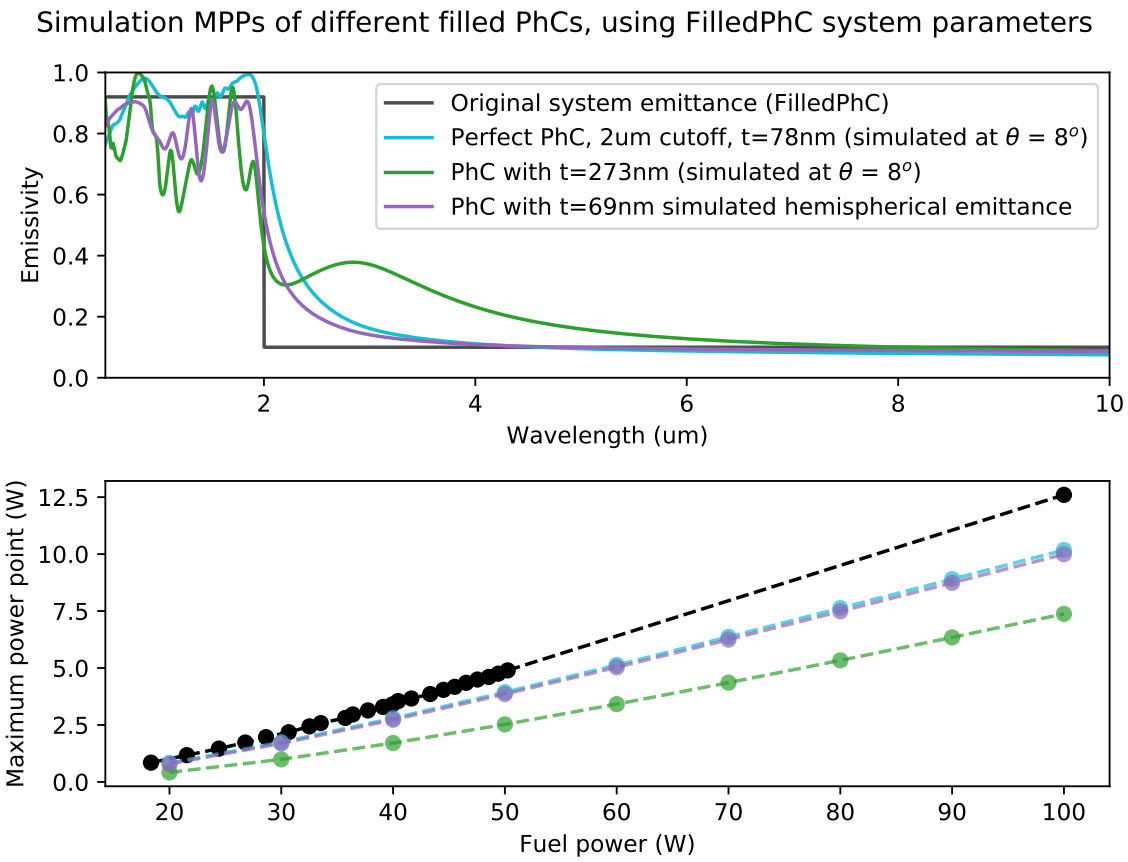

Figure 5-23: System performance simulation with a system whose original emitter was a filled PhC with $\varepsilon_{in} = 0.92$ and $\varepsilon_{out} = 0.16$, shown in black. (Parameters available in Appendix D and [3]). The original step function emitter yields far higher power (12 W than any of the filled PhCs.

Chapter 6

Testing high-temperature stability

A good TPV emitter should be able to sustain its optical performance at high temperatures for extended periods of time, on the order of thousands of hours, either continuously or over multiple thermal cycles.

However, at high temperatures, the optical properties of the photonic crystal (PhC) can change if there is a change to the PhC structure, the optical properties of the materials (tantalum and hafnium oxide), or both.

In particular, there are the following concerns:

- Changes in intrinsic optical properties
  - Tantalum is known to form tantalum carbide and/or oxide when not protected, therefore the entire surface is coated with hafnium oxide and the PhC is intended to be operated under vacuum conditions.
  - Hafnium oxide is known to undergo phase changes when annealed (amorphous, trigonal, monoclinic), but it is not clear, for now, how if any phase changes have affected the PhC properties.
  - One study of anneals of HfO_2 / W / HfO_2 stack (100 nm HfO_2, 20 nm tungsten, 100 nm HfO_2) at vacuum of 3×10^{-6} mbar observed that, at temperatures above 700 °C, voids or cracks began to form in the HfO_2 layer, allowing residual O_2 in the chamber to react with the tungsten and form volatile WO_x. This is attributed to how the phase change of HfO_2

from trigonal to monoclinic leads to "a volume increase in the HfO_2 unit cell by 3.5% (t -> m) and anisotropy of thermal expansion of monoclinic phase." The HfO_2 films the authors used had been made by magnetron sputtering. [95]

  - Two potential mechanisms for the oxidation of metals include inter-layer diffusion of O from HfO_2 to the metal, and O_2 diffusion from the outside environment; however, as the enthalpy of formation of HfO_2 is low at $-909\,\mathrm{kJ\,mol^{-1}}$, metal oxidation at the cost of the oxide is unlikely. Instead, the reaction of metal with residual ambient O_2 is more likely [84]

- Changes in structure: deformation, delamination, cracking
  - Thermal expansion is of a particular concern for the filled PhC. Tantalum and HfO_2 have relatively close coefficients of thermal expansion [36] (coefficients included in Appendix G), but thermal stresses become significant at high temperatures
  - Creep: at high temperatures, over time, materials tend to deform due to stresses (including thermal stresses)

Although the conformal PhC showed minimal degradation after annealing continuously 300 hours at 1000 °C at 5×10^{-6} Torr [6] and Veronika's first filled PhC was annealed for 24 hours under the same conditions without degradation [1, 6], the conformal PhC is only coated with HfO_2, and Veronika's first filled PhC were less densely filled than the final filled PhC I made.

6.1 Simulated optical performance at high temperature

Although I have not measured the emission of the photonic crystal at high temperatures, I have simulated it using the Lorentz-Drude parameters for tantalum at 1478 K, measured from a flat tantalum wafer at high temperature.

The high temperature simulated spectra of the perfect filled and conformal pho-

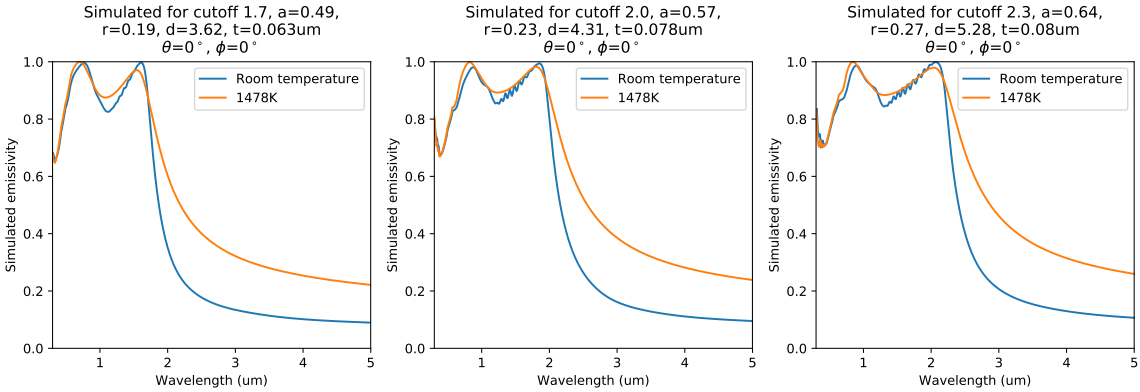

Figure 6-1: At high temperature, the simulated photonic crystal spectra show high out-of-band emittance and a less sharp transition from high to low emittance. (Parameters for perfect optimized filled photonic crystals used.)

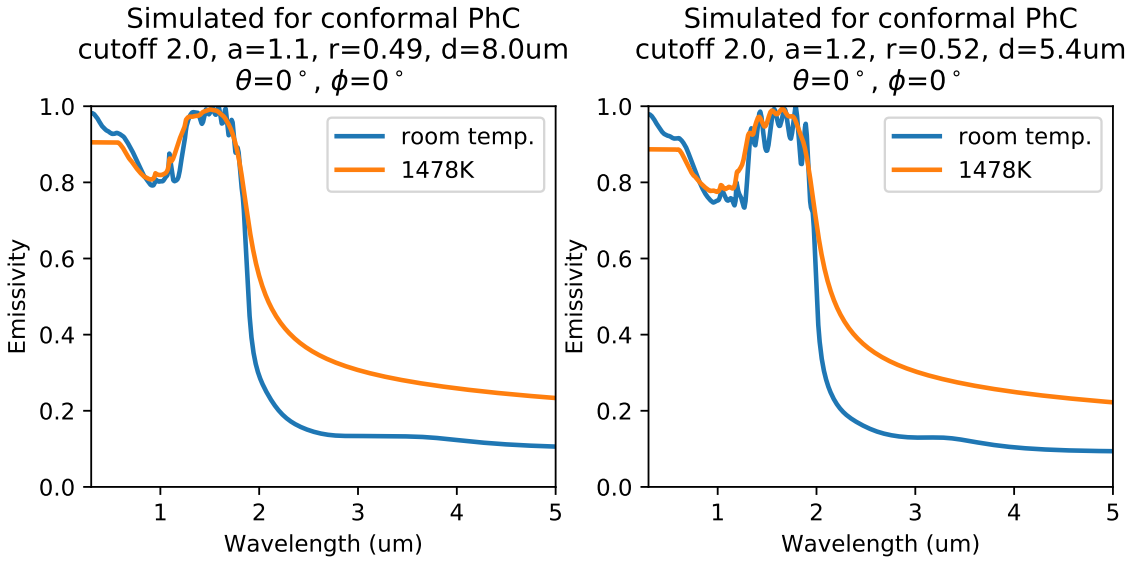

Figure 6-2: At high temperature, the simulated photonic crystal spectra show high out-of-band emittance and a less sharp transition from high to low emittance. (Parameters for perfect conformal photonic crystals used.)

tonic crystals, as shown in Figure 6-1 and 6-2 respectively, show high out-of-band emittance and a less sharp transition from high to low emittance.

This is also the case with the fabricated filled PhC (Figure 6-3): at high temperatures, high out-of-band emittance and a less sharp cutoff transition is expected.

6.2 Cracking in the fabricated filled photonic crystal

I began to observe cracks in the fabricated filled photonic crystal (seen as areas of dark contrast in Figure 6-4) after the second pass of planarization and etch back (on the middle piece). Interestingly, the crack sometimes passes through the center but also sometimes along the edge of the cavities.

The cracks might have appeared during the annealing step of the spin-on glass deposition, where the sample is heated to 475 °C under vacuum.

Cracks were also visible after the last fabrication step to make the filled photonic crystal (Figure 6-5). Unlike the crack shown in Figure 6-4, the cracks pictured here appear to have more twists and bends.

The crack propagation is likely to related the mechanical properties of the HfO_2, which is nonuniform throughout the cavity although the deposition method is the same. The HfO_2 is clearly polycrystalline, as seen in Figure 6-6.

The quality of hafnium oxide may be nonuniform within the cavity, as shown in Figure 6-7. The bottom row shows the photonic crystal after the additional layer of HfO_2 has been deposited: the extra layer appears as a distinct layer, and there are also cracks parallel to the cavity sidewalls are also visible. In the top row, which is a cross section after the last processing step, cracks are also visible parallel to the cavity sidewalls.

This may be due to differences in focused ion beam milling rates, as gallium ions mills different materials differently. Differences in mechanical properties may lead to differences in milling rates, which in turn can appear as contrast in the resulting images.

However, I have not studied these cracks closely, or studied the mechanical prop-

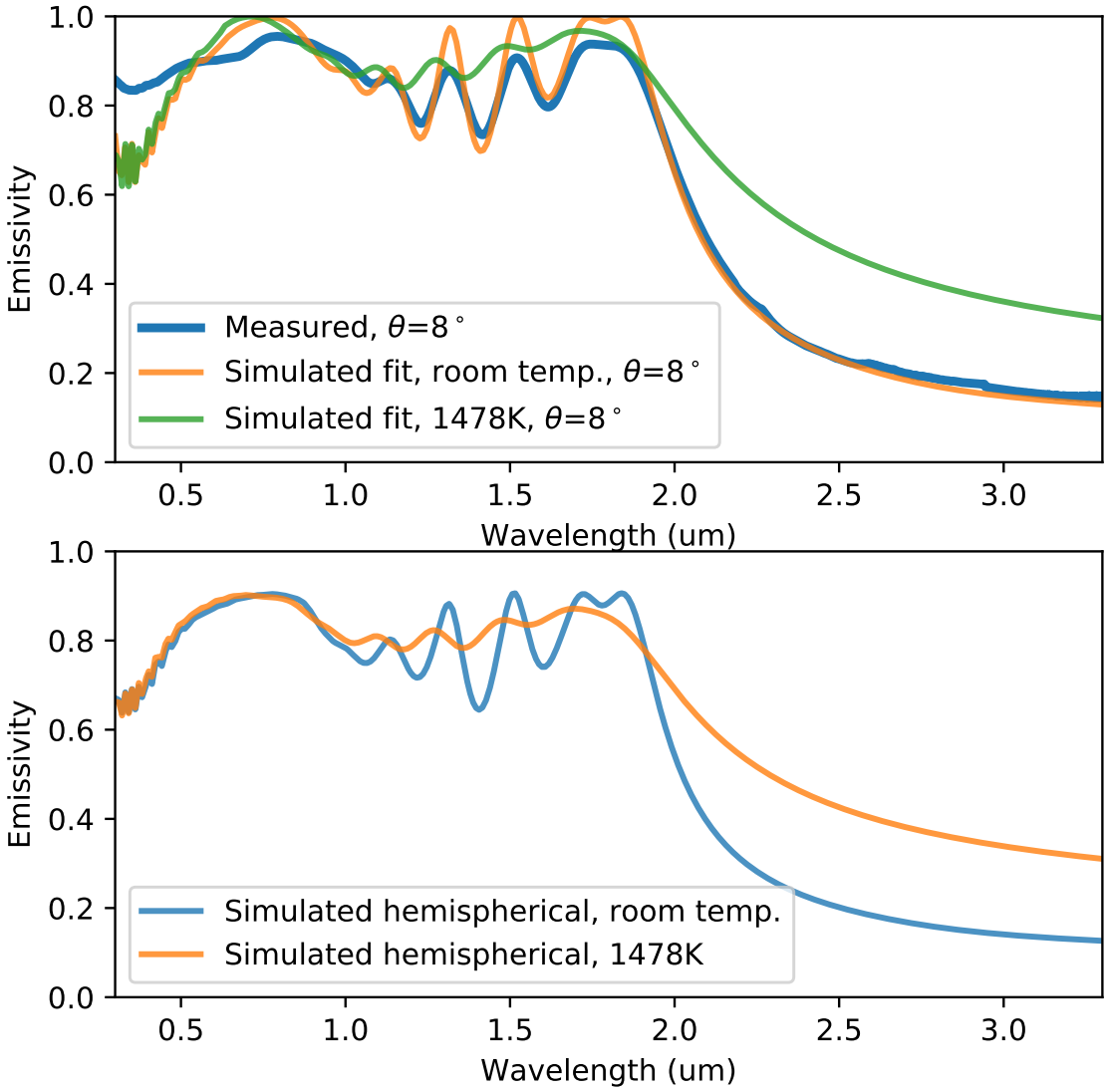

Figure 6-3: At high temperature, the simulated spectra of the fabricated filled photonic crystal show high out-of-band emittance and a less sharp transition from high to low emittance.

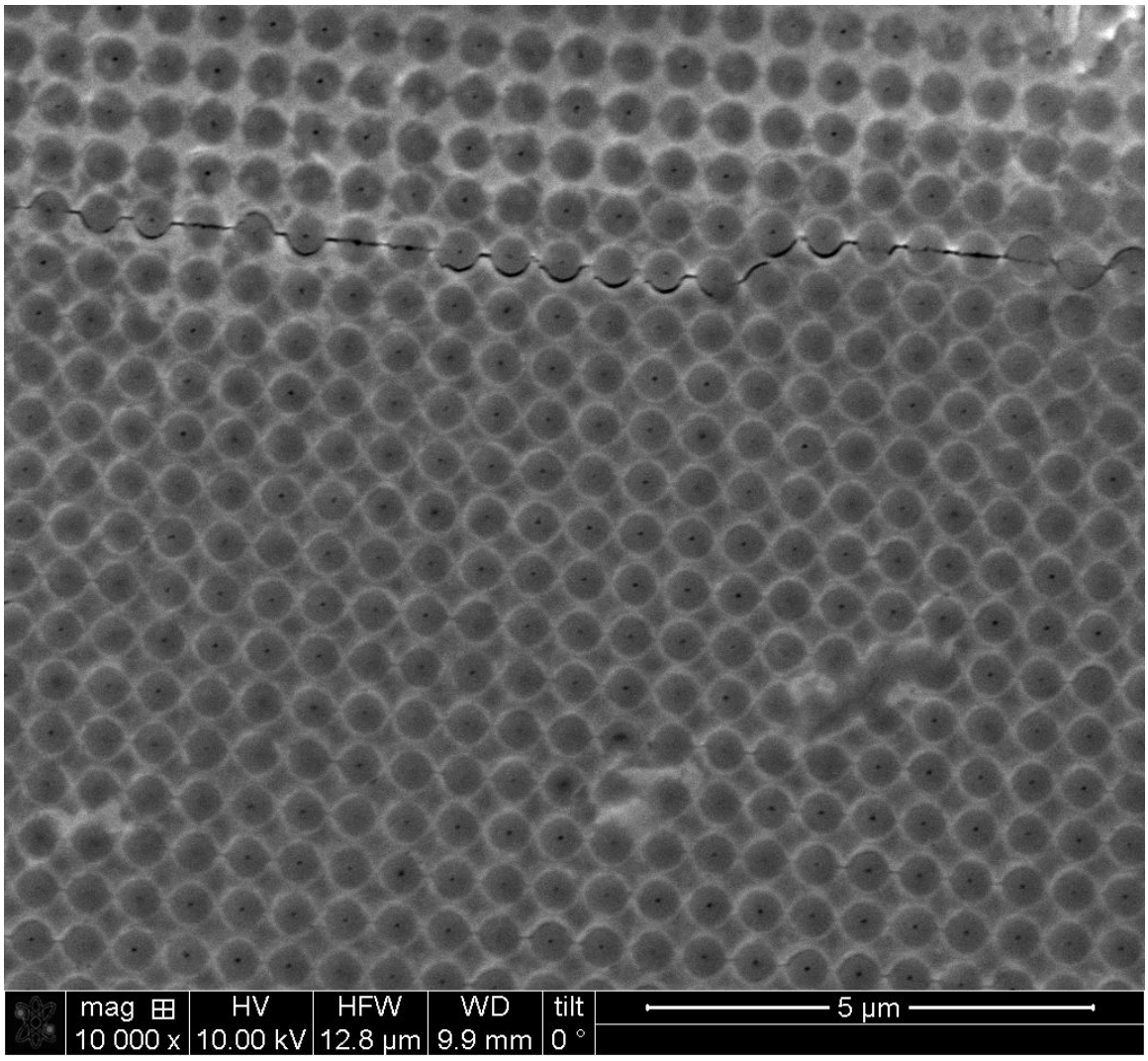

Figure 6-4: A crack observed after second pass of planarization and etch back (and before additional HfO_2 deposition), that spans more than 10 µm. It is not clear where on the sample (close to which corner) this image was taken.

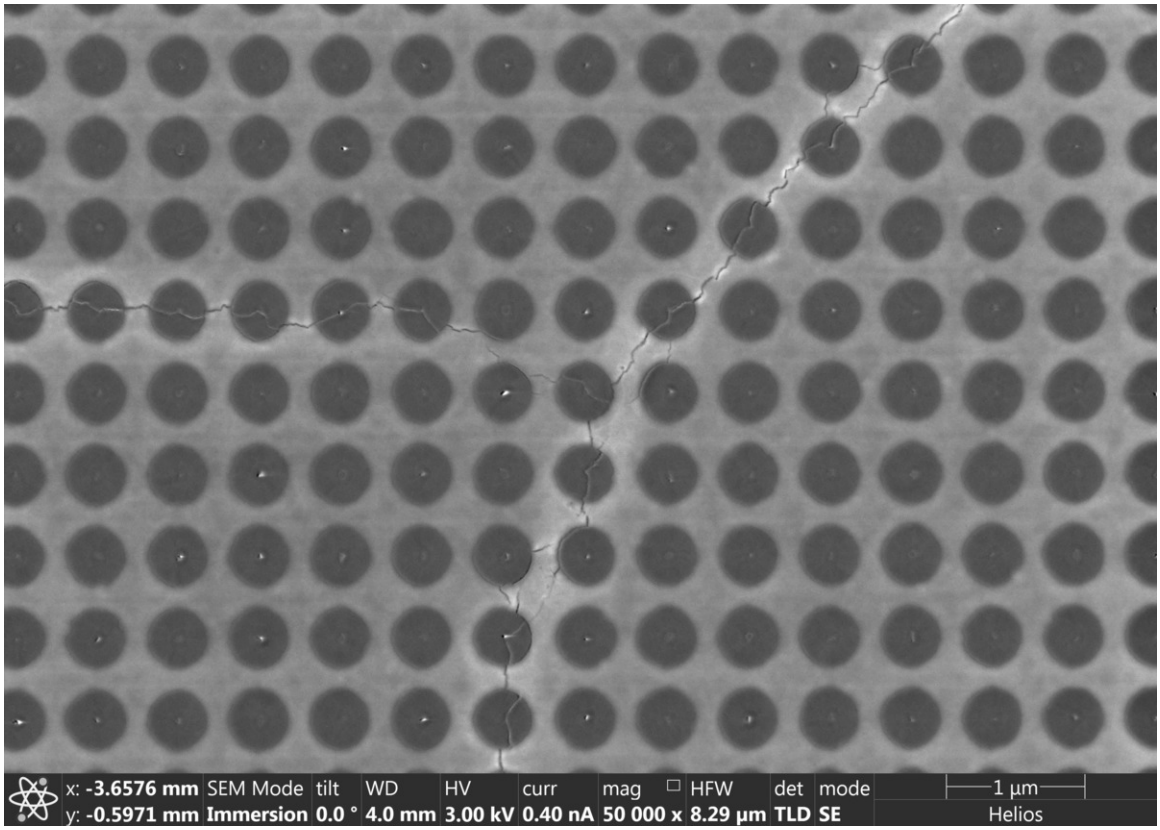

Figure 6-5: The cracks observed after the last fabrication processing steps seem to take a more circuitous path.

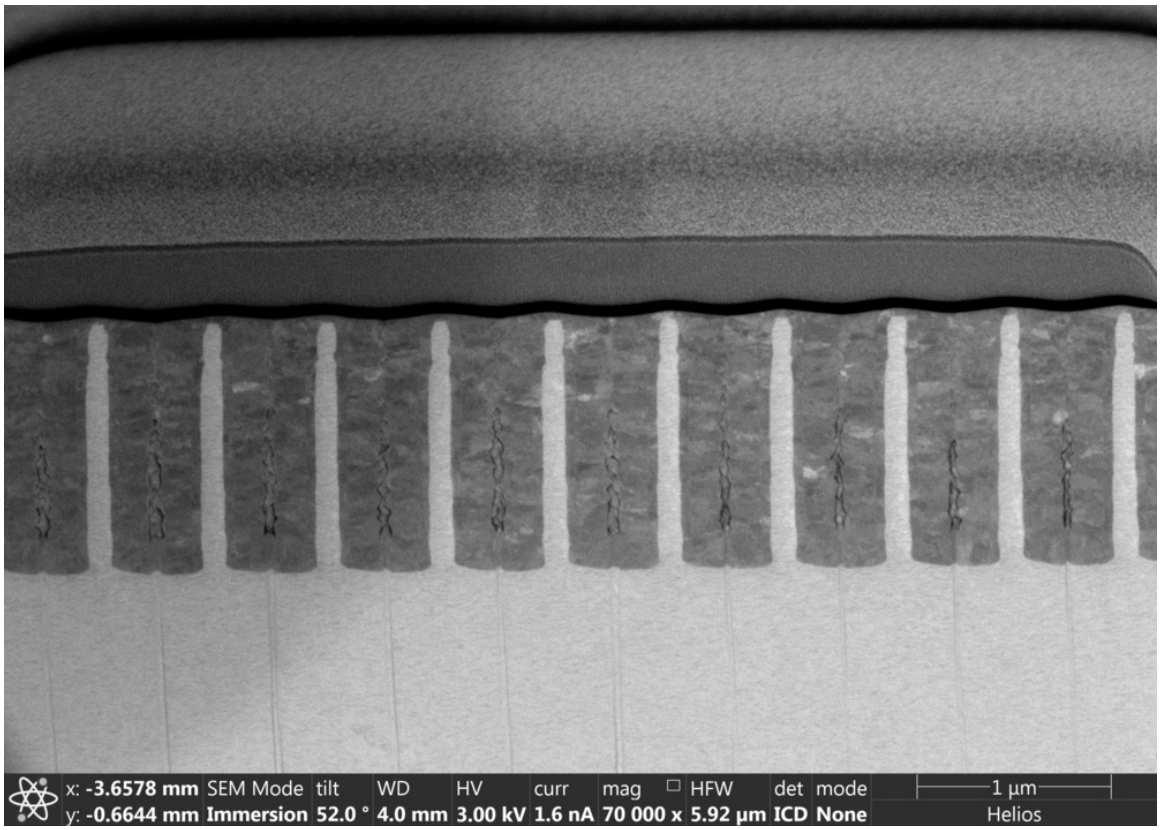

Figure 6-6: The cracks observed after the last fabrication processing steps seem to take a more circuitous path.

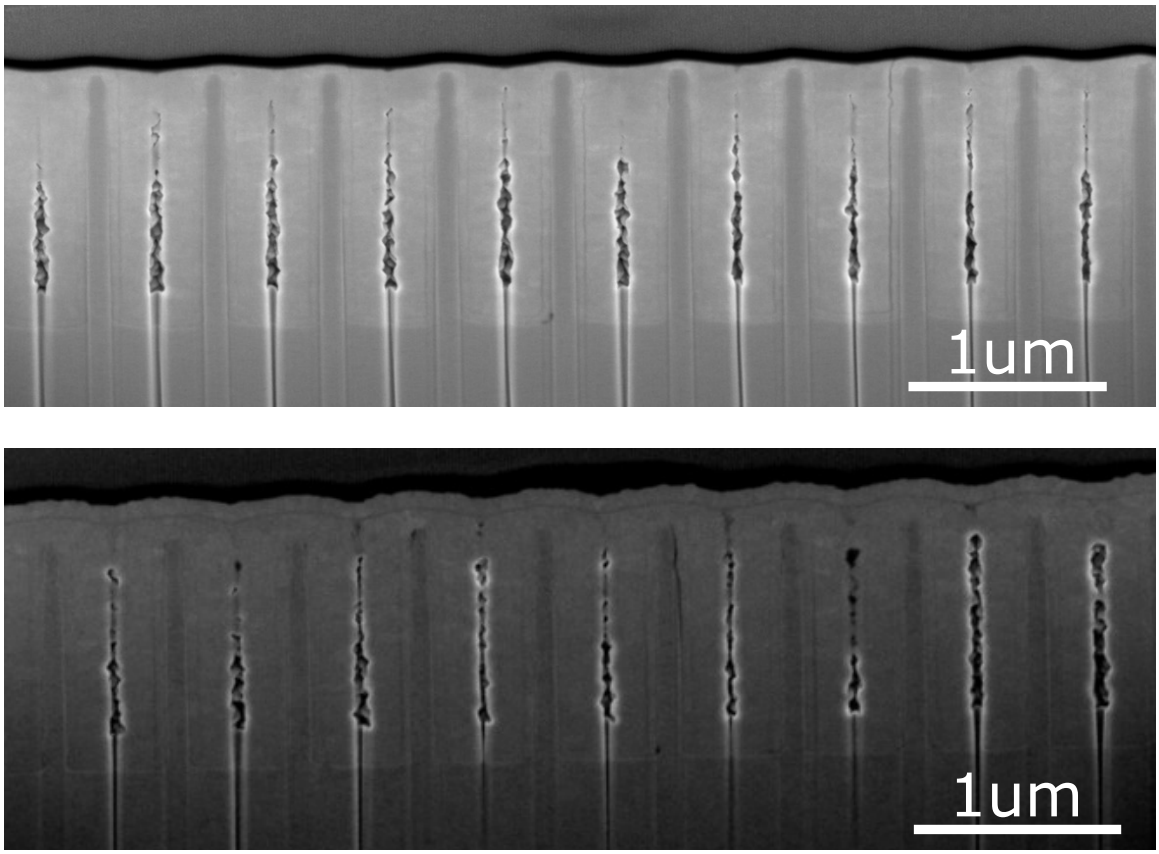

Figure 6-7: Contrast between different areas of HfO_2, which are revealed by focused ion beam milling, may indicate nonuniform quality of HfO_2 and different mechanical properties. Top row is the photonic crystal after the last processing step: vertical lines in the HfO_2 are visible, parallel to the cavity sidewalls. Bottom row: after the additional layer of HfO_2 has been deposited, it appears as a distinct layer; cracks parallel to the cavity sidewalls are also visible.

erties of the photonic crystal.

6.3 High temperature continuous anneals under vacuum

Step	Temperature range
Ramp-up	Room temperature to 275 °C at 5 °C min^{-1}
Hold	275 °C for 1 hour
Ramp-up	275 - 1000 °C at 5 °C min^{-1}
Hold	1000 °C for varying lengths of time
Cool	No set rate; cooled naturally

Table 6.1: Procedure for annealing photonic crystal sample

Length	Figures	Result
Before anneal	Figure 6-8	-
30 min	Figure 6-9	No observable degradation
1 hour	Figure 6-10	No observable degradation
3 hours	Figure 6-11	No observable degradation
6 hours	Figure 6-12	No observable degradation
12 hours	Figure 6-13	No observable degradation
24 hours	Figure 6-14	No observable degradation
48 hours	Figure 6-15	No observable degradation

Table 6.2: Lengths of continuous anneals

I annealed the photonic crystal sample at 1000 °C under vacuum (at $\sim 1 \times 10^{-6}$ mbar) for varying lengths of time, then measured the emittance spectrum. The procedure for temperature control shown in Table 6.1): the ramp-rate was 5 °C min^{-1}, and a hold at 275 °C was included to allow the sample to off-gas (which manifests as an increase in pressure, as in Figure 6-9a).

I did continuous anneals for increasingly longer periods of time: 30 minutes, then 1, 3, 6, 12, 24, and 48 hours. The results are summarized as shown in Table 6.2.

Overall there was no observable degradation after each of the anneals.

One minor change that seems present in the spectra after 12, 24, and 48 hours is the red-shifting of the cutoff wavelength. That is, the drop in emittance from high

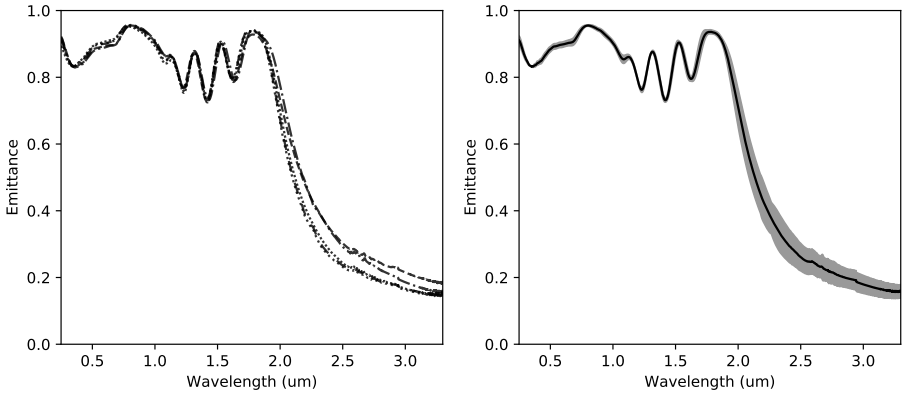

Figure 6-8: Spectra of photonic crystal before any annealing. Left: individual spectra, right: mean with confidence interval.

to low seems to occur for a longer wavelength. This is probably consistent with a broadening of some of the cavities, perhaps due to creep.

While these results show that this filled photonic crystal is robust at least for the short term under vacuum, more studies are required to understand its stability at high-temperatures.

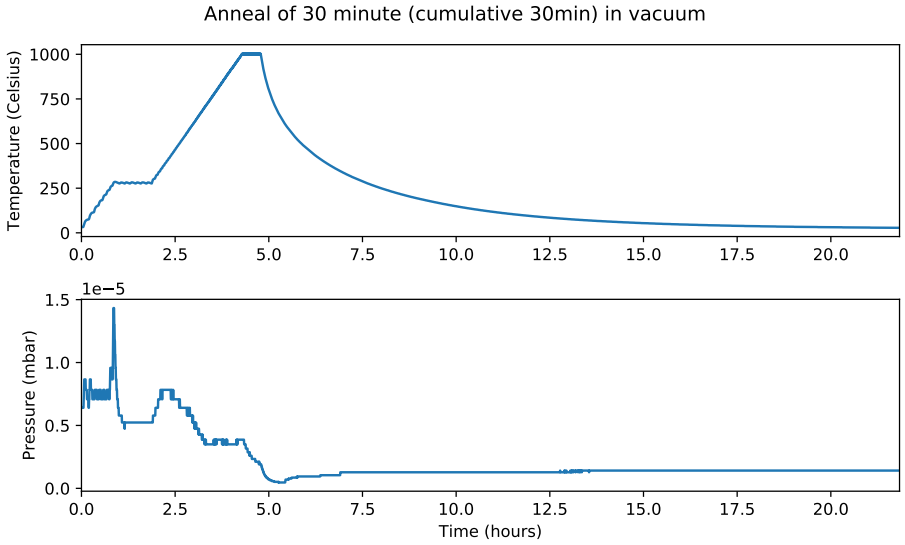

(a) 30 minute anneal (at 1000 °C): Pressure increases during hold at 275 °C, then again during ramp-up to 1000 °C.

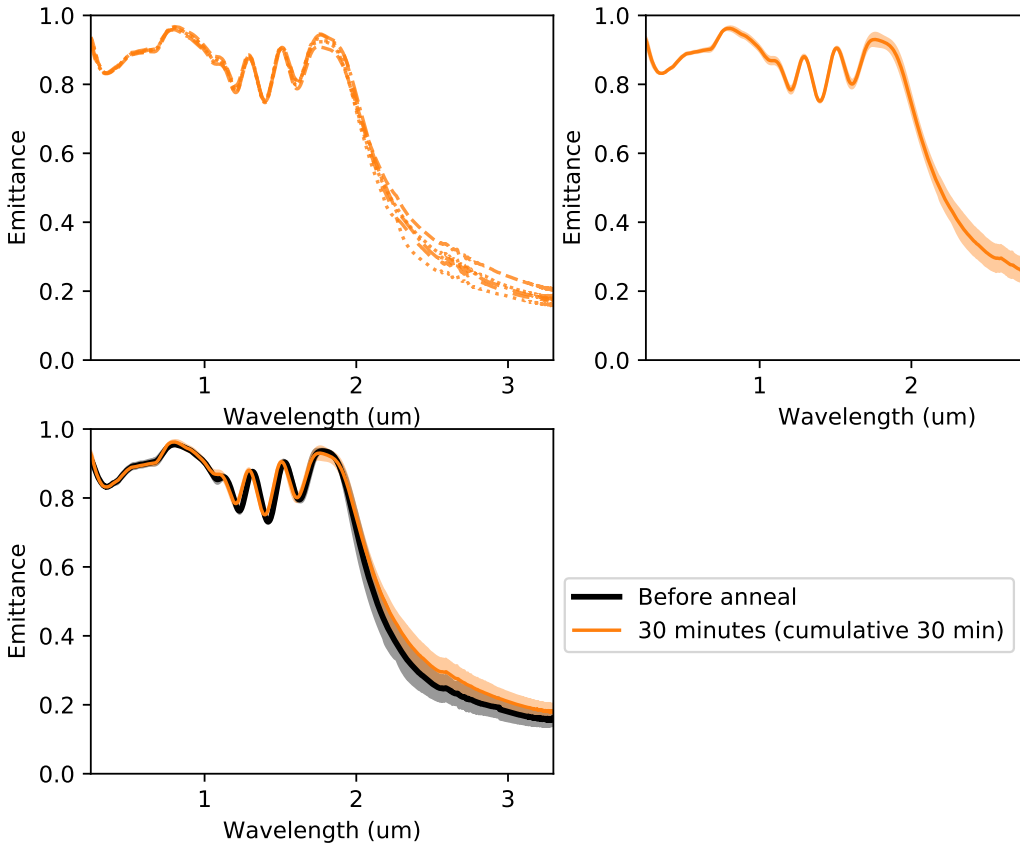

(b) There is no observable degradation after 30 minutes of annealing. Top left: plots of individual spectra, top right: mean with confidence interval, bottom left: comparison with spectrum before anneal.

Figure 6-9: Results of 30 minute (cumulative 30 min) anneal at 1000 °C

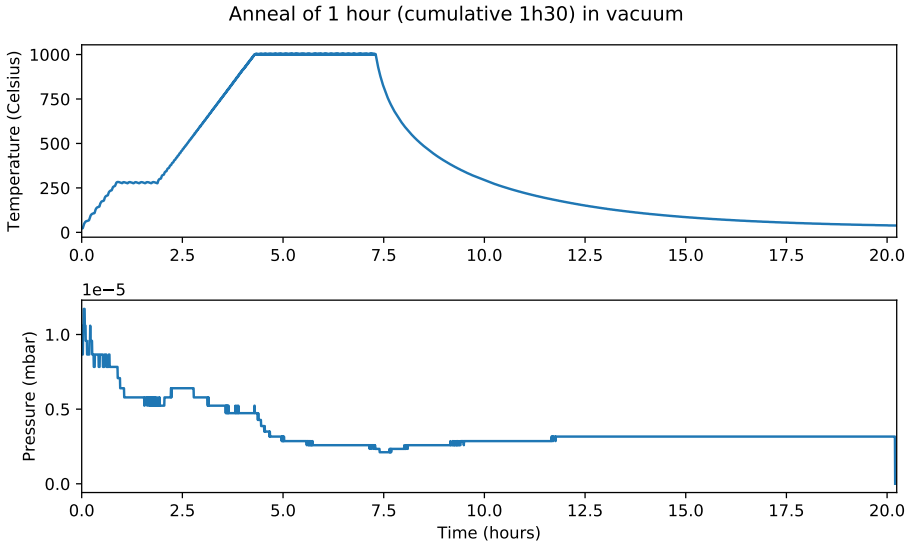

(a) 1 hour anneal (at 1000 °C): Pressure increases slightly during ramp-up to 1000 °C, then decreases.

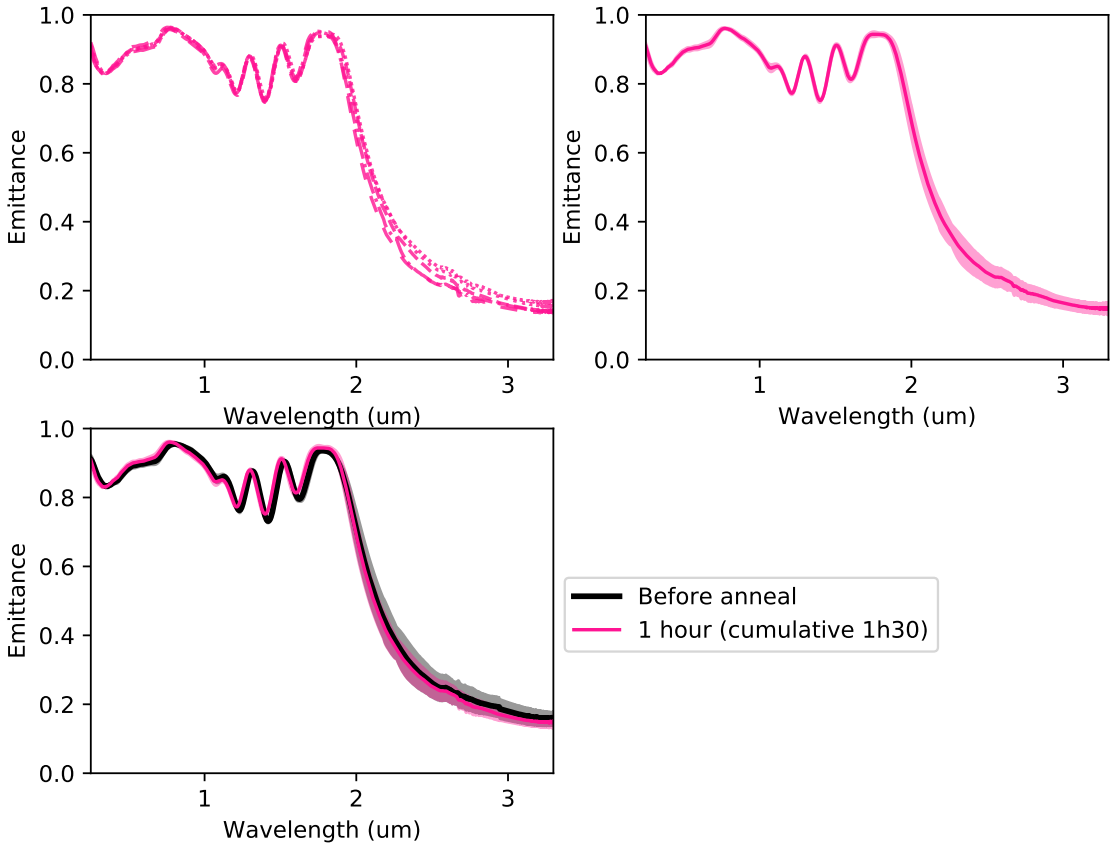

(b) There is no observable degradation after 1 hour of annealing. Top left: plots of individual spectra, top right: mean with confidence interval, bottom left: comparison with spectrum before anneal.

Figure 6-10: Results of 1 hour anneal (cumulative 1.5h) at 1000 °C

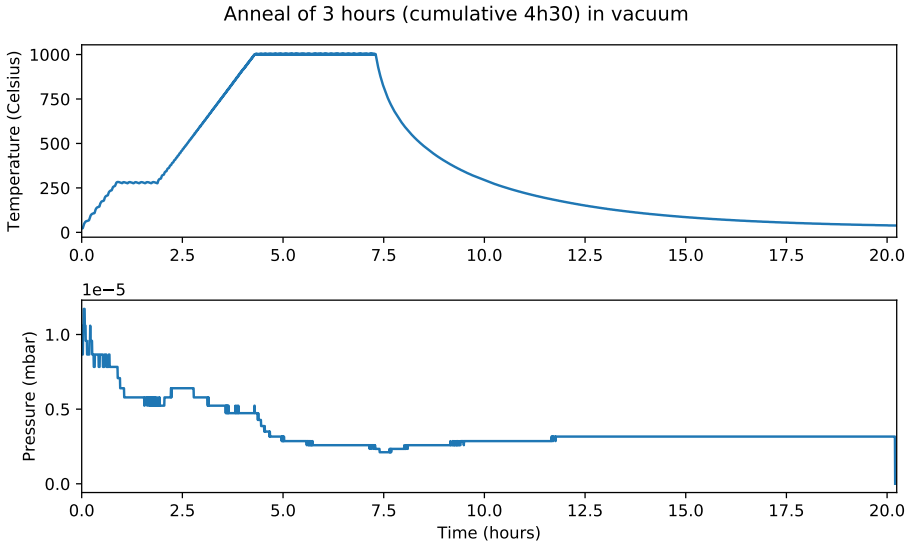

(a) 3 hour anneal (at 1000 °C): Pressure increases slightly during ramp-up to 1000 °C, then decreases.

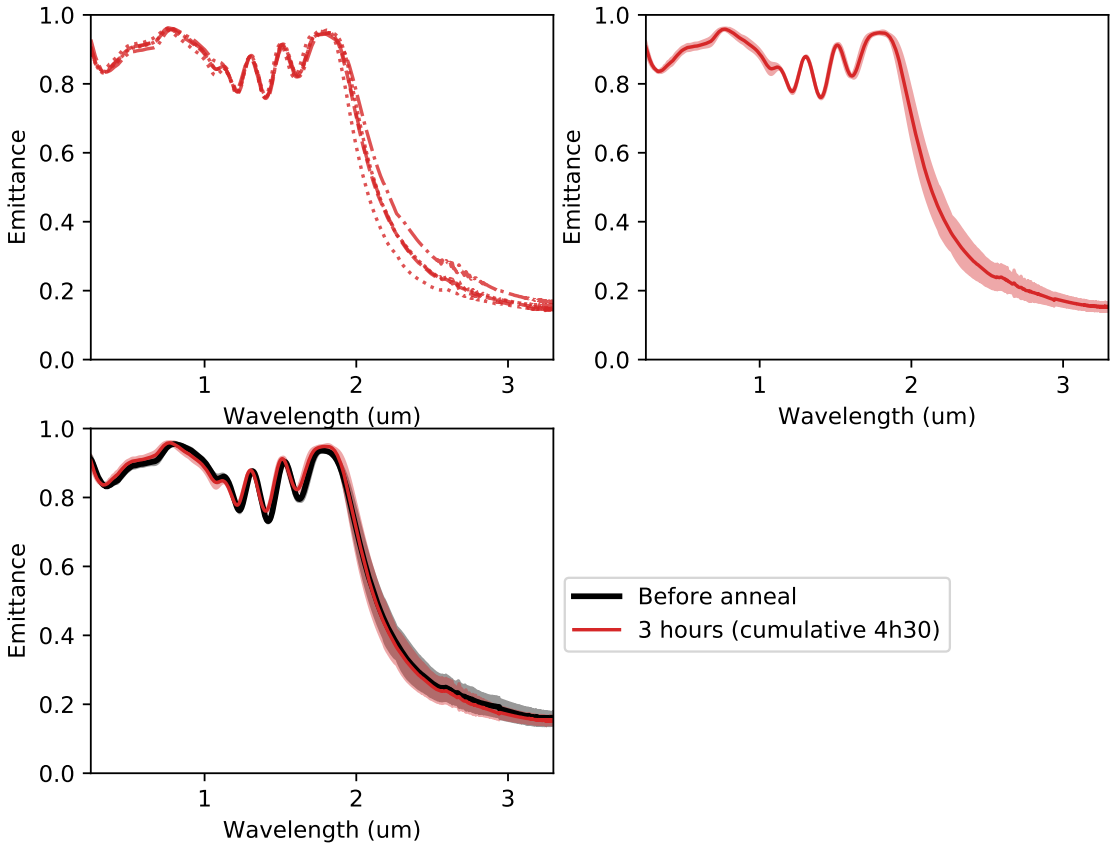

(b) There is no observable degradation after 3 hours of annealing. Top left: plots of individual spectra, top right: mean with confidence interval, bottom left: comparison with spectrum before anneal.

Figure 6-11: Results of 3 hour (cumulative 4.5h) anneal at 1000 °C

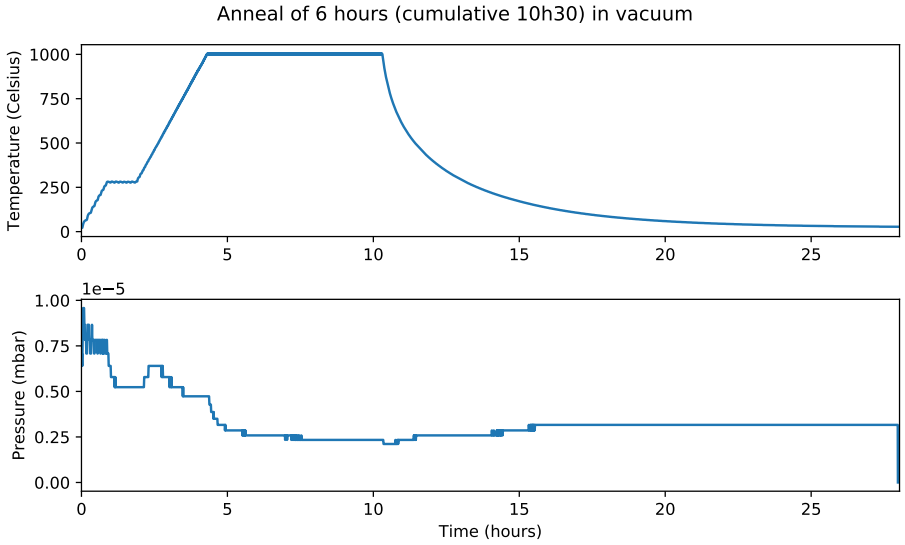

(a) 6 hour anneal (at 1000 °C): Pressure increases slightly during ramp-up to 1000 °C, then decreases.

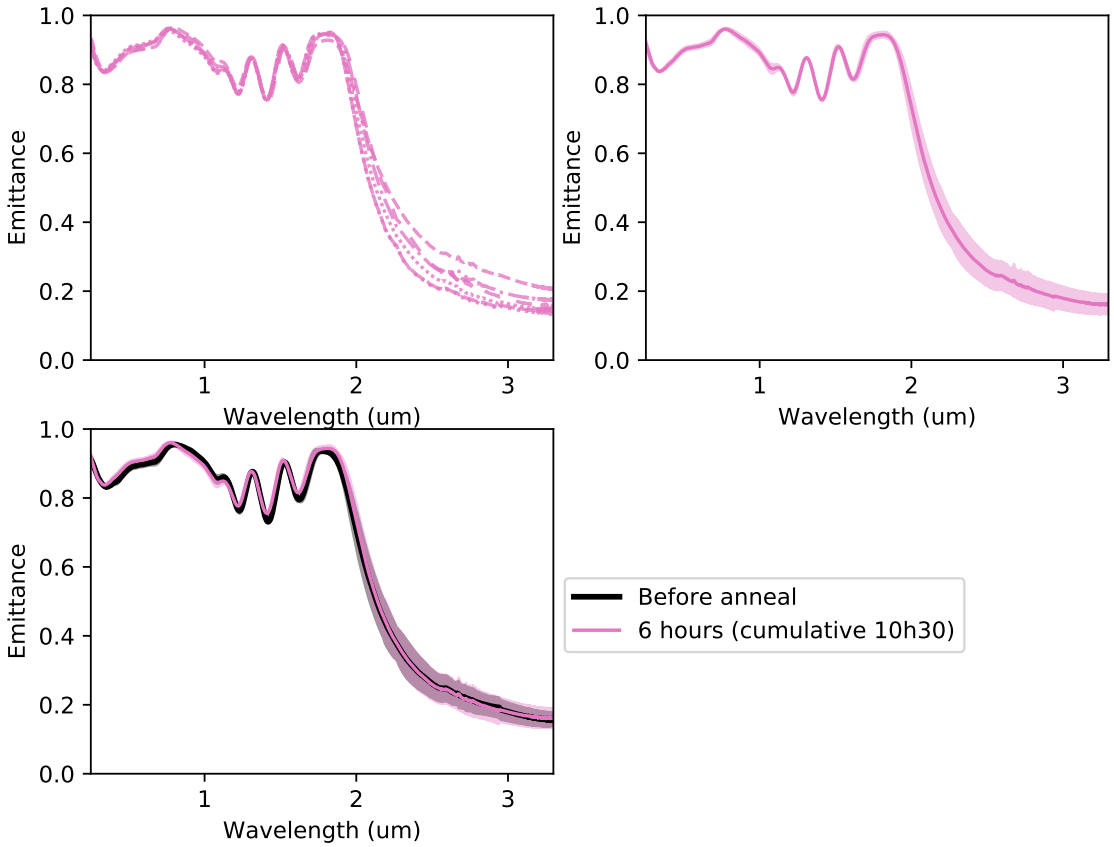

(b) There is no observable degradation after 6 hours of annealing. Top left: plots of individual spectra, top right: mean with confidence interval, bottom left: comparison with spectrum before anneal.

Figure 6-12: Results of 6 hour (cumulative 10.5h) anneal at 1000 °C

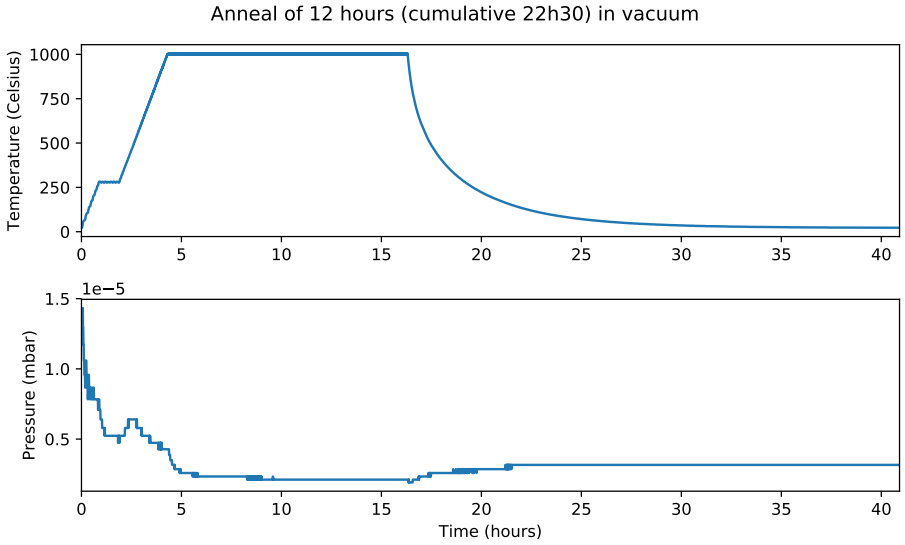

(a) 12 hour anneal (at 1000 °C): Pressure increases slightly during ramp-up to 1000 °C, then decreases.

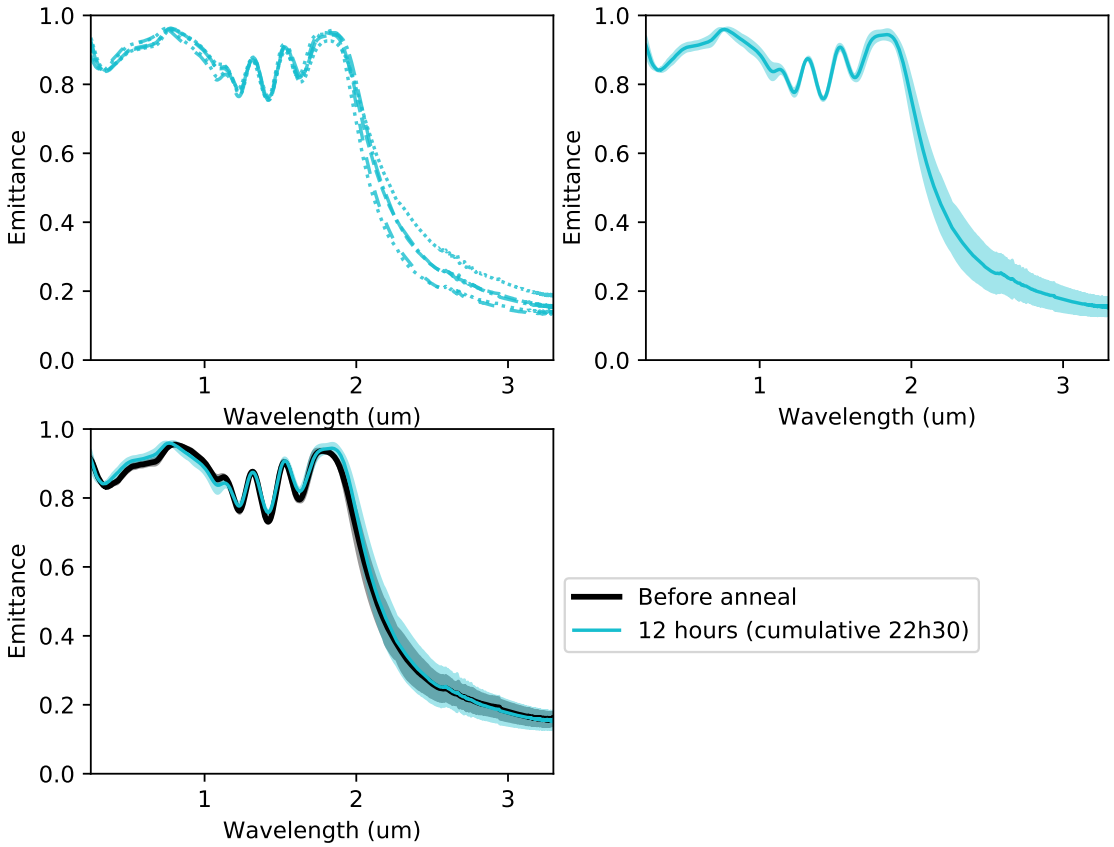

(b) There is no observable degradation after 12 hours of annealing. Top left: plots of individual spectra, top right: mean with confidence interval, bottom left: comparison with spectrum before anneal.

Figure 6-13: Results of 12 hour (cumulative 22.5h) anneal at 1000 °C

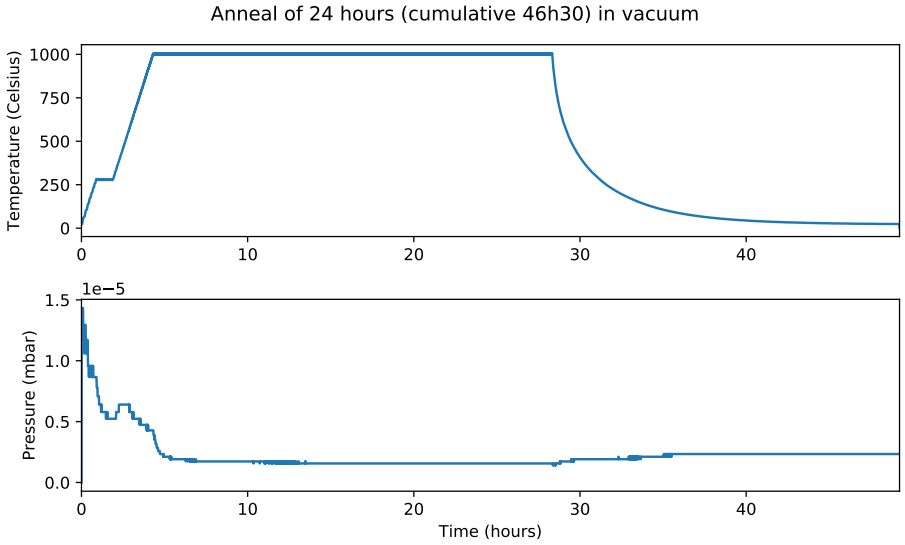

(a) 24 hour anneal (at 1000 °C): Pressure increases slightly during ramp-up to 1000 °C, then decreases.

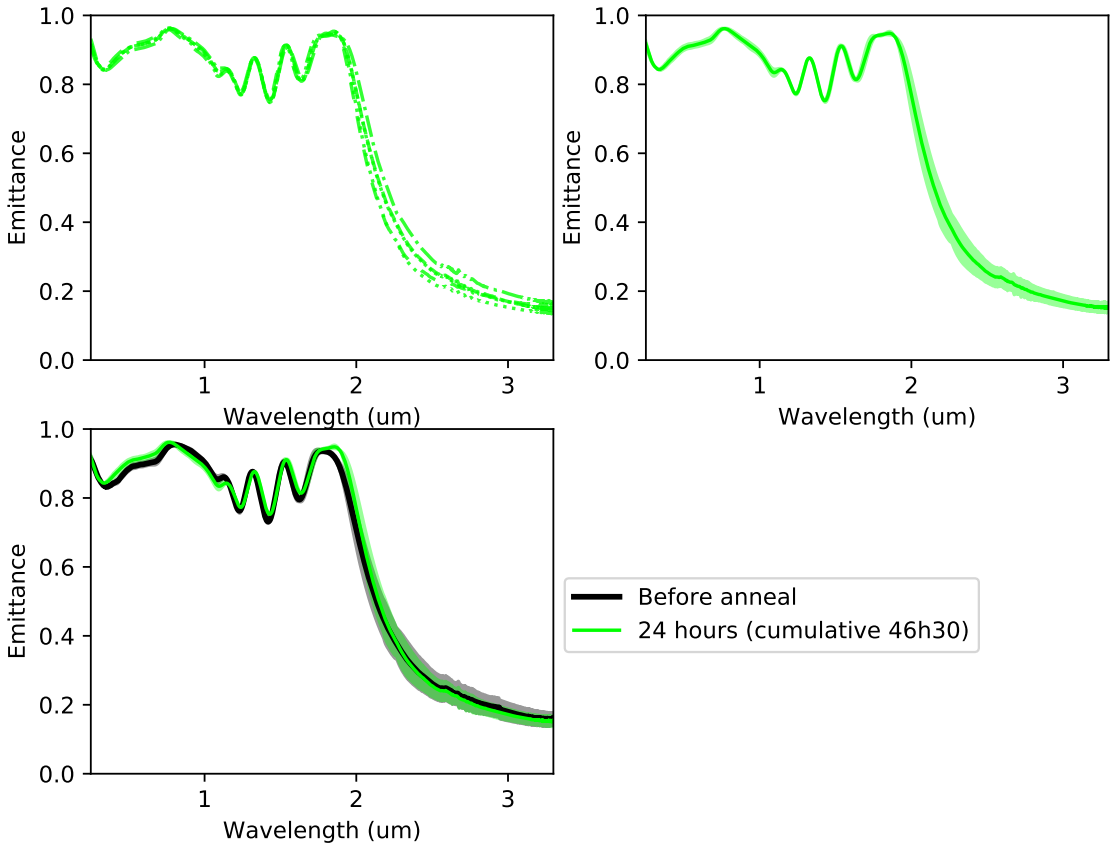

(b) There is no observable degradation after 24 hours of annealing. Top left: plots of individual spectra, top right: mean with confidence interval, bottom left: comparison with spectrum before anneal.

Figure 6-14: Results of 24 hour (cumulative 46.5h) anneal at 1000 °C

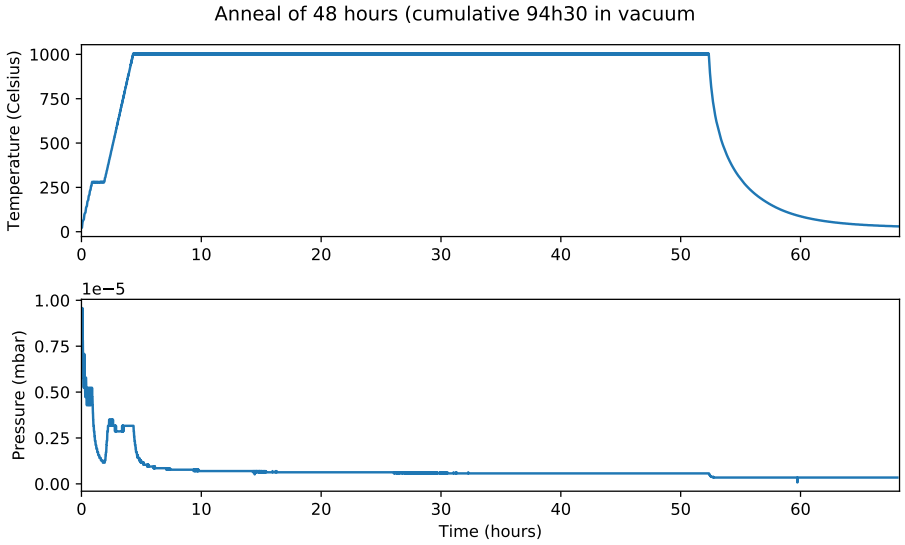

(a) 48 hour anneal (at 1000 °C): Pressure increases slightly during ramp-up to 1000 °C, then decreases.

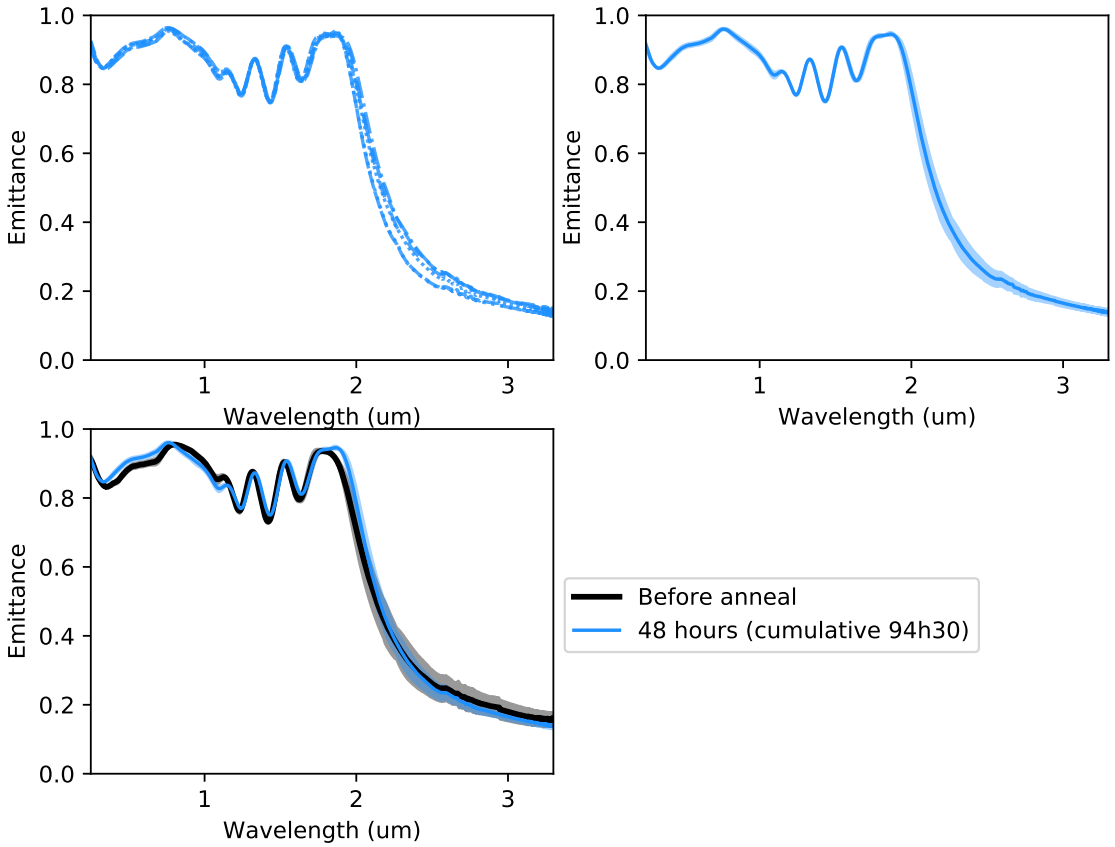

(b) There is no observable degradation after 48 hours of annealing. Top left: plots of individual spectra, top right: mean with confidence interval, bottom left: comparison with spectrum before anneal.

Figure 6-15: Results of 48 hour (cumulative 94.5h) anneal at 1000 °C

Chapter 7

Conclusions

In this thesis, the fabrication of a filled PhC with close to full theoretical performance has been described.

The fabricated photonic crystal, at both normal and off-normal angles has an in-band emittance of 0.7-0.9 and an out-of-band emittance of about 0.2, and exhibits a sharp transition from high to low emittance around 2 µm, the target cutoff wavelength, as shown in Figure 7-1. Moreover, I have been able to achieve this performance despite not achieving perfect geometric features: while the capping layer is not flat and the cavity still has a hollow air core, their impact on the optical properties appears to be negligible.

7.1 Evaluation of fabricated filled photonic crystal emitter

I evaluate the fabricated emitter based on the metrics first described in the introduction: optical performance, high-temperature stability, and estimated system impact.

7.1.1 Optical metrics

One note is that the calculations of the optical metrics are based on a likely over-estimation of the in-band emittance. These calculations are based on the simulated

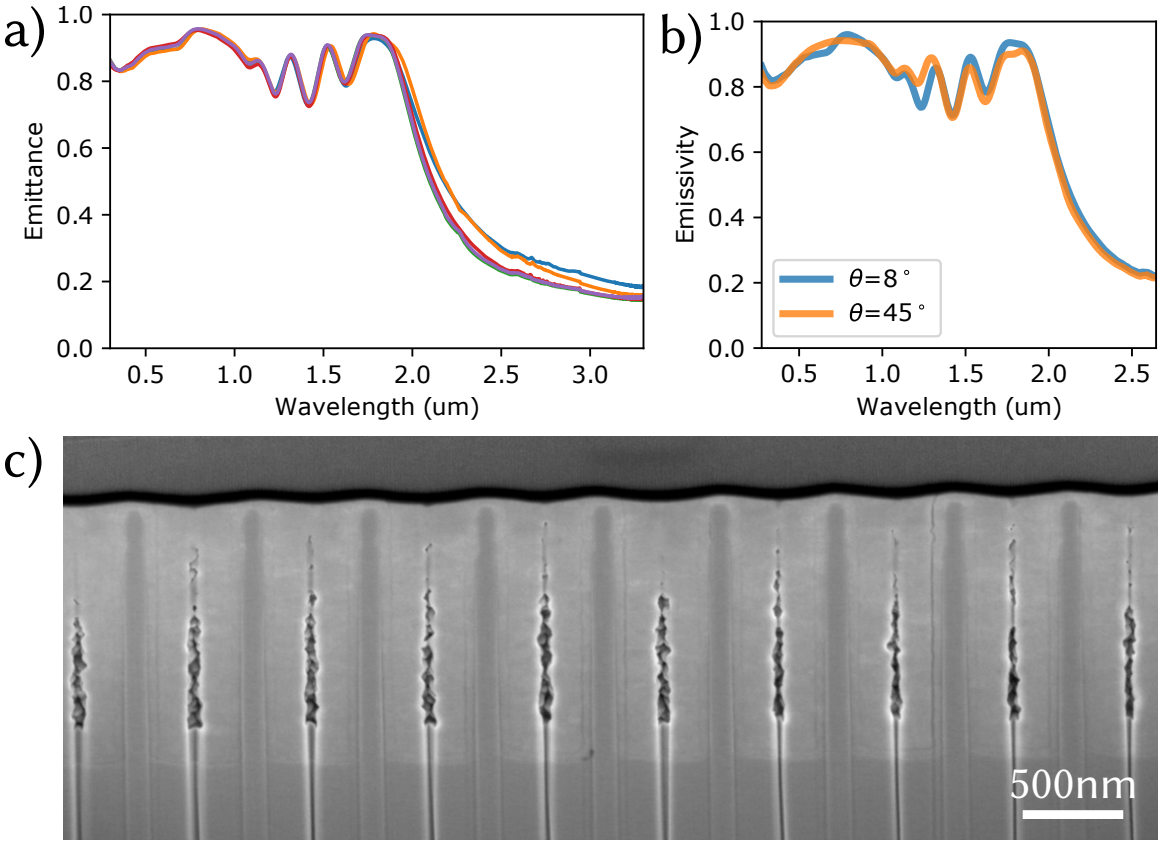

Figure 7-1: Fabricated filled photonic crystal.

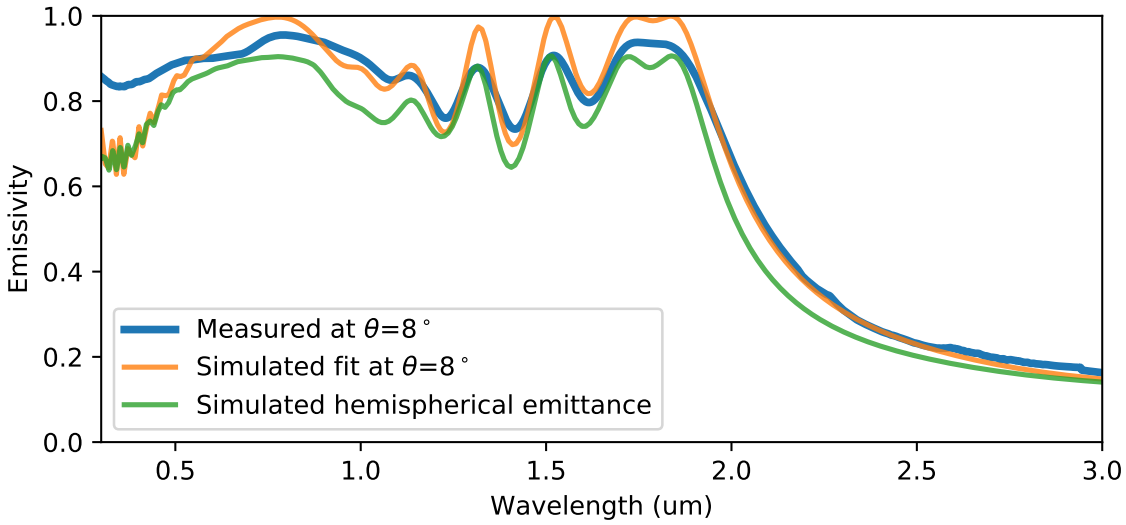

Figure 7-2: The actual hemispherical in-band emittance is likely lower in the in-band region, because the simulated fit overestimates the amplitude of the peaks at 8°.

hemispherical emittance, which is itself based on parameters derived from simulated fit to the measured room temperature emittance spectrum (Figure 7-2).

The actual hemispherical in-band emittance is likely lower in the in-band region, because the simulated fit overestimates the amplitude of the peaks at 8°.

The fabricated filled PhC is an improvement over the conformal photonic crystals for all optical metrics (see Figure 7-3), and has performance comparable to those of the perfect filled photonic crystals.

PhC type	Cutoff wavelength (µm)	Period a (µm)	Radius r (µm)	Depth d (µm)	Capping layer thickness t
Conformal PhC (hemispherical, simulated) [83]	2.0	1.1	0.49	8.0	-
Conformal PhC (hemispherical, Energy Environ. Sci.) [3]	2.0	1.2	0.52	5.4	-
Perfect filled PhC (simulated $\theta = 0, \phi = 0$) [87]	2.0	0.57	0.23	4.31	0.078
Perfect filled PhC (simulated, hemispherical) [87]	2.0	0.57	0.23	4.31	0.078
Shallower than filled PhC (simulated, hemispherical) [87]	2.0	0.57	0.23	1.5	0.078
Fabricated filled PhC (simulated, hemispherical)	2.0	0.551	0.222588	1.34	0.0635

Table 7.1: Parameters for PhCs shown in Figure 7-3

7.1.2 High temperature stability

The photonic crystal showed no observable degradation after a continuous 48 hours of annealing at 1000 °C under vacuum of 1×10^{-7} mbar to 1×10^{-5} mbar, as shown in Figure 7-4.

While this emitter's high-temperature stability should be investigated over longer times (thousands of hours) as well as over multiple thermal annealing cycles, in the short term the high-temperature stability of this photonic crystal is robust.

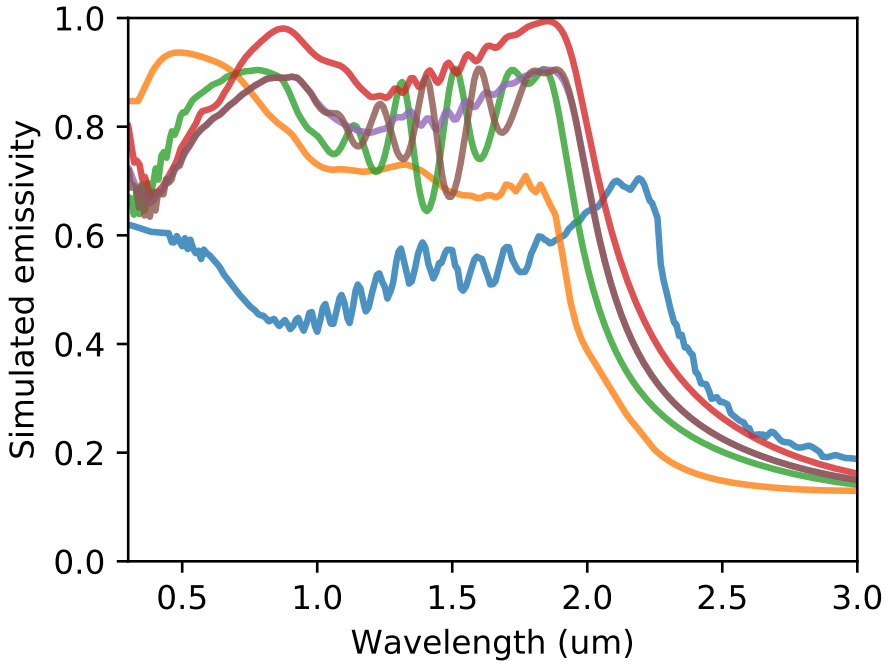

(a) Close up of spectra shown in (b). Labels in (b). The simulated hemispherical emittance of the fabricated filled PhC is shown in green.

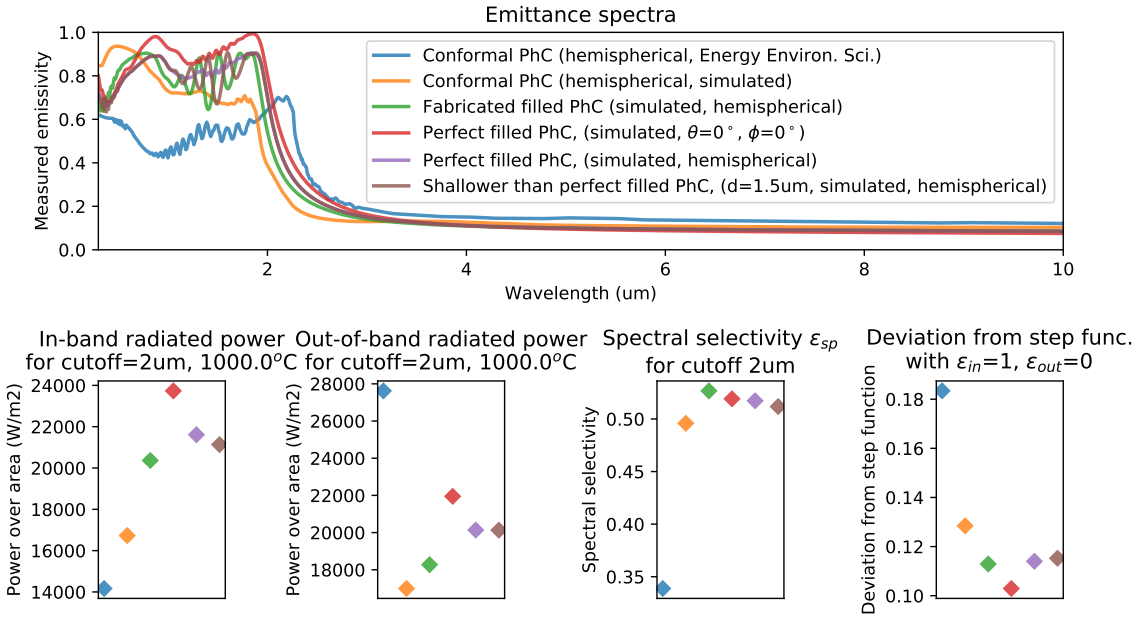

(b) Metrics for several PhCs. Numerical values are shown in Table 7.2.

Figure 7-3: The performance of the fabricated filled PhC is an improvement over the conformal photonic crystals, and has performance comparable to those of the perfect filled photonic crystals.

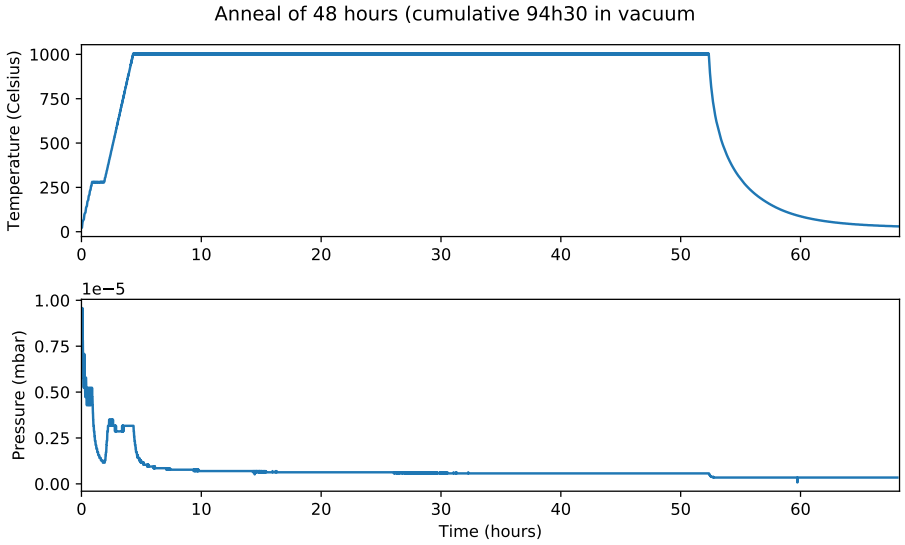

(a) 48 hour anneal (at 1000 °C): Pressure increases slightly during ramp-up to 1000 °C, then decreases.

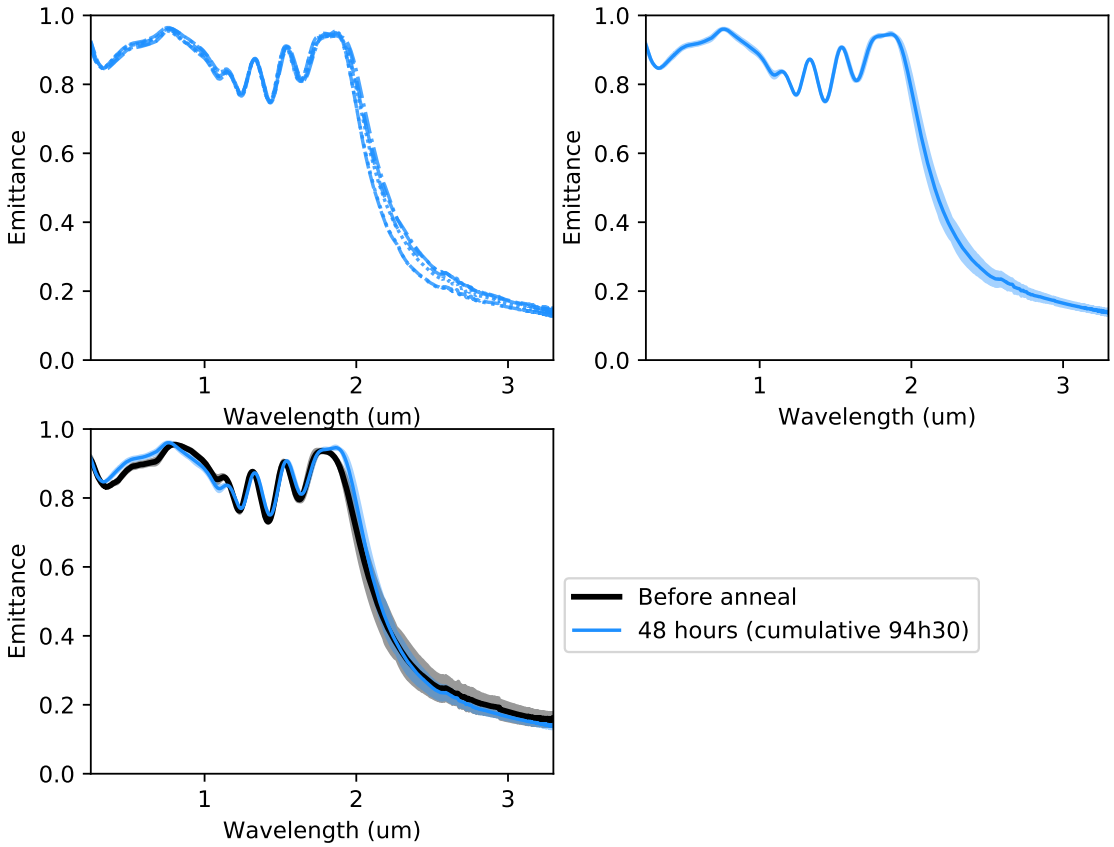

(b) There is no observable degradation after 48 hours of annealing. Top left: plots of individual spectra, top right: mean with confidence interval, bottom left: comparison with spectrum before anneal.

Figure 7-4: Results of 48 hour (cumulative 94.5h) anneal at 1000 °C

PhC type	In-band radiated power per area for cutoff 2 µm, 1000 °C ($W\,m^{-2}$)	Out-of-band radiated power per area for cutoff 2 µm, 1000 °C ($W\,m^{-2}$)	Spectral selectivity for cutoff 2 µm	Deviation from step function with $\varepsilon_{in} = 1$, $\varepsilon_{out} = 0$
Conformal PhC (hemispherical, Energy Environ. Sci.)	14166.093	27622.25	0.33878	0.18339
Conformal PhC (hemispherical, simulated)	16729.474	16991.957	0.49587	0.12844
Perfect filled PhC, (simulated, θ=0°, ϕ=0°)	23734.703	21950.499	0.51915	0.10292
Perfect filled PhC, (simulated, hemispherical)	21611.118	20136.574	0.5173	0.11401
Shallower than perfect filled PhC, (d=1.5um, simulated, hemispherical)	21134.664	20131.784	0.51179	0.11524
Fabricated filled PhC (simulated, hemispherical)	20365.147	18275.47	0.52674	0.11291

Table 7.2: Numerical values of metrics for PhCs shown in Figure 7-3

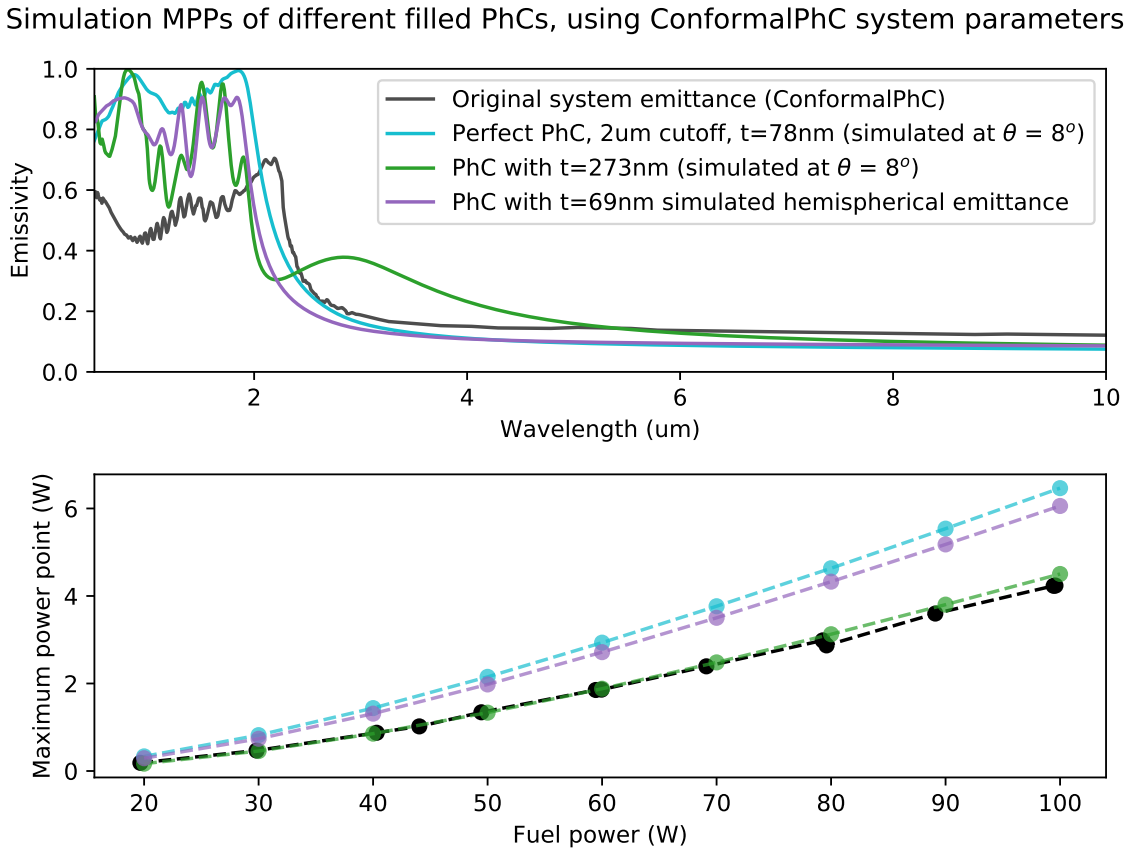

Figure 7-5: The actual hemispherical in-band emittance is likely lower in the in-band region, because the simulated fit overestimates the amplitude of the peaks at 8°.

7.1.3 Estimated system impact

According to system simulations (using parameters of system whose original emitter was a conformal PhC, Figure 7-5), an increase of up to 37.5% in system output power is expected. The original power output was 4.4 W, while up to 6.0 W is expected for the fabricated filled PhC, and up to 6.5 W can be expected for a perfect filled PhC.

7.2 Future work

We can use the framework of practical metrics to guide future work.

- Optical properties
  - Although the filled photonic crystal has close to full theoretical performance, its in-band emittance is lower compared to what is possible according to the simulations (but the reason for this is not clear). A further increase in in-band emittance would increase the system output power.
  - The cavity depth could be increased: the ideal cavity depth is about 4.3 µm, while the depth of the final filled photonic crystal is about 1.3 µm.
- High temperature stability
  - One question is under what conditions and through what mechanism (degradation of structure, of material) the photonic crystal fails. The photonic crystal could be subjected to anneals of longer duration (1000 hours, 10000 hours), thermal cycling, and higher temperatures (>1000 °C). In addition, it would be useful to image the same area before and annealing to see how cracks have formed or propagated, or how the photonic crystal materials have deformed.
- Large area fabrication
  - Since radiated power from the photonic crystal is governed by Planck's law, larger areas lead to higher power. Currently, our group's fabrication

method uses interference lithography; it may be more appropriate to use a stepper for lithography, in the future.

- System integration
  - The full system performance of a prototype system with this filled photonic crystal could be tested. This would first require integrating the photonic crystal with the microcombustor via brazing.
  - To accommodate different system configurations (for example a the photonic crystal arranged in a cylindrical configuration), the photonic crystal could be fabricated on thinner and more flexible substrates.

- Cost:
  - The current process for filling cavities with hafnium oxide (standard mode and exposure mode atomic layer deposition) is both expensive and time-consuming. Alternative methods for filling the cavities could be investigated.
  - The photonic crystal could be made of cheaper materials, such as using SiO_2 as the dielectric as in [87].

Appendix A

Photonic crystal parameters

PhC type	Cutoff (µm)	Period, a (µm)	Radius, r (µm)	Depth, d (µm)	Source
For InGaAsSb	2.3	1.22	0.55	7.16	[6] Ch. 2
For InGaAs	2.0	1.1	0.49	8.0	[6] Ch. 2
For GaSb	1.7	0.96	0.43	8.0	[6] Ch. 2
For 2.0 micron	2.0	1.16	0.53	8.50	[87]
For GaSb, I	1.8	0.95	0.43	8.00	[40]
For InGaAs, II	2.0	1.11	0.51	8.00	[40]
for InGaAsSb, III	2.3	1.23	0.57	8.00	[40]

Table A.1: Unfilled or bare tantalum photonic crystal parameters

PhC type	Cutoff (µm)	Period, a (µm)	Radius, r (µm)	Depth, d (µm)	Source
For 2.0 micron (sim.)	2.0	1.3	1.1	8	[78]
For 2.0 micron (expt.)	2.0	1.35	1.0-1.1	6.2-6.8	[78]
For InGaAsSb	2.3	1.28	0.59	5.11	[6] appendix
For InGaAs	2.0	1.18	0.52	6.79	[6] appendix
For GaSb	1.7	0.95	0.40	6.40	[6] appendix
PhC I for InGaAsSb	2.3	1.22	0.55	7.16	[83]
PhC II for InGaAs	2.0	1.1	0.49	8.0	[83]
PhC III for GaSb	1.8	0.96	0.43	8.0	[83]
Fabricated PhC [83]	-	1.37	0.53	6.7	
Fabricated and integrated PhC for InGaAs	2.0	1.2	0.52	5.4	[3]

Table A.2: Conformal or coated photonic crystal parameters, coated with t = 20-40 nm of HfO_2

PhC type	Cutoff (µm)	Period, a (µm)	Radius, r (µm)	Depth, d (µm)	HfO_2 capping layer thickness t	Source
Optimized I	1.7	0.49	0.19	3.62	0.063	[87]
Optimized II	2.0	0.57	0.23	4.31	0.078	[87]
Optimized III	2.3	0.64	0.27	5.28	0.080	[87]

Table A.3: Metallodielectric or filled photonic crystal parameters, filled and capped with HfO_2

Appendix B

Simulation and calculation of hemispherical emittance

The hemispherical emittance ε' is the emittance across all angles, where the emittance is a measure of how close the emission is to that of a blackbody. Ideally, the in-band emittance $\varepsilon'_{\text{in-band}}$ is close to 1, while the out-of-band emittance $\varepsilon'_{\text{out-of-band}}$ is close to 0. In addition, the hemispherical emittance is temperature dependent, as the optical properties of a material change with temperature.

$$\varepsilon'(\lambda, T) = \frac{1}{\pi} \int_0^{2\pi} \int_0^{\pi/2} \varepsilon(\lambda, T, \theta, \phi) \cos\theta \sin\theta d\theta d\phi \tag{B.1}$$

The radiated in-band power density (power per area) $M_{\text{rad, in-band}}$, can be calculated from the hemispherical emittance ε', the cutoff or band-gap wavelength λ_{PV}, and the blackbody spectrum $e_b(\lambda, T)$ [98]:

$$M_{\text{rad,in}} = \pi \int_0^{\lambda_{PV}} \varepsilon'(\lambda, T) e_b(\lambda, T) d\lambda \tag{B.2}$$

I estimated the hemispherical emittance of PhCs using simulations, because in most cases it is feasible only to measure the emittance at one or two angles (near-normal and off-normal). However, it is neither feasible to simulate all angles θ and ϕ and to integrate over all of them.

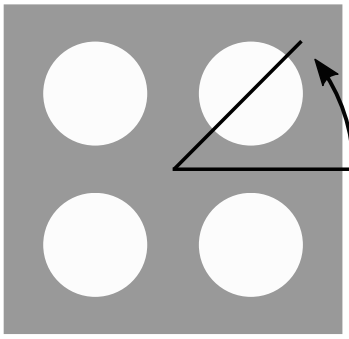

(a) In the ϕ plane, the PhC top surface is symmetric and the range of 0 to $\pi/4$ is unique, making it possible to integrate in ϕ from 0 to $\pi/4$ rather than 0 to 2π.

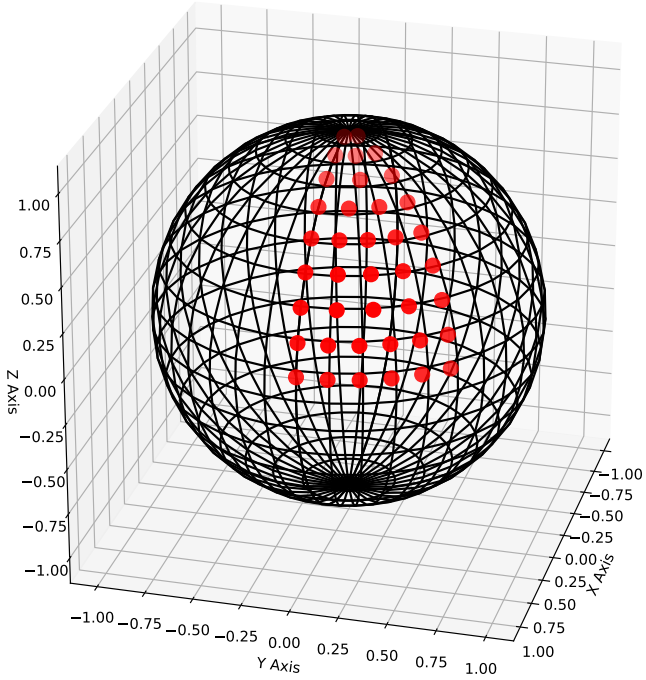

(b) I picked equivalently spaced points (θ, ϕ) on one-eighth of the hemisphere, according to the method in [99].

Figure B-1

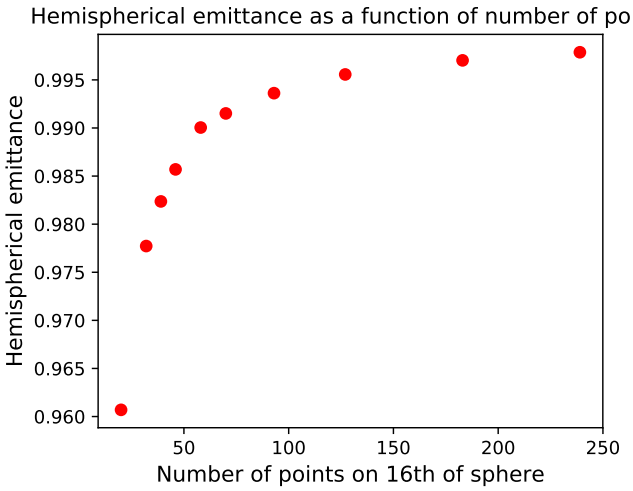

Figure B-2: Hemispherical emittance converges to 1 as number of points (θ, phi) increases. Points plotted: 10, 20, 25, 30, 40, 50, 70, 100, 150, 200.

I selected a number of angles (θ, ϕ) on one sixteenth of a sphere (or one eighth of a hemisphere) to simulate and integrate. By taking advantage of the PhC surface symmetry it is possible to only integrate ϕ from 0 to $\pi/4$ rather than the full 2π, as shown in Figure B-1a, which allows the hemispherical emittance integration to be modified as shown in equation B.3 (notice the 8, and $\pi/4$):

$$\varepsilon(\lambda, T) = \frac{8}{\pi} \int_0^{\pi/4} \int_0^{\pi/2} \varepsilon'(\lambda, T, \theta, \phi) e_b(\lambda, T) \cos\theta \sin\theta d\theta d\phi \tag{B.3}$$

After that I picked equivalently spaced points (θ, ϕ) on this one-eighth hemisphere, according to the method in [99] (I chose this instead of a random point-picking method, and also in this document the convention for θ and ϕ are flipped), the results of which are shown in Figure B-1b.

The question then is how many points (θ, ϕ) are required to properly calculate the hemispherical emittance. For this I used the blackbody emittance $\varepsilon = 1$ as a check: for each point (θ, ϕ) the emittance is 1, and the integration (trapezoidal rule) should converge to a hemispherical emittance of 1 for every wavelength, as shown in Figure B-2.

I also calculated the percent error of the blackbody integral calculated using these hemispherical emittance values, a shown in Figure B-3. I used as the true value the

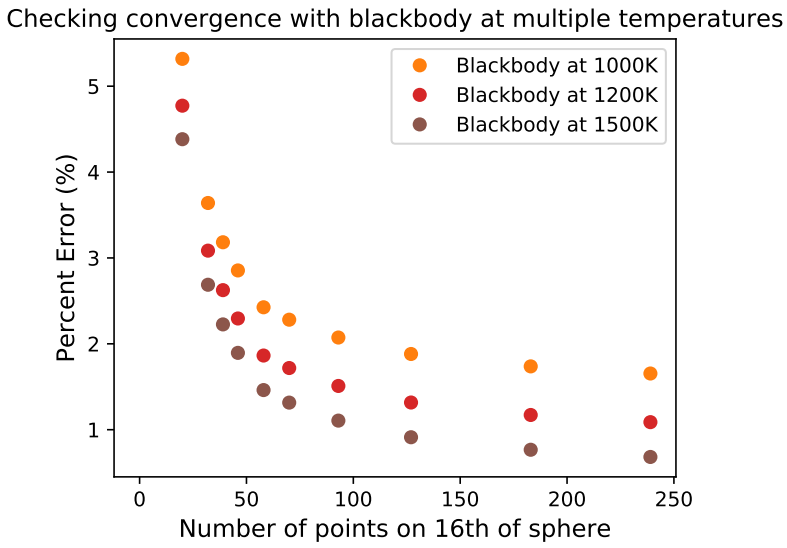

Figure B-3: Percent error of blackbody integration decreases as number of points (θ, ϕ) increases. With at least 25 points, the percent error is less than 3%. Points plotted: 10, 20, 25, 30, 40, 50, 70, 100, 150, 200.

Stefan-Boltzmann constant times temperature to the power of four, σT^4. With at least 25 points, the percent error is less than 3%.

In order to calculate the hemispherical emittance, I used a total of thirty-nine points, at the angles indicated in Table B.1.

θ (degrees)	ϕ (degrees)
0°	0°
5°	0°, 45°
15°	0°, 22.5°, 45°
25°	0°, 22.5°, 45°
35°	0°, 15°, 30°, 45°
45°	0°, 11.25°, 22.5°, 33.75°, 45°
55°	0°, 11.25°, 22.5°, 33.75°, 45°
65°	0°, 11.25°, 22.5°, 33.75°, 45°
75°	0°, 9°, 18°, 27°, 36°, 45°
85°	0°, 9°, 18°, 27°, 36°, 45°

Table B.1: 39 points on one-eighth of the hemisphere: (θ, ϕ), given in degrees

For each PhC design I did thirty-nine simulations corresponding to emittance at each of the above angles. The spectra are shown in Figures B-4 and B-5. In Figure B-6, I have compared the hemispherical, $\theta = 0°$, and $\theta = 45°$ emittances. Sometimes θ

$= 45^\circ$ emittance is used as an approximation for the hemispherical emittance.

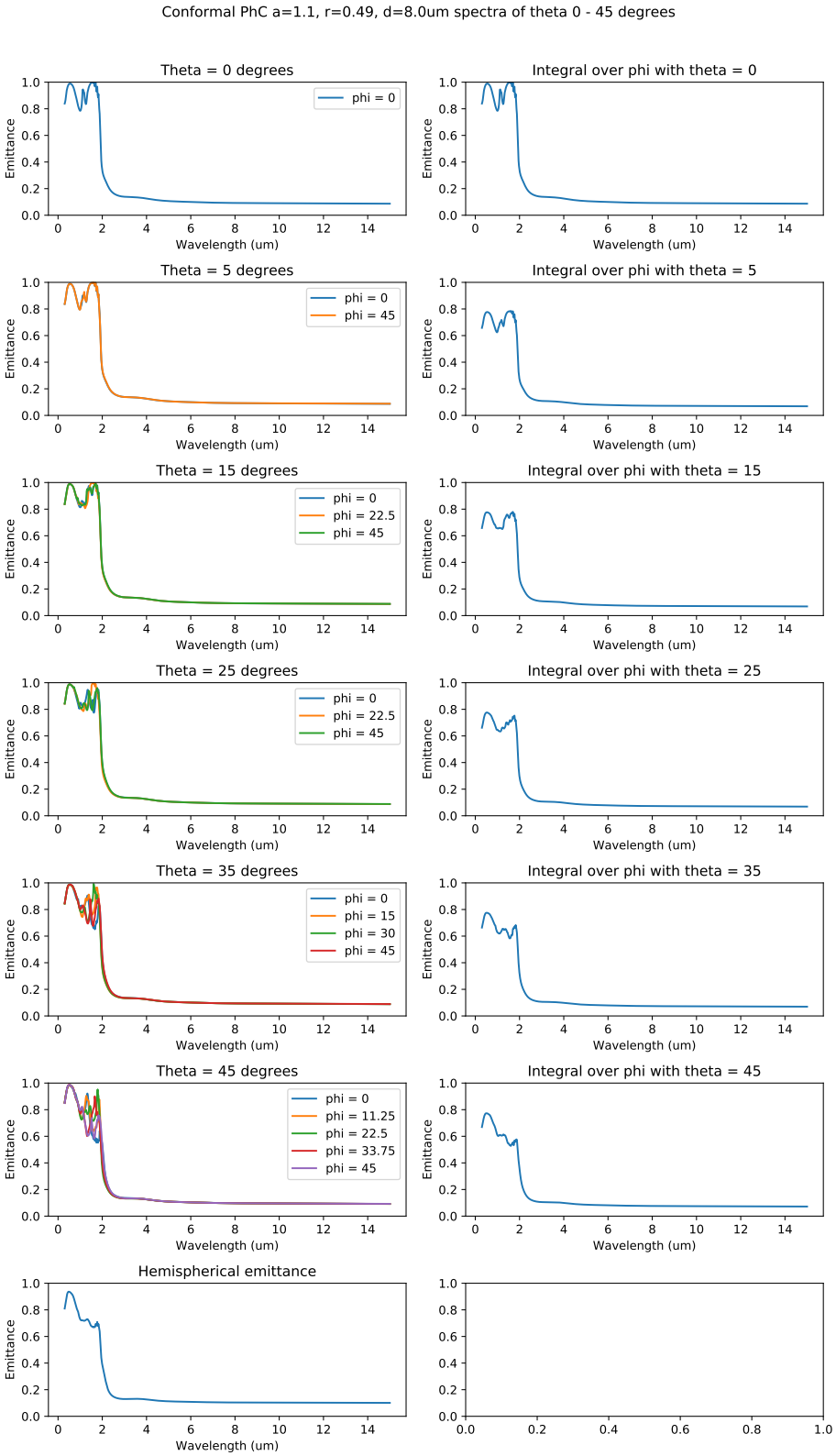

Figure B-4: Showing spectra and integral over ϕ for θ 0° through 45°, for conformal PhC with a=1.1, a=1.1, r=0.49, d=8.0um

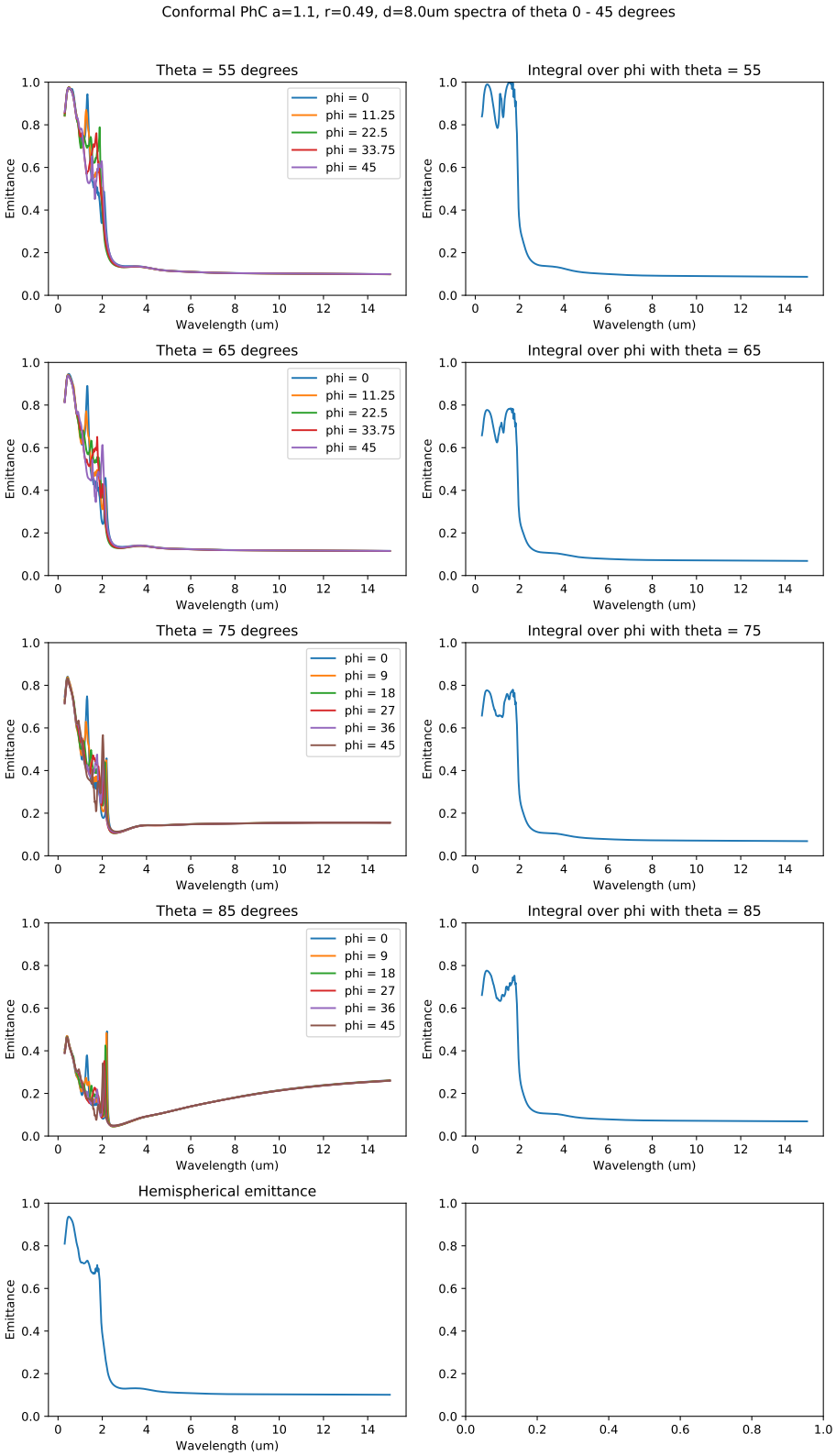

Figure B-5: Showing spectra and integral over ϕ for θ 55° through 85°, for conformal PhC with a=1.1, r=0.49, d=8.0um

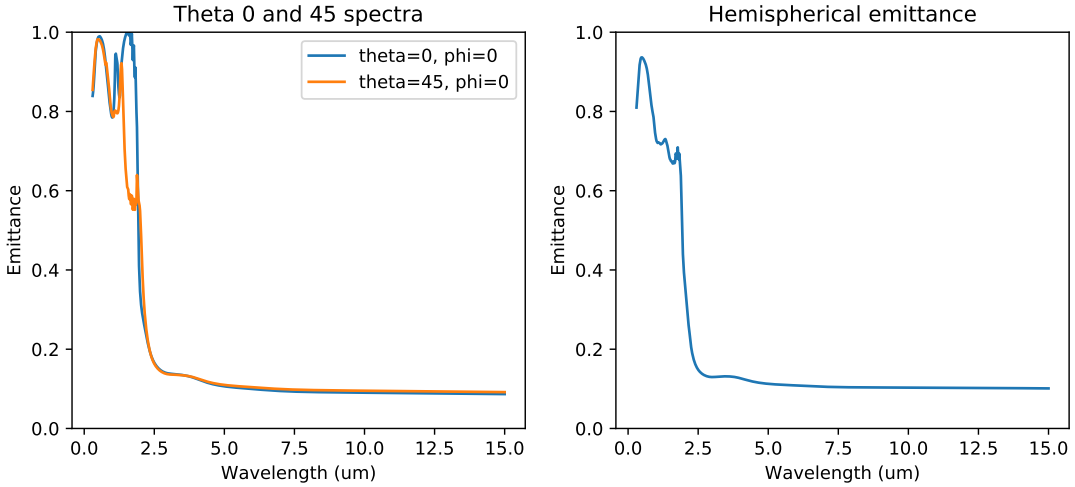

Figure B-6: The PhC spectra at $\theta = 0^\circ$ and 45° and look quite different, with 45° showing a lower in-band emittance. The 45° emittance looks approximately similar to the hemispherical emittance. For conformal PhC with a=1.1, r=0.49, d=8.0um

Appendix C

Troubleshooting the calibration of reflectance measurements

While the absolute reflectance (emittance is calculated as 1 - reflectance) is important for estimating both TPV output power and efficiency, it is not easy to measure accurately for the following reasons:

- The reflectance is measured across a broad wavelength from visible to near-infrared (typically 0.3 to 2.5 or 3.3 nm)
- A photonic crystal reflectance transitions from low at short wavelengths to high at long wavelengths
- There is usually a minimum sample area required either for properly mounting the sample or for the spectrophotometer beam.

One particular problem that our group encountered was that the detector of our primary spectrophotometer (Agilent Cary 5000) had a nonlinear response, which we had to account for in our calibration procedure. The photometric linearity problem was eventually fixed by a service engineer.

I also used two other spectrophotometers, and measured absolute reflectance on instruments that enabled absolute reflectance measurements. However, these absolute reflectance measurements were not always accurate either.

In the end, my group converged to a three to four point calibration procedure,

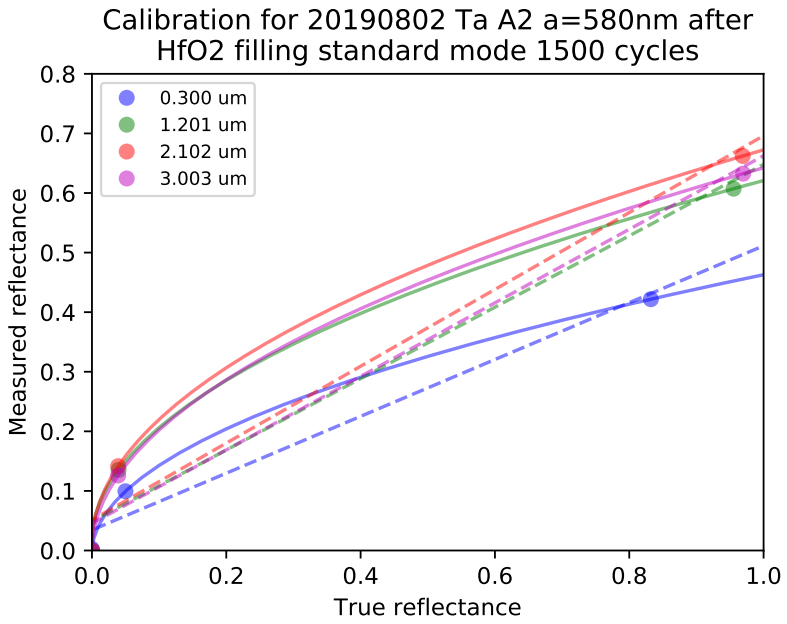

Figure C-1: At first we only had three reference points. When the detector appeared nonlinear (most of the time), we did the calibration based on the three point quadratic fit (solid lines) rather than the linear fit (dotted lines).

using up to three mirrors. We also measured the same flat tantalum wafer and compared it from day to day.

In this appendix, I will detail the calibrations for relative reflectance that were developed with by my labmate Walker Chan, as well the measurements I did to further demonstrate that the spectrophotometer's detector response was not linear.

C.1 Calibration procedure for relative reflectance, from three to four points

Originally, we used three points for relative reflectance measurement calibration: blocked beam (zero), and high and low reflectance standards from Ocean Optics.

However, when we plotted measured vs. true reflectance for several wavelengths (Figure C-1), we found that the detector response appeared to be nonlinear. Because a quadratic fit to the three points (solid lines) was much better than the linear fit (dotted lines), we used a three point quadratic calibration to correct our raw measurements.

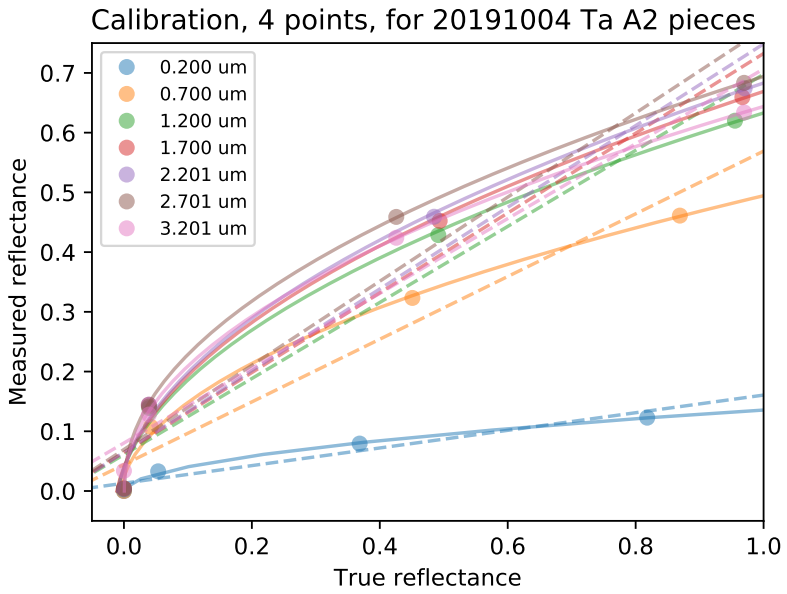

Figure C-2: We added a fourth reference point (a beamsplitter with 40-50%) as an intermediate reflectance standard. For a case like this when the detector was nonlinear, we used a four point quadratic calibration.

However, this left a great deal of uncertainty about the true reflectance for the intermediate reflectance region, so we searched for an intermediate reflectance standard, and used a UV fused silica polka dot beamsplitter from Thorlabs, which reflects about 40-50%.

When we used these four points (Figure C-2), it was consistent with our hypothesis that a quadratic fit would be better.

Eventually the UV-vis spectrophotometer was fixed and the detector response became linear again, as shown in Figure C-3.

The spectra that were corrected using the three point quadratic calibration included the first two filled photonic crystals (those made by Veronika), the measurements I did on my filled PhC until they were filled and diced.

The spectra that were corrected using the four point linear calibration include the piece measurements (top, middle, bottom) after fully filling, and all measurements of the middle piece post further processing.

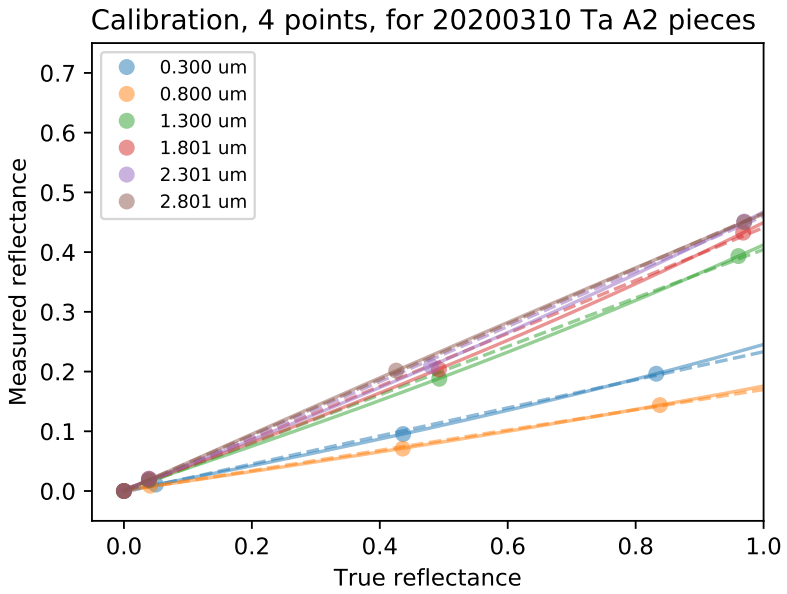

Figure C-3: The spectrophotometer was fixed and the detector response became linear.

C.2 Measuring photometric linearity with neutral density filters

To check the photometric linearity of the spectrophotometer, I measured the transmission through various neutral density filters, and plotted the measured vs. true transmission for several wavelengths (Figure C-4).

For 500-1100 nm the detector response was mostly linear, but deviates for longer wavelengths, especially around 2700 nm (Figure C-4c) which was nearly quadratic.

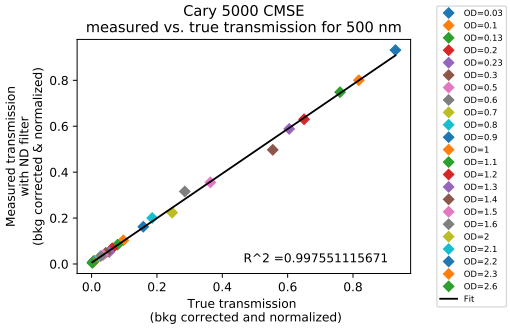

(a) Measured vs. true transmission for 500nm with several neutral density filters

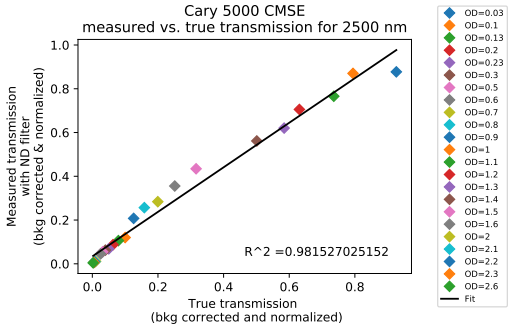

(b) Measured vs. true transmission for 2500nm with several neutral density filters

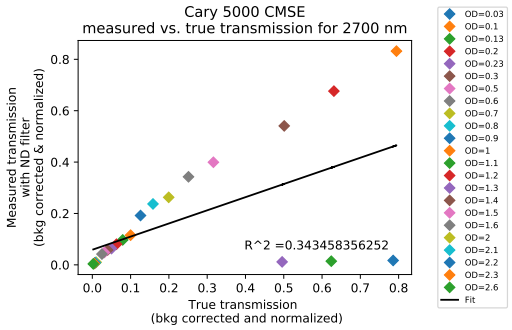

(c) Measured vs. true transmission for 2700nm with several neutral density filters

Figure C-4: Checking photometric linearity through neutral density filters

Appendix D

System performance modeling

While I use four optical metrics (in-band radiated power per area, out-of-radiated power per area, spectral selectivity, deviation from a step function emittance) to estimate an emitter's optical performance, often there is no one set of parameters that optimize all four optical metrics. Therefore I also calculated system performance using the model described by my labmate Dr. Walker Chan, in chapter 2 of his PhD thesis [8] and one of his papers [100]. The system parameters come from three systems described in my labmates' paper on a prototype system demonstration [3].

D.1 Model, in brief

The model is based on a fuel-based (combustion-based) TPV system. The microburner is two-sided, with two planar emitters in thermal contact; a planar cell faces and is separated from each emitter by some distance.

The model includes three parts: thermal, optical, and electrical.

While the model is described elsewhere [8, 100], I have included some of the equations because the original equations imply some of the variables and do not explicitly include them.

The thermal model involves a heat balance equation:

$$Q_{comb} = Q_{exh} + Q_{side} + Q_{cond} + Q_{emit} \tag{D.1}$$

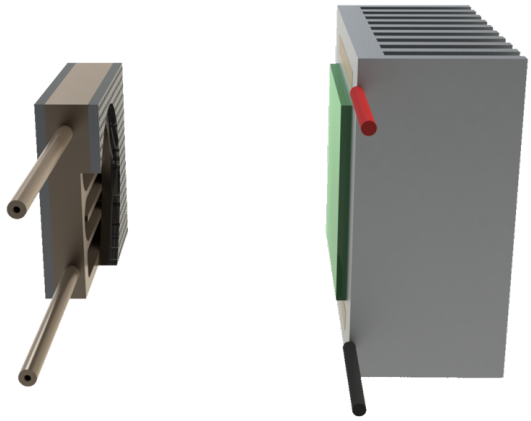

Figure D-1: TPV system schematic, image courtesy of Dr. Walker Chan. On the left side is a microburner with a photonic crystal emitter on each face; on the right side is a photovoltaic cell (mounted on a heat sink). Only one of the cells is shown (there would be one of the left side of the microburner as well).

where Q_{comb} is the heat of combustion in W, Q_{exh} is the exhaust heat loss, given by the sum of the heat absorbed by the combustion products (CO_2, H_2O) and any excess oxygen or nitrogen. In turn the heat absorbed by each gas is calculated by integrating the heat capacity $C_p(T)$ from the original ambient temperature T_a to the final hot side temperature T_b, and multiplying it by the flow rate of the gas species $\dot{n}_i$:

$$Q_{exh} = \sum_{i \in \text{products}} \dot{n}_i \int_{T_a}^{T_b} C_{p,i}(T) dT \tag{D.2}$$

Q_{side} is radiation from the sides of the microburner:

$$Q_{side} = A_{side} \pi \int_0^{\infty} \varepsilon_{side} e_b(\lambda, T_b) d\lambda \tag{D.3}$$

where $e_b(\lambda, T_b)$ comes from Planck's law:

$$e_b(\lambda, T_b) = \frac{2hc^2}{\lambda^5} \frac{1}{e^{hc/\lambda k_B T_b} - 1} \tag{D.4}$$

The factor of π comes from integrating over the solid angle:

$$\pi = \int_0^{\pi/2} \int_0^{2\pi} \sin\theta \cos\theta d\phi d\theta \tag{D.5}$$

Q_{cond} is the conduction heat loss from the tubes of the microburner:

$$Q_{cond} = \frac{k_t A_t (T_b - T_a)}{L_t} \tag{D.6}$$

where k_t is the conductivity of the tube material, A_t is the total cross sectional area of all tubes, and L_t is the length.

Q_{emit} is the net heat flux emitted by the emitter, but it is not necessarily described by by Planck's law and the emittance, because of reflections that can occur at the cell.

In the optical model, the emitter and the cell each form one end of a cavity. With detailed balance, the fluxes out of the emitter and cell can each be expressed as follows, in terms of the emitter area A_e, the view factor F, reflectivity of cell $\rho_c(\lambda)$, reflectivity of emitter $\rho_e(\lambda)$, emissivity of cell ε_e, wavelength λ, and temperature of hot side T_b:

$$q_{eo} = A_e \pi \int_0^{\infty} \frac{1}{1 - F^2 \rho_c(\lambda) \rho_e(\lambda)} \varepsilon_e(\lambda) e_b(\lambda, T_b) d\lambda \tag{D.7}$$

and

$$q_{co} = A_e \pi \int_0^{\infty} \frac{F \rho_c(\lambda)}{1 - F^2 \rho_c(\lambda) \rho_e(\lambda)} \varepsilon_e(\lambda) e_b(\lambda, T_b) d\lambda \tag{D.8}$$

Technically the emissivity of the emitter also depends on the hot side temperature ($\varepsilon_e(\lambda, T_b)$) but we use the room temperature reflectance and assume that the emittance remains the same at high temperatures ($\varepsilon_e(\lambda)$).

The net flux out of the emitter is

$$q_{eo} - q_{ei} = A_e \pi \int_0^{\infty} \frac{1 - F^2 \rho_c(\lambda)}{1 - F^2 \rho_c(\lambda) \rho_e(\lambda)} \varepsilon_e e_b(\lambda, T_b) d\lambda \tag{D.9}$$

$$q_{ci} = A_e \pi \int_0^\infty \frac{F}{1 - F^2 \rho_c(\lambda)\rho_e(\lambda)} \varepsilon_e(\lambda) e_b(\lambda, T_b) d\lambda \tag{D.10}$$

In the limit of $\rho_c(\lambda) = 0$, however

$$q_{eo} - q_{ei} = A_e \pi \int_0^\infty \varepsilon_e(\lambda) e_b(\lambda, T_b) d\lambda \tag{D.11}$$

$$q_{ci} = F A_e \pi \int_0^\infty \varepsilon_e(\lambda) e_b(\lambda, T_b) d\lambda \tag{D.12}$$

with $q_{ci} = F q_{eo}$.

D.2 System parameters of three TPV systems

Three systems are described in [3], including a system with Inconel, a conformal PhC, and a filled PhC.

The main differences among the systems are the emittance spectra, and the edge emissivity, the latter which leads to side losses. The side losses as well as out-of-band radiation losses are dominant loss mechanisms for the systems.

Parameters	Inconel	Conformal PhC	Filled PhC
Edge emissivity (on side)	0.80	0.55	0.15
In-band emittance ε_{in}	0.80	0.58	0.92
Out-of-band emittance ε_{out}	0.80	0.18	0.16

Table D.1: Emitter and edge emissivities for the three systems

The emittances are also plotted in Figure D-2.

Otherwise, the system parameters common to all three systems are as follows:

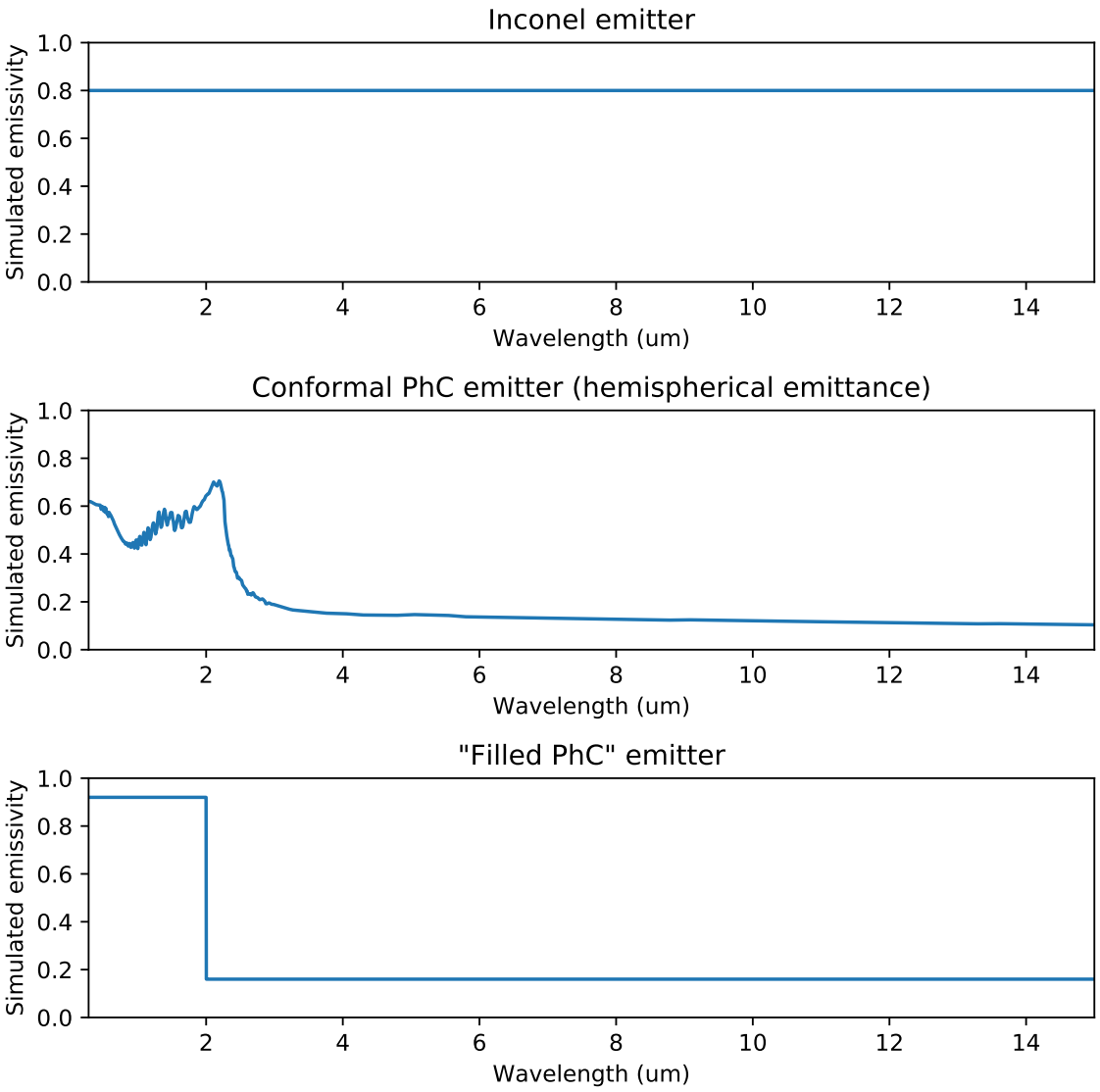

Figure D-2: Emittances of the three systems.

Oxygen source	Oxygen, with excess
Fuel type	Propane
Cutoff (µm)	2
Cell type	InGaAs
Copies of emitters and cells	2 each
Emitter dimensions (mm x mm)	20 x 20
Cell dimensions (mm x mm)	20 x 20
Emitter-cell separation (mm)	1
$\frac{k_t A_t}{L_t}$	0.0044487
A_{sides} (cm^2)	3.54

Table D.2: System parameters common to all three systems

I_0	n	R_s	R_{sh}	a	b	MIM
0	1.80213603596	0.0279098399174	208	np.log(5.99791552864e-05)	0	30

Table D.3: InGaAs cell parameters

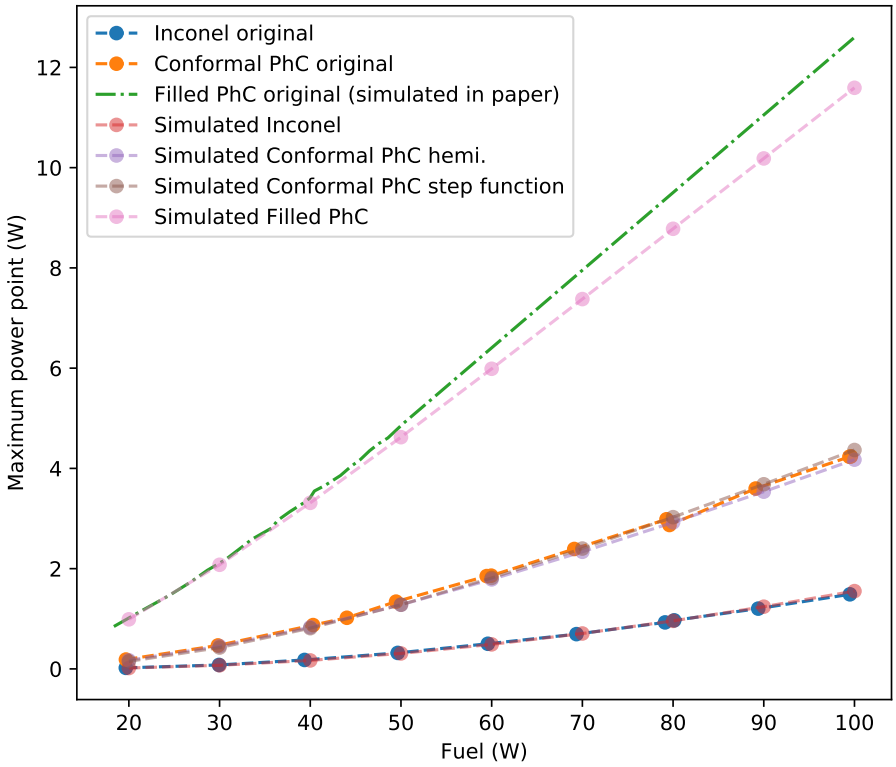

Figure D-3: Comparison of simulated systems with original results from *Energy Environ. Sci.* [3]. There is a good match for the Inconel and conformal PhC systems; however, my calculation underestimates electrical power output for the filled PhC system.

D.3 Reproducing *Energy Environ. Sci.* results using system modeling

As shown in Figure D-3, I was able to reproduce the results for the Inconel and conformal PhC systems; on the other hand, the powers I calculated for the filled PhC are lower than the ones simulated in the original paper.

Appendix E

Spin-on glass tests on silicon

I used spin-on glass as the planarization material on top of the photonic crystals. This appendix describes my initial tests on silicon as well as troubleshooting with spin-on glass.

While spin-on glass is reputed to be good for planarization, it forms SiO_2 whose quality is lower compared to that of thermal of CVD oxides [97] and whose etch rate would be different from that of ALD HfO_2.

The specific type of spin-on glass I used is based on silicates (a network of Si-O bonds), which is easier to use than other kinds of spin-on glass such as silsesquioxanes (an example being HSQ). I purchased Silicates 15A from Filmtronics. The active ingredient is silicic acid, ethyl ester (which is similar to tetraethylorthosilicate); other ingredients include the solvents isopropanol, acetone, ethanol, and water.

E.0.1 Mechanism of spin-on glass

The spin-on glass is a colloidal solution of three-dimensional Si-O-Si cage-like silicate particles (of about 1500Da) [101]. The spin-on glass film is prepared by spincoating, prebaking, and annealing, as shown in Table E.1.

1. In the presence of water, silicate species undergo hydrolysis particles that create Si-O-H groups required for condensation reactions (both water and alcohol condensation reactions) as shown in Figure E-1. The particles can crosslink with

	Spincoating Prebake Repeat for second coating	Spin at 3000rpm for 60s ∼80 °C for 60s 200 °C for 60s Spincoat and prebake again	
Option 1 Anneal, in air at 475 °C	1. Ramp 25-475 °C over 1.5 hour, 5 °C/ min 2. Hold at 475 °C for 1 hour 3. Cool down 475-25 °C for 2 hours, 3.75 °C min^{-1}	Option 2 Anneal, in air at 850 °C	1. Ramp 25-850 °C over 2.5 hour, 5 °C/ min 2. Hold at 850 °C for 20 minutes 3. Cool down 850-600 °C for 1 hour 3 min, 4 °C min^{-1} 4. Cool down 600-25 °C min^{-1} for 1.5 hour, 6 °C min^{-1}

Table E.1: Procedure for preparation of spin-on glass films

each other in the presence of water and other particles. Condensation produces particles of about 1500Da. There are still some remaining Si-O-H and Si-O-R groups that are the basis for further crosslinking [101, 102].

2. Prebaking removes the carrier solvents. The prebake is done in a sequence of increasing temperatures because this 1) allows the solvent to evaporate slowly and reduces excess thermal shock and 2) a low initial prebake can improve planarization and reduce film defects [103].
3. The prebake also opens Si-O bonds at the surface of the film; as the film cools, it takes moisture from the atmosphere and the Si-O bonds turn into Si-OH. The moisture is released during the anneal. [101, 102]
4. The anneal collapses the cage-like structure of the silicates and allows for crosslinking and densification. The overall structure becomes a network. During the anneal, the mainly three species degas: water and alcohol (byproduct of condensation). At temperatures above about 300 °C, thermal energy drives the crosslinking. [101, 102]
5. The anneal temperatures I tried were 475 °C and 850 °C; I was told to avoid the 500-800 °C because the film would absorb in this range, resulting in silanols [101].

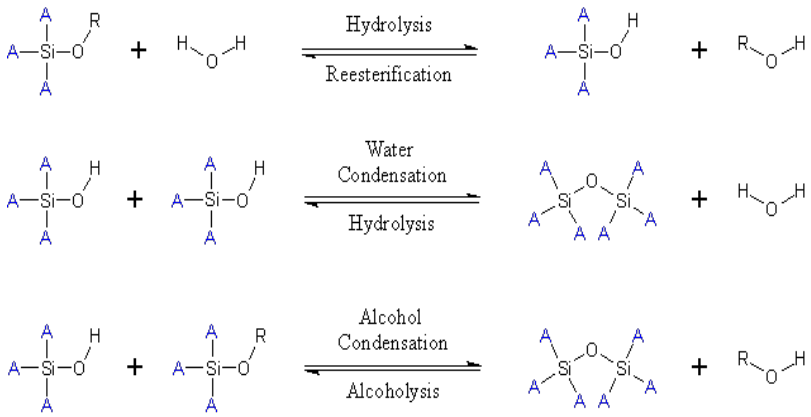

(a) Hydrolysis and condensation reactions of silicate species. [102]

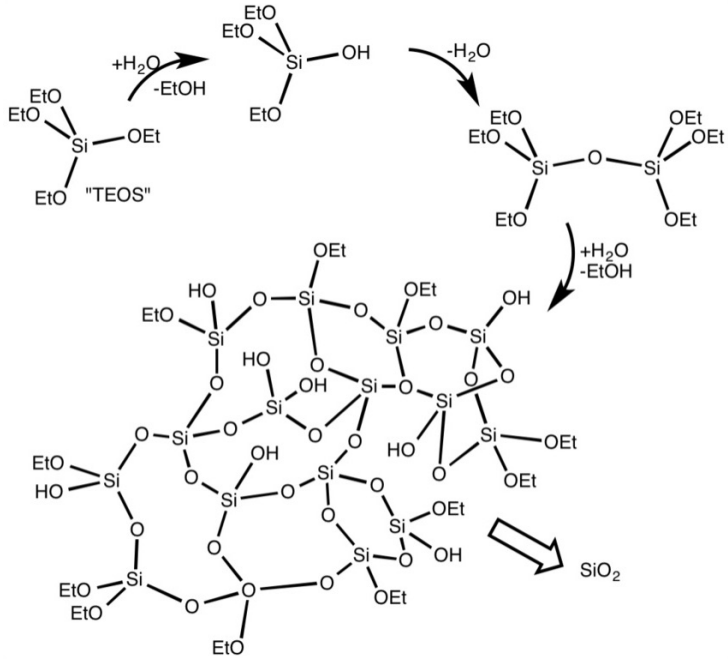

(b) Formation of silica particles [104]

Figure E-1: Mechanism for silicate-based spin-on glass

E.0.2 First coating of spin-on glass on silicon PhCs

While first SOG coatings on silicon PhCs had cracks throughout the film, both SOG films (one annealed at 475 °C and the other at 850 °C) showed good planarization. The cracks, shown in Figure E-2, seem to occur mostly in the centers of the PhC cavities. Some cross sections are shown in Figure E-3.

To evaluate how long the etch back should be, I did three measurements for each cross section image: 1) distance from top of SOG to HfO_2 trough 2) distance from top of SOG to HfO_2 crest 3) distance from top of SOG to top of silicon cavity. The averages are shown in Figure E-5 (and summarized in Table E.2). As expected, the 850 °C film is slightly thicker than 475 °C.

The etch back was an argon ion milling process, done by Dr. Bob Geil at University of North Carolina, Chapel Hill, under the following conditions: 500 W source, 150 W substrate, 200 sccm argon. For test etches of flat films on silicon, the etch time was 4 minutes. The etch rates for the flat films were: SOG annealed at 475 °C in air was 26.2 nm min^{-1}, SOG annealed at 850 °C in air was 21.3 nm min^{-1}, ALD HfO_2 was 9.8 nm min^{-1}.

After the etch back, the HfO_2 top surface of the PhC is, though not completely flat, is noticeably flatter. The average HfO_2 crest to trough distance decreased from 240 nm to 90.6 nm for the 475 °C anneal sample, from 234 nm to 85.3 nm for the 850 °C anneal sample. Figure E-6 shows comparisons cross sections before and after argon ion milling, while Figure E-4 shows the PhC top surfaces.

Measurements before and after argon ion milling, as well as the calculated etch rates for the Si PhC are summarized in Table E.2. The etch rates are calculated using one equation for the crest and one equation for the trough (the two unknowns are the etch rates of SOG and HfO_2).

Most notably, the calculated etch rate of HfO_2 on the Si PhC at around 19 nm min^{-1} was apparently twice the etch rate of flat HfO_2 on Si (9.8 nm min^{-1}). The calculated SOG etch rate on the Si PhC is also higher than that on flat Si, but the increase is not as dramatic.

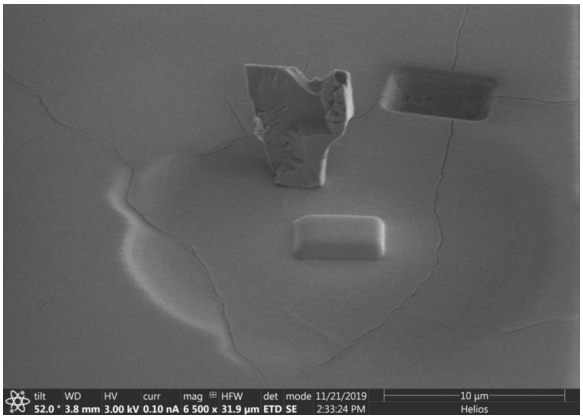

(a) The SOG film (475 °C anneal) shows cracks. Also shown: dust, FIB-milled hole, platinum rectangle. 52° tilt.

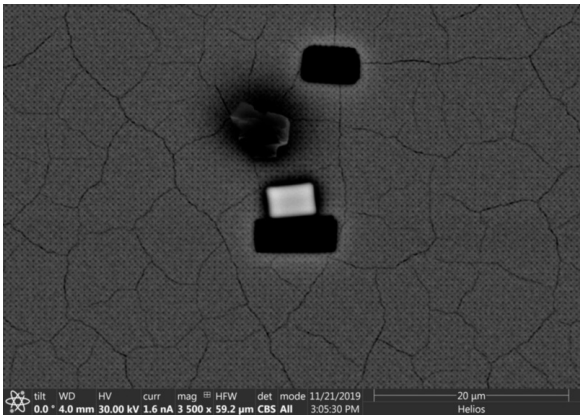

(b) With CBS detector, underlying PhC structure and SOG film cracks are visible. 0° tilt. 475 °C anneal.

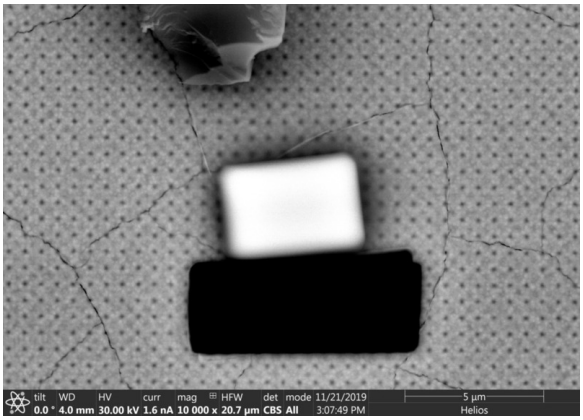

(c) Closeup shows that cracks mainly go through cavity centers (as opposed to outside of cavities). CBS detector, 0° tilt, 475 °C anneal.

Figure E-2: First SOG coating on silicon PhCs

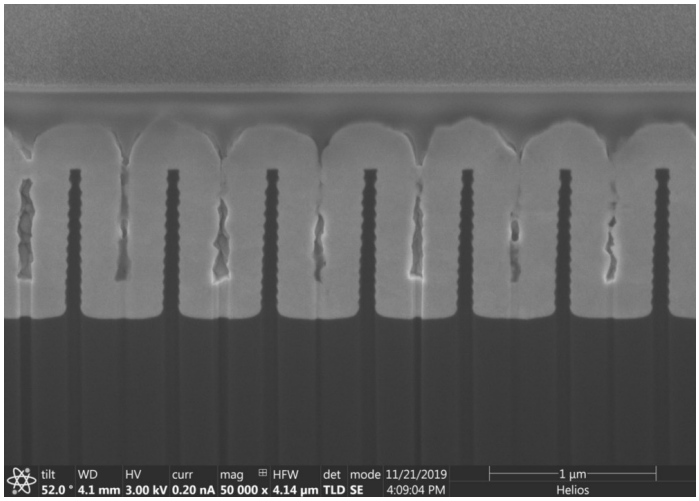

(a) SOG film annealed at 475 °C shows good planarization. From top to bottom: platinum, platinum, spin-on glass, HfO_2, silicon.

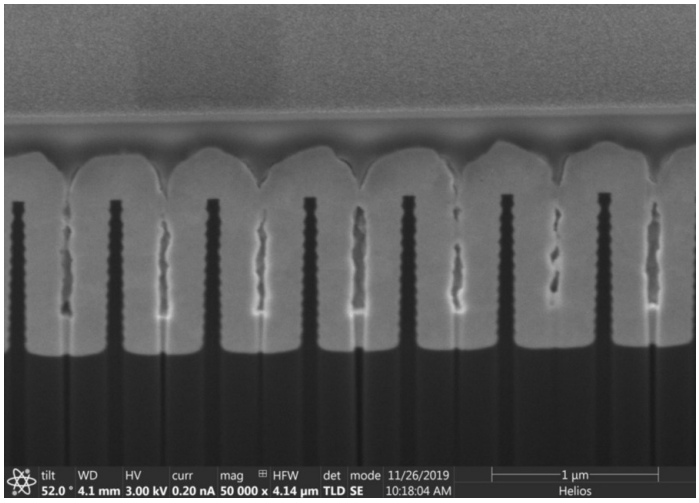

(b) SOG film annealed at 850 °C shows good planarization. From top to bottom: platinum, platinum, spin-on glass, HfO_2, silicon.

Figure E-3: Cross sections of first coating of SOG on silicon PhCs, annealed at 475 °C and 850 °C.

		475 °C SOG	850 °C SOG
SOG film	Average from top of SOG to top of silicon cavity	577 nm	577 nm
	Average from top of SOG to HfO_2 crest	230 nm	210 nm
	Average from top of SOG to HfO_2 trough	470 nm	444 nm
Argon ion milling test etches	Etch rate of flat film on Si	26.2 nm min^{-1}	21.3 nm min^{-1}
	Etch time for silicon PhC	470 / 26.2 ∼17.5 min	444 / 21.3 ∼20.5 min
	Flat ALD HfO_2 on Si etch rate = 9.8 nm min^{-1}	-	-
Post-milling FIB images	Average distance from top of Si cavity to HfO_2 crest	162 nm	110 nm
	Average distance from HfO_2 crest to trough	90.6 nm	85.3 nm
	Average distance from top of Si cavity to HfO_2 trough	71.0 nm	110 - 85.3 = 24.7 nm
Etched amounts	Etch time	17.5 min	20.5 min
	Crest area SOG	230 nm	210 nm
	Crest area HfO_2	577 - 230 - 162 = 185 nm	577 - 210 - 110 = 257 nm
	Trough area SOG	470 nm	444 nm
	Trough area HfO_2	577 - 470 - 71 = 36 nm	577 - 444 - 24.7 = 108.3 nm
Calculated etch rates	SOG	30.17 nm min^{-1}	29.97 nm min^{-1}
	HfO_2	18.73 nm min^{-1}	19.05 nm min^{-1}
	Ratio of HfO_2 to SOG etch rate	0.621	0.635

Table E.2: Measurements of first coating of SOG, before and after argon ion milling

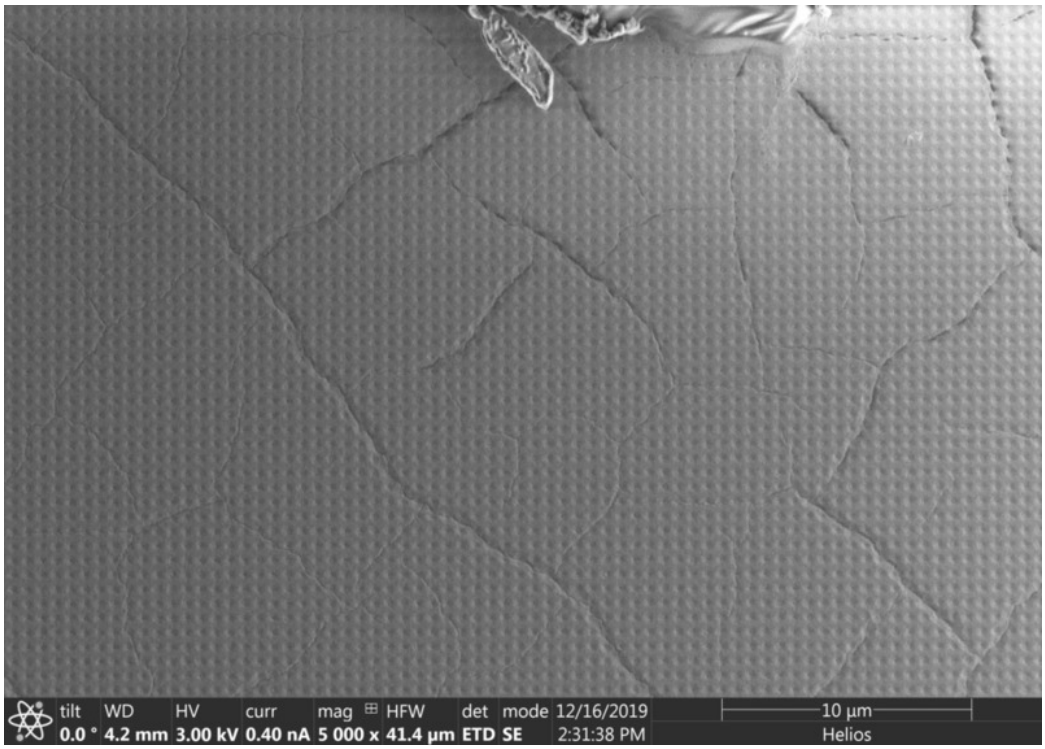

(a) 475 °C anneal sample

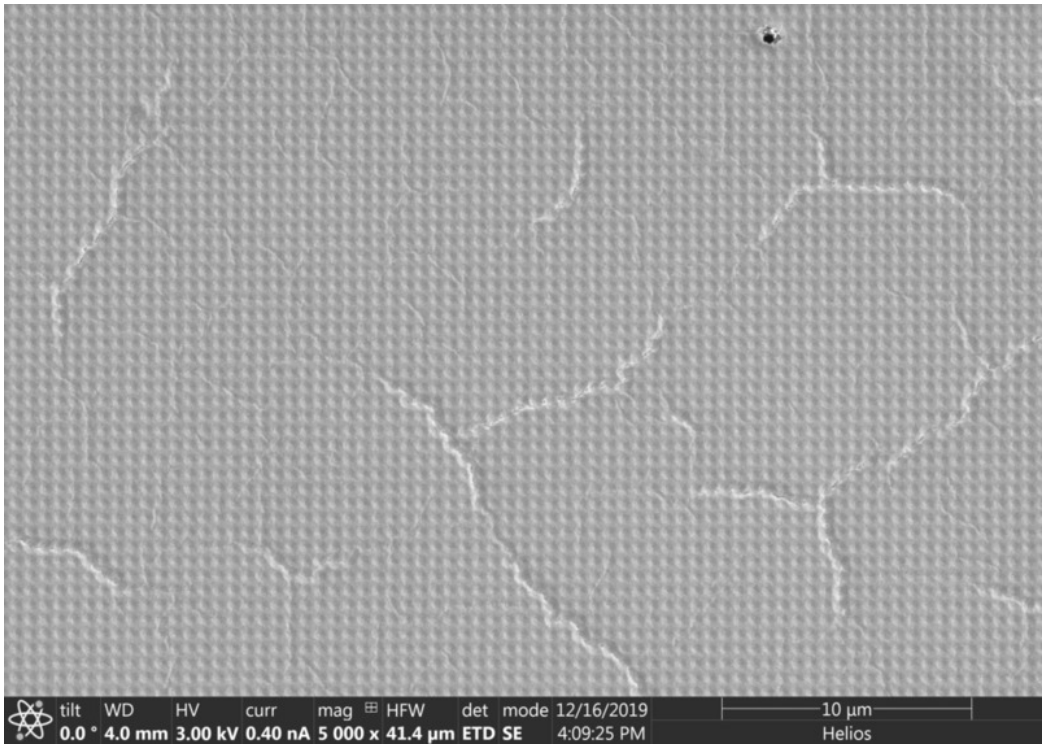

(b) 850 °C anneal sample

Figure E-4: SEM of PhC top surfaces after etch back of first SOG coating shows the top surfaces are not yet flat.

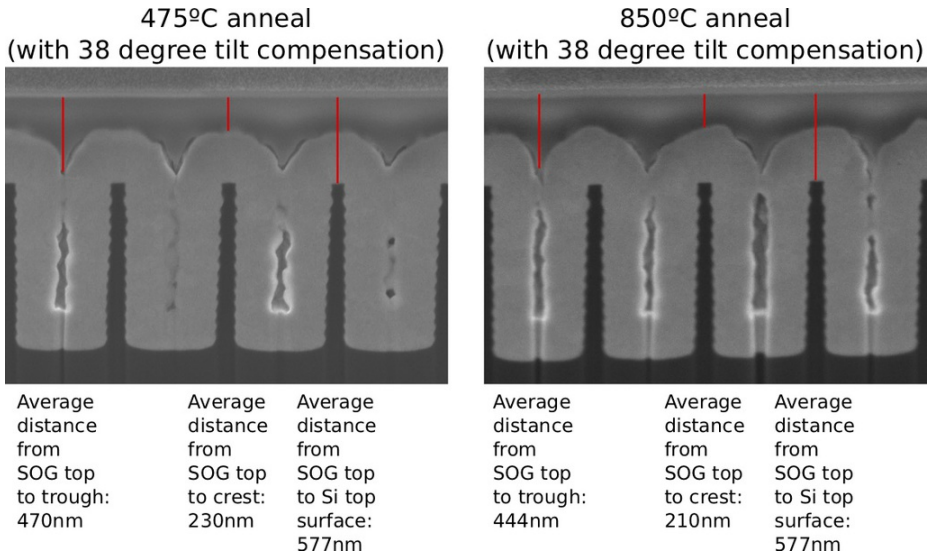

(a)

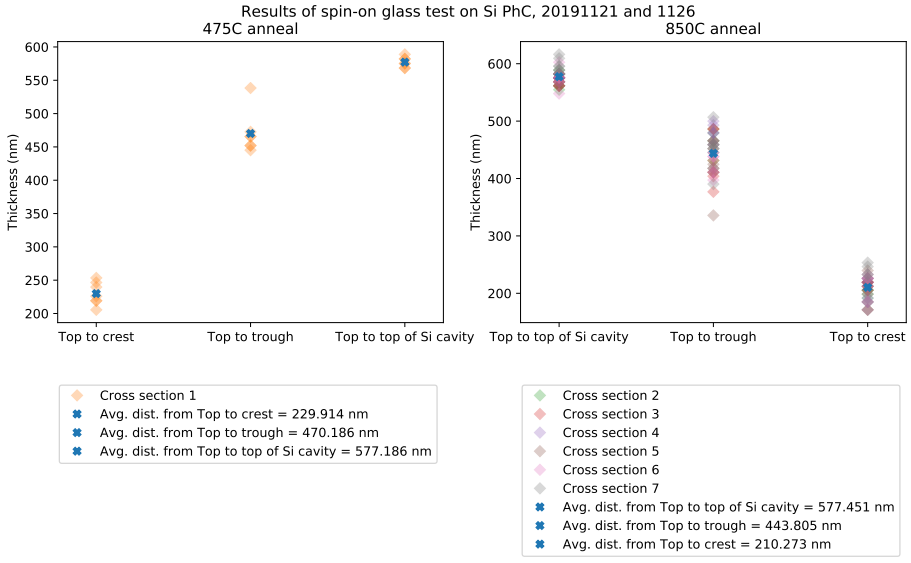

(b)

Figure E-5: Measurements of cross sections of first coating of SOG on silicon PhCs, annealed at 475 °C and 850 °C.

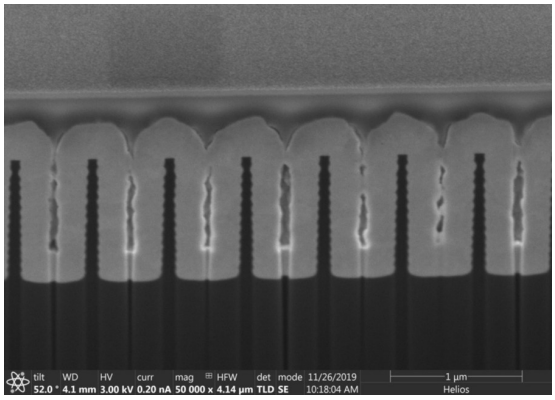

(a) SOG on silicon PhC annealed at 475 °C, before argon milling.

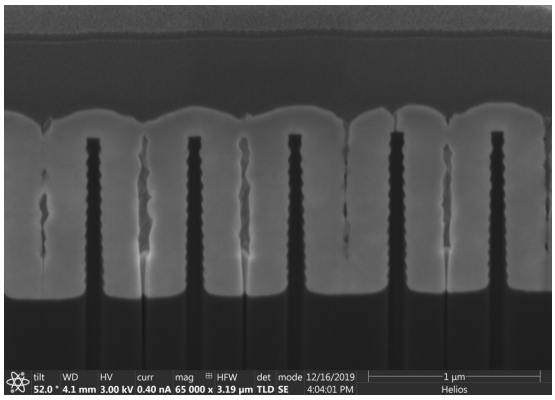

(b) 475 °C sample after argon milling.

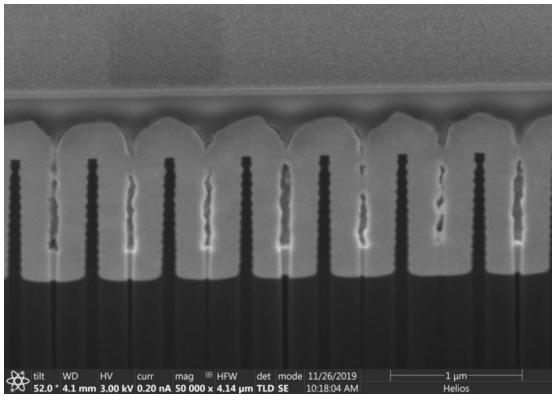

(c) SOG on silicon PhC annealed at 850 °C, before argon milling.

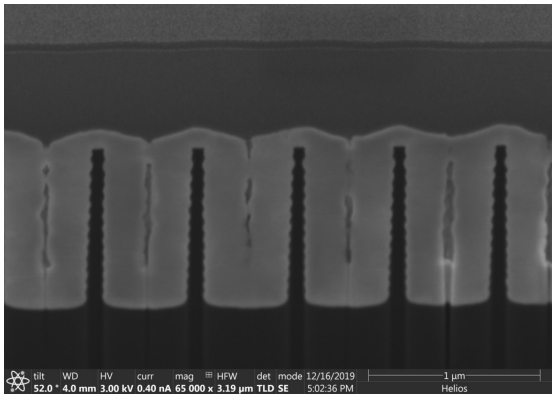

(d) 850 °C sample after argon milling.

Figure E-6: Comparisons of cross sections before and after argon ion milling the first SOG coating.

The inconsistency in etch rates may be because there is variation across the sample in thickness of HfO_2 and SOG.

E.0.3 Second coating of spin-on glass on silicon PhCs

Because the planarization and etch back process can be iterated, I did a second coating, which also planarized well, as shown in Figure E-8. I calculated the etch times using the same etch rates as before (flat films on Si), and slightly shortened the etch time (15.3min to 15min and 14.4min to 14min).

FIB cross sections, taken after argon ion milling the second SOG coating, shows that the samples were not etched for long enough. While some cross sections show a

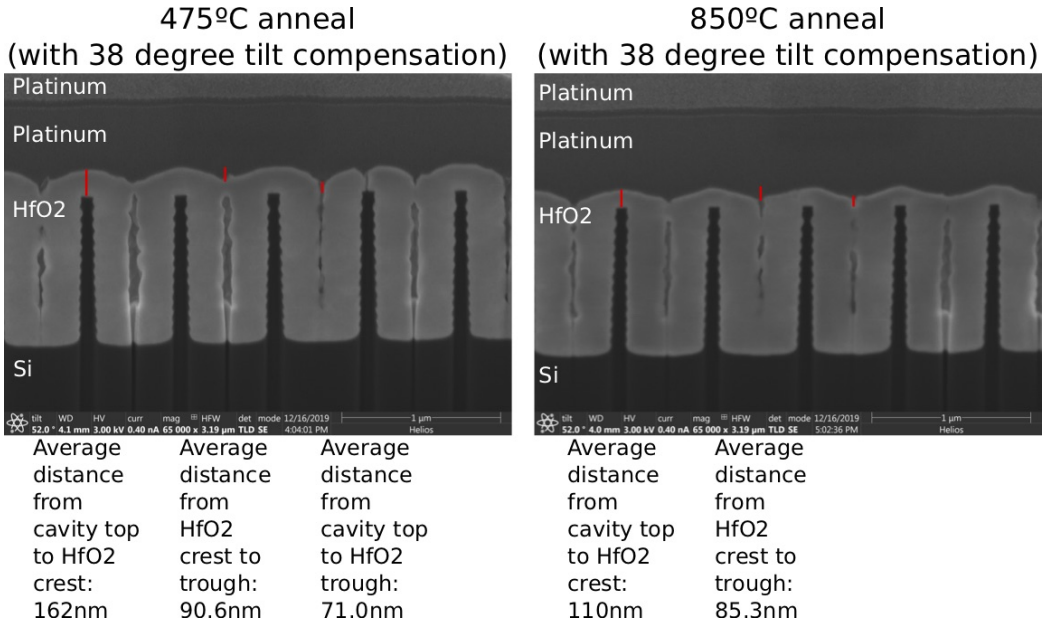

(a)

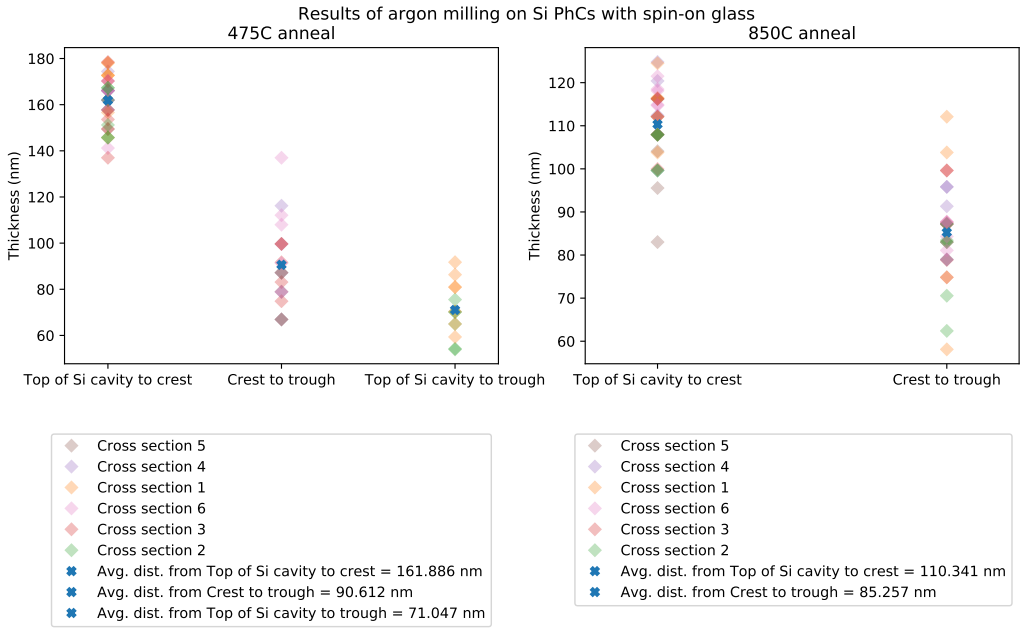

(b)

Figure E-7: Measurements of cross sections after argon ion milling on first coating of SOG on silicon PhCs, annealed at 475 °C and 850 °C.

that the HfO_2 crest area is slightly flattened (Figure E-9), residual SOG is also visible (Figure E-10). On the whole, it appeared that the very little to no HfO_2 was etched.

Because the samples were not etched for long enough, overall there was no decrease in Δz HfO_2 crest to height difference, as shown in Table E.4. The "increase" in Δz may be due to variation across the PhC piece: in other words, some areas of the PhC piece may have cross sections with thicker HfO_2 tops.

The measurements before depositing the second SOG film and after argon milling are summarized in Table E.3).

I was unable to do a proper calculation of etch rates based on these measurements, but this also could be due to variation across the PhC piece. In particular, when I calculated the SOG etch rate using the measurement in the trough, I got an etch rate that was inconsistent with the measurement in the crest: to etch all the SOG in the crest would have taken longer than the actual etch time. I did not calculate the HfO_2 etch rate.

E.1 Spin-on glass troubleshooting on silicon

Before depositing SOG on tantalum PhCs, I had to troubleshoot some issues, including SOG spincoating issues and checking SOG compatibility with a vacuum furnace anneal.

E.1.1 Adhesion issues while spincoating under high humidity

The spincoating issue was an adhesion issue for the second coating. While the first SOG coating looked to be mostly clear of defects, the second coating spun nonuniformly, creating a film that appeared to be full of bubbles (Figure reffig:spincoat-problems1). I used 2cm x 2cm blank silicon pieces.

The culprit was the cleanroom humidity, which at 44% reading (perhaps it was not well-calibrated) was apparently too high, despite the manufacturer's catalog saying 44% was fine. The temperature was 64 Fahrenheit.

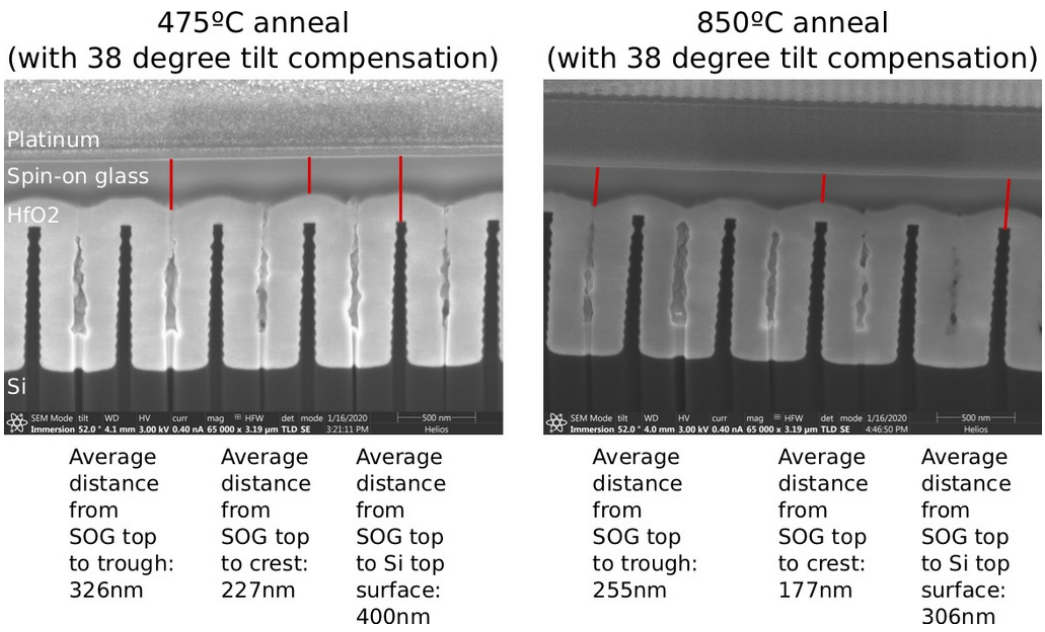

(a)

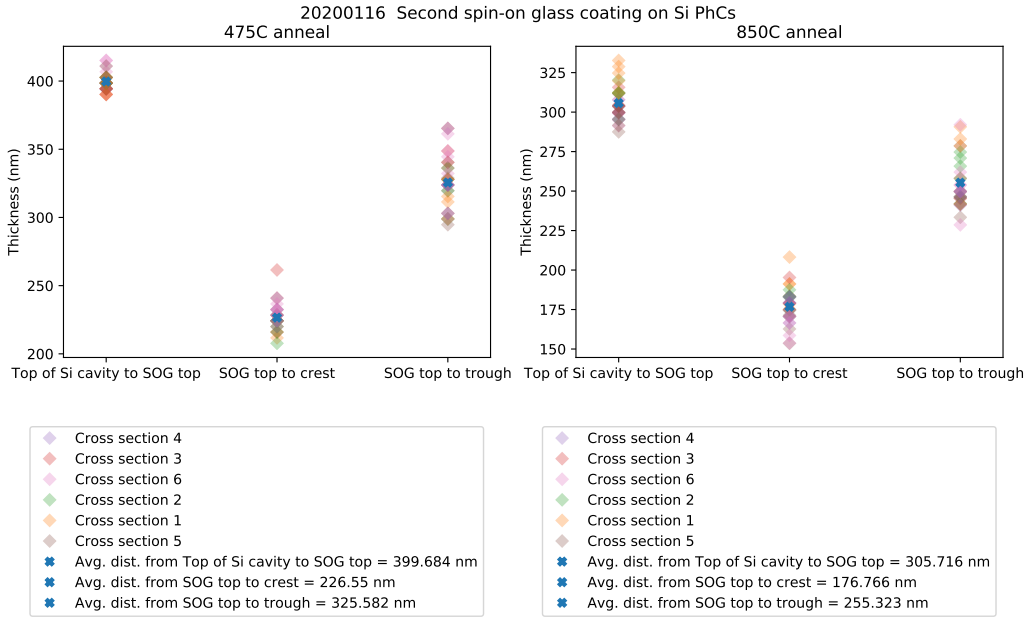

(b)

Figure E-8: Second SOG coating planarized well both the 475 °C and 850 °C anneal samples.

		475 °C SOG	850 °C SOG
SOG	Average from top of SOG to top of silicon cavity	400 nm	306 nm
	Average from top of SOG to HfO_2 crest	227 nm	177 nm
	Average from top of SOG to HfO_2 trough	326 nm	255 nm
Argon ion milling test etches	Etch rate of flat film on Si (test etches were not done, so assuming same as Table E.2)	26.2 nm min^{-1}	21.3 nm min^{-1}
	Etch time for silicon PhC	400 / 26.2 = 15.3min, did 15min	306 / 21.3 = 14.4 min, did 14min
	Flat ALD HfO_2 on Si etch rate = 9.8 nm min^{-1}	-	-
Post-milling FIB images	Average distance from top of Si cavity to HfO_2 crest	146.9 nm	104.1 nm
	Average distance from HfO_2 crest to trough	103.4 nm	86.3 nm
	Average distance from top of Si cavity to HfO_2 trough	146.9-103.4=43.5 nm	104.1-86.3 = 17.8 nm
Etched amounts	Etch time	15 min	14 min
	Crest area SOG	227 nm	177 nm
	Crest area HfO_2	400 - 227 - 147 = 26 nm	306 - 177 - 104.1 = 24.9 nm
	Trough area SOG (assuming Δz corresponds to remaining SOG)	326 - 103.4 = 222.6 nm	255 - 86.3 = 168.7 nm
	Trough area HfO_2	0 nm	0 nm
Calculated etch rates: SOG only	Amount of SOG etched in crest $\sim$ amount of SOG etched in trough, meaning that almost no HfO_2 etched	14.84 - 15.13 nm min^{-1}	12.05 - 12.64 nm min^{-1}

Table E.3: Measurements of second coating of SOG, before and after argon ion milling

	Average for 475 °C SOG	Average for 850 °C SOG
After ALD, before SOG	470-230 = 240 nm	444-210 = 234 nm
After first SOG coating + etch back	90.6 nm	85.3 nm
After second SOG coating + etch back	103.4 nm	86.3 nm

Table E.4: Progression of HfO_2 crest to trough distance, or Δz, on silicon PhCs

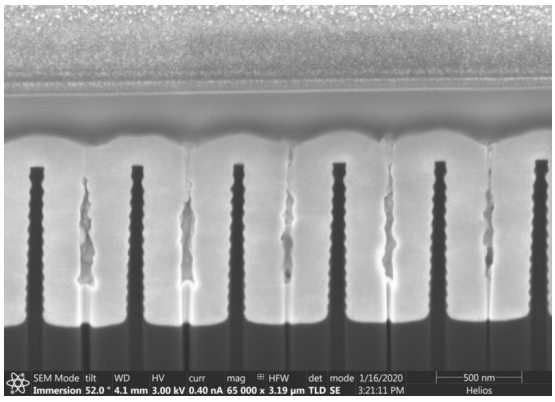

(a) SOG on silicon PhC annealed at 475 °C, before argon milling.

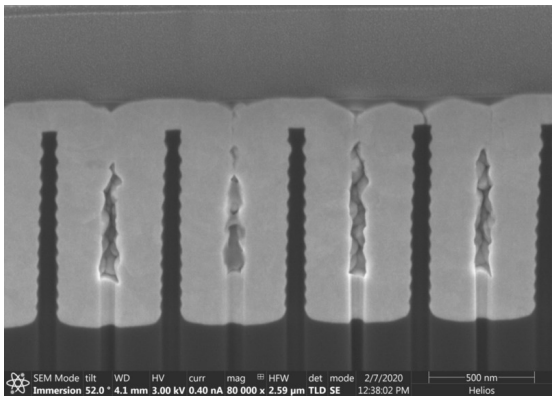

(b) 475 °C sample after argon milling.

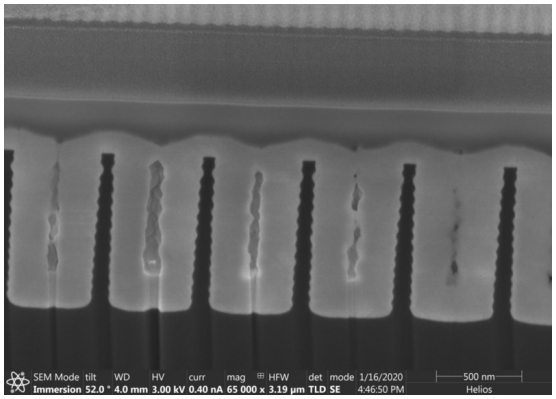

(c) SOG on silicon PhC annealed at 850 °C, before argon milling.

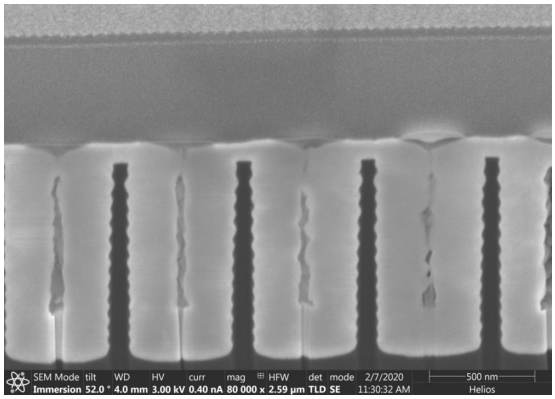

(d) 850 °C sample after argon milling.

Figure E-9: Comparisons of cross sections before and after argon ion milling the second SOG coating. Both samples post argon ion milling show residual spin-on glass.

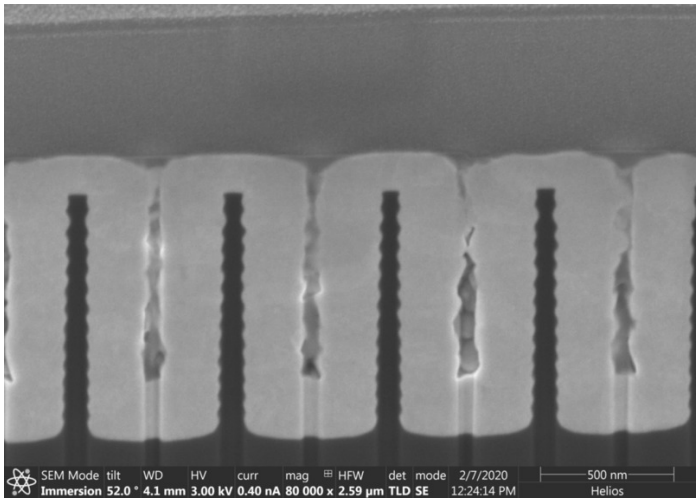

(a) 475 °C anneal sample

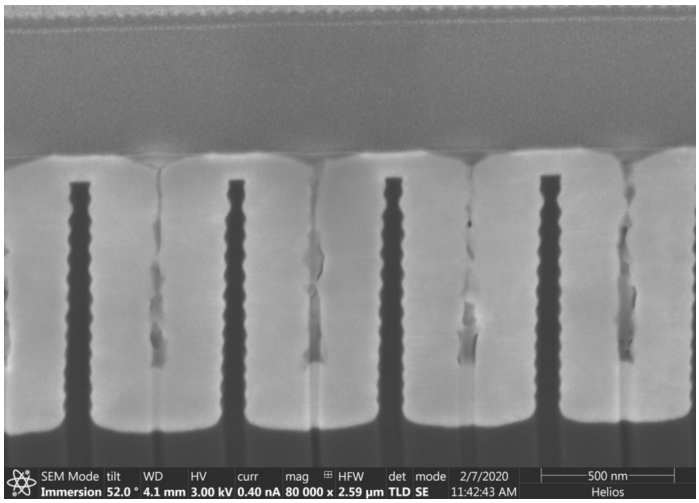

(b) 850 °C anneal sample

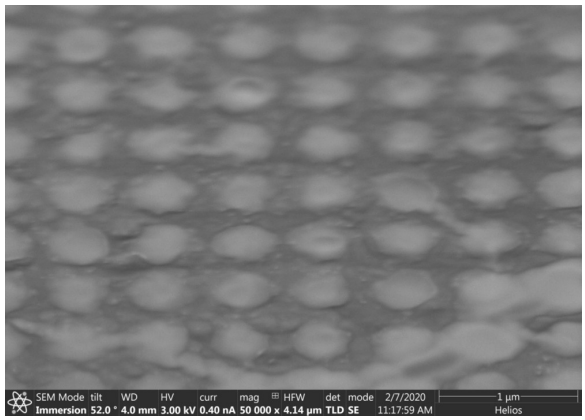

(c) Top surface of 850 °C anneal sample, 52° tilt

Figure E-10: Residual SOG is visible in both the cross sections and the top surface.

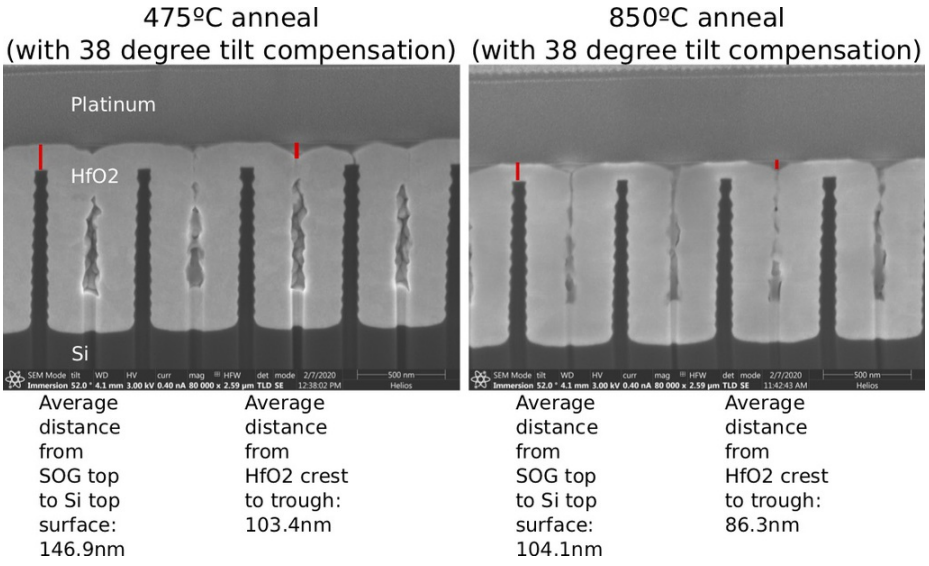

(a)

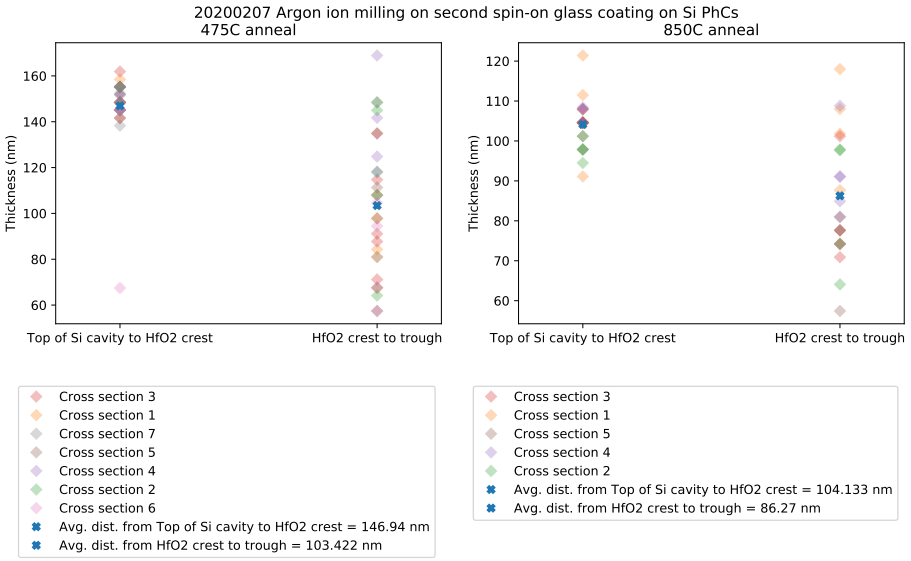

(b)

Figure E-11: Measurements of cross sections after argon ion milling the second coating of SOG on silicon PhCs, annealed at 475 °C and 850 °C.

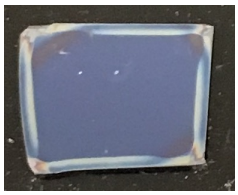

(a) Initial spin-coating tests showed no apparent problems.

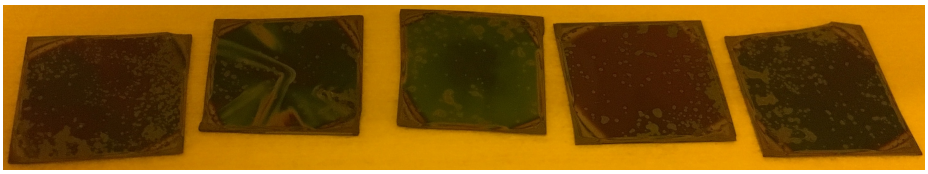

(b) However, at a different time, all of the second coatings on small blank 2cm x 2cm silicon pieces looked abysmal.

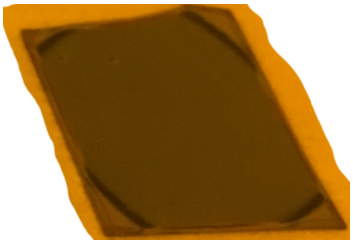

(c) A single SOG coating looked to be without any defects.

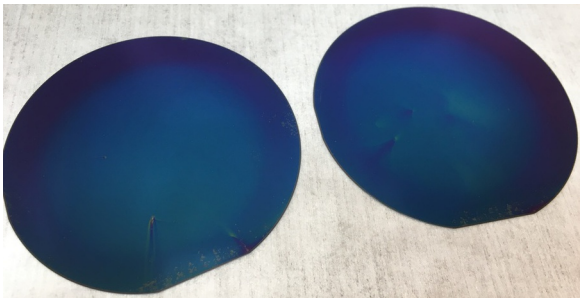

(d) Two SOG coatings on 3-inch blank silicon wafers looked fine.

Figure E-12: SOG spincoating problems

Although I tried a number of methods[101, 103] to try to create a “favorable environment" for spincoating in the spinner bowl none of the methods yielded good spincoating results on days with “high" humidity. A favorable environment for spincoating was one that would keep the vapors from the film from drying out as quickly. The methods included the following

- No descum to clean the silicon pieces, in case the adhesion issue begins in the first layer but is not apparent until the second layer
- Longer (90s) or shorter (30s) prebake times (normal = 60s)
- Acetone or isopropanol in the spin bowl to “wet" it, where isopropanol is less aggressive than acetone
- A fresh pipette before each spincoating, to avoid particulate buildup in the pipette
- The spin exhaust was covered, to minimize drying
- Reduced dispense volume
- Lower acceleration
- Isopropanol rinse of sample before second coating
- Some combinations of the aforementioned

On two days with 44% humidity, none of the SOG coatings looked good (Figure E-13), while on a day with 33% humidity all SOG coatings looked fine (Figure E-14), which supports the conclusion that SOG should be spun on low-humidity days.

E.1.2 SOG compatibility with vacuum furnace anneal

I did a thermogravimetric analysis-mass spectrometry (TGA-MS) to investigate what species offgas when the spin-on glass is annealed, to ensure that annealing SOG would not contaminate the vacuum furnace. I ran a 475 °C anneal as follows: ramp 5 °C min^{-1} to 475 °C, hold at 475 °C for 60 minutes, then cool down at 3.75 °C min^{-1}.

The three likely species that offgas, once the sample is prebaked, are:

1. Water

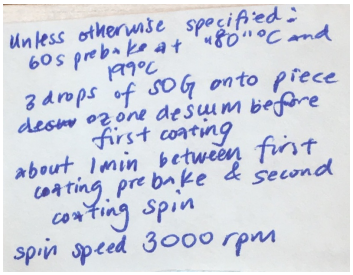

(a) Conditions for spincoating

(b)

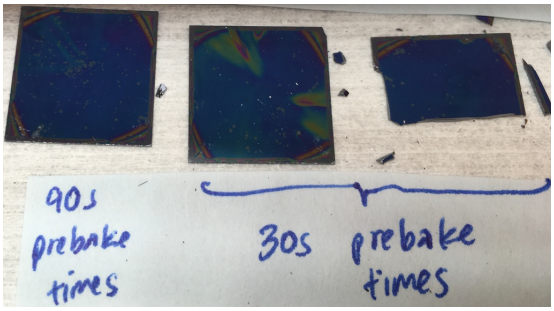

(c)

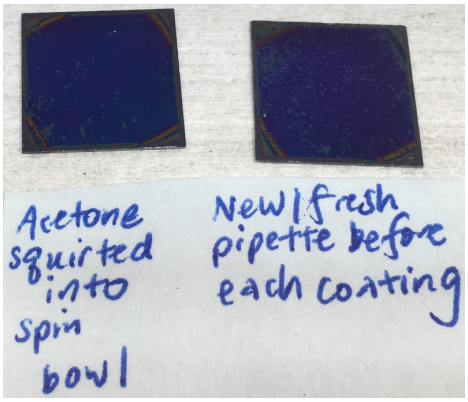

(d)

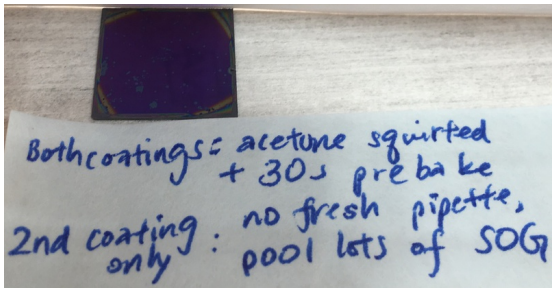

(e)

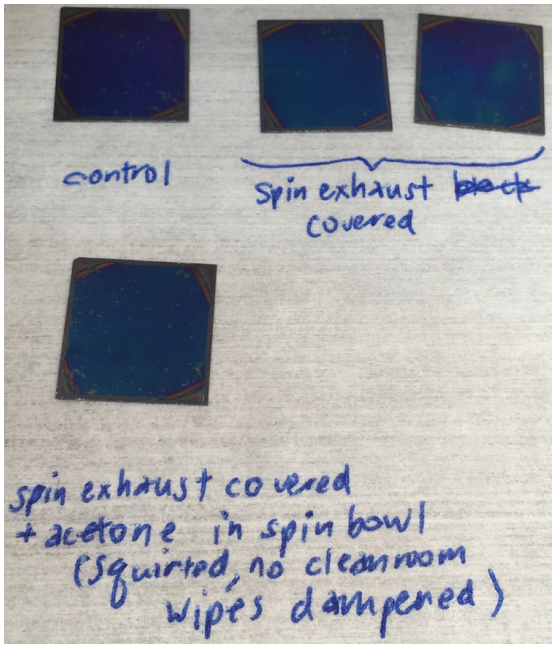

(f)

Figure E-13: a-e) Day 1, f) Day 2, both with 44% humidity, 64 Fahrenheit temperature

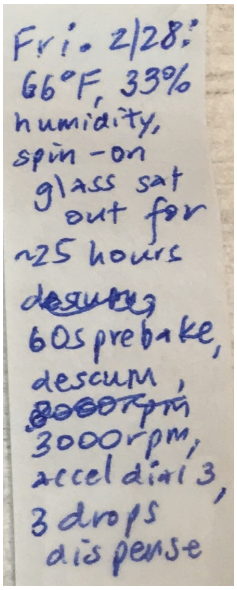

(a) Conditions for spincoating

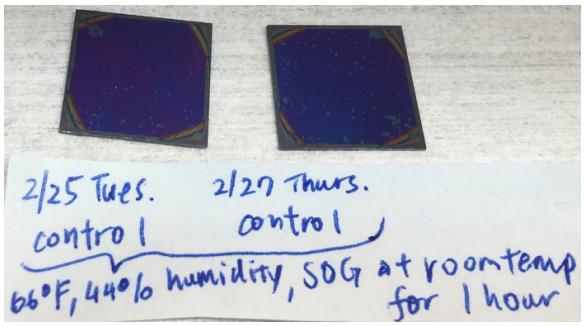

(b) Comparison to controls from Day 1 and 2

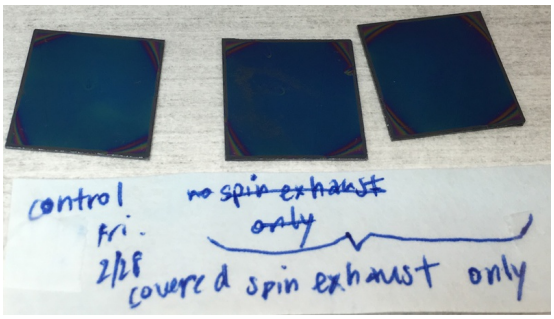

(c)

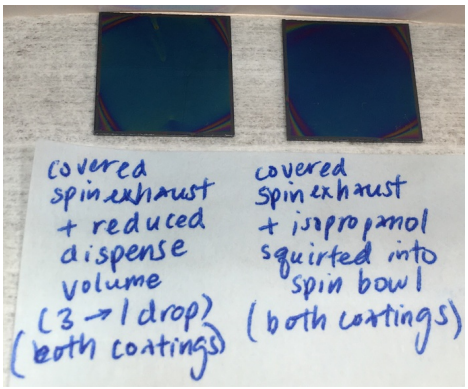

(d)

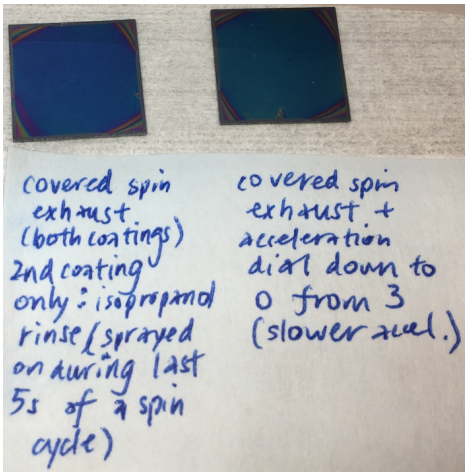

(e)

Figure E-14: Day 3 with 33% humidity, 66 Fahrenheit temperature

- Moisture that adhered to the sample as it cooled after prebake
- Byproduct of water condensation

2. Alcohol, a byproduct of alcohol condensation
3. Small silicate species of size on the order of hundreds of Da (whereas the silicate particles in the SOG are supposed to be about 1500Da) [101]

I looked up on the NIST database the mass spectra of the five components of SOG: isopropanol, acetone, ethanol, water, and silicic acid, ethyl ester [105]. Instead of silicic acid, ethyl ester, I used the spectrum of tetraethyl silicate because I could not find one for silicic acid, ethyl ester.

I did two runs:

1. Measured 1-50amu range with medium speed scan (0.5 seconds per mass) (Figures E-15, E-16)
    - Most of the peaks for water and the solvents fall under 50amu (and entirely under 60amu)
    - First dried the SOG at 80 °C in an vacuum oven (20-25 inches Hg) for 30 minutes
2. Measured 60-210amu on the slow scan (1 second per mass) setting for high sensitivity (Figure E-17)
    - This was to look for any larger fragments corresponding to
    - First dried the SOG at 80 °C in an vacuum oven (20-25 inches Hg) for 30 minutes

Figures E-15 and E-16 show respectively the TGA and MS data for the first run. Figure E-17 shows the second run; the MS did not show any fragments of size 60-210amu.

To contextualize the MS results for the first run (1-50amu), I compared the MS data with the NIST spectra of the five components, in two ways: 1) in Figure E-18, I plotted the spectrum of each of the five components and colored in blue the peaks that corresponded to those detected in the MS 2) in Figure E-19, I compared

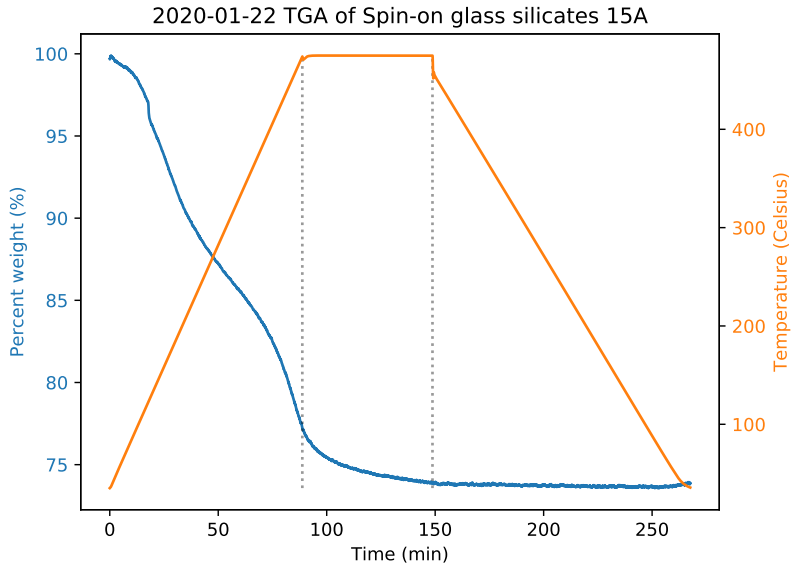

Figure E-15: Thermogravimetric analysis (TGA) results of the first TGA run.

the measured mass spectrum with the stacked spectra of the five components, which shows which measured peaks correspond to those of the five components. Figure E-18 shows that the several of high-signal peaks of the five components were not detected in the MS. In Figure E-19, there are a number of unaccounted-for peaks, but these could be attributed to noise or to small silicate fragments.

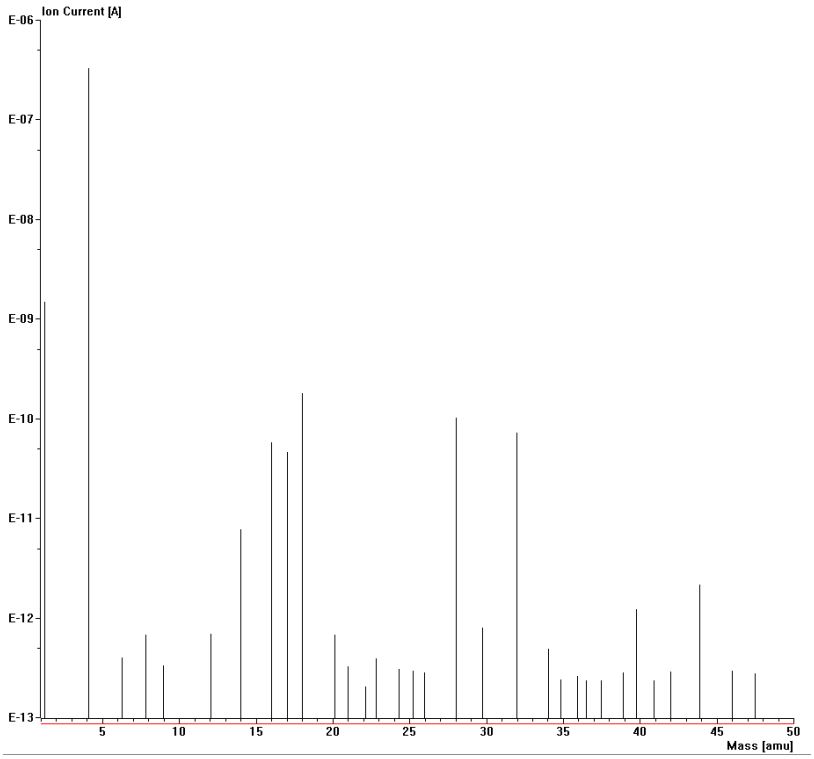

(a) Ion current (A) reading for masses 1-50amu

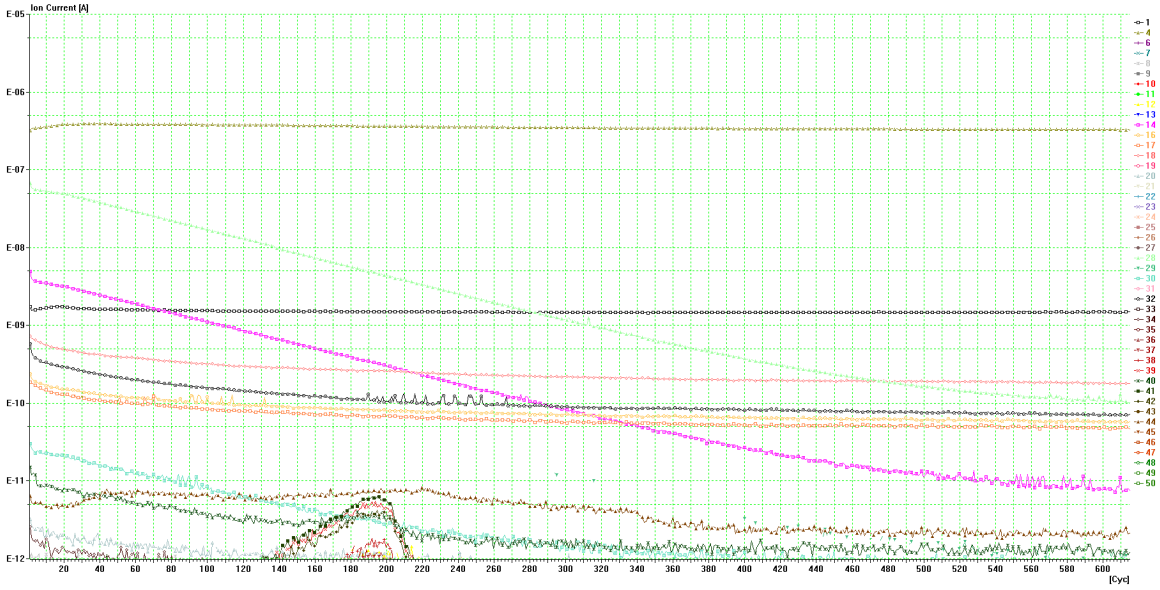

(b) Mass traces as a function of time (in cycles, where one cycle is 50 amu x 0.5 seconds)

Figure E-16: Results of first TGA-MS run

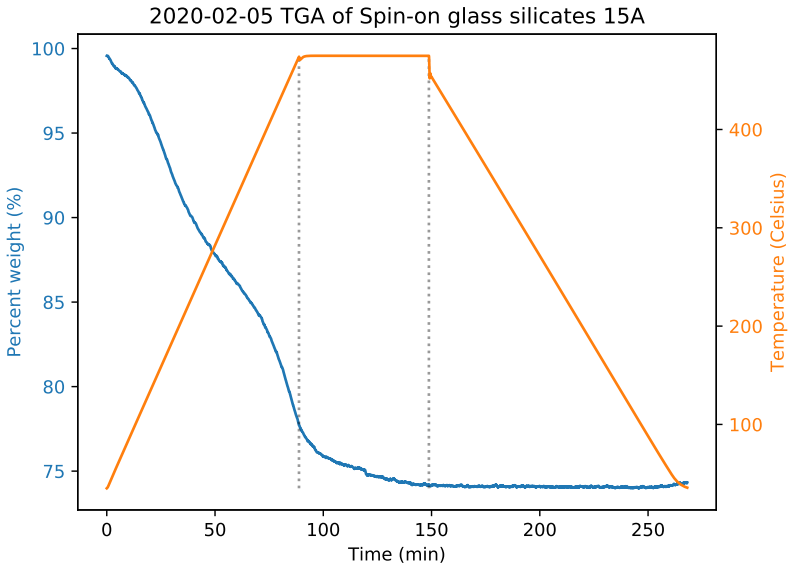

(a) TGA results for second run

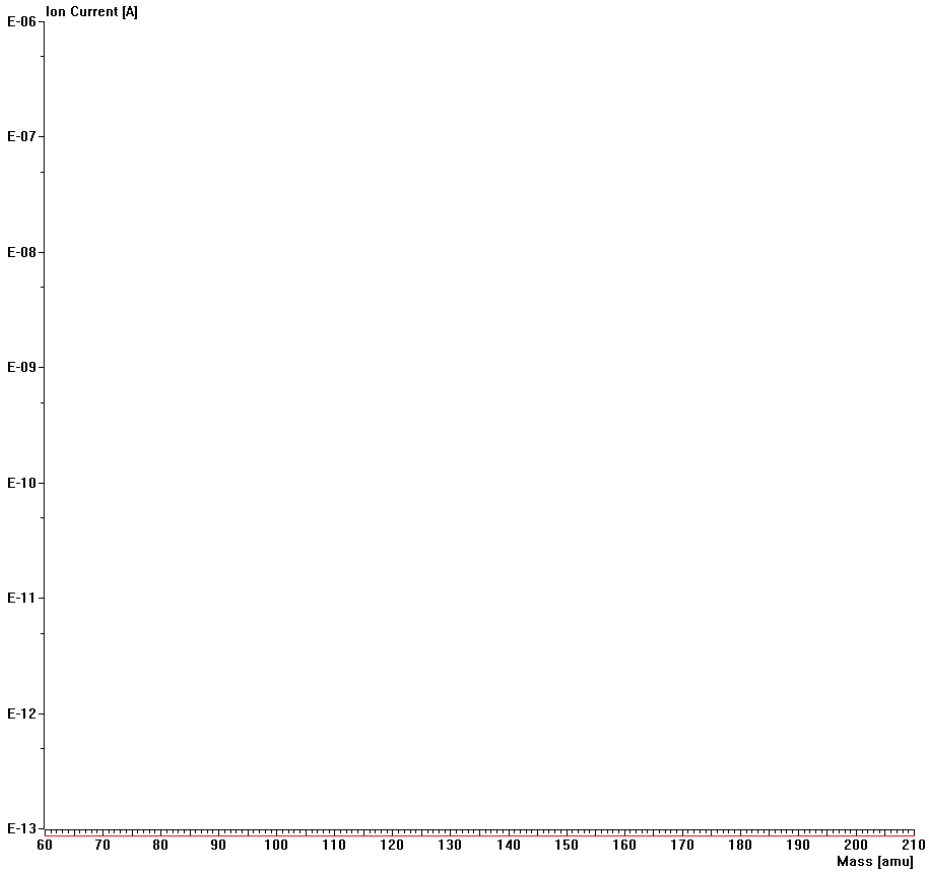

(b) No fragments in the size range 60-210amu were detected.

Figure E-17: Thermogravimetric analysis (TGA) and MS results of the second TGA-MS run.

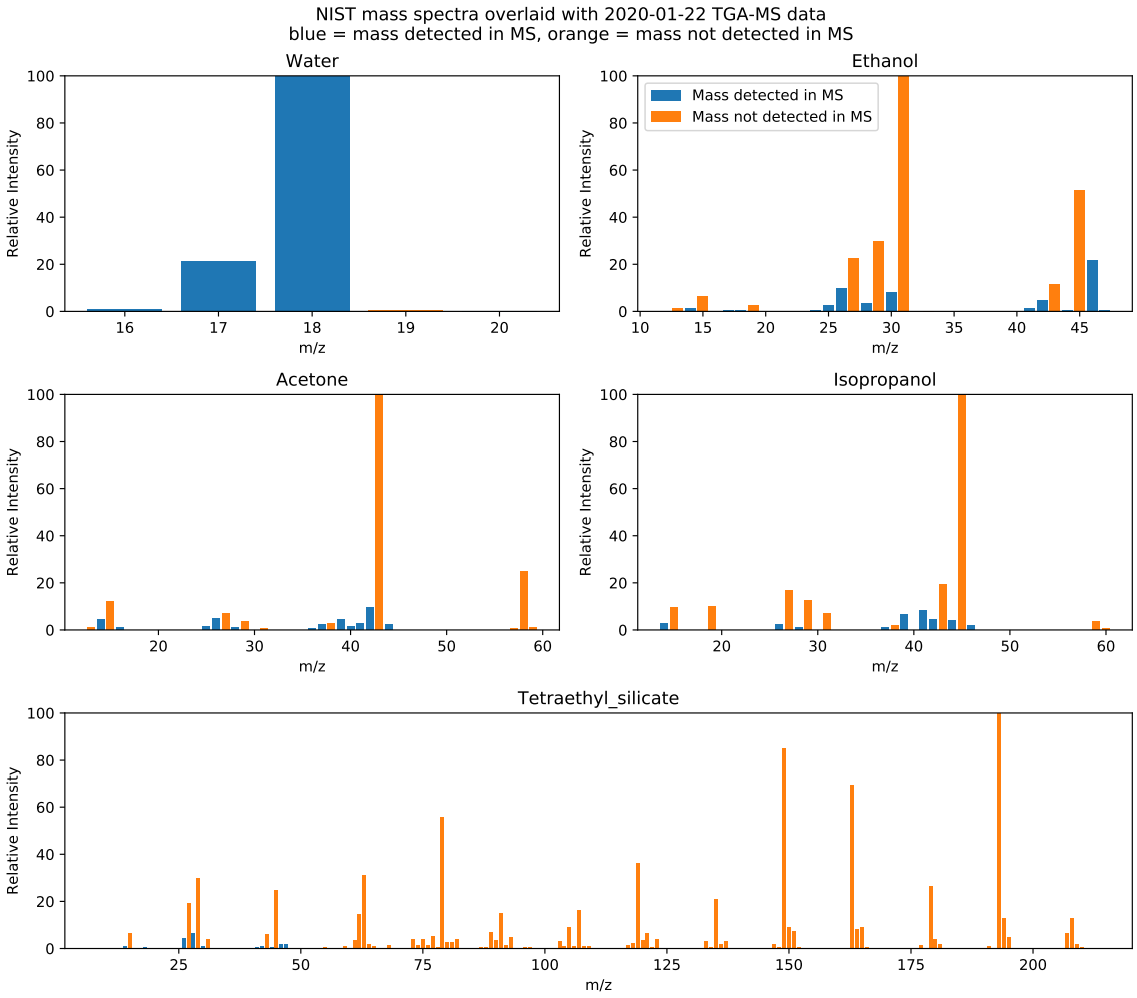

Figure E-18: Comparison of NIST spectra of SOG components with MS data (1-50amu): blue shows peaks detected in MS, while orange shows peaks that were not detected in MS.

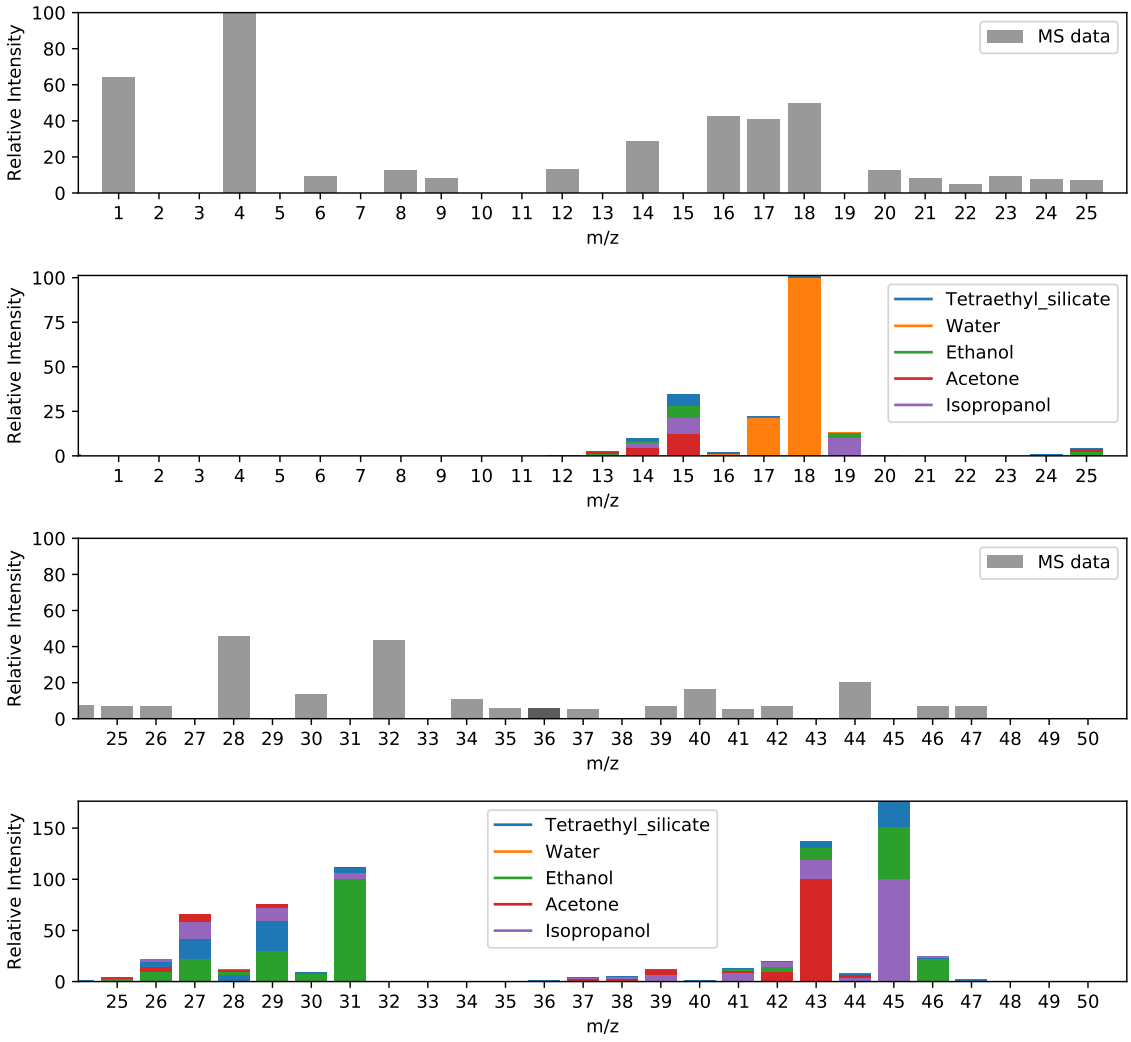

Figure E-19: Comparison of peaks detected in MS (gray, 1-50amu) with NIST spectra of SOG components. The peaks with mass 1 amu and 4 amu can be attributed to hydrogen and helium respectively.

Appendix F

Investigating alternate methods for planarization

While I ultimately used spin-on glass for planarization, I also tried several methods to deposit HfO_2 to evaluate if it would be possible to planarize the uneven surface, including: sputtering, electron beam evaporation, and sol-gel-based chemical solution deposition.

Although another common method for planarization is chemical-mechanical polishing (CMP), I decided against this because of concerns that CMP would be too dirty and that the full tantalum wafer was not flat enough.

All initial deposition experiments were done on silicon pieces and silicon PhC pieces filled with HfO_2.

The sol-gel planarization tests are detailed in Appendix H.

F.1 RF Sputtering of hafnium oxide on silicon PhCs

For the initial run we deposited about 85 nm of HfO_2. I used the RF sputtering tool in Professor Vladimir Bulović's group, with the assistance of Ella Wassweiler, with conditions as described in Table F.1. I measured the thickness and a refractive index of $\sim$2 on a flat HfO_2 on silicon sample using a spectroscopic ellipsometer.

However, according to focused ion beam (FIB) cross sections (Figure F-2), it

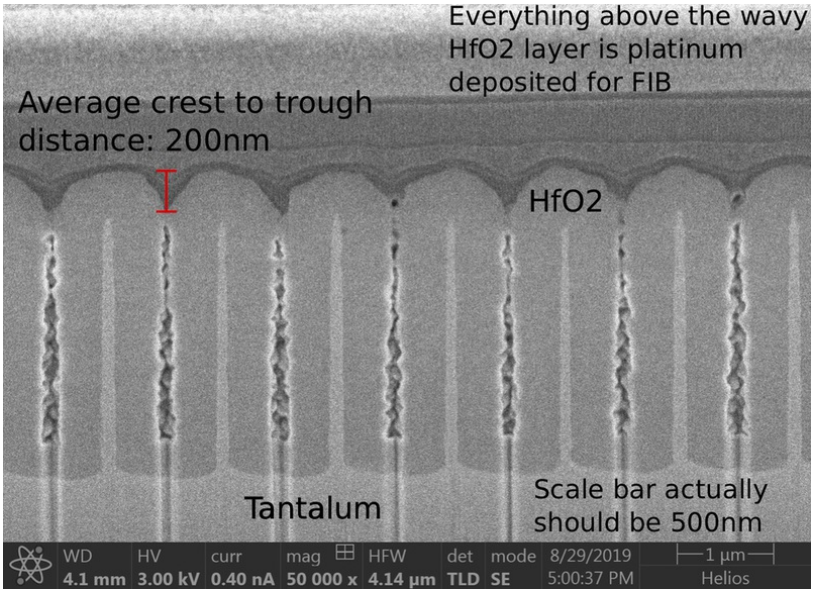

(a) The average crest to trough z-height difference in the HfO_2 top surface is 200nm. This SEM image has a tilt angle correction of 52° but it should be 38°.

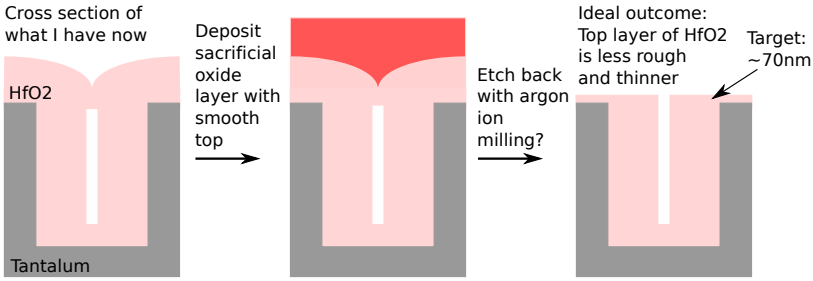

(b) The approach is to deposit a sacrificial layer and etch back until the desired thickness.

Figure F-1: Approach for smoothing out uneven HfO_2 top surface

Target	3-inch diameter HfO_2 target, purchased from Kurt Lesker
Base pressure	2.3-2.5 $\times 10^{-6}$ Torr
Deposition rate	0.1-0.2 Å s^{-1}
Power	60 W
Gas flow	Argon, 10 sccm
Growth pressure	3 mTorr
Spincoating	Dispense

Table F.1: Conditions for HfO_2 sputtering in Bulović group

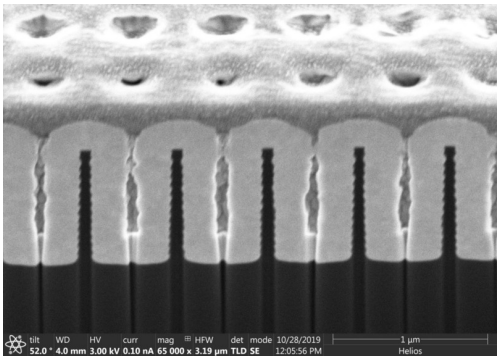

(a) Before sputtering, on average the thickest areas were 242 nm, thinnest areas were 91 nm, $\Delta z = 151$ nm. This SEM image has no tilt angle correction.

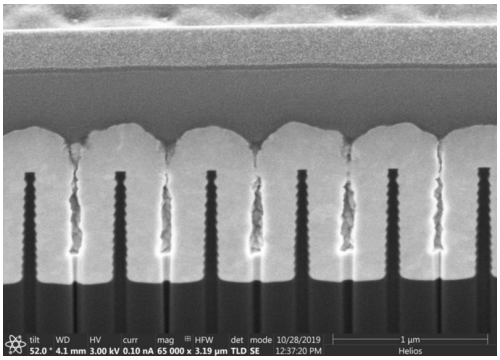

(b) After sputtering, on average the thickest areas were 348 nm, thinnest areas were 167 nm, $\Delta z = 181$ nm. This SEM image has no tilt angle correction.

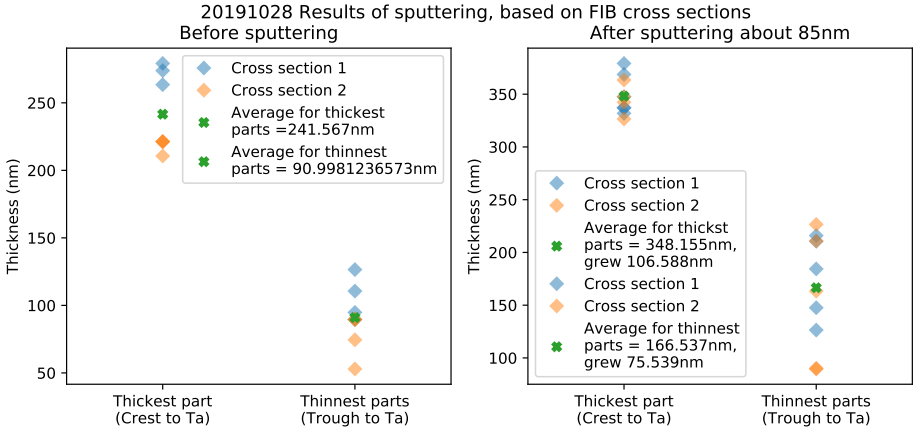

(c) The thicker parts of the HfO_2 top surface grew more quickly ($\Delta z = 107$ nm) than the thinner parts ($\Delta z = 76$ nm).

Figure F-2: First HfO_2 sputtering run

appeared that sputtering preferentially deposited in the crest areas of the HfO_2 top surface, resulting in a greater Δz between the crest and trough after sputtering than before sputtering.

The atomic force microscopy (AFM) measurements (Figure F-3) also did not conclusively indicate much of a difference in Δz between before and after sputtering.

The objective of the second sputtering was to reduce the sputtering pressure and sputter a thicker film (hundreds of nanometers) to see if the film would eventually smooth out. Although Kurt Lesker had recommended reducing the sputtering pressure from 3 mTorr to 1.5 mTorr, the vacuum was unstable unless it was set to 3 mTorr

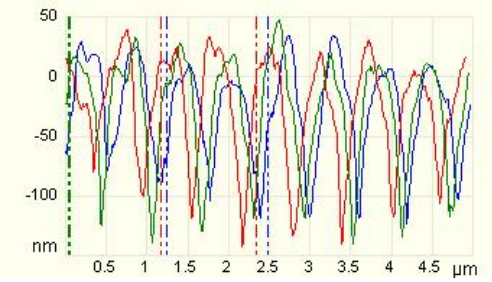

(a) Before sputtering, Δz looks to be about 150 nm.

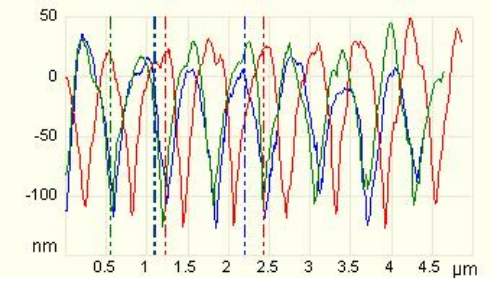

(b) After sputtering, Δz looks to be about 150 nm.

Figure F-3: First HfO_2 sputtering run: Atomic force microscopy (AFM) results do not show much difference between before and after sputtering.

as in the original case.

According to ellipsometry results the thickness of the sputtered film ranged from about 273-297 nm.

The FIB images (Figure F-5) did not show a smoother HfO_2 top surface; the average Δz was about 183 nm and not very different from the original 200 nm.

F.2 Electron-beam evaporation of hafnium oxide on silicon PhCs

Jim Daley of NSL did e-beam evaporation and deposited about 170-180 nm, with n = 1.8-1.9.

The FIB image (Figure F-5a) shows that the evaporated film did not planarize the HfO_2 top surface. Moreover, 1) more material evaporated on the crest areas than the trough areas 2) the evaporated film did not fill the troughs well, 3) the evaporated film shows cracks at the top, and 4) the evaporated and ALD films are distinct, which likely means their etch rates would be different.

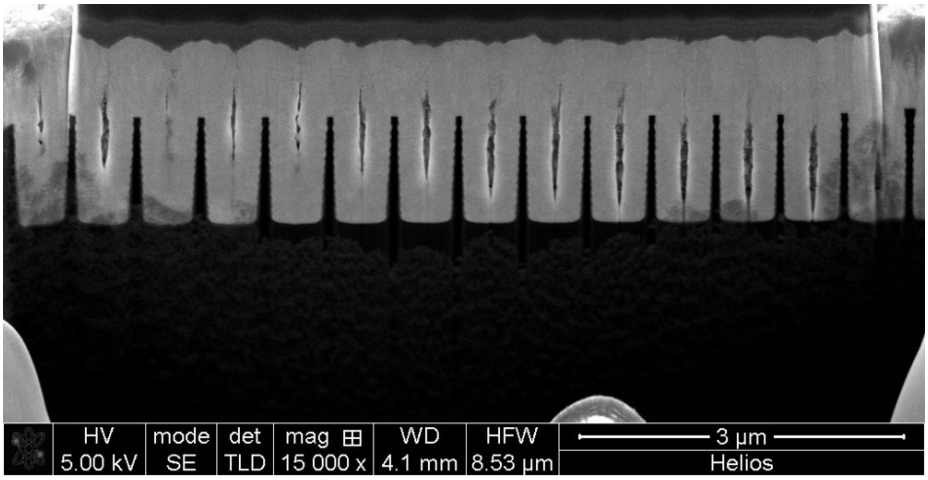

(a) This FIB cut after the second sputtering run is not particular good, because it is neither perpendicular to the surface nor cutting across equal points in the cavity, but the left side of the clearly shows an uneven top surface. On the right side the surface only looks somewhat smooth because it depicts an area away from the cavity center.

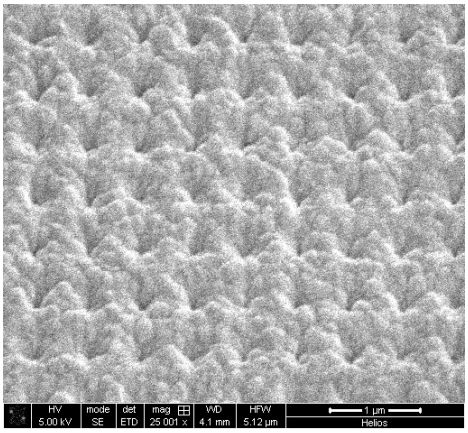

(b) The top surface of the sample after sputtering looks uneven. 52° tilt.

Figure F-4: Results of second HfO_2 sputtering run

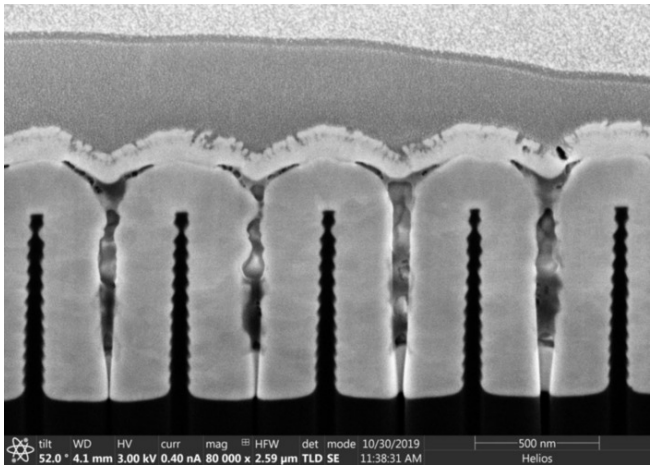

(a) The evaporated film does not planarize the HfO_2, in addition to suffering from a few other imperfections.

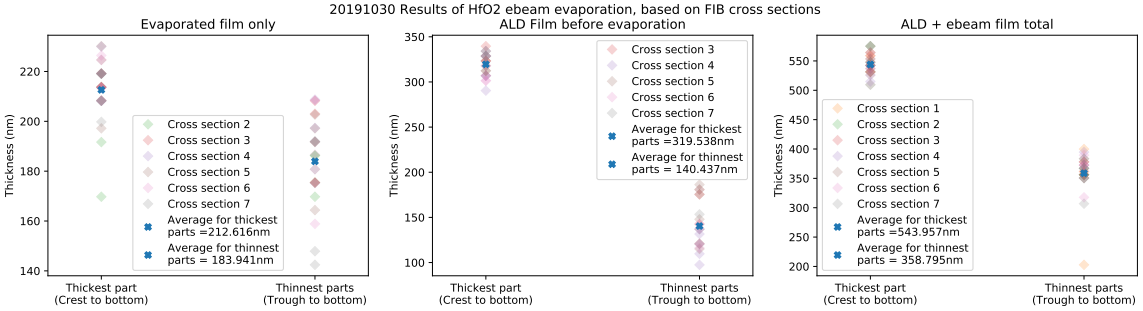

(b) The leftmost graph shows that more material (213 nm) evaporated on the crest area of HfO_2 rather than trough area (184 nm), increasing the Δz of the HfO_2 top surface.

Figure F-5: Electron beam evaporation of HfO_2

Appendix G

Some materials properties

Some materials properties for tantalum, tungsten, and hafnium oxide are included here.

Surface diffusivity of Ta	[84]	$D(\mathrm{cm}^2/\mathrm{s}) = 18\ \exp(\text{-}2.6\ \mathrm{eV}\ /\ k_B T)$
Surface diffusivity of W	[84]	$D(\mathrm{cm}^2/\mathrm{s}) = 0.24\ \exp(\text{-}2.85\ \mathrm{eV}\ /\ k_B T)$

Table G.1: Diffusion for metals (Arrhenius equation $D = D_0 e^{(-\frac{E_a}{k_B T})}$)

Material	Melting point
Tantalum	$3290\,\mathrm{K} = 3017\,^{\circ}\mathrm{C}$
Tungsten	$3695\,\mathrm{K} = 3422\,^{\circ}\mathrm{C}$
HfO_2	$3031\,\mathrm{K} = 2758\,^{\circ}\mathrm{C}$

Table G.2: Melting points

O_2 interstitial diffusion through HfO_2	[67]	$E_a \sim 2.2\,\text{eV}$ (1D metamaterial emitter, annealed 1156-1545C)
Some other experimental results for O_2 diffusion through HfO_2	[106]	E_a = 1eV in annealed amorphous HfO_2 near 1000K
	[106]	2.4eV for neutral oxygen in monoclinic HfO_2
	[106]	0.69-0.96eV for the doubly positively charged oxygen vacancy in monoclinic HfO_2
	[106]	0.6eV for O2- exchange diffusion and 1.8eV for O2- interstitial diffusion in monoclinic HfO_2
Some computational results for O_2 diffusion through HfO_2	[106]	COMB: $D(\text{m}^2/\text{s})$ = 3.3e-9 exp(-0.53eV / k_BT)
	[106]	MBKS, 1625-2000K (1352 - 1727C): $D(\text{m}^2/\text{s})$ = 2.4e-5 exp(-2.2eV / k_BT)
	[106]	MBKS, 1000-1600K (727 - 1327C): $D(\text{m}^2/\text{s})$ = 7.0e-11 exp(-0.36eV / k_BT)
Other computational results for oxygen interstitial diffusion through HfO_2	[107]	O^0: Exchange activation barrier = 0.8eV, interstitial activation barrier = 1.3eV
	[107]	O^-: Exchange activation barrier = 0.3eV, interstitial activation barrier = 1.1eV
	[107]	O^{2-}: Exchange activation barrier = 0.6eV, interstitial activation barrier = 1.8eV

Table G.3: Diffusion for HfO_2

Material	Reference	Temperature range	Thermal expansion coefficient
Tantalum (both “worked" and “annealed" tantalum)	[108]	20-500 °C	6.6×10^{-6} /K
Tungsten	[109]	400-500 °C	4.8×10^{-6} /K
Monoclinic HfO_2 (anisotropic)	[110]	850 °C	a direction 9.7×10^{-6}/K, b axis 1.6×10^{-6}/K, c direction 14.1×10^{-6}/K
		950 °C	a direction 10.0×10^{-6}/K, b axis 1.4×10^{-6}/K, c direction 14.7×10^{-6}/K
		1050 °C	a direction 10.2×10^{-6}/K, b axis 1.0×10^{-6}/K, c direction 15.3×10^{-6}/K

Table G.4: Thermal expansion coefficients

Appendix H

Preliminary tests with hafnium oxide sol-gel: planarization and cavity filling

I used a HfO_2 sol-gel, metallo-organic HfO_2 liquid precursor, to try to planarize filled photonic crystal samples (as detailed in) as well as to fill bare metallic photonic crystal cavities. This appendix briefly discusses the preliminary efforts on both fronts, as well as the preparation of films on flat silicon wafers.

None of these efforts were successful.

The sol-gel was purchased from Kojundo Chemical Laboratory in Japan (product "Hf-05 MOD material," product number HFK01LB, same manufacturer as that used in [111]). The sol-gel is composed of solvents, stabilizer (which needs to break down at high temperature) and the HfO_2 precursor.

H.1 Planarization of silicon photonic crystals already filled with hafnium oxide

H.1.1 Spincoating sol-gel onto a filled photonic crystal

The sol-gel can be spuncoat and annealed to make HfO_2 films, as described in Table H.1, following instructions in the company-supplied manual.

I prepared films on both a flat silicon wafer and a HfO_2-filled silicon PhC.

Spincoating	Dispense (For 3-inch wafer only: spin at 500rpm for 10s) Accelerate to 2000rpm over 5s Spin at 2000rpm for 60s
Drying	120 °C hot plate in a fume hood for 30 minutes
Anneal (in air)	Ramp 25 to 470 °C over 1 hour 30 minutes, $\sim$5 °C min^{-1} Hold at 470 °C for 30 minutes Ramp 470 to 550 °C over 16 minutes, $\sim$5 °C min^{-1} Hold at 550 °C for 1 hour Cool down 550 to 25 °C over 1 hour 45 minutes, $\sim$5 °C min^{-1}

Table H.1: Procedure for preparation of sol-gel-based HfO_2 films

On flat silicon samples, the film did not look smooth (Figure H-1), with strand-like things visible, and the measured index of refraction, ranging from 1.48-1.64, was lower than expected (expected $n \sim 1.9$). According to the manufacturer the strand-like things are probably grain boundaries, which can play a role in lowering the index of refraction; large pores can occur in grain boundaries if the stabilizer cannot degas after it breaks down. Another factor that prevents the densification of the film is if HfO_2 does not fully oxidize (it might have OH ends). The manufacturer also said that a higher index of refraction can be obtained by annealing at higher temperatures.

On the silicon PhCs, the sol-gel-based film did not planarize the top surface and the film quality itself was not good. As shown in Figure H-2, there were two kinds of film imperfections: 1) discontinuities in the film that appear roughly periodically, probably corresponding to the trough areas of the HfO_2 top surface in the PhC, and 2) even in continuous areas of the film there appeared to be bubbles, which suggests

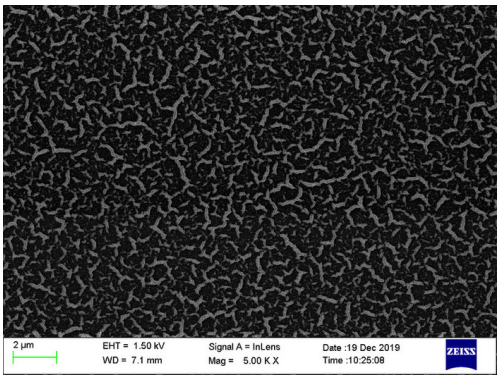

(a) At 5000x magnification, strand-like things are scattered across the sample.

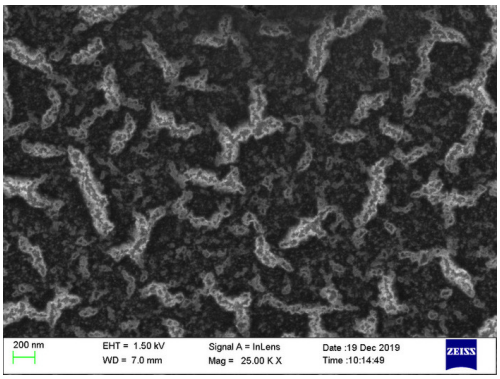

(b) This image is at 10° tilt, 25000x magnification.

Figure H-1: HfO_2 sol-gel on flat silicon

that the stabilizer did not degas.

The failure to planarize is likely because the deposited volume decreases during processing: first the solvent and stabilizer degasses, and then the ceramic shrinks at high temperature to reduce surface energy. According to the manufacturer, adhesion should be easy; in fact with the solvent (isoamyl acetate) it is expected that capillary action will bring the solvent into the cavities.

The key to successful planarization and film densification appears to anneal, if possible, so that the stabilizer breaks down and degasses but does not lead to the ceramic shrinking. Because this is only possible if the stabilizer breakdown and ceramic shrinking occur at different temperatures and are not directly connected, the manufacturer provided thermogravimetric analysis (TGA) and differential thermal analysis (DTA) results (Figure H-3). The solvent appears to evaporate by 120 °C, leading to most of the weight loss and the first DTA peak. Around 350-450 °C, the second peak, the precursor breaks down and degasses (the degassing leads to the decrease in weight). The manufacturer also suggested that the film may shrink around 350-450 °C.

H.1.2 Pipetting sol-gel onto a filled photonic crystal

I also tried to pipette sol-gel onto a filled photonic crystal, but no HfO_2 film could be seen on cross section (Figure H-4).

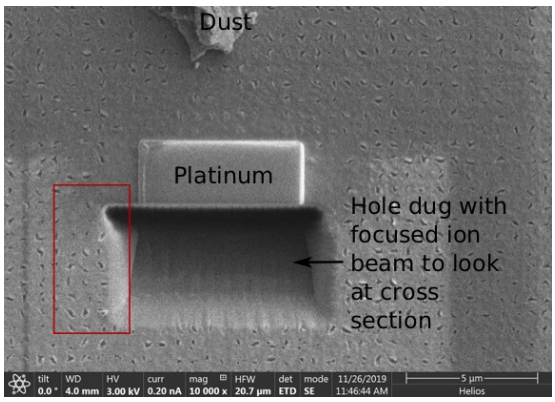

(a) Top view of HfO_2 film (and imaging area, with the deposited platinum rectangle and hole dug for cross section imaging) shows the film nonuniform and "pock-marked" in what appears to be a periodic array. The red rectangle indicates close-up area shown in b). 0° tilt.

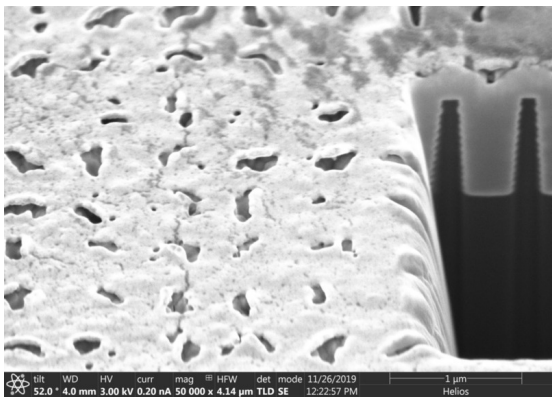

(b) This 52° tilt image of the area enclosed with a red rectangle in a) shows the film has discontinuities, showing the underlying HfO_2. The continuous areas of the film also appear to have bubble-like discolorations.

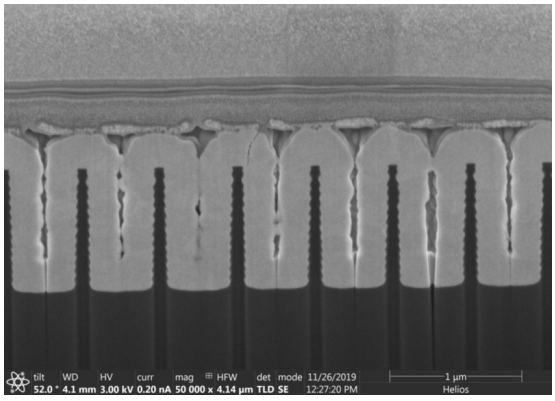

(c) The HfO_2 thin film above the ALD HfO_2 shows discontinuities and did not planarize the PhC.

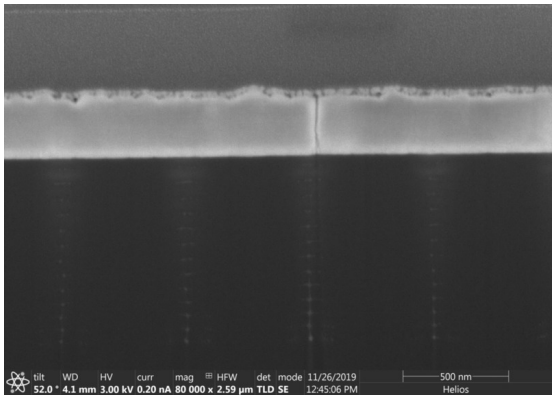

(d) The sol-gel-based HfO_2 is visible distinct from the HfO_2 deposited by ALD. This image shows an area of the PhC between cavities.

Figure H-2: HfO_2 sol-gel spuncoat on a silicon PhC

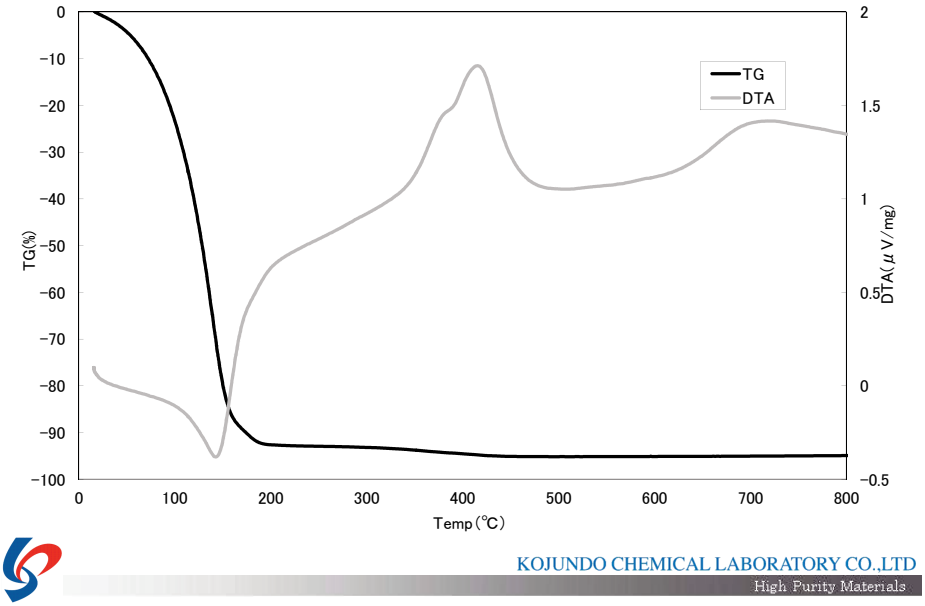

Figure H-3: TGA-DTA results provided by Kojundo Chemical Laboratory. The precipitous loss of weight (TGA) at the beginning corresponds to loss of solvent, which is corroborated by the first DTA peak. The second DTA peak and weight loss around 350-450 °C probably corresponds to precursor breakdown and degassing. The third DTA peak around 700 °C is potentially a phase transition.

H.2 Filling bare silicon photonic crystals

To try to fill empty cavities, I tried the following:

1. Pour (pipette) sol-gel onto bare silicon PhC and dry out with hot plate
2. Immerse bare silicon PhC in a sol-gel solution for about 1.5 hour, remove from the bath, then dry on a hot plate and anneal (the anneal is as described in Table H.1)

H.2.1 Pipetting sol-gel onto an unfilled photonic crystal

This method was not successful; it appeared to only partially fill some of the cavities on some areas of the wafer (see Figures H-5 and H-6).

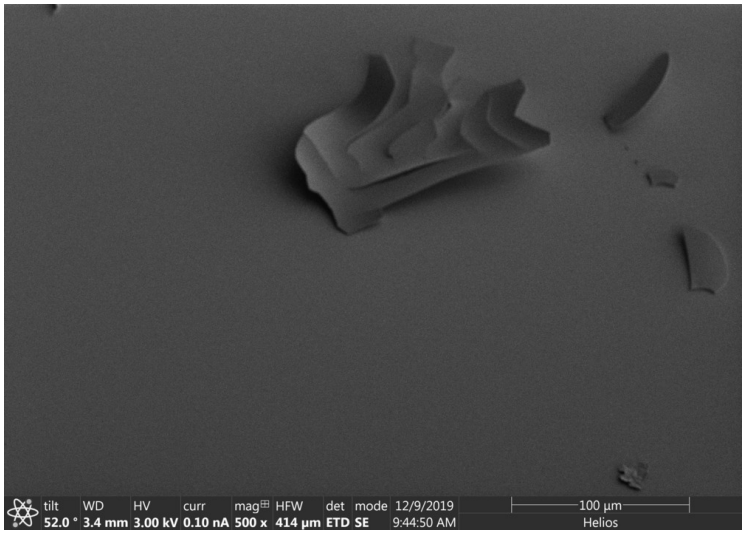

(a) Top view from SEM: large flakes were visible although it was unclear what these were.

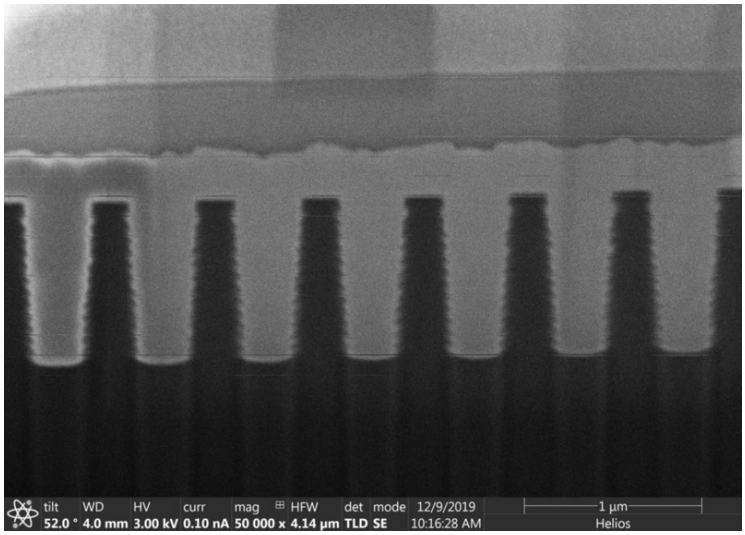

(b)

Figure H-4: Results of pipetting sol-gel onto a filled photonic crystal

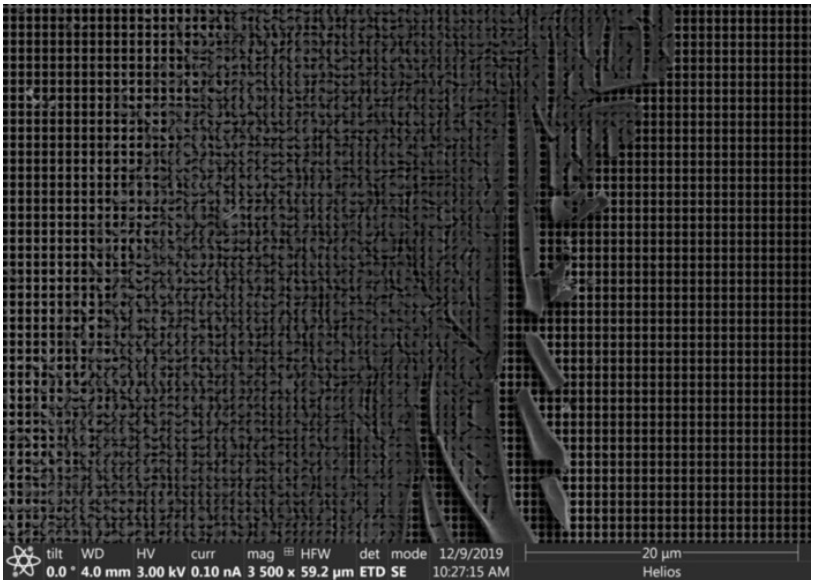

(a) Some areas appeared to have no HfO_2, while some other areas looked as though they may be partially filled.

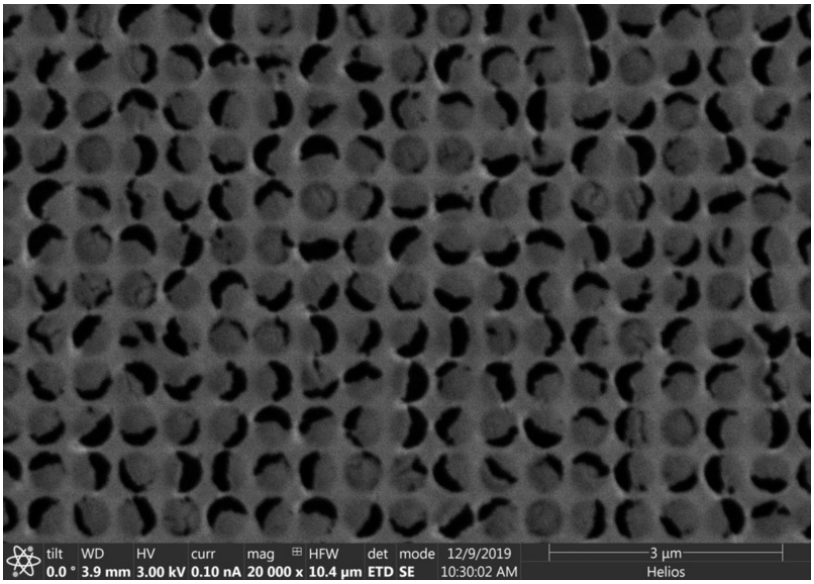

(b) It was difficult to tell from the top how well the cavities had been filled.

Figure H-5: Results of pipetting sol-gel onto an unfilled silicon photonic crystal, top view

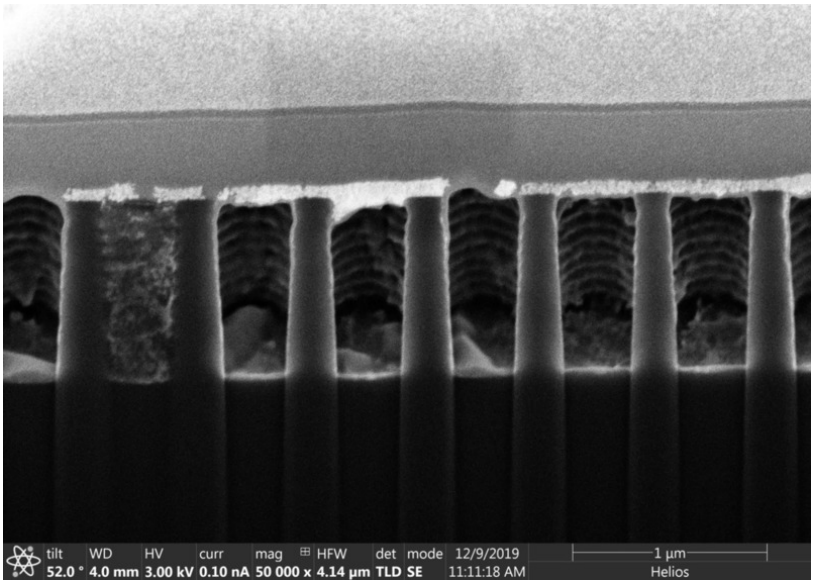

(a) The cavities were not filled; instead a film formed on at the top of the surface.

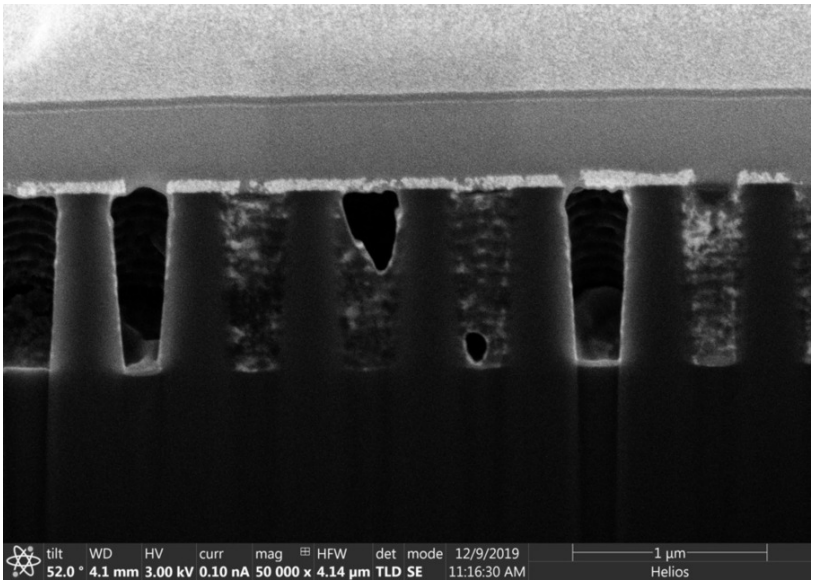

(b) Some of the cavities appeared as though they might be partially-filled, but it is unclear why the material in the cavities appeared darker compared to the material on the top of the cavities.

Figure H-6: Results of pipetting sol-gel onto an unfilled silicon photonic crystal, cross section

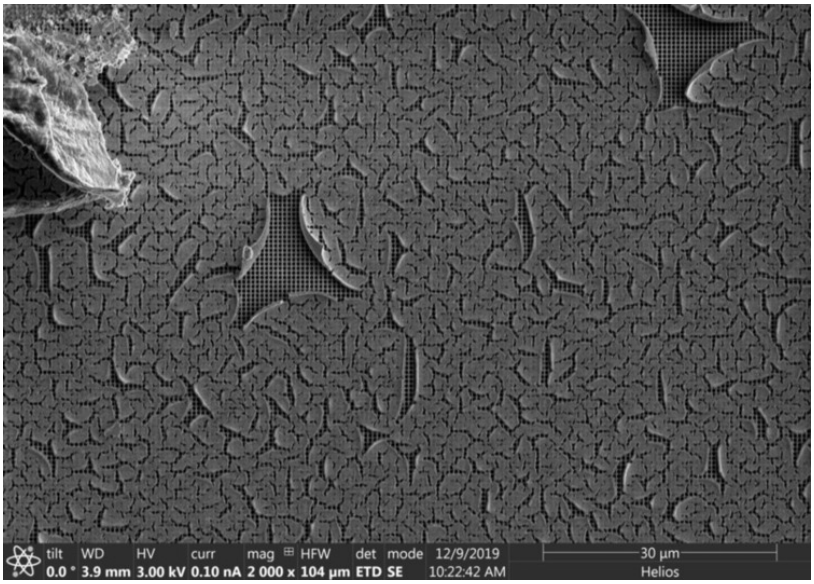

(a) A discontinuous film formed on the top surface of the photonic crystal; parts of the film appear to have peeled.

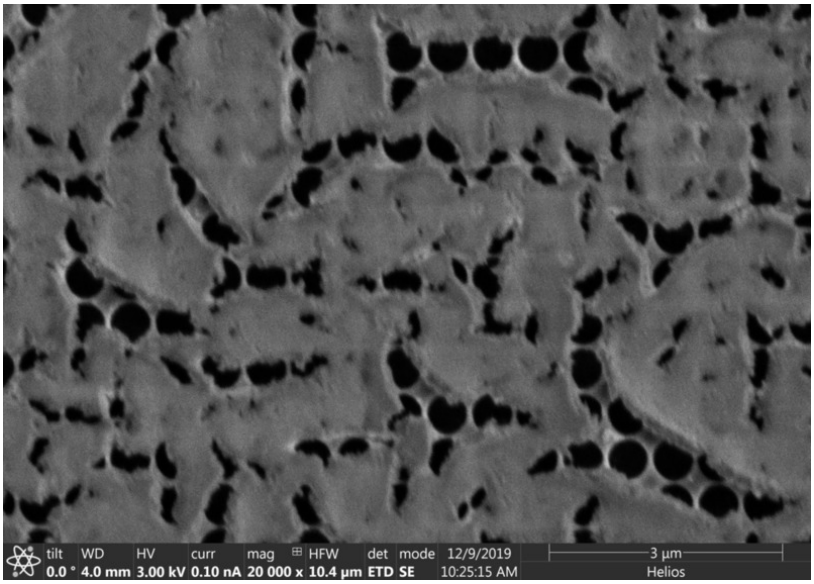

(b) Closer look at the film on the top surface of the photonic crystal.

Figure H-7: Results of immersing an unfilled silicon photonic crystal into sol-gel solution, top view

H.2.2 Immersing an unfilled photonic crystal in sol-gel

In this case, a discontinuous film formed on the top surface of the photonic crystal, and in parts of the film appeared to be peeling off (Figure H-7).

Bibliography

[1] V. Stelmakh, W.R. Chan, M. Ghebrebrhan, M. Soljačić, J.D. Joannopoulos, and I. Čelanović. Fabrication of an omnidirectional 2d photonic crystal emitter for thermophotovoltaics. *J. Phys.: Conf. Series*, 773:012037, 2016.

[2] R. Sakakibara, V. Stelmakh, W.R. Chan, M. Ghebrebrhan, J.D. Joannopoulos, M. Soljačić, and I. Čelanović. Improved omnidirectional 2d photonic crystal selective emitter for thermophotovoltaics. *J. Phys.: Conf. Series*, 1052, 2018.

[3] W.R. Chan, V. Stelmakh, M. Ghebrebrhan, M. Soljačić, J.D. Joannopoulos, and I. Čelanović. Enabling efficient heat-to-electricity generation at the mesoscale. *Energy Environ. Sci.*, 10:1367, 2017.

[4] H.H. Kolm. Solar-battery power source. Quarterly Progress Report, Solid State Research, Group 35 35, MIT Lincoln Laboratory, 1956.

[5] R.E. Nelson. A brief history of thermophotovoltaic development. *Semicond. Sci. Technol.*, 18:S141, 2003.

[6] V. Stelmakh. *A Practical High Temperature Photonic Crystal for High Temperature Thermophotovoltaics*. PhD thesis, Massachusetts Institute of Technology, 2017.

[7] C.-X. Zu and H. Li. Thermodynamic analysis on energy densitites of batteries. *Energy Environ. Sci.*, 4:2614–2624, 2011.

[8] W.R. Chan. *High efficiency thermophotovoltaic microgenerators*. PhD thesis, Massachusetts Institute of Technology, 2015.

[9] A. H. Epstein. Millimeter-scale, mems gas turbine engine. *Proc. ASME Turbo Expo,*, GT-2003-28, 2003.

[10] O. Dessornes, S. Landais, R. Valle, A. Fourmaux, S. Burguburu, C. Zwyssig, and Z. Kozanecki. Advances in the development of a microturbine engine. *J. Eng. Gas Turbines Power*, 136(7):71201, 2014.

[11] A. Gomez, J. J. Berry, S. Roychoudhury, B. Coriton, and J. Huth. From jet fuel to electric power using a mesoscale, ecient stirling cycle. *Proc. Combust. Inst.*, 31(2):3251–3259, 2007.

[12] A. Kundu, J. H. Jang, J. H. Gil, C. R. Jung, H. R. Lee, S.-H. Kim, B. Ku, and Y. S. Oh. Micro-fuel cells current development and applications. *J. Power Sources*, 170:67–78, 2007.

[13] A. Bieberle-Hutter, D. Beckel, A. Infortuna, U. P. Muecke, J. L. M. Rupp, L. J. Gauckler, S. Rey-Mermet, P. Muralt, N. R. Bieri, N. Hotz, M. J. Stutz, D. Poulikakos, P. Heeb, P. Müler, A. Bernard, R. Gmur, and T. Hocker. A micro-solid oxide fuel cell system as battery replacement. *J. Power Sources*, 177(1):123–130, 2008.

[14] K. Yoshida, S. Tanaka, S. Tomonari, D. Satoh, and M. Esashi. High-energy density miniature thermoelectric generator using catalytic combustion. *J. Microelectromech. Syst.*, 15:195–203, 2006.

[15] C. H. Marton, G. S. Haldeman, and K. F. Jensen. Portable thermoelectric power generator based on a microfabricated silicon combustor with low re- sistance to flow. *Ind. Eng. Chem. Res.*, 50(14):8468–8475, 2011.

[16] L. Fraas, J. Avery, L. Minkin, and J. Strauch. Design and thermal modeling of a portable fuel fired cylindrical tpv battery replacement. Technical report, Sandia National Laboratories, 2010.

[17] X. Wang, W.R. Chan, V. Stelmakh, M. Soljačić, J.D. Joannopoulos, I. Čelanović, and P.H. Fisher. Prototype of radioisotope thermophotovoltaic system using photonic crystal spectral control. *J. Phys.: Conf. Ser.*, 660:012034, 2015.

[18] X. Wang. *Toward high efficiency radioisotope thermophotovoltaic system by spectral control*. PhD thesis, Massachusetts Institute of Technology, 2017.

[19] A. Datas and A. Martí. Thermophotovoltaic energy in space applications: Review and future potential. *Sol. Energy Mater. Sol. Cells*, 161:285–296, 2017.

[20] L.M. Fraas. Economic potential for thermophotovoltaic electric power generation in the steel industry. *40th IEEE Photovoltaic Specialists Conference*, 2014.

[21] H. Yugami, H. Sai, K. Nakamura, N. Nakagawa, and H. Ohtsubo. Solar thermophotovoltaic using al2o3/er3al5o12 eutectic composite selective emitter. *IEEE Photovoltaic Spec. Conf.*, 28:1214–1217, 2000.

[22] E. Horne. Hybrid thermophotovoltaic power systems. Technical report, EDTEK, Inc., 2002.

[23] V.M. Andreev, A.S. Vlasov, V.P. Khvostikov, O.A. Khvostikova, P.Y. Gazaryan, S.V. Sorokina, and N.A. Sadchikov. Solar thermophotovoltaic converters based on tungsten emitters. *Journal of Solar Energy Engineering*, 129:298–303, 2007.

[24] A. Datas and C. Algora. Development and experimental evaluation of a complete solar thermophotovoltaic system. *Prog. Photovol. Res. Appl.*, 21:1025–1039, 2013.

[25] A. Lenert, D.M. Bierman, Y. Nam, W.R. Chan, I. Čelanović, M. Soljačić, and E.N. Wang. A nanophotonic solar thermophotovoltaic device. *Nature Nanotechnology*, 9:126–130, 2014.

[26] M. Shimizu, A. Kohiyama, and J. Yugami. High-efficiency solar-thermophotovoltaic system equipped with a monolithic planar selective absorber/emitter. *J. Photon. Energy*, 5:053099, 2015.

[27] A. Kohiyama, M. Shimizu, and H. Yugami. Unidirectional radiative heat transfer with a spectrally selective planar absorber/emitter for high-efficiency solar thermophotovoltaic systems. *Appl. Phys. Express*, 9:112302, 2016.

[28] A. Datas and C. Algora. Detailed balance analysis of solar thermophotovoltaic systems made up of single junction photovoltaic cells and broadband thermal emitters. *Sol. Energy Mater. Sol. Cells*, 94:2137–2147, 2010.

[29] V. Rinnerbauer, A. Lenert, D.M. Bierman, Y.X. Yeng, W.R. Chan, R.D. Geil, J.J. Senkevich, J.D. Joannopoulos, E.N. Wang, M. Soljačić, and I. Čelanović. Metallic photonic crystal absorber-emitter for efficient spectral control in high-temperature solar thermophotovoltaics. *Adv. Energy. Mater.*, 2014.

[30] T. Burger, C. Sempere, B. Roy-Lainde, and A. Lenert. Present efficiencies and future opportunities in thermophotovoltaics. *Joule*, 4(8):1660–1680, 2020.

[31] V. M. Andreev, S. V. Sorokina, N. K. Timoshina, V. P. Khvostikov, and M. Z. Shvarts. Solar cells based on gallium antimonide. *Semiconductors*, 43(5):668–671, 2009.

[32] B. Wernsman, R. R. Siergiej, S. D. Link, R. G. Mahorter, M. N. Palmisiano, R. J. Wehrer, R. W. Schultz, G. P. Schmuck, R. L. Messham, S. Murray, C. S. Murray, F. Newman, D. Taylor, D. M. DePoy, and T. Rahmlow. Greater than 20thermophotovoltaic radiator/module system using reflective spectral contro. *IEEE Trans. Electron Devices*, 51(3):512–515, 2004.

[33] M. W. Dashiell, J. F. Beausang, H. Ehsani, G. J. Nichols, D. M. Depoy, L. R. Danielson, P. Talamo, K. D. Rahner, E. J. Brown, S. R. Burger, P. M. Fourspring, W. F. Topper, P. F. Baldasaro, C. A. Wang, R. K. Huang, M. K. Connors, G. W. Turner, Z. A. Shellenbarger, G. Taylor, J. Li, R. Martinelli, D. Donetski, S. Anikeev, G. L. Belenky, and S. Luryi. Quaternary ingaassb thermophotovoltaic diodes. *IEEE Trans. Electron Devices*, 53(12):2879–2888, 2006.

[34] C.H. Henry. Limiting efficiencies of ideal single and multiple energy gap terrestrial solar cells. *J. Appl. Phys.*, 51:4494, 1980.

[35] Z. Omair, G. Scranton, L.M. Pazos-Outón, T.P. Xiao, M.A. Steiner, V. Ganapati, P.F. Peterson, J. Holzrichter, H. Atwater, and E. Yablonovitch. Ultra-efficient thermophotovoltaic power conversion by band-edge spectral filtering. *Proc. Natl. Acad. Sci. U.S.A.*, 116(31):15356–15361, 2019.

[36] Y.X. Yeng. *Photonic Crystals for High Temperature Applications*. PhD thesis, Massachusetts Institute of Technology, 2014.

[37] D. Fan, T. Burger, S. McSherry, B. Lee, A. Lenert, and S.R. Forrest. Near-perfect photon utilization in an air-bridge thermophotovoltaic cell. *Nature*, 586:237, 2020.

[38] E. Rephaeli and S. Fan. Absorber and emitter for solar thermophotovoltaic systems to achieve efficiency exceeding the shockley-queisser limit. *Opt. Express*, 17(17):15145–15159, 2009.

[39] R. Sakakibara, V. Stelmakh, W.R. Chan, M. Ghebrebrhan, J.D. Joannopoulos, M. Soljačić, and I. Čelanović. Practical emitters for thermophotovoltaics: a review. *J. Photonics Energy*, Accepted.

[40] Y.X. Yeng, W.R. Chan, V. Rinnerbauer, J.D. Joannopoulos, M. Soljačić, and I. Čelanović. Performance analysis of experimentally viable photonic crystal enhanced thermophotovoltaic systems. *Opt. Express*, 21(S6):A1035, 2013.

[41] W. Yang, S. Chou, C. Shu, H. Xue, and Z. Li. Research on micro-thermophotovoltaic power generators with different emitting materials. *J. Micromech. Microeng.*, 15:S239, 2005.

[42] L. Fraas, J. Samaras, J. Avery, and L. Minkin. Antireflection coated refractory metal matched emitters for use with gasb thermophotovoltaic generators. *IEEE*, 2000.

[43] E. Doyle, K. Shukla, and C. Metcalfe. Development and demonstration of a 25 watt thermophotovoltaic power source for a hybrid power system. Tech. rep. tr04-2001, National Aeronautics and Space Administration, 2001.

[44] C. Ungaro, S.K. Gray, and M.C. Gupta. Solar thermophotovoltaic system using nanostructures. *Optics Express*, 23(19), 2015.

[45] T. Aicher, P. Kästner, A. Gopinath, A. Gombert, A. W. Bett, T. Schlegl, C. Hebling, and J. Luther. Development of a novel tpv power generator. *AIP Conference Proceedings*, 738:71, 2004.

[46] K. Qiu, A.C.S Hayden, and E. Entchev. Tpv power generation system using a high temperature metal radiant burner. *AIP Conference Proceedings*, 890:27–36, 2007.

[47] K.W. Stone, D.L. Chubb, D.M. Wilt, and M.W. Wanlass. Testing and modeling of a solar thermophotovoltaic power system. *AIP Conference Proceedings*, 199:199–209, 1996.

[48] K.C. Chen, D. Osborn, P. Sarmiento, A. Prasad, and S. Earath. Small, efficient thermophotovoltaic power supply. Technical Report DAAG55-97-C-0003, U.S. Army Research Office, 1999.

[49] B. Bitnar, W. Durisch, J.-C. Mayor, J. Sigg, and H.R. Tschudi. Characterisation of rare earth selective emitters for thermophotovoltaic applications. *Solar Energy Materials and Solar Cells*, 73:221–234, 2002.

[50] S. Bitnar, W. Durisch, G. Palfinger, F. von Roth, U. Vogt, A. Brönstrup, and D. Seiler. Practical thermophotovoltaic generators. *Semiconductors*, 28:941–945, 2004.

[51] R.E. Nelson. Tpv systems and state-of-art development. In T. J. Coutts, G. Guazzoni, and J. Luther, editors, *Fifth Conference on Thermophotovoltaic Generation of Electricity*, volume 653 of *American Institute of Physics Conference Series*, pages 3–17, 2003.

[52] W.R. Chan, P. Bermel, R.C.N. Pilawa-Podgurski, C.H. Marton, K.F. Jensen, J.J. Senkevich, J.D. Joannopoulos, M. Soljačić, and I. Čelanović. Toward high-energy-density, high-efficiency, and moderate-temperature chip-scale thermophotovoltaics. *Proc. Natl. Acad. Sci. U.S.A.*, 110(14):5309–5314, 2013.

[53] D.M. Bierman, A. Lenert, W.R. Chan, B. Bhatia, I. Čelanović, M. Soljačić, and E.N. Wang. Enhanced photovoltaic energy conversion using thermally based spectral shaping. *Nature Energy*, 1, 2016.

[54] H. Sai, Y. Kanamori, and H. Yugami. High-temperature resistive surface grating for spectral control of thermal radiation. *Appl. Phys. Lett.*, 82(11):1685–1687, 2003.

[55] H. Sai and H. Yugami. Thermophotovoltaic generation with selective radiators based on tungsten surface gratings. *Appl. Phys. Lett.*, 85:3399, 2004.

[56] A. Heinzel, V. Boerner, A. Gombert, B. Bläsi, V. Wittwer, and J. Luther. Radiation filters and emitters for the nir based on periodically structured metal surfaces. *Journal of Modern Optics*, 47(13):2399–2419, 2000.

[57] H. Qiao, J. Yang, F. Wang, Y. Yang, and J. Sun. Femtosecond laser direct writing of large-area two-dimensional metallic photonic crystal structures on tungsten surfaces. *Opt. Express*, 23(20):26617–26627, 2015.

[58] M. Suemitsu, T. Asano, M. De Zoysa, and S. Noda. Wavelength-selective thermal emitters using si-rods on mgo. *Appl. Phys. Lett.*, 112:011103, 2018.

[59] M. Suemitsu, T. Asano, T. Inoue, and S. Noda. High-efficiency thermophotovoltaic system that employs an emitter based on a silicon rod-type photonic crystal. *ACS Photonics*, 7(1):80–87, 2020.

[60] J. Hao, J. Wang, X. Liu, W.J. Padilla, L. Zhou, and M. Qiu. High performance optical absorber based on a plasmonic metamaterial. *Appl. Phys. Lett.*, 96:351104, 2010.

[61] B. Zhang, J. Hendrickson, and J. Guo. Multispectral near-perfect metamaterial absorbers using spatially multiplexed plasmon resonance metal square structures. *J. Opt. Soc. Am. B*, 30:656, 2013.

[62] C. Shemelya, D. DeMeo, N. Pfiester Latham, X. Wu, C. Bingham, W. Padilla, and T.E. Vandervelde. Stable high temperature metamaterial emitters for thermophotovoltaic applications. *Appl. Phys. Lett.*, 104:201113, 2014.

[63] W. Li, U. Guler, N. Kinsey, G.V. Naik, A. Boltasseva, J. Guan, V.M. Shalaev, and A.V. Kildishev. Refractory plasmonics with titanium nitride: Broadband metamaterial absorber. *Adv. Mater.*, 26:7959–7965, 2014.

[64] D. Woolf, J. Hensley, J.G. Cederberg, D.T. Bethke, A.D. Grine, and E.A. Shaner. Heterogeneous metasurface for high temperature selective emission. *Appl. Phys. Lett.*, 105:0181110, 2014.

[65] D.N. Woolf, E.A. Kadlec, D. Bethke, A.D. Grine, J.J. Nogan, J.G. Cederberg, D.B. Bruckel, T.S. Luk, E.A. Shaner, and J.M. Hensley. High-efficiency thermophotovoltaic energy conversion enabled by a metamaterial selective emitter. *Optica*, 5(2):213–218, 2018.

[66] P.N. Dyachenko, S. Molesky, A. Yu Petrov, M. Störmer, T. Krekeler, S. Lang, M. Ritter, Z. Jacob, and M. Eich. Controlling thermal emission with refractory epsilon-near-zero metamaterials via topological transitions. *Nat. Commun.*, 7:11809, 2016.

[67] M. Chirumamilla, G.V. Krishnamurthy, K. Knopp, T. Krekeler, M. Graf, D. Jalas, M. Ritter, M. Störmer, A.Y. Petrov, and M. Eich. Metamaterial emitter for thermophotovoltaics stable up to 1400 °c. *Nature Scientific Reports*, 9:7241, 2019.

[68] C. Schlemmer, J. Aschaber, V. Boerner, and J. Luther. Thermal stability of micro-structured selective tungsten emitters. *AIP Conference Proceedings*, 653:164–173, 2003.

[69] N. R. Denny, S. E. Han, D. J. Norris, and A. Stein. Effects of thermal processes on the structure of monolithic tungsten and tungsten alloy photonic crystals. *Chem. Mater.*, 19:4563–4569, 2007.

[70] N. R. Denny, F. Li, D. J. Norris, and A. Stein. In situ high temperature tem analysis of sintering in nanostructured tungsten and tungsten molybdenum alloy photonic crystals. *J. Mater. Chem.*, 20(8):1538–1545, 2010.

[71] K.A. Arpin, M.D. Losego, and P.V. Braun. Electrodeposited 3d tungsten photonic crystals with enhanced thermal stability. *Chem. Mater.*, 23:4783–4788, 2011.

[72] S. G. Rudisill, Z. Wang, and A. Stein. Maintaining the structure of templated porous materials for reactive and high-temperature applications. *Langmuir*, 28:7310–7324, 2012.

[73] K.A. Arpin, M.D. Losego, A.N. Cloud, H. Ning, J. Mallek, N.P. Sergeant, L. Zhu, Z. Yu, B. Kalanyan, G.N. Parsons, G.S. Girolami, J.R. Abelson, S. Fan, and P.V. Braun. Three-dimensional self-assembled photonic crystals with high temperature stability for thermal emission modification. *Nat. Commun.*, 4, 2013.

[74] H. J. Lee, K. Smyth, S. Bathurst, J. B. Chou, M. Ghebrebrhan, J. D. Joannopoulos, N. Saka, and S.-G. Kim. Hafnia-plugged microcavities for thermal stability of selective emitters. *Appl. Phys. Lett.*, 102(24), 2013.

[75] U. Guler, A. Boltasseva, and V.M. Shalaev. Refractory plasmonics. *Sciecne*, 344:263–264, 2014.

[76] V. Tomer, R. Teye-Mensah, J.C. Tokash, N. Stojilovic, W. Kataphinan, E.A. Evans, G.G. Chase, R.D. Ramsier, D.J. Smith, and D.H. Reneker. Selective emitters for thermophotovoltaics: erbia-modified electrosopun titania nanofibers. *Solar Energy Materials and Solar Cells*, 85:477–488, 2005.

[77] V. Rinnerbauer, S. Ndao, Y.X. Yeng, J.J. Senkevich, K.F. Jensen, J.D. Joannopoulos, M. Soljačić, and I. Čelanović. Large-area fabrication of high aspect ratio tantalum photonic crystals for high-temperature selective emitters. *J. Vac. Sci. Technol. B*, 31(1):011802, 2013.

[78] V. Rinnerbauer, Y.X. Yeng, W.R. Chan, J.J. Senkevich, J.D. Joannopoulos, M. Soljačić, and I. Čelanović. High-temperature stability and selective thermal emission of polycrystalline tantalum photonic crystals. *Opt. Express*, 21(9):11482–11491, 2013.

[79] V. Stelmakh, D. Peykov, W. R. Chan, J. J. Senkevich, J. D. Joannopoulos, M. Soljačić, I. Čelanović, R. Castillo, K. Coulter, and R. Wei. Thick sputtered tantalum coatings for high-temperature energy conversion applications. *Journal of Vacuum Science and Technology A: Vacuum, Surfaces, and Films*, 33:061204, 2015.

[80] Y.X. Yeng, M. Ghebrebrhan, P. Bermel, W.R. Chan, J.D. Joannopoulos, M. Soljačić, and I. Čelanović. Enabling high-temperature nanophotonics for energy applications. *Proc. Natl. Acad. Sci. U.S.A.*, 109(7):2280–2285, 2012.

[81] V. Stelmakh, V. Rinnerbauer, R.D. Geil, P.R. Aimone, J.J. Senkevich, J.D. Joannopoulos, M. Soljačić, and I. Čelanović. High-temperature tantalum tungsten alloy photonic crystals: Stability, optical properties, and fabrication. *Appl. Phys. Lett.*, 103:123903, 2013.

[82] P. Nagpal, D.P. Josephson, N.R. Denny, J. DeWilde, D.J. Norris, and A. Stein. Fabrication of carbon / refractory metal nanocomposites as thermally stable metallic photonic crystals. *J. Mater. Chem.*, 21:10836, 2011.

[83] V. Stelmakh, V. Rinnerbauer, W.R. Chan, J.J. Senkevich, J.D. Joannopoulos, M. Soljačić, and I. Čelanović. Performance of tantalum-tungsten alloy selective emitters in thermophotovoltaic systems. *Proc. of SPIE*, **9115**:911504–1–8, 2014.

[84] D. Peykov, Y. X. Yeng, I. Čelanović, J. D. Joannopoulos, and C. A. Schuh. Effects of surface diffusion on high temperature selective emitters. *Opt. Express*, 23(8):9979, 2015.

[85] W.R. Chan, V. Stelmakh, W.R. Allmon, C.M. Waits, M. Soljačić, J.D. Joannopoulos, and I. Čelanović. An integrated microcombustor and photonic crystal emitter for thermophotovoltaics. *J. Phys.: Conf. Series*, 773:012108, 2016.

[86] J.B. Chou, Y.X. Yeng, A. Lenert, V. Rinnerbauer, I. Čelanović, M. Soljačić, E.N. Wang, and S.-G. Kim. Design of wide-angle selective absorbers/emitters with dielectric filled metallic photonic crystals for energy applications. *Opt. Express*, 22(S1):A144–A154, 2014.

[87] Y.X. Yeng, J.B. Chou, V. Rinnerbauer, Y. Shen, S.-G. Kim, J.D. Joannopoulos, M. Soljačić, and I. Čelanović. Global optimization of omnidirectional wavelength selective emitters/absorbers based on dielectric-fileld anti-reflection coated two-dimensional metallic photonic crystals. *Opt. Express*, 22(18):21711–21718, 2014.

[88] I. Čelanović, N. Jovanić, and J. Kassakian. Two-dimensional tungsten photonic crystals as selective thermal emitters. *Appl. Phys. Lett.*, 92:193101, 2008.

[89] Ivan Čelanović. *Thermophotovoltaics: Shaping the Flow of Thermal Radiation.* PhD thesis, Massachusetts Institute of Technology, 2006.

[90] M. Ghebrebrhan, P. Bermel, Y.X. Yeng, I. Čelanović, M. Soljačić, and J.D. Joannopoulos. Tailoring thermal emission via q matching of photonic crystal resonances. *Phys. Rev. A*, 83:033810‘, 2011.

[91] V. Rinnerbauer, Y. Shen, J.D. Joannopoulos, M. Soljačić, F. Schäffler, and I. Čelanović. Superlattice photonic crystal as a broadband solar absorber for high temperature operation. *Opt. Express*, 22(7):A1895–A1906, 2014.

[92] V. Liu and S. Fan. S^4: A free electromagnetic solver for layered periodic structures. *Computer Physics Communications*, 183:2233–2244, 2012.

[93] N. Jovanić, I. Čelanović, and J. Kassakian. Two-dimensional tungsten photonic crystals as thermophotovoltaic selective emitters. *AIP Conference Proceedings*, 890:47–55, 2008.

[94] M. Araghchini, Y.X. Yeng, N. Jovanić, P. Bermel, L.A. Kolodziejski, M. Soljačić, I. Čelanović, and J.D. Joannopoulos. Fabrication of two-dimensional tungsten photonic crystals for high-temperature applications. *J. Vac. Sci. Technol. B*, 29:61402, 2011.

[95] Gnanavel Vaidhyanathan Krishnamurthy, Manohar Chirumamilla, Surya Snata Rout, Kaline P. Furlan, Tobias Krekeler, Martin Ritter, Hans-Werner Becker, Alexander Yu Petrov, Manfred Eich, and Michael Störmer. Structural degradation of tungsten sandwiched in hafnia layers determined by in-situ xrd up to 1520 °c. *Nature Scientific Reports*, 11(3330), 2021.

[96] M. Shimizu, A. Kohiyama, and H. Yugami. Evaluation of thermal stability in spectrally selective few-layer metallo-dielectric structures for solar thermophotovoltaics. *J. Quant. Spectrosc. Radiat. Transfer*, 212:45–49, 2018.

[97] Krishna Saraswat. Deposition and planarization. EE 331 Notes.

[98] M.F. Modest. *Radiative heat transfer*. Oxford : Academic, 3 edition, 2013.

[99] Markus Deserno. How to generate equidistributed points on the surface of a sphere.

[100] W. Chan, R. Huang, C. Wang, J. Kassakian, and J. Joannopoulos. Modeling low-bandgap thermophotovoltaic diodes for high-efficiency portable power generators. *Solar Energy Materials and Solar Cells*, 94:509–514, 2010.

[101] Scott Wheelock. Email correspondence, 2019.

[102] Filmtronics. Spin-on glass materials: A review of science and practical application. Training presentation.

[103] Filmtronics. Spin-on glasses: Spin-on dielectric materials that fill your needs. Catalog.

[104] Smokefoot. Own work, cc by-sa 3.0. Wikipedia article "Stöber process".

[105] NIST Mass Spectrometry Data Center and William E. Wallace (director). *"Mass Spectra"*, volume NIST Chemistry WebBook, NIST Standard Reference Database Number 69. Eds. P.J. Linstrom and W.G. Mallard, National Institute of Standards and Technology, Gaithersburg MD, 20899, Retrieved January 23, 2020.

[106] W. Shen, N. Kumari, G. Gibson, Y. Jeon, D. Henze, S. Silverthorn, C. Bash, and S. Kumar. Effect of annealing on structural changes and oxygen diffusion in amorphous hfo2 using classical molecular dynamics. *Journal of Applied Physics*, 123:085113, 2018.

[107] A.S. Foster, A.L. Shluger, and R.M. Nieminen. Mechanism of interstitial oxygen diffusion in hafnia. *Phys. Rev. Lett.*, 89:225901, 2002.

[108] P. Hidnert. Thermal expansion of tantalum. *Bureau of Standards Journal of Research*, 2:887–896, 1929.

[109] P. Hidnert and W.T. Sweeney. Thermal expansion of tungsten. *Scientific Papers of the Bureau of Standards*, 20:483–487, 1925.

[110] R.P. Haggerty, P. Sarin, Z.D. Apostolov, P.E. Driemeyer, and W.M. Kriven. Thermal expansion of hfo2 and zro2. *Journal of the American Ceramic Society*, 97(7):2213–2222, 2014.

[111] Z.J. Wang, T. Kumagai, H. Kokawa, M. Ichiki, and R. Maeda. Preparation of hafnium oxide thin films by sol–gel method. *J. Electroceram.*, 21:499–502, 2008.